Washington University in St. Louis
Washington University Open Scholarship

Engineering and Applied Science Theses & Dissertations | McKelvey School of Engineering

Summer 8-15-2016

Calcium Carbonate Formation in Energy-Related Subsurface Environments and Engineered Systems

Qingyun Li
Washington University in St. Louis

Follow this and additional works at: https://openscholarship.wustl.edu/eng_etds

 Part of the Environmental Engineering Commons, Environmental Sciences Commons, and the Geology Commons

Recommended Citation
Li, Qingyun, "Calcium Carbonate Formation in Energy-Related Subsurface Environments and Engineered Systems" (2016). *Engineering and Applied Science Theses & Dissertations*. 188.
https://openscholarship.wustl.edu/eng_etds/188

This Dissertation is brought to you for free and open access by the McKelvey School of Engineering at Washington University Open Scholarship. It has been accepted for inclusion in Engineering and Applied Science Theses & Dissertations by an authorized administrator of Washington University Open Scholarship. For more information, please contact digital@wumail.wustl.edu.

WASHINGTON UNIVERSITY IN ST. LOUIS

Department of Energy, Environmental and Chemical Engineering

Dissertation Examination Committee:
Young-Shin Jun, Chair
Katharine M. Flores
John D. Fortner
Daniel E. Giammar
Carl I. Steefel
Fuzhong Zhang

Calcium Carbonate Formation in Energy-Related Subsurface Environments and Engineered Systems

by

Qingyun Li

A dissertation presented to the
Graduate School of Arts & Sciences
of Washington University in
partial fulfillment of the
requirements for the degree
of Doctor of Philosophy

August 2016
St. Louis, Missouri

© 2016, Qingyun Li

Table of Contents

List of Figures

List of Tables

Acknowledgments

First and foremost, I would like to express my thanks to my advisor, Dr. Young-Shin Jun, who has accompanied me during the wonderful journey of Ph.D. research and has been a very supportive and instructive mentor along the way. During this five year journey, seemingly short in retrospect, she helped me transform from a new graduate student to an independent researcher. Beyond research, I am equally grateful for her encouragement, instructions, and training in ways to improve on my writing, presentation, and communication skills. All my gains along this journey incorporate Dr. Jun's efforts, and will always be with me on my way ahead.

I also owe thanks to my thesis committee members, Dr. Daniel Giammar, Dr. John Fortner, Dr. Fuzhong Zhang, Dr. Katherine Flores, and Dr. Carl Steefel, for their time and valuable advice and comments while serving on my committee. Dr. Daniel Giammar has also been a great mentor during my research rotation, and have inspired me with his solid aqueous chemistry knowledge, organized schedules, and devotion to teaching and guiding young generations. Dr. Katherine Flores and her graduate student Kelly Kranjc kindly helped me in conducting tests using their nanoindentor and taught me to analyze and interpret the data. Dr. Carl Steefel has been a very supportive collaborator too. He patiently guided me through reactive transport modeling which was a new area for me, and spent long hours modifying CrunchTope codes for my system. During our discussions, I was also inspired by his genuineness and persistence in getting the final results.

I am grateful for collaborative efforts by Dr. Yoon Mook Lim at Yonsei University, who taught me basic mechanical engineering concepts and helped me to start my cement mechanical property tests. I would also like to thank Dr. Byeongdu Lee, Dr. Xiaobing Zuo, and Dr. Sönke Seifert at Argonne National Laboratory for assisting me in collecting GISAXS data at the Advanced Photon Source. I am especially thankful for Dr. Byeongdu Lee's patient instruction and

lectures that built my basic knowledge of GISAXS measurement and data analysis. For publishing research outcomes, I appreciate Prof. James Ballard's assistance in polishing each of my manuscripts and many of my abstracts, and for being a great technical writing instructor.

I am truthfully appreciative of the ENCL group members, Dr. Yandi Hu, Dr. Yi Yang, Dr. Xuyang Liu, Dr. Jessica Ray, Dr. Chelsea Neil, Yujia Min, Lijie Zhang, Haesung Jung, Doyoon Kim, and Xuanhao Wu, for their collaboration and discussions in research, and their friendship in life. I am thankful for all my amazing friends who crossed paths with me in my Ph.D. years. They shared with me laughter and sorrows, tolerated my flaws, and added unforgettable memories to my journey.

This research was supported by the Consortium for Clean Coal Utilization and the National Science Foundation's Career Award (EAR-1057117), and by the Center for Nanoscale Control of Geologic CO_2, an Energy Frontier Research Center funded by the U.S. Department of Energy, Office of Science, Office of Basic Energy Sciences, under Award Number DE-AC02-05CH11231. These funding sources are gratefully acknowledged.

Finally, my most sincere gratitude goes to my family for their unconditional love and trust during my ups and downs alike. Particularly, I would like to thank my parents for bringing me into this world and leading me to see the world as worth experiencing, worth understanding, worth fighting or struggling in, and ultimately worth loving. Without their cultivation of my personality and views, I would never have become who I am.

Qingyun Li

Washington University in St. Louis

August 2016

Dedicated to Planet Earth, our home

ABSTRACT OF THE DISSERTATION

Calcium Carbonate Formation in Energy-Related Subsurface Environments and Engineered Systems

by

Qingyun Li

Doctor of Philosophy in Energy, Environmental and Chemical Engineering

Washington University in St. Louis, 2016

Professor Young-Shin Jun, Chair

Geologic CO_2 sequestration (GCS) in subsurface saline aquifers is a promising strategy to mitigate climate change caused by increasing anthropogenic CO_2 emissions from energy production. At GCS sites, interactions between fluids and geomedia are important because they can affect CO_2 trapping efficiency and the safety of CO_2 storage. These interactions include the dissolution and precipitation of minerals. One of the most important minerals is calcium carbonate, because it can permanently trap CO_2.

In this work, Portland cement was used as a model geomedium to investigate the chemical reactions, mechanical alterations, transport of reactive fluids, and the interplay of all these aspects. Also, because Portland cement is used in building and decommissioning CO_2 injection wells, its alteration is important for wellbore integrity. Wellbore cement can deteriorate as a result of extensive reactions with injected CO_2. Typically, a carbonated layer forms, which can partially reduce CO_2 attack by clogging pores in the cement. We conducted high temperature/pressure experiments using Portland cement paste samples, and after 10 days of reaction, quantified the

chemical changes using scanning electron microscope backscattering electron imaging and X-ray diffraction. The mechanical changes were quantified as well using a three-point bending setup and nanoindentation. The experimental results showed that after CO_2 attack, the cement samples decreased in strength by ~80%, and this decrease was closely related to the formation of a wide and weak portlandite-depleted zone in the cement matrix immediately inside of the carbonated layer. The effects of 0.05 M of sulfate ions were also examined. Interestingly, the additional sulfate ions were found to mitigate CO_2 attack by forming a more protective and less soluble carbonated layer, and thus a thinner portlandite-depleted zone.

To further investigate the detailed mechanisms by which the wide and weak portlandite-depleted zone formed and the carbonated layer's surface dissolved, we set up a one-dimensional continuum reactive transport model using the CrunchTope software. Two mechanisms were found to be critical in reproducing our main observations: First, the precipitated $CaCO_3$ could not fill the entire pore spaces in the carbonated layer. The inefficiency of $CaCO_3$ precipitation in filling all the pores might be due to fractures and defects in the carbonated layer, or due to the extent of pore-size-dependent precipitation. Second, nucleation kinetics had to be incorporated into the model to predict the mineral precipitation observed in the reaction solution and to capture the dissolution of the carbonated layer's surface.

To acquire parameters for the incorporation of nucleation kinetics, $CaCO_3$ nucleation experiments were conducted primarily using atomic force microscopy and synchrotron-based *in situ* grazing incidence small angle X-ray scattering. Newly obtained interfacial energies were compared for mica and quartz systems, and a slightly higher interfacial energy was found in the quartz system. The effects of salinity were investigated in the range of 0.15–0.85 M ionic strengths, and we found a decrease of interfacial energies at high salinity. The kinetic factors, including the

apparent activation energy and the pre-exponential factor in the nucleation rate equation, were experimentally obtained for the first time by varying temperatures in the range of 12–31 ^{o}C. These parameters provided the key information for modeling nucleation in geomedia and synthesizing well controlled materials in materials science.

The $CaCO_3$ nucleation studies advanced our current understanding of nucleation under various conditions, and the acquired parameters were indispensable for our numerical simulations of the cement deterioration. The reactive transport modeling work revealed the important mechanisms in the cement–CO_2 reactions, and provided many insights for understanding the chemical and mechanical alterations of geomedia. The investigation of cement deterioration quantitatively coupled the chemical and mechanical changes of the cement samples, and proved that the molecular scale of water–rock reactions can have a substantial impact on the change of the bulk geomedia. Such information can be also be applied to shale/sandstone–CO_2 interactions. Overall, this dissertation presents a platform to understand fluid–geomedia interactions, combining experimental and modeling approaches, and connecting basic sciences and real applications. The advanced understanding of fluid–geomedia interactions will help improve GCS operation and thus address the climate change challenge.

Chapter 1: Introduction

1.1 Background

1.1.1 Geologic CO_2 Sequestration

With the growth of population and development of technology, global demands for energy are skyrocketing. Despite alternative renewable energy sources, such as wind, solar, and nuclear energies, most energy is still produced by comparatively inexpensive burning of coal, oil, and natural gas. The rate of atmospheric CO_2 emission from fossil fuel burning, 35.9 $GtCO_2$/year (billion tonnes of carbon per year) in 2014, keeps increasing at a faster rate.[1] The atmospheric CO_2 concentration increased from 310 ppm in 1950 to 390 ppm in 2015,[1] and is believed to have caused an increase in average global temperature (0.8 ^oC since 1950)[2] and consequential changes in weather and climate, including rising sea levels, severe weathers, ocean acidification, and ice cap shrinkage.[3]

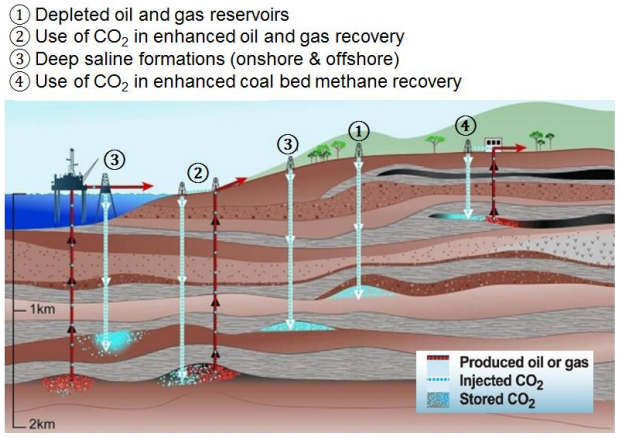

Figure 1.1 Schematic of geologic CO_2 sequestration (IPCC, 2005).[4]

To decrease CO_2 emissions, CO_2 capture and storage (CCS) is a promising approach. It has the potential to contribute to a 19% overall reduction of CO_2 concentrations.[4, 5] CCS includes

capturing CO_2 from large point sources, transporting it to sequestration sites, and sequestering it in deep oceans or geologic formations, such as depleted oil/gas reservoirs and deep saline aquifers (Figure 1.1).[4, 6] Suitable geologic formations should be deeper than 800 m, usually 1.5–3 km deep, to enable CO_2 (critical point 31.1 ^oC and 73.8 bar) to remain in a supercritical phase with reduced volume. The formation should have a caprock of low permeability shale，and have sufficiently permeable formation rocks to facilitate CO_2 injection and storage. [7, 8]

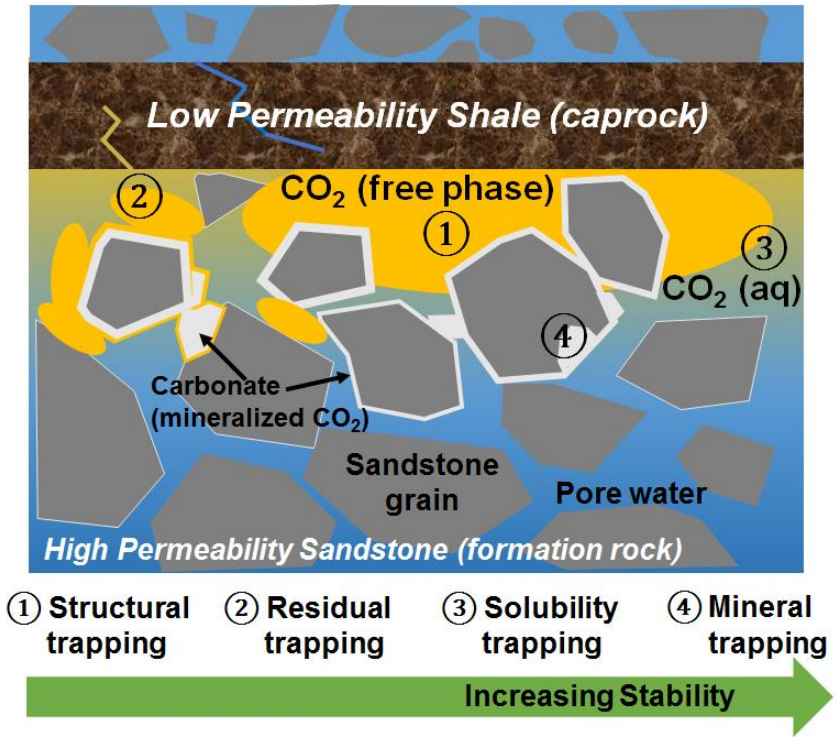

Figure 1.2 CO_2 trapping mechanisms.

To safely and efficiently store CO_2 in the geologic formation for thousands of years, it is important to be aware of and understand the interactions among CO_2, brine, and rocks in the subsurface environment.[7, 9] Several mechanisms can trap the injected CO_2, as shown in Figure 1.2, and each can be affected by CO_2–brine–mineral interactions.[8] Structural/stratigraphic trapping is the dominant mechanism in the short term. When CO_2 is injected, it rises to the top of formation

water due to its lower density compared to brine where it is trapped by low permeable caprock. Residual trapping refers to the residual CO_2 free phase becoming disconnected and trapped in pore spaces as the CO_2 plume migrates. CO_2 can dissolve into brine and stay as an aqueous species in the brine: This is solubility trapping. As CO_2 dissolves, the aqueous CO_2 can speciate to H^+, HCO_3^- or CO_3^{2-} ions. The brine is acidified by CO_2 dissolution, which can dissolve minerals in the formation rock to release cations such as Ca^{2+}, Mg^{2+}, and $Fe^{2+/3+}$. These cations can precipitate with carbonate ions to form secondary carbonate minerals, thus trapping CO_2 in the mineral form. This process, called mineral trapping, is the most stable trapping mechanism.

In some GCS sites where reactive minerals are less abundant, such as the Cranfield (USA) and Sleipner (North Sea) fields,[10, 11] CO_2 mineralization can take thousands of years. However, in other sites, CO_2 mineralization is observed in a short time. For example, the CarbFix site (Iceland) reported that 95% of injected CO_2 mineralized to calcite in 2 years after injection. In the cementitious materials used in building injection sites, mineralization is usually obvious after exposure to CO_2 for only several hours to several days.[12]

1.1.2 Calcium Carbonate and Its Nucleation

The mineralized CO_2 takes the form of carbonate minerals, such as $CaCO_3$, $MgCO_3$, and $FeCO_3$. Among these carbonate minerals, $CaCO_3$ is the most common form. Beyond its formation in subsurface systems, $CaCO_3$ also plays crucial roles in much wider applications and fields. In nature, it is one of the most abundant minerals in the Earth's crust, and it can be formed by abiotic or biotic processes in groundwater, soil, hot springs, etc..[13] Precipitated $CaCO_3$ exists in several polymorphs: Beginning with the thermodynamically most stable phase, they are calcite, aragonite, vaterite, and amorphous $CaCO_3$ (ACC). $CaCO_3$ precipitates can change the porosity and permeability of porous media,[14, 15] and alter the surface properties of substrates, such as by

increasing the reactive surface area and enhancing adsorption of heavy metals.[16-18] In everyday life, $CaCO_3$ is applied widely: Beneficial uses include paper filler/coatings, plastic fillers, paint extenders, and even food additives, tablets, or as inert fillers of tablets. In manufacturing $CaCO_3$, the grain sizes, purity, and polymorphs of $CaCO_3$ are controlled by reaction conditions and times.[13, 19] In agriculture, $CaCO_3$ is used to improve soil quality;[20] and in water treatment, $CaCO_3$ can remove heavy metals by adsorption.[17, 18] Conversely, $CaCO_3$ formation can cause scaling in pipelines and fouling on reverse osmosis membranes.[21-23]

Because of the importance of $CaCO_3$, it has been intensively studied, with abundant information already available. Thus, it is an ideal model mineral for investigating new complex systems. For example, it has been used an a model material to study mineral growth pathways,[24, 25] phase transformation,[26, 27] aggregation or coagulation,[28] epitaxial attachment,[29] and mineral nucleation.[30-36] Among these studies using $CaCO_3$ as a model material, studies on nucleation have been conducted mostly via indirect analyses of aqueous chemistry or via observation of microscale nuclei. Direct observations of nanoscale nuclei are sparse. Nucleation refers to the process of forming a nanoscale new phase out of a mother phase (Figure 1.3). It is a very important process in geosciences and in materials sciences. For example, nucleation can generate large surface areas for further mineral evolution,[37-39] and it can also alter the permeability of the medium if it occurs in nanometer pore throats.[40] Considering the significance of the nucleation process, it would be very useful if reactive transport models could include this kinetic pathway in addition to the mineral growth pathway. The incorporated nucleation pathway in modeling, however, is seldom available in current modeling codes, because the required parameters are insufficient, even for the widely studied $CaCO_3$. Moreover, the effects of subsurface fluid conditions and chemistries, such as high temperature and high salinity, on nucleation behaviors remain elusive.

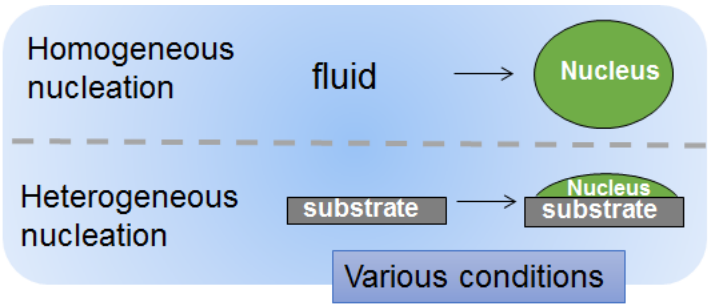

Figure 1.3 Illustration of nucleation as the process of forming a solid phase nucleus out of a liquid phase. Homogeneous nucleation refers to nucleation in solution, and heterogeneous nucleation refers to nucleation on substrates.

1.1.3 Wellbore Cement Deterioration

As mentioned above, CO_2 mineralization can be easily found in wellbore cement if the cement is exposed to injected CO_2. This is because cement is a basic material, and thus, reactive with acidic CO_2. The mostly commonly used cement, Portland cement, is produced by heating a mixture of clay and lime to about 1,450 ^oC until the mixture fuses to produce cement clinker. The clinker is cooled and ground to fine powder, containing mainly calcium oxide and calcium silicate.[41] Upon mixing with water, these components experience hydration reactions with water, and harden to produce mechanical support.

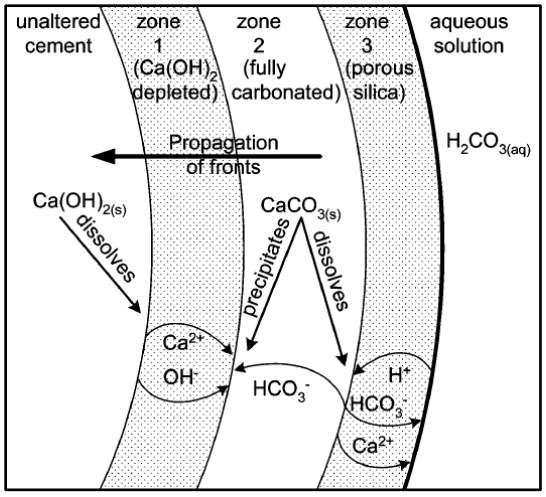

Figure 1.4 Chemical reactions in cement in the presence of CO_2 (Kutchko et al., 2007).[42]

Portland cement is used widely in construction, and is also used for building injection wells. Chemical reactions of cement with CO_2 are shown in Figure 1.4, and they can deteriorate cement's mechanical properties, although they can also lead to CO_2 mineralization. The CO_2-altered cement has altered porosity, permeability, strength, and mineralogy, and can influence CO_2 transport in the subsurface. It may also contain opened fractures that facilitate CO_2 leakage. Therefore, further understanding of quantitative linkage between chemical and mechanical changes can help us understand and predict wellbore integrity in wellbores, and it can also serve as an excellent example for investigating roles of $CaCO_3$ formation in energy-related subsurface operations. Improved knowledge about CO_2–brine–cement is applicable to other geomedia where dissolution of primary minerals and precipitation of secondary minerals is predicted when CO_2 is present. For example, in the case of shales, which are often caprocks at GCS sites, it is important to analyze their chemical and mechanical changes. The difference of shales from cement systems is that the porosity and permeability of the shale are lower, the mineralogy is more complicated, and the minerals are less reactive. However, as with cement, exposure to CO_2 can alter shales' mineralogy through dissolution and reprecipitation,[43] and these reactions could change the wettability, structure, and mechanical properties of the shale.[44, 45] As in the cement systems, the alterations of the shale matrix or shale fractures will determine whether CO_2 transport will be facilitated or hindered.

1.1.4 Reactive Transport Modeling (RTM)

To investigate interactions between fluid and geomedia, experimental approaches are indispensable. However, it is difficult to obtain results for geologic time scales or for each varying temperature, pressure, aqueous chemistry, or geomedia property. Reactive transport modeling is

thus an ideal approach to help understand and predict the system.[46, 47] In the model, one sets up a geomedium or a solid mineral, and adds the fluid flowing through the medium or passing the mineral surface. As the fluid moves, it also interacts with the minerals via dissolution, precipitation, sorption, and catalytic surface reactions. Both the solid phases and the fluids may continue to transform throughout the entire process.

In terms of wellbore cement deterioration caused by CO_2 injection, reactive transport modeling can predict the chemical reactions,[48] the distribution of solids and aqueous species in space, and the results can be extrapolated to predict the scenario for thousands of years equal to the expected CO_2 storage time. In addition to predicting long-term outcomes of cement–CO_2 interactions, reactive transport modeling can also provide detailed mechanistic understanding of these systems. This mechanistic understanding is important, because it enables more accurate prediction for long term reactions, and it also reveals the significance of pore scale mineral–fluid interactions. Some of the pore scale mechanisms have not been investigated for cement deterioration systems, such as the nucleation kinetics mentioned in Section 1.1.2, and their influences on the overall system. Hence, reactive transport modeling incorporated with these pore scale insights would be helpful for better understanding wellbore cement deterioration.

1.2 Objectives and Tasks

1.2.1 Knowledge Gaps

As introduced in section 1.1.3, wellbore integrity is crucial for safety of CO_2 storage. In building wellbores in GCS sites, cement provides necessary mechanical support. From a practical view, the chemical deterioration of cement would become apparent and important only if it caused

mechanical deterioration. However, quantitative coupling of chemical and mechanical properties during CO_2 attack on cement has not been systematically studied. Although it is known that the chemical reactions can decrease local permeability in part of the CO_2-altered zone[49-51] and also decrease the overall strength,[52] the quantitative relationship between alteration extent and strength decrease is not completely clear. It is also not clear which part of the altered zone has the most critical effect on overall strength decrease.

Apart from CO_2, there are many other dissolved species in the formation brine as well. For example, sulfate is one of the most abundant ions, and its concentration has a range of 0.01 M–0.05 M.[53] Sulfate also plays important roles in water–rock interactions due to its adsorption on mineral surfaces,[54, 55] including $CaCO_3$ surfaces. Because CO_2 attack on cement is coupled with $CaCO_3$ formation, it is expected that sulfate ions will interfere with cement's chemical and mechanical changes during CO_2 attack. However, the detailed interferences have not been studied before.

For understanding the mechanisms during CO_2 attack on cement, reactive transport modeling has proven effective,[48, 49, 56-60] and yet most studies focus on porosity-permeability relationships of the media and the advection and diffusivity of the fluids. There are limited studies investigating pore scale precipitation mechanisms. The lack of focus on the pore scale mechanisms is likely due to the absence of a modeling code incorporated with these important mechanisms, such as nucleation kinetics and pore scale precipitation.

As one of the most important processes in geomedia–fluid interaction, nucleation deserves more attention both experimentally and in modeling. The lack of the parameters for setting up nucleation kinetics in modeling needs to be filled by experimental measurements using new

techniques for *in situ* observations of nanoscale nuclei, and these parameters have not been available in the past. The two categories of missing parameters are the thermodynamic parameters (most importantly the interfacial energies involved in nucleation) and the kinetic factors. Previous studies have provided limited values for interfacial energies for $CaCO_3$ nucleation in solution,[61] and very recently also for $CaCO_3$ nucleation on substrates,[31] but there have been no reported values for kinetic factors such as the activation energy. In addition to parameters for incorporating nucleation in modeling, nanoscale observation of nucleus formation is also instructive in that it can provide new information on the influences of various conditions on nucleation behaviors, such as nuclei size, relative rates of nucleation and growth, and aggregation tendency. Such information can guide materials synthesis as well as helping us better understand geomedia–fluids interactions.

1.2.2 Specific Objectives and Tasks

In order to fill the knowledge gaps and provide important information for safer and more efficient GCS applications, the following objectives and tasks are specified.

Objective 1: Quantitatively examine chemical reactions and mechanical deterioration in cement after exposure to CO_2 under GCS conditions in the presence and absence of additional sulfate ions.

Hypothesis 1: Chemical reactions of cement with CO_2 under GCS conditions involve dissolution of cement components and precipitation of $CaCO_3$ in the cement matrix. The precipitated $CaCO_3$ can hinder CO_2 transport into the inner core of the cement and decelerate cement deterioration. After CO_2 attack, the overall strength of the cement sample will decrease, and this decrease is related to the loss of materials in cement matrices caused by dissolution. The presence of additional sulfate ions will change the rate of CO_2 attack, but will not change the mechanisms of the CO_2 attack.

Objective 2: Set up a reactive transport model to simulate the reactive transport of CO_2 in cement; identify the most important pore scale mechanisms and incorporate them into the modeling framework to reproduce the experimental observations in CO_2-deteriorated cement.

Hypothesis 2: The modeling results will be greatly affected by $CaCO_3$ nucleation kinetics and $CaCO_3$ precipitation in pore spaces. The experimental observations will be reproduced at continuum scales only if these pore scale processes are incorporated. The modeling results will suggest influences of more complicated environments on cement alteration, such as the effects by additional sulfate ions. The results will also imply strategies for mitigating CO_2 attack on cement. The model will serve as a benchmark example to demonstrate the roles of pore scale insights in larger scale subsurface field sites.

Objective 3: Experimentally obtain the interfacial energy, the activation energy, and the pre-exponential factor for modeling $CaCO_3$ nucleation according to nucleation rate equation: $J = A\exp(-\frac{E_a}{kT})\exp\left(-\frac{\Delta G^*}{kT}\right)$; and examine $CaCO_3$ nucleation behaviors with different substrates, salinities, and temperatures.

Hypothesis 3: A full set of thermodynamic and kinetic factors required for incorporating nucleation kinetics in modeling will be obtained by experimentally measuring nucleation rates with different supersaturations of the solutions and with different temperatures. The varying substrates, salinities, and temperatures will impact nucleation behaviors as well as altering interfacial energies and kinetic factors.

1.3 Overview of Dissertation

The three objectives have been accomplished in three tasks. **Task 1** elucidated the quantitative relations between chemical and mechanical alterations of wellbore cement using experimental approaches, and clarified the effects of additional sulfate ions on cement alteration. **Task 2** set up a reactive transport model using CrunchTope based on the experimental system in Task 1, and numerically simulated the cement deterioration process with an updated CrunchTope code. The updated code has incorporated nucleation kinetics and the minimum porosity. **Tasks 3** experimentally determined the interfacial energies and kinetic factors for $CaCO_3$ nucleation on environmentally abundant mineral substrates, and evaluated the influences of substrates, salinity, and temperature on these parameters and on nucleation behaviors.

Task 1 regarding experimental study of cement deterioration is presented in **Chapters 2 and 3**. In **Chapter 2**, experiments were conducted with Portland cement paste samples submerged in CO_2-saturated brine under GCS conditions (100 bar, 95 ^oC, and 0.5 M NaCl in brine) for 10 days. After the experiment, mechanical properties were tested using a three-point bending setup for overall strength of the samples, and using a nanoindentation setup for hardness of microscale zones. Chemical reactions were characterized by observing the polished cross sections using backscattered electron imaging. The chemical and mechanical alterations were quantitatively related, and the most important zone within the deteriorated cement is identified. **Chapter 3** utilized the same experimental method, but focused on the effects of additional 50 mM of sulfate ions (added as Na_2SO_4) on the chemical reactions and the resulting mechanical changes. Additional tests were conducted to support the hypothesized mechanisms of sulfate ion interactions with the $CaCO_3$ formed in the cement matrices.

Task 2 on reactive transport modeling of cement deterioration is addressed in **Chapter 4**. The experimental data obtained in Task 1 regarding the mineral fronts (i.e., the edges of a mineral block) in the cement matrices were used for this task, and additional data were obtained by reacting cement samples for 1, 3, and 6 days. A 1D continuum model was set up using software package CrunchTope to simulate the experimental observations. A code was added to CrunchTope to allow users to set a minimum allowed porosity in the geomedia, and also to allow mineral precipitation to initiate with nucleation kinetics, as opposed to beginning with growth on pre-existing mineral seeds.

Task 3 regarding $CaCO_3$ nucleation on mineral substrates is addressed in **Chapters 4–6**. In these chapters, nucleation was observed using *in situ* grazing incidence small angle scattering (GISAXS) which can provide information on nucleus sizes and shapes. The nucleation rates were obtained at different supersaturations for $CaCO_3$ ($\log_{10}(IAP/K_{sp})=10^{1.3}–10^{2.0}$) to obtain the interfacial energy, and at different temperatures (12 ^{o}C–31 ^{o}C) to extract the activation energy. In addition to parameters, nucleation behavior was further investigated using complimentary techniques such as atomic force microscopy (AFM), Raman spectroscopy, and scanning electron microscopy. In **Chapter 4**, a detailed method to analyze GISAXS data is presented, and $CaCO_3$ nucleation on mica was compared with that on quartz. **Chapter 5** investigated the effects of high salinity on interfacial energies, kinetic factors, and nucleation behaviors. In **Chapter 6**, GISAXS measurements were calibrated with visual observations of nuclei using AFM, and the activation energy and the pre-exponential factor were obtained for nucleation $CaCO_3$ on quartz according to the nucleation rate equation: $J = A\exp(-\frac{E_a}{kT})\exp\left(-\frac{\Delta G^*}{kT}\right)$. This chapter also delineated the change of nucleation behaviors at different temperatures.

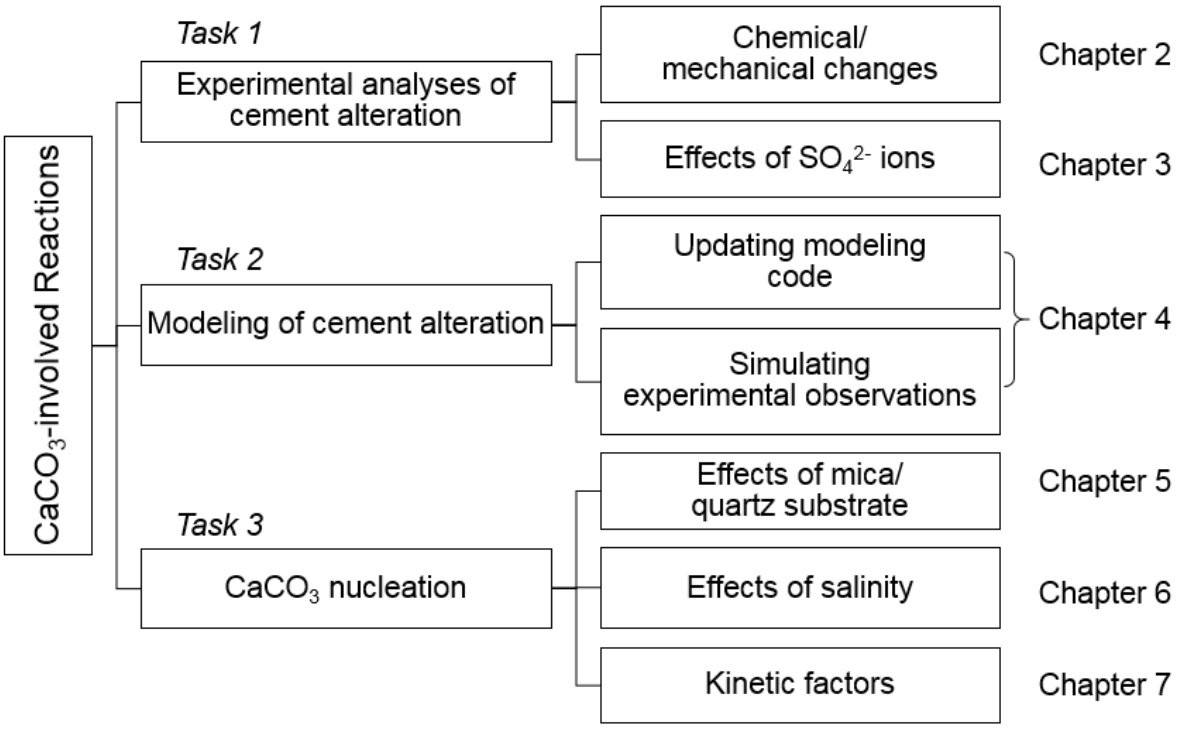

Figure 1.5 Overview of dissertation tasks and relating chapters.

Chapter 2: Chemical Reactions of Portland Cement with Aqueous CO_2 and Their Impacts on Cement's Mechanical Properties under Geologic CO_2 Sequestration Conditions

Results of this chapter have been published in *Environmental Science & Technology*, 2015, 49 (10), 5476-5483

Abstract

Understanding chemical and mechanical alterations of geomedia is important for geologic CO_2 sequestration (GCS). Among the geomedia, wellbore cement is the most reactive when CO_2 is present, and it is critical for wellbore integrity. In this chapter, chemical and mechanical alterations were analyzed for cement paste samples reacted for 10 days under GCS conditions. The reactions were at 95 ^oC, and had 100 bar of either N_2 (control condition) or CO_2 contacting the reaction brine solution with an ionic strength of 0.5 M, adjusted by NaCl. Chemical analyses showed that the $3 \times 1.1 \times 0.3$ cm^3 samples were significantly attacked by aqueous CO_2 and developed layer structures with a total attacked depth of 1220 μm. Microscale mechanical property analyses showed that the hardness and indentation modulus of the carbonated layer were 2–3 times greater than for the intact cement, but those in the portlandite-dissolved region decreased by ~50%. The strength and elastic modulus of the bulk cement samples were reduced by 93% and 84%, respectively. The properties of the microscale regions, the layer structure, microcracks, and swelling of the outer layers combined to affect the overall mechanical properties. These findings

improve understanding of wellbore integrity from both chemical and mechanical viewpoints, and can be utilized to improve the safety and efficiency of CO_2 storage.

2.1 Introduction

Geologic CO_2 sequestration (GCS) is a promising technique to reduce anthropogenic CO_2 emission to the atmosphere, and thus help mitigate climate change.[4, 62] In the application of GCS, CO_2 is captured and injected into a geologic formation through injection wells. These wells are either built for GCS, are old wells for depleted oil/gas reservoirs, or are wells for enhanced oil recovery. The majority of well liners are cast using concrete containing Portland cement and aggregates. The main anhydrous phases of different types of Portland cement are 21–67% alite ($3CaO{\cdot}SiO_2$, or C_3S), 0–49% belite ($2CaO{\cdot}SiO_2$, or C_2S), 1–17% aluminate phase ($3CaO{\cdot}Al_2O_3$, or C_3A), and 6–18% ferrite phase ($4CaO{\cdot}Al_2O_3{\cdot}Fe_2O_3$, or C_4AF), with the composition varying to serve specific purposes.[41, 63] After hydration, calcium silicate hydrates (C-S-H), portlandite ($Ca(OH)_2$, or CH), and other hydrated phases will coexist with anhydrous phases in the hardened cement. To speak concisely, this study uses the general term "cement" for hardened cementitious materials containing a mixture of anhydrous cement and its hydrated products. Among different types of Portland cement, ordinary Portland cement (OPC) is the most general type, and Class H and Class G, which have less Al content and a slightly lower ratio of C_3S/C_2S than OPC, are typically used for oil well cementing.[41, 63] Portland cement has a pH above 12.5,[41, 63, 64] while CO_2 produces carbonic acid in the presence of water. Therefore, injecting CO_2 through wells or using cement to seal wells after CO_2 injection will lead to CO_2 attack on the cement, threatening the wellbore integrity, and thus will affect the efficiency and safety of GCS. Injected CO_2 may leak

through the wellbore via different pathways, such as cement pore spaces and cracks, and interfaces between cement and surroundings, which may finally lead the way vertically upwards for CO_2 to escape.[49, 59, 65, 66] Among these pathways, the interfaces of casing/cement and cement/reservoir rocks are the most likely leakage pathways.[50, 58, 67-74]

In recent years, investigations have been carried out on aqueous CO_2 attack on well cements for GCS scenarios, either through field sample analyses,[67, 70, 75, 76] bench-top experiments,[42, 51, 68, 72-74, 77-87] or modeling.[48, 49, 56-58, 60, 78, 87-89] At CO_2 sequestration sites, where temperature (31–110 C^o) and pressure (73.8–600 bar) are generally high,[12, 62, 90] CO_2 exists as a supercritical (sc) phase, saturated by a small amount of water, or exists as aqueous CO_2 in the formation brine, forming carbonic acid, and driving pH down to ~3 before mineral dissolution gradually buffers pH up to ~5.[62] Both supercritical and aqueous CO_2 attack on wellbore cement require water to be present, so that carbonic acids can be formed.[12] It is commonly reported that the CO_2 attack on cement starts with CH-dissolution and C-S-H decalcification, followed by precipitation of $CaCO_3$ and amorphous silica (am-SiO_2).[12] The precipitated $CaCO_3$ forms a carbonation layer in cement structure, which hinders the further penetration of carbonic acid solution into the cement materials.[12, 42, 73, 77]

Knowledge about cement deterioration under GCS relevant conditions is accumulating, but many gaps remain. For example, the linkage between chemical attack and mechanical property deterioration is still weak. Another knowledge gap is related to the effect of the abundant aqueous species, sulfate (SO_4^{2-}), on cement during CO_2 attack. This chapter focuses on the first knowledge gap, seeking to quantify the mechanical deterioration of cement by the known extent of chemical reactions. The second knowledge gap is addressed in Chapter 3. Connecting chemical and mechanical alterations is crucial because cement is cast to provide mechanical integrity of the wells.

Chemical attacks on cement are a vital concern if they threaten its mechanical properties.[12] However, information on mechanical property changes of cement after CO_2 injection is limited.[12]

Several studies have examined cement's microscale mechanical properties, such as hardnesses and localized porosities, permeabilities, and elasticities. Kutchko et al. (2007) found through experimental studies that after exposure to CO_2 the hardness of the carbonated zone in cement was enhanced to about twice that of unaltered cement.[42] A similar increase in the hardness of the carbonated zone in cement is also found in other studies.[73, 78, 91] Due to the low permeability of the carbonated layer, the carbonation of cement was reported to decrease the permeability of cement materials.[50, 51, 77, 89, 92, 93] In many dynamic flow systems, the permeability of the microscale cement–rock interface or cement fractures was found to either decrease[49, 68, 69, 71, 86, 87, 91] or increase[80] with time, due to mineral dissolution and precipitation processes after exposure to CO_2. For much longer reaction times (i.e., tens to hundreds of years), the predictive modeling work by Gherardi et al. (2012) showed that the $CaCO_3$ and other secondary phases will finally dissolve and increase the permeability of cement.[48]

Limited studies have reported on cement's mechanical property changes at the macroscale. Barlet-Gouedard et al. (2009) briefly showed that after exposure to CO_2 under GCS relevant conditions for one day, the compressive strength of bulk cementitious material decreased by half, and remained at a plateau for 5 weeks,[52] and Fabbri et al. reported a decrease of 25% in strength after a 2-month exposure.[94] Also, the connection between micro- and larger scale mechanical properties is still not clear. Using microscale mechanical properties to predict large scale changes should be approached only with caution.[87, 91] Therefore, there are urgent needs to quantitatively bridge the chemical reactions and mechanical property changes, obtain more knowledge on mechanical properties at macroscales, and connect micro- and larger scales of the mechanical

property changes, thus building a systematic understanding of how chemical reactions affect the integrity of cement materials.

This study aims to examine and quantify the mechanical changes of cement materials after chemical reactions with respect to their strength, elasticity, and fracture surface roughness at the macroscale, and the hardness and indentation modulus at the microscale. Findings of this study provide an important link between key chemical reactions and the resulting mechanical property changes. The multidisciplinary approach helps understand and predict wellbore integrity under GCS conditions from both geochemical and mechanical standpoints, and hopes to benefit both communities.

2.2 Experimental Section

2.2.1 Cement Paste Preparation

Ordinary Portland cement (OPC) was used in this study. Although Class H and Class G Portland cement are the most commonly used types for wellbore cementing, OPC is the basis of all other types of Portland cement, and is responsible for the intense chemical reactions under GCS conditions.[41, 42] OPC used in this study was manufactured by QUIKRETE®, and its X-ray fluorescence (XRF) analysis is presented in the Supporting Information (Table 2-S1). Cement and ultrapure deionized (DI) water were mixed with a water–to–cement ratio of 0.5, which allowed thorough mixing and was within the typical range of 0.3–0.6 for a paste.[41] The cement slurry was cast in 3 cm (l) $\times$ 1.1 cm (w) $\times$0.3 cm (h) custom-made rubber molds. The sample dimensions were designed to be small enough to allow us to determine obvious mechanical property changes of the entire sample after reactions for 10 days. The molded samples were hardened for three days

at ~100% relative humidity under room conditions before de-molding and high temperature/pressure reactions. After three days, OPC can develop 40% of its full strength under room conditions.[63] The samples are still vulnerable to enable reasonably fast reaction rates of chemical attack, while they are strong enough to avoid sample damage during de-molding. The chemical reactions with newly hardened cement are close to situations where cement is used to seal decommissioned CO_2 injection wells or defective wellbores. In addition, because cement that has fully hardened for a longer time has similar chemical components to newly hardened cement, old well cement and newly hardened cement are similarly altered by chemical attacks, with consequently similar mechanical property changes.

2.2.2 High Pressure and High Temperature Reaction Conditions

After hardening, cement samples were de-molded, rinsed with DI water, and reacted under two conditions at 95 ^{o}C. The "N2" condition represents a system without chemical attacks, achieved by injecting N_2 at 100 bar into the reactor. This condition was the control, where the cement samples underwent high temperature/pressure curing and developed higher strength than if cured only at ambient conditions.[63] The "CO2" condition represents a system with CO_2 attack, mimicking the situation after CO_2 injection, achieved by injecting CO_2 at 100 bar into the reactor. Under the CO2 condition, cement curing and CO_2 attack happened at the same time. To differentiate the condition names from the chemical formulas of CO_2 and N_2, this study uses normal font (no subscripts) for the condition names. Under both conditions, eight samples were submerged in a brine of 0.5 molar (M) NaCl. The solid-to-liquid ratio was 1/16 by volume. The experimental temperature, pressure, and salinity were within the range of GCS application (31−110 °C, 73.8−600 bar, and 0.01−2 M NaCl).[12, 62, 90] The comparatively high end of the temperature range was selected to enable reasonable reaction rates for bench-scale study. More

information on our experimental temperature and pressure is available in the Supporting Information Section 2-S1. After the reactor of the CO2 condition reached 95 ^{o}C and 100 bar of CO_2, and before the reaction started, the pH of the brine was 3.0 ± 0.1, measured by a pH electrode workable at 1–139 bar and 20–120 ^{o}C (Corr Instruments, TX). More information on our reactor and setup is provided in the Supporting Information Section 2-S1.

2.2.3 Chemical Analyses after Reactions

Reaction under the CO2 condition (CO2 samples) lasted 10 days, long enough to allow the cement samples to develop significant mechanical changes compared to the control condition, but still have an intact core. When the reaction time was completed, the reactor was gradually degassed for 1 hour to minimize possible damage by depressurization. The aqueous phase was collected and acidified by HNO_3. Aqueous metal concentrations were measured by inductively coupled plasma-optical emission spectrometry (ICP-OES). The cement samples were rinsed by DI water, oven-dried at 80 °C for eight hours to remove pore waters but not combined water.[41, 95] No phase decomposition by the drying process was observed. The samples were then tested by a three-point bending setup, as described in the following section 2.2.4. After the bending tests, three of the most representative samples from each condition were mounted in epoxy resin, and the $w \times h$ cross section was ground flat using increasingly finer SiC papers and polished with a series of diamond pastes decreasing to 0.1 μm particle size. The polished cross sections were imaged by a backscattered electron (BSE) detector on a scanning electron microscope (SEM, JEOL 7001LVF FE-SEM), coupled with energy dispersive X-ray spectrometry (EDS) to analyze the elemental composition. Both BSE-SEM and EDS were operated in low vacuum mode (10 Pa), with a working distance of 10 mm, an accelerating voltage of 10.00 kV, and a probe current of 16 μA. In the BSE images, the brightness of a phase is approximately related to the average atomic number:

the lighter the phase, the larger the average atomic number.[41, 96, 97] The brightest areas are anhydrous phases, followed by grey CH and C-S-H phases, and the darkest areas are pores or cracks.[41, 98] Within the anhydrous phases, the Al-containing phases, C_3A and C_4AF, are brighter than alite and belite.[99] To relate the BSE images to the optical appearance of the polished surfaces, the samples were imaged also by an optical microscope (Zeiss Imager Microscope).

To identify the phases of the cement samples, X-ray diffraction (XRD) was performed by a Rigaku X-ray Diffractometer. XRD powder samples were ground from each layer in the CO_2-altered cement samples (which developed layered structures). In this way, the mineralogy could be analyzed for each separate layer. No layer structures were observed in samples reacted under the N2 conditions (N2 samples), and the powders were ground from the bulk cement sample.

2.2.4 Solid Sample Analyses for Mechanical Property Changes after Reactions

Three-point bending tests. To obtain the mechanical strength, elastic modulus, and toughness indices of the reacted samples, three-point bending tests were conducted on the oven-dried specimens, using a three-point bending setup in a mechanical test frame (Instron® Model 5583 mechanical test frame) with a 500 N maximum load cell (Instron® Model 2525-816). The setup of the bending test is shown in Figure 2.1a. A custom-made sample stage on which samples were bent was built with steel and aluminum. At the maximum loading force of ~65 N, the data showed that the fixture did not experience deformation. The distance between the two supporting points was 2.2 cm, and the weight of the loading rod was 0.23 N, which generated 0.08 MPa stress within the sample, far less than the stress required to generate fractures. The 0.23 N was added to the loading force to calculate flexural stresses. The Bluehill software package (Instron®) was used to control the actuator and to acquire data. The loading rod pushed down at a speed of 0.05 mm/min, and the displacement of the loading point was recorded as the deflection of the sample beam (δ).

Under the loading force, compressive and tensile stresses developed in the direction of the beam axis and generated flexural stresses in the beam. The maximum compressive stress was at the top surface under the loading rod, and the maximum tensile stress was at the bottom surface, directly beneath the loading point. Because most cementitious materials can withstand about 10 times more compressive stress than tensile stress,[52, 100] fractures start from the bottom surface. For a rectangular beam in bending, the load force is converted to flexural stress (σ_f) by[101]

$$\sigma_f = \frac{3FL}{2wh^2}, \qquad \text{Eq. (2.1)}$$

and the elasticity of the beam is represented by elastic modulus (E_f) calculated from

$$E_f = \frac{CL^2}{6h}, \qquad \text{Eq. (2.2)}$$

where F is the applied force, L is the distance between supporting points, w and h are the width and height of the sample, and C is a constant representing the slope of the linear part of the stress–deflection curve. The strength of the cement sample is represented by the modulus of rupture (MOR), which is the maximum stress that a sample can withstand before breaking.

The post-crack behavior of our samples was compared by the shape of the stress-deflection curve after the main drop. The energy absorbed by a sample is related to the area under the stress-deflection curve. After the main crack occurs, if a stress-deflection curve drops to zero immediately, the sample is considered brittle, and does not absorb energy after the crack event; if the curve drops gradually, the sample is quasi-brittle, and can absorb more energy after the main crack. This comparative method is adapted from standard ASTM C 1609[4] (formerly ASTM C 1018).[102]

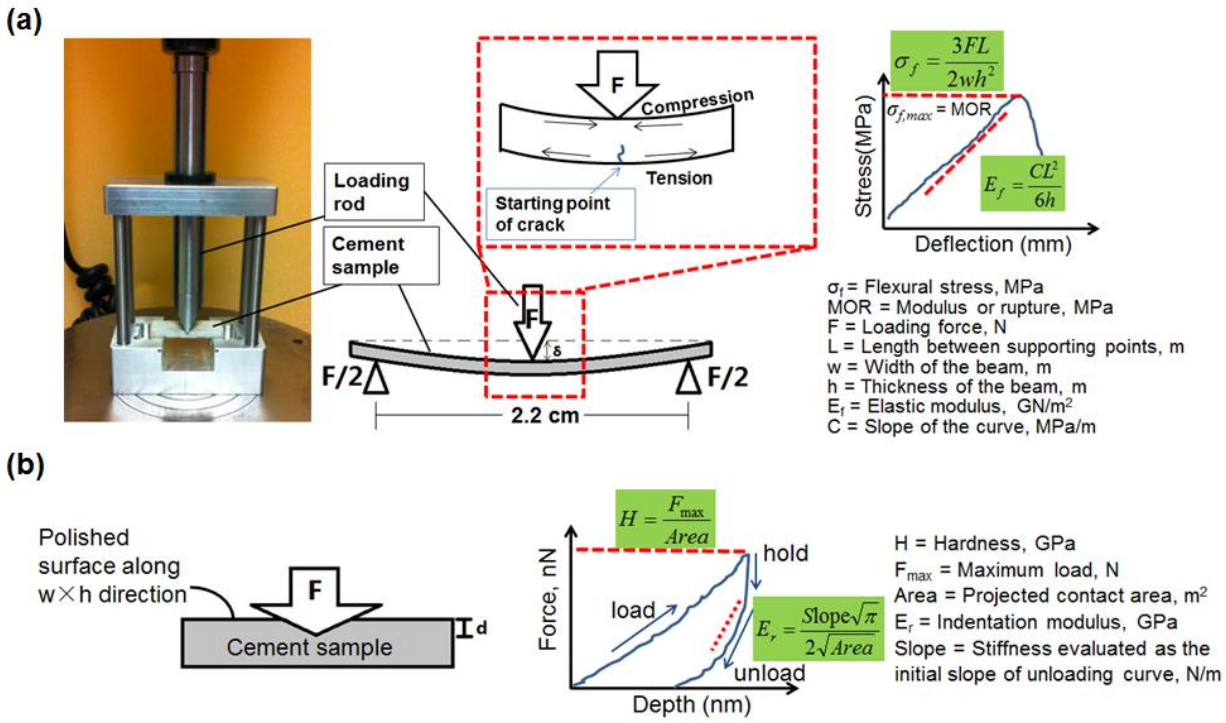

Figure 2.1 (a) Diagram of three-point bending test. Loading force (F) and the deflection of the beam (δ) were recorded. During the bending process, the top surface of the beam has the maximum compression, and the bottom surface has the maximum tension. The crack starts from the bottom surface. A demonstration stress–deflection curve is also shown. (b) Diagram of nanoindentation. A demonstration indentation curve is shown on the right. Unit conversion factors are not included in the equations.

Fracture roughness comparison. In this study, the roughnesses of the fracture surfaces of N2 and CO2 samples were qualitatively compared by observing the fracture surfaces after bending tests, and quantitatively compared by calculating the length of fracture surface profile lines, which spanned a projected length of 2 mm parallel to the *h* direction, as shown in Figure 2-S2. The fracture surface profile lines were obtained by a laser scanning profilometer (Keyence, LJ-V7080). The distance between two adjacent points on the profile lines was 100 μm. The profile roughness parameter R_L is defined as the ratio of the actual profile length to the projected profile length, and is always equal to or larger than 1. The larger the R_L, the rougher the surface. A diagram

of the laser scanner setup and the profile roughness calculation is available in the Supporting Information (Figure 2-S2).

In fracture mechanics, the fracture surface of a brittle material is usually described as fractal, meaning that the pattern is self-similar at any scale, so that the fracture surface profile length depends on resolution.[103] To eliminate the effect of measurement scale and resolution on the roughness measurement, the profile roughness or the surface roughness, extrapolated to infinitely small scale,[104] and the fractal dimensions[103, 105, 106] have been suggested to quantify the surface roughness. Because the quantification of surface roughness is not the focus of this study, and because results for surface roughness could vary significantly using measurements by different methods,[103] this study uses the profile line for comparisons of roughness.

Nanoindentation. To acquire the mechanical properties of the different microstructural regions in the reacted cement samples, the hardness and indentation modulus were measured through nanoindentation testing (HYSITRON TI 950 TriboIndenter) of the polished cross sections. A diagram of the indentation setup is shown in Figure 2.1b. A diamond Berkovich probe was used to indent the sample at a displacement rate of 50 nm/s to a maximum depth of 250 nm, holding at 250 nm for 5 seconds before unloading from the surface at a speed of 50 nm/s. The hardness (H) and indentation modulus (E_r) were calculated by

$$H = \frac{F_{max}}{Area} \text{ , and} \qquad \text{Eq. (2.3)}$$

$$E_r = \frac{Slope\sqrt{\pi}}{2\sqrt{Area}} \text{ ,} \qquad \text{Eq. (2.4)}$$

where F_{max} is the maximum load, $Area$ refers to the projected contact area, and $Slope$ is the initial slope of the load–displacement curve upon unloading. E_r is a measure of the stiffness of the indented material.

2.2 Results and Discussion

2.2.1 Appearance of CO_2-Attacked Cement Samples

After 10 day reactions, N2 samples were grey, while CO2 samples had developed an orange tint on the surface (inserted pictures in Figure 2.2a). Four out of eight CO_2 samples developed bumps on their surface. The orange color of the surface of CO_2 and acid attacked cement materials has been widely reported.[12, 42, 73] However, up till now, the specific mineral phase that appears orange has not been identified.[12] It has been proposed that the orange phase is likely Fe(III) oxides re-precipitated from iron dissolved from Fe(III)-containing phases, but this has not been supported by experimental results.[12] Thus, we tested whether the orange color is given by Fe(III). Additional CO2 samples were soaked in strong nitric acid for 1 day. After the acid treatment, the orange color became more distinct. The samples were rinsed with DI water and dried for SEM-EDS and XRD analysis. EDS analysis (Figure 2-S6) showed that the orange color saturation was well correlated with the Fe content in the samples, and the orange color indicates Fe(III). On the other hand, interestingly, no crystallized Fe(III) phases were identified by XRD, indicating that these Fe(III) phases were either amorphous (e.g., amorphous Fe(III) (hydr)oxides) or very sparse. These Fe(III) phases may affect further geochemical reactions, and more discussion is in the Supporting Information Section 2-S2.

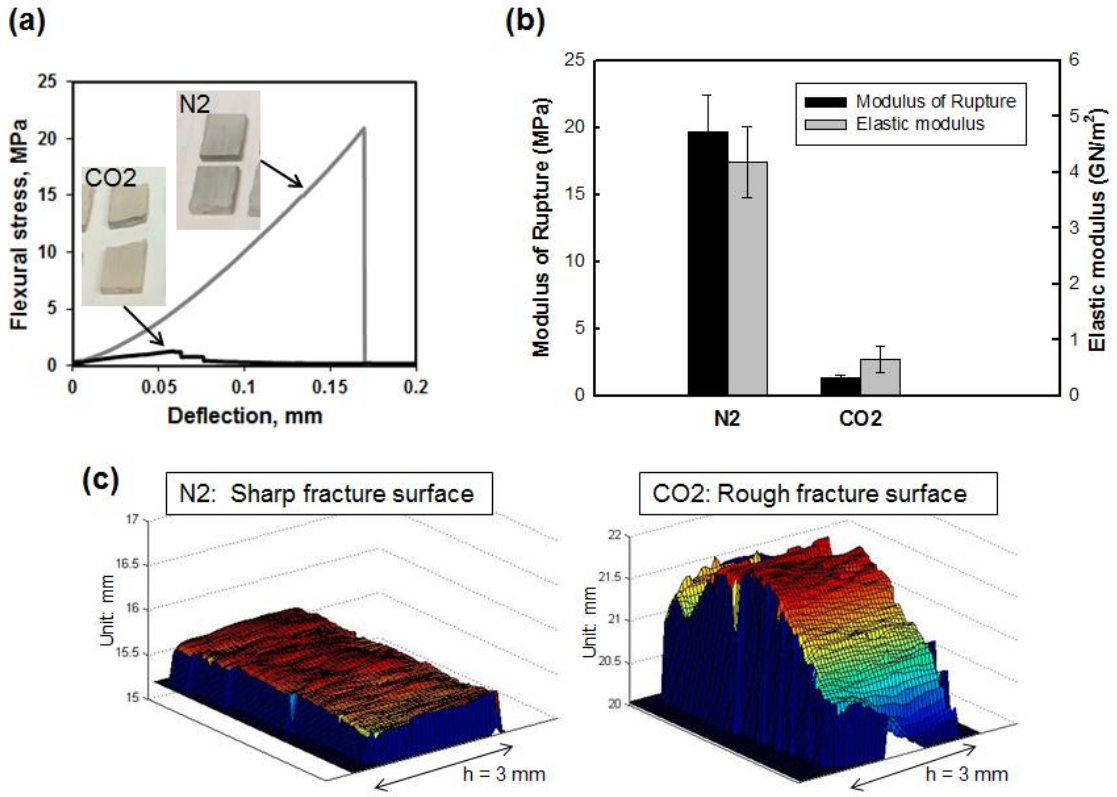

Figure 2.2 Mechanical property analyses by three-point bending tests. (a) Typical stress–deflection curves of samples reacted under different conditions. Inserted pictures show the appearances of typical samples after the bending tests. The curves of CO2 samples have fluctuations, indicating layer structures. The stress–deflection curves of N2 samples are smooth and linear, and fail without yielding when the sample is broken. (b) The strength (represented by the modulus of rupture) and the elastic modulus of the samples, calculated according to Eqs. 2.1–2.2. The CO2 samples have lower strength and elastic moduli. (c) Typical surface profiles of N2 and CO2 samples. The N2 samples have sharp fracture surfaces, while the CO2 samples have rough fracture surfaces.

2.2.2 Chemical Reactions during CO_2 Attack

Cement dissolution. To analyze the dissolution of the cement samples, aqueous concentrations of Ca and Si were measured by ICP-OES. Due to secondary precipitation during degassing and cooling of our system, the measured concentrations were likely to be lower than *in situ* concentrations. Concentrations of Al, Fe, and Mg were below the detection limits. As shown in Table 2-S2, the aqueous concentrations of Ca and Si under the CO2 condition were 147.6 ±

0.6 mM and 5.33 ± 0.03 mM (Ca/Si = 27.7); those under the N2 condition were 9.0± 0.3 mM and 1.62 ± 0.01 mM (Ca/Si = 5.6), respectively. The Ca/Si atomic ratio in the cement clinker before hydration was 3.0, measured by XRF. Both aqueous Ca and Si concentrations indicate that CO2 samples had much more dissolution than the control samples. Also, under both CO2 and N2 conditions, Ca dissolved faster than Si. Under the CO2 condition, Ca was specially preferred to dissolve.

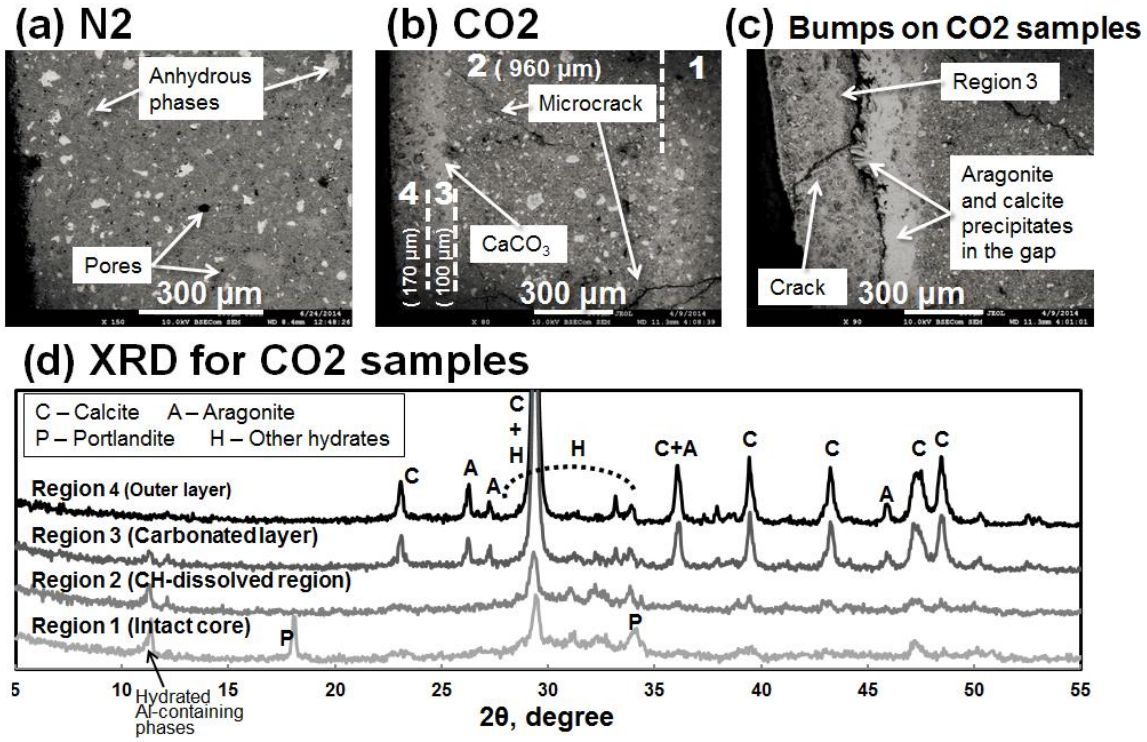

Figure 2.3 (a – b) BSE images of polished cross sections of N2 and CO2 samples. The inner core is on the right, and the edge is on the left of each image. Four regions are shown in the CO2 image. Region 1 is the intact part. The main reactions in Regions 2–4 are described by Eqs. 2.5–2.8. Microcracks are commonly observed in Region 2, indicated by the arrow. (c) BSE image of a polished intersection crossing a bump on the CO2 samples. The bump formed along with a gap in Region 2. Using Raman spectroscopy, both aragonite and calcite were identified as precipitates in the gap (Figure 2-S4d). (d) XRD patterns of different regions of CO2 samples. The intact core has undissolved portlandite; Region 2 does not have peaks corresponding to portlandite, indicating its complete dissolution; Region 3 has substantial $CaCO_3$, including both aragonite and calcite. Region 4 also has undissolved $CaCO_3$.

Identifying mineral phases in the reacted samples. CO_2 attack on cement samples is clearly shown in the SEM-BSE images in Figures 2.3b-c. Layer structures composed of four regions developed in the CO_2 attacked cement. From the inner core to the sample surface, Region 1 is the intact cement; Region 2 is the CH-dissolved region with all $Ca(OH)_2$ dissolved and C-S-H partially dissolved, leaving the area more porous and the BSE images showing more black pore areas; Region 3 is the carbonated layer, where $CaCO_3$ appears as a dense grey phase in the BSE image; and finally, Region 4 is the sample surface directly in contact with the bulk acidic brine, where $CaCO_3$ has been dissolved. In the last decade, the attack of CO_2 on cement under GCS relevant conditions has been characterized. The main chemical reactions in each regions are:[12, 42, 73]

Region 2: $Ca(OH)_2 \rightarrow Ca^{2+} + OH^-$; Eq. (2.5)

$C\text{-}S\text{-}H \rightarrow Ca^{2+} + OH^- + am\text{-}SiO_2$; Eq. (2.6)

Region 3: $Ca^{2+} + HCO_3^- + OH^- \rightarrow CaCO_3 + H_2O$; Eq. (2.7)

Region 4: $CaCO_3 + H_2CO_3 \rightarrow Ca^{2+} + 2HCO_3^-$; Eq. (2.8)

In this work, these chemical reactions were confirmed by EDS results (Figure 2-S3) and XRD results (Figure 2.3d). From XRD results, portlandite was identified for the intact Region 1. Extensive formation of $CaCO_3$, mostly as calcite and partially as aragonite, was observed in Region 3. The XRD result for Region 4 also has $CaCO_3$ peaks, which are from the interface of Region 3 and Region 4, and from the $CaCO_3$ precipitated on the sample surface after the reaction (i.e., degassing and cooling of the reactor, and drying of the samples). No $Ca(OH)_2$ was observable from the XRD spectra of Region 2, indicating complete dissolution of portlandite in Region 2. The

broad peak for amorphous silica could not be observed in the presence of strong $CaCO_3$ peaks. No expansive minerals (e.g., ettringite or clay minerals) were identified from EDS or XRD analysis.

In the CO2 samples, because of the loss of materials by dissolution, Region 2 is a comparatively fragile region, where many microcracks were observed in BSE images. The cracks may have formed either during the reaction or during the oven-drying, which may have caused internal stress. The cracks usually end at the inner side of Region 3, shown by the arrow in Figure 2.3b. Interestingly, the bumps on the surface of the CO2 samples developed along with a gap at the outer edge of Region 2. In the gap, more $CaCO_3$ precipitated as calcite and aragonite, as identified by Raman spectroscopy (Figure 2-S4d). The bumps were formed during the reaction, because their curvature cannot be achieved by a short period of time for brittle cement during degassing, and because they appeared on the sample surface before any treatment of the samples after being taken out from the brine solution. The mechanism of formation of the bumps will be discussed in the later section.

The optical images of the polished surfaces also clearly show the layer structure of the CO_2 attacked samples, and are shown in Figures 2-S4a–c, with comparison to the control samples. The total attacked thickness in the CO2 samples (Regions 2–4) is 1220 $\pm$ 90 μm. Specifically, the thicknesses of Regions 2, 3, and 4 are about 960 $\pm$ 100 μm, 100 $\pm$ 17 μm, and 170 $\pm$ 35 μm, respectively.

2.2.3 Deteriorated Macroscale Mechanical Properties and Changes in Fracture Mechanics

Three-point bending tests. Results from three-point bending tests revealed that chemical reactions caused mechanical property changes in the bulk cement samples. Compared to

the control N2 samples (MOR = 20 $\pm$ 2 MPa, and E_f = 4.2 $\pm$ 0.6 GN/m^2), the strength and elasticity of the CO2 samples were deteriorated by 93% and 84%, respectively. The dramatic decreases in both the strength and elastic modulus of the CO2 samples are plotted in Figure 2.2b.

The typical stress–deflection curves in Figure 2.2a show that CO2 samples have obvious fluctuations in their stress–deflection curves, which are related to their layer structure. When a sample has a layer structure perpendicular to the direction of loading force, the layer farthest from the loading point breaks first. As the loading point continues to push down on the beam, the layer next to the farthest layer, if not broken, takes on the role of resisting the load force. This sequential breaking is reflected in the fluctuations of the stress–deflection curve. The N2 samples do not show fluctuations in the stress–deflection curves. In the stress–deflection curves of N2 samples, the curves increase linearly as the deflection increases. The slightly concave shape at the beginning of the curve is due to the imperfect contact of the tip of the loading rod with the top surface of the sample, or the contact of the supporting points with the bottom surface of the sample.

The stress–deflection curves also indicate that CO_2 attack changed the post-crack behavior of our cement samples: the N2 samples are brittle, whereas the CO2 samples are quasi-brittle. This difference indicates that the CO_2-attacked cement samples, although having lower strength, have a relatively higher resistance to breaking after the critical crack.

Changes in fracture roughness. The CO2 samples had rougher fracture surfaces. The profile roughness parameters of the CO2 samples were scattered in the range of 1.02–2.39, with a median of 1.14; while the profile roughness parameters of the N2 samples were in the range of 1.00–1.05, with a median of 1.00. The roughnesses of the N2 and CO2 samples can also be visually compared from the typical surface profiles in Figure 2.2c, generated using the laser scanner. The

rougher fracture surfaces of the CO2 samples are likely due to the abundant (micro)cracks in the sample. It is probable that the fracture proceeded in the CO2 samples by connecting pre-existing (micro)cracks in the CO_2 attacked regions, thus producing rough fracture surfaces in these regions. The intact core did not have microcracks, and was expected to have flat fracture surfaces. However, because the intact core was thin, a difference in roughness of different regions could not be resolved.

2.2.4 Enhanced Microscale Mechanical Properties of the Carbonated Layer at the Cost of the CH-Dissolved Region

By employing nanoindentation, the hardnesses and indentation moduli of microsize areas on the polished cross sections can be compared, as shown in Figure 2.4. The hardness (0.8 ± 0.5 GPa) and the indentation modulus (17 ± 8 GPa) of the intact core of the CO2 samples are the same as those of the control samples (0.9 ± 0.7 GPa and 18 ± 12 GPa for hardness and indentation modulus, respectively). The carbonated layers, Region 3, of the CO2 samples have a significantly higher hardness of 2.4 ± 1.0 GPa and a higher indentation modulus of 39 ± 11 GPa, both 2–3 times that of the control hardness. On the other hand, due to the dissolution of materials, Region 2 has ~50% lower hardness and indentation modulus than the intact core. Region 4 is dissolved from the carbonated layer, and its hardness and indentation modulus have decreased to less than half the values of the carbonated layer.

Increased hardness of the carbonated layer in cement materials after CO_2 attack under GCS relevant conditions has been reported by previous studies; however, much less attention was paid to the hardness of the CH-dissolved region.[42, 73, 78] Due to the dense $CaCO_3$ phase, the initial carbonation of cement has been reported to increase the compressive strength of cement materials,

but the strength may decrease for longer CO_2 attack.[52, 92, 93] In our study, the decrease in hardness and indentation modulus in Region 2 is also quantified, clearly showing the weakening in the microscale. This new information is a key link to decreased strength and elastic modulus of the bulk samples.

2.2.5 Linking Micro- and Macroscale Mechanical Properties

This study showed that in microscale, the carbonated layer is denser and harder than the intact cement, while the CH-dissolved region is weaker. On the large scale, the bulk samples have significant decreases in strength and elastic modulus, which correspond to the microscale mechanical property changes of the CH-dissolved region, rather than those of the carbonated layer. This correlation suggests that the mechanical properties at microscale and macroscale need to be carefully considered. The structure of how strong and weak microscale components are assembled may lead to the weakening of the bulk material. In the specific case of this study, the structure of microscale components is illustrated in Figure 2.4b. Both bumps on the cement surface and microcracks in Region 2 deserve careful consideration to account for the change in the mechanical properties of the bulk sample.

First, intense CO_2 attack may cause swelling of outer layers of cement, forming bumps on the surface, and further cause spalling when the bumps break and fall out. The BSE image of the cross section of the CO2 sample (Figure 2.3c) shows that the swelling layers are Region 3 and 4, which protrude outwards, and have detached from the inner part of the sample, forming a gap between Region 3 and inner regions. Such a geometry of swelling suggests that large amounts of $CaCO_3$ precipitated over a comparatively large space in a short period of time. The time period may not have been long enough for the abundant $CaCO_3$ to find space in the pores in the CH-dissolved region through ion diffusion. Thus, the $CaCO_3$ preferentially precipitated outward and

detached from the core, forming a gap in the weak Region 2. The swelling led to buckling of the surface layers, which then stressed and cracked the outer surface, opening fast pathways for further chemical attack (Figure 2.3c and Figure 2.4b). Delamination of carbonated layers, swelling, and later on spalling, were also observed in other studies on CO_2 corrosion of cement materials cured longer than 28 days before reaction in GCS relevant conditions, but the formation processes have not been discussed.[52, 78, 79] Here, we provide new insight on the mechanism of formation of these sample defects.

Second, Region 2 is a mechanically weak space, where microcracks are likely to occur due to even slight stresses. Some microcracks stretch through the carbonate layer, reducing the integrity of the carbonate layer and decreasing the strength of the overall structure. Because of the weak nature of Region 2, swelling and spalling are also apt to occur. The weakness of Region 2 is extremely important, because both microcracks and the space caused by swelling can serve as important pathways through which CO_2 leaking is enabled.[65]

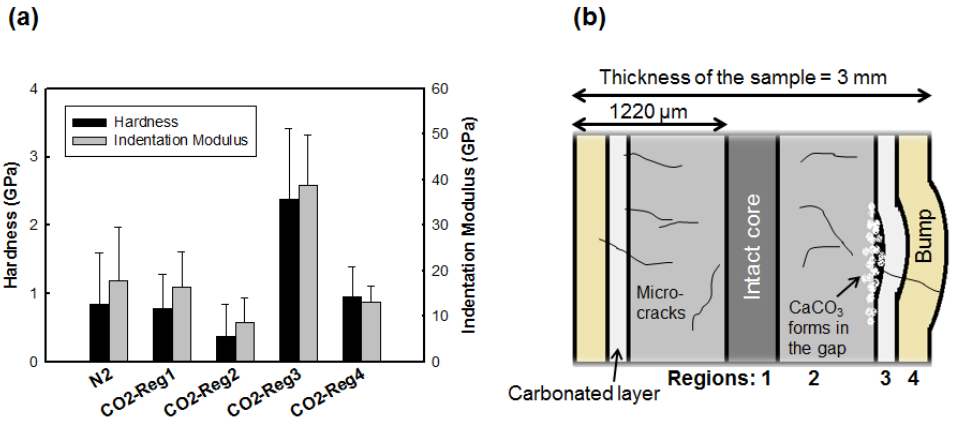

Figure 2.4 (a) Hardness and indentation moduli of N2 and CO2 samples. The CO2 samples are shown with respect to Regions 1–4. The intact Region 1 is similar to the control samples, and the carbonated Region 3 has enhanced hardness and indentation modulus. Region 2 has deteriorated mechanical properties. (b) Diagram of the structure of the CO2 samples, view on the $w \times h$ cross section, showing how different regions with different mechanical properties (as shown in (a)) are assembled together. The left and right edges are the surfaces of the sample.

2.3 Environmental Implications

Cement deterioration by CO_2 attack is closely related to wellbore integrity, and must be well understood for safer CO_2 storage. One way to understand cement deterioration is through a combination of chemical and mechanical alterations. We showed that a 1220 μm attacked depth on both sides of a 3 mm thick cement sample can lead to a ~90% decrease in strength and elasticity, and we also tested the mechanical properties of each layer. The quantified thicknesses span the chemical and mechanical perspectives. They can be used to calibrate not only reactive transport models,[48, 49, 56, 59, 60, 107] but also mechanical models (through simulating bulk mechanical properties by combining local properties).[52, 87, 89] By calibrating the models, we can improve our understanding of the mechanisms in interactions between reactive transport fluid and cementitious materials, as well as the mechanisms for constructing bulk mechanical properties using microsize properties. The better understood mechanisms will lead to more robust prediction for systems under different conditions. The experimental methods developed in this study also serve as a good reference for future studies combining chemical and mechanical analyses.

The findings of this study highlighted the importance of the CH-dissolved region in linking micro- and macroscale mechanical property changes. In past studies of CO_2 attack on wellbore cement, the CH-dissolved region has not been fully considered. For example, the hardness of CO_2-altered cement was reported only for the carbonated layer by Kutchko et al.[42] and Zhang et at;[78] a 30% decrease of Young's modulus in the CH-dissolved region was briefly mentioned by Manson et al.;[73] and the decrease of strength was attributed to microcracks at the front of carbonated layer by Fabbri et al.,[89] but was not linked with the property of the CH-dissolved region.

Furthermore, we highlighted the importance of structure in affecting the strength of bulk cement. Previous modeling considered only the complete dissolution of $CaCO_3$ as the critical point, past which the carbonated layer loses its protective role. This study provided new information, namely that the protective ability of the $CaCO_3$ layer can also be reduced by bumps on the surface. Also, the microcracks in Region 2 and the gap caused by formation of bumps can decrease the strength of the bulk material, and also lead to rougher fracture surfaces. The decreased strength can enable easier formation of cracks, which can allow CO_2 to pass through and further weaken the cement by continuing CO_2 attack. The rougher fracture surfaces imply that if dissolution and precipitation reactions are to be studied in the fracture, a longer fracture path with a larger exposed area and greater tortuosity should be considered for CO_2-attacked samples.

Acknowledgments

We would like to thank Dr. Ruth Okamoto for providing access to the three-point bending machine, and thank Dr. Spencer Lake for letting us to use the laser scanner. SEM-BSE images were collected at Washington University's Institute of Materials Science & Engineering. This study was supported by the Consortium for Clean Coal Utilization and the National Science Foundation's Career Award (EAR-1057117). Ms. Qingyun Li is supported by the Center for Nanoscale Control of Geologic CO_2, an Energy Frontier Research Center funded by the U.S. Department of Energy, Office of Science, Office of Basic Energy Sciences under Award Number DE-AC02-05CH11231. Dr. Katharine M. Flores and Ms. Kelly Kranjc acknowledge support from the Air Force Office of Scientific Research under Grant No. FA9550-12-1-0059.

Supporting Information for Chapter 2

2-S1 Experimental Setups

To conduct the experiments, we used a bench-top high temperature and pressure reactor, purchased from Parr Instruments, IL. The reactor is made from HC alloy-276, with a volume of 300 mL. To avoid contamination from alloy dissolution in acidic brine, a Teflon liner was used to contain the reaction solutions. The reactor module was previously used in several of studies in our lab.[108-115] The pressure was controlled by a syringe pump (Teledyne ISCO, Lincoln, NE) linked to the reactor, and the temperature was controlled by a thermocouple, a heater, and a temperature controller (Parr Instrument Company, IL).

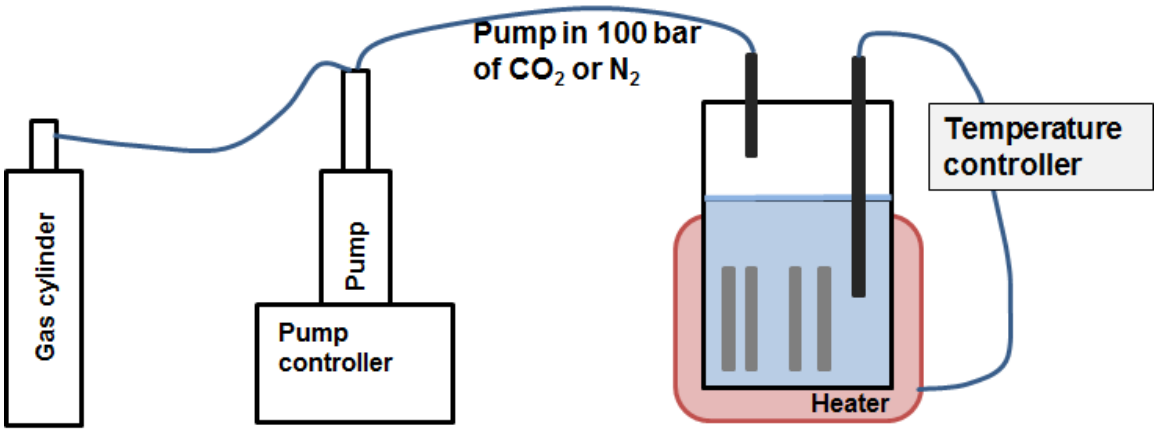

Figure 2-S1 Experimental setup for high temperature/pressure experiments. The temperature is controlled at 95 °C and the pressure is controlled at 100 bar.

The conditions used in this study were 95 °C, 100 bar, and 0.5 M NaCl ionic strength. These conditions are within the range of conditions observed in GCS sites (31 – 110 °C, 73.8–600 bar, and 0.01–2 M NaCl).[90] The comparatively high end of the temperature range was selected to enable reasonable reaction rates for bench-scale study. Our SEM and XRD analyses showed that our reacted samples were in good consistency with those reported in other studies on CO_2 attack

under moderate temperatures.[12, 42, 73] No additional reactions were found due to a comparatively high temperature. Using a typical geopressure gradient of 0.1 bar/m, and a typical geothermal gradient of 0.03 ^{o}C/m, we can roughly obtain a pressure of 234 bar corresponding to 95 ^{o}C (or (95 - 25)/0.03 = 2333 m depth). This pressure is higher than the 100 bar we used. However, because the CO_2 attack on cement mainly depends on CO_2 solubility in the brine, and because we can get similar CO_2 solubilities at 100 bar and 234 bar of CO_2, we do not anticipate that our current findings will prove significantly different from those obtained at 95 ^{o}C and 234 bar. For example, calculated from Duan's equation using 95 ^{o}C and 0.5 M NaCl, the solubility of CO_2 at 100 bar is ~ 0.72 M. If using a 2 M NaCl solution at 95 ^{o}C and 234 bar, the CO_2 solubility is 0.81M, similar to the solubility used in this study.

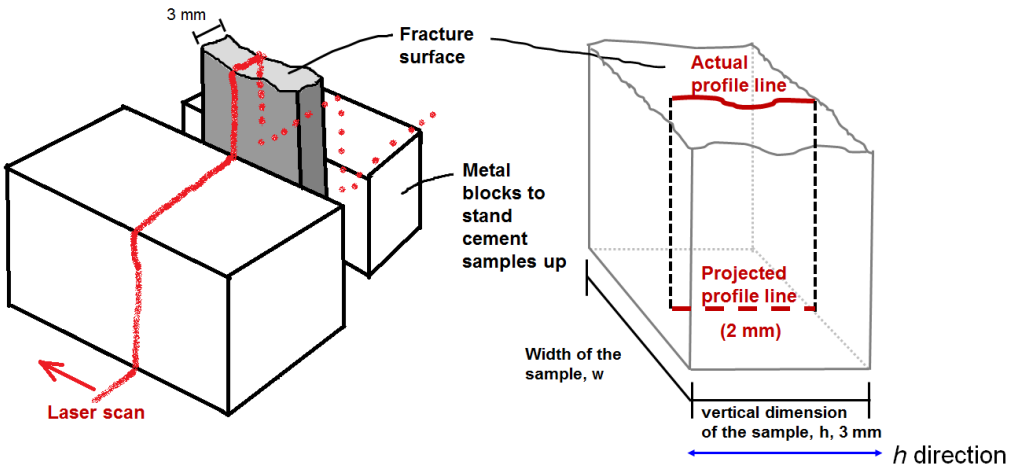

Figure 2-S2 Diagram for fracture roughness quantification by laser scanner (left), and an example profile line (right). Each sample has ~ 100 profile lines, with projected lines parallel to the *h* direction. The profile line roughness parameter (R_L) is calculated as the ratio of length of actual profile line to the length of projected line. Because of the occasional artifact in the laser scanner data at sample edges, we removed data with artifact, and used a projected profile line shorter than 3 mm. Each ~ 2 mm profile line is given by 21 points, including the end-points.

2-S2 Additional Data for Chemical Analyses

Table 2-S1 X-ray fluorescence analysis of cement before hydration.

	wt%
K_2O	0.2
CaO	53.8
TiO_2	0.16
MnO	0.05
Fe as Fe_2O_3	3.64
Fe as FeO	0
Na_2O	0.2
MgO	2.5
Al_2O_3	2.6
P_2O_5	0.10
SiO_2	19.0
Loss on ignition	19.0

Table 2-S2 Aqueous chemistry after degassing.

Condition	CO2	N2	Original Clinker
Ca, mM	147.6 ±0.6	9.0± 0.3 mM	--
Si, mM	5.33 ± 0.03	1.62 ± 0.01	--
Ca/Si	27.7	5.6	3.0

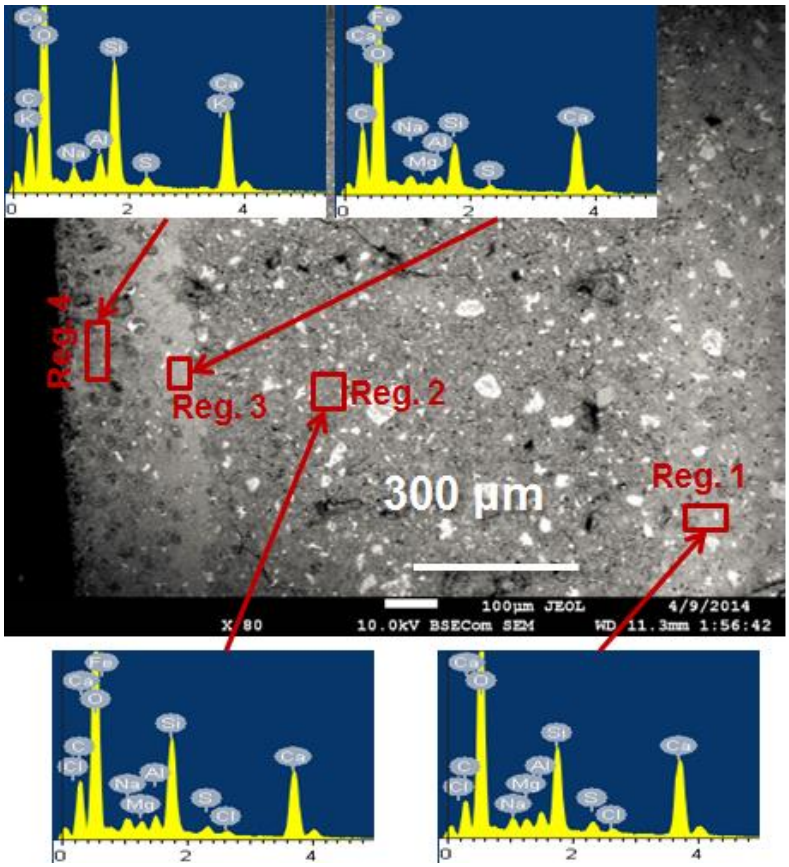

Figure 2-S3 EDS results showing different compositions in the four regions in CO2 samples, which are consistent with Eqs. 2.5–2.8 in the main part. Region 1 is the intact cement. Region 2 has Ca dissolved from portlandite and partially from C-S-H, and the Ca/Si ratio in Region 2 is less than that in Region 1. Region 3 has $CaCO_3$ precipitation, and has enhanced peaks for Ca, C, and O. Region 4 is the surface of the cement, where $CaCO_3$ has dissolved more than amorphous silica. To clearly show the presence of portlandite in the intact core, XRD results are shown in the main text.

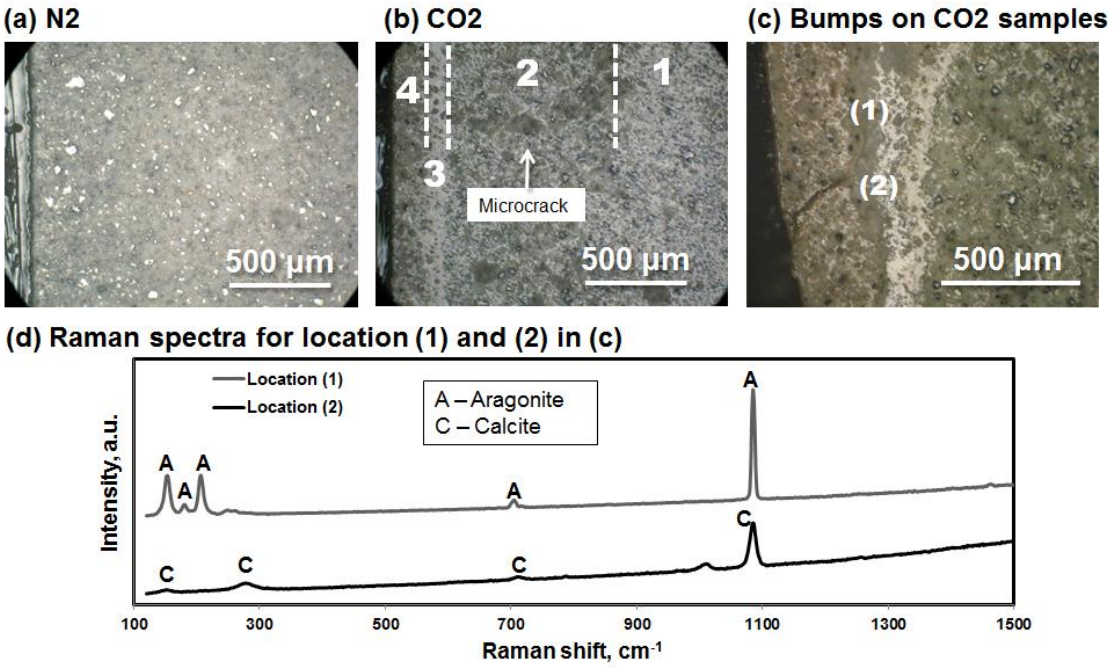

Figure 2-S4 Optical images of polished cross sections of (a) N2 and (b and c) CO2 samples. (a) and (b) are not from the same spots as (a) and (b) in Figure 2.1 of the main text. Microcracks in Region 2 of CO2 samples are not as obvious as shown by BSE images. (d) Minerals formed in the fracture gap were identified as a mixture of aragonite and calcite.

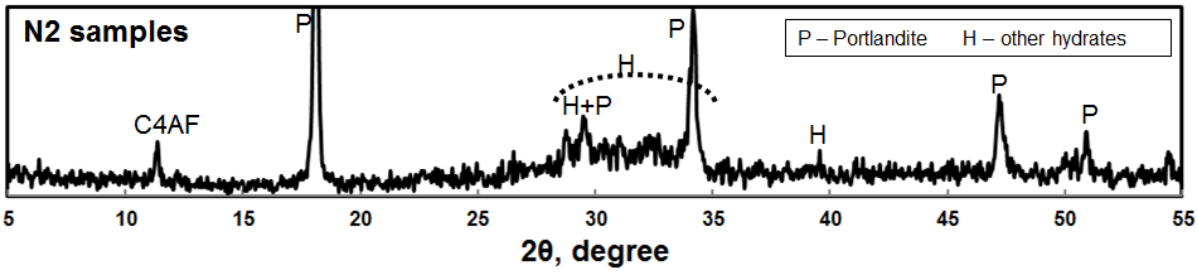

Figure 2-S5 XRD for N2 samples

Correlation between Fe content and orange color in the acid-treated samples. Additional CO2 samples were soaked in strong nitric acid for 1 day. After the acid treatment, the orange color became more distinct. The samples were rinsed using DI water and dried for SEM-EDS and XRD analyses (Figure 2-S6). The Fe(III) phases can co-exist with other minerals (for example amorphous SiO_2), in three ways: adsorption of Fe(III) species onto amorphous SiO_2 surfaces, incorporation of Fe into amorphous SiO_2 grains, or co-existence of Fe(III) (hydr)oxide phases with amorphous SiO_2 grains adjacent to each other. When Fe(III) (hydr)oxide is distributed within amorphous SiO_2, tiny amount can generate orange color.[116] After strong acid treatment, the Fe(III) (hydr)oxides were not fully dissolved. There are several possible reasons. First, the dissolution of Fe(III) (hydr)oxides may have been slow;[117] second, the local pH at the surface of the cement may have been near neutral or even basic; and third, the co-existence of comparatively insoluble SiO_2 with Fe(III) (hydr)oxides may have helped prevent dissolution of Fe(III) (hydr)oxides.

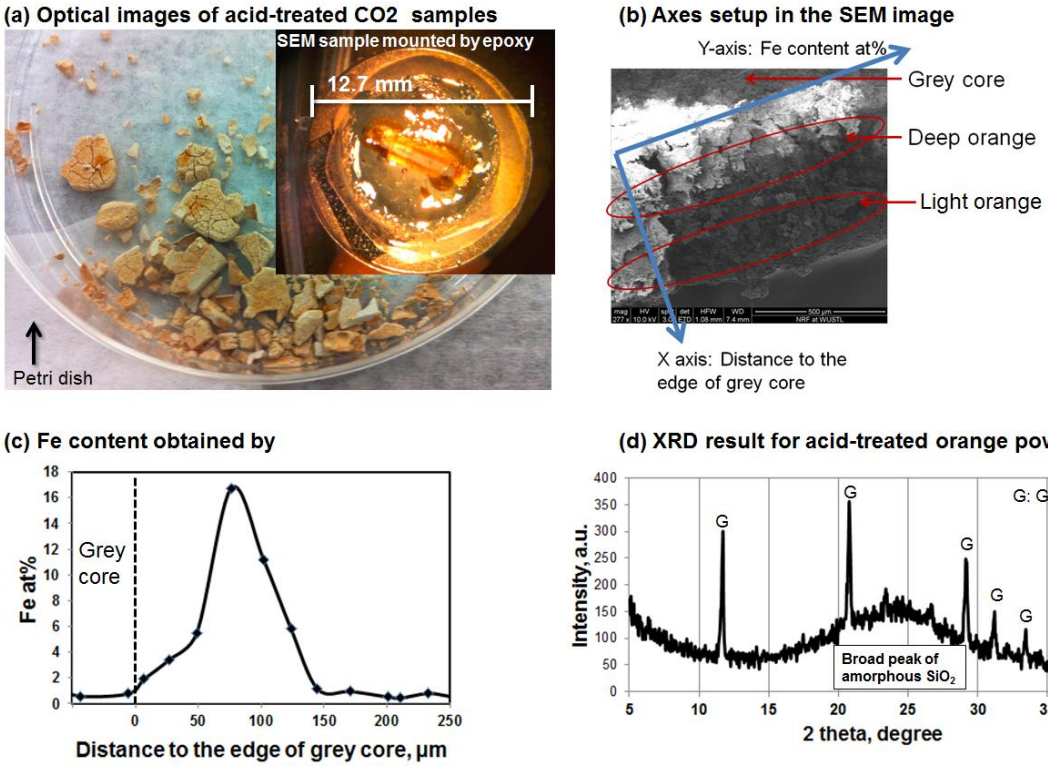

Figure 2-S6 (a-c) Correlation of orange color and Fe content by SEM-EDS. (d) XRD of orange powders. The sharp peaks were from gypsum that originally exists in cement. Due to the slow gypsum dissolution rate, they were not dissolve by HNO_3. The broad peak at 2θ = 15–35 is from am-SiO_2. No Fe(III) phases were identified.

2-S3 Additional Data and Discussions for Mechanical Property Analyses

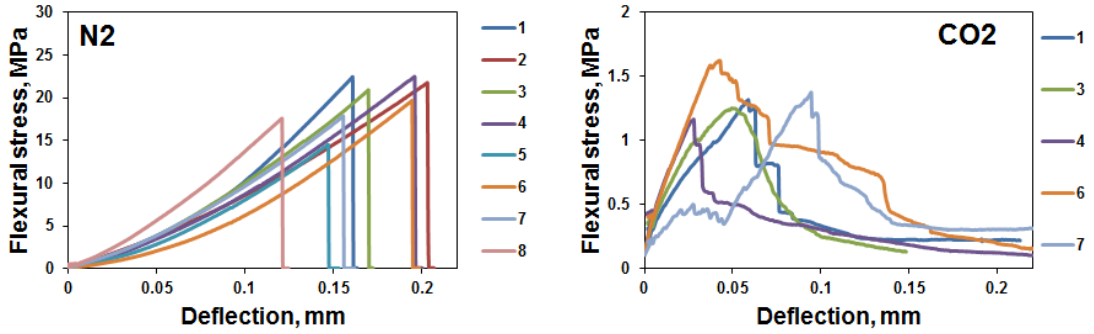

Figure 2-S7 Groups of stress-deflection curves for N2 and CO2 samples. Samples #2, #5, and #8 for CO2 were defective before the bending tests, and were not used for statistical analyses.

Reproduced with permission from [Qingyun Li, Yun Mook Lim, Katharine M. Flores, Kelly Kranjc, and Young-Shin Jun. Chemical Reactions of Portland Cement with Aqueous CO_2 and Their Impacts on Cement's Mechanical Properties under Geologic CO_2 Sequestration Conditions. *Environmental Science & Technology*, 2015, 49 (10), 5476-5483.] Copyright [2015] American Chemical Society.

Chapter 3: Effects of Sulfate during CO_2 Attack on Portland Cement and Their Impacts on Mechanical Properties under Geologic CO_2 Sequestration Conditions

Results of this chapter have been published in *Environmental Science & Technology*, 2015, 49 (11), 7032-7041

Abstract

The chemical/mechanical alterations of cement can be affected by complex aqueous chemistries. In this chapter, we extent the study in Chapter 2 to investigate the effects of sulfate ions on chemical and mechanical alterations of cement during CO_2 attack under geologic CO_2 sequestration (GCS). Cement paste samples were reacted in brine with 0.05 M sulfate and 0.4 M NaCl at 95^oC, under 100 bar of either N_2 or supercritical CO_2. The results were compared to those obtained from systems without additional sulfate at the same temperature, pressure, salinity, and initial brine pHs. After 10 reaction days, chemical analyses using backscattered electron scanning secondary microscopy (BSE-SEM) and inductively coupled plasma optical emission spectrometry (ICP-OES) showed that the CO_2 attack in the presence of additional sulfate was much less severe than that in the system without additional sulfate. The results from three-point bending tests also indicated that sulfate significantly mitigated the deterioration of the cement's strength and elastic modulus. In all our systems, typical sulfate attacks on cement via formation of ettringite were not observed due to short reaction times. The protective effects of sulfate on cement against CO_2 attack resulted from SO_4^{2-} adsorption and/or gypsum coating on the $CaCO_3$ grains in the carbonated layer, which inhibited dissolution of $CaCO_3$. Findings from this study provide new, important

information for understanding the integrity of wellbores at GCS sites, and thus promote safer GCS operations.

3.1 Introduction

In applications of geologic CO_2 sequestration (GCS) to mediate climate change caused by anthropogenic CO_2 emission to the atmosphere,[4] one of the big concerns is the possible leakage of injected CO_2 through cementitious materials in wellbores.[12] The cement types used in wellbores are mostly oil well Portland cement (Class H and Class G).[41] These cements use ordinary Portland cement (OPC) as their basis, with a reduced amount of aluminum phases to resist sulfate attack, and with slightly lower ratios of C_3S to C_2S.[41, 63] Anhydrous Portland cement contains 21–67% alite ($3CaO{\cdot}SiO_2$, or C_3S), 0–49% belite ($2CaO{\cdot}SiO_2$, or C_2S), 1–17% aluminate phase ($3CaO{\cdot}Al_2O_3$, or C_3A), and 6–18% ferrite phase ($4CaO{\cdot}Al_2O_3{\cdot}Fe_2O_3$, or C_4AF).[41, 63] Once cement is mixed with water, hydration produces calcium silicate hydrates (C-S-H), portlandite ($Ca(OH)_2$ or CH), and other hydrates, including hydrates of C_3A, C_4AF, etc., and the cement hardens. Usually, these hydrates coexist with the remaining anhydrous phases in a hardened cement material. To be concise, we use the term "cement" to mean the hardened mixture of anhydrous cement and its hydrated products.

As a basic material, cement can be chemically attacked by injected supercritical (sc) CO_2, which forms carbonic acid in the presence of water. At GCS sites, CO_2 attack on cement will be more severe than attack by atmospheric CO_2, because a large amount of CO_2 is present and the temperature (31–110 ^oC) and pressure (73.8–600 bar) in field sites are usually high.[12, 62, 90] In the past decade, CO_2 attack on wellbore cement at GCS relevant conditions has been studied by field sample analysis,[67, 70, 75, 76] experimental studies,[42, 51, 68, 72-74, 77-80, 82-84, 86-88, 91, 94, 118] reactive transport

modeling,[48, 49, 56-60] and modeling of cement's mechanical properties.[87, 91] Based on the previous studies, under GCS conditions, cement develops a layered structure due to chemical reactions.[12, 42] Once the cement contacts aqueous CO_2 or water-saturated $scCO_2$, it will partially dissolve and release Ca^{2+} from cement. These Ca^{2+} ions will re-precipitate as $CaCO_3$ with carbonate species (HCO_3^- or CO_3^{2-}), and form a carbonated layer together with other secondary phases such as amorphous silica. The carbonated layer is close to the surface of the cement, hindering further diffusion of acidic brine into the cement. At the outside of the carbonated layer, $CaCO_3$ is dissolved by acidic brine, leaving the less soluble phases, such as amorphous silica.[12, 42] A few studies have also examined the changes in mechanical properties of cement caused by CO_2 injection. They found that the $CaCO_3$ layer is harder than the intact cement,[42, 73, 78] that the permeability and porosity of cement decrease in the early stage of CO_2 attack,[49-51] and that the compressive strength of cement decreases after exposure to CO_2.[52]

However, there are still many knowledge gaps. One is that we have not yet made a holistic connection between chemical reactions and mechanical changes, and for the mechanical properties, it is not clear how microscale mechanical properties (e.g., microhardness, local permeability, etc.) are linked with larger scale properties (e.g., strength, elasticity, etc.). Our published work (presented in Chapter 2 in this dissertation) aimed at filling this knowledge gap, and found that a bulk CO_2-attacked cement has a ~90% decrease in strength, and that the weakened CH-dissolved region as the key to connecting micro and larger scale mechanical properties.[119]

Another important knowledge gap is that we need a better understanding about the effects of aqueous sulfate (SO_4^{2-}) on cement during CO_2 attack. By far, CO_2 is the most studied species that attacks wellbore cement under GCS relevant conditions. Several studies have also considered the reactive transport of H_2S into cement and the resultant formation of pyrite and ettringite,

providing information on the practice of acid gas (H_2S) co-injection that reduces GCS cost.[78, 79, 82] However, the possible interactions between sulfate ions and cement during CO_2 attack under GCS conditions have not been studied. In formation waters, SO_4^{2-} concentrations are usually between 0.01 M–0.05 M,[53] and can be as high as 0.15 M even before CO_2 injection.[120] Moreover, SO_4^{2-} can be produced by co-injection of H_2S, during which S can be oxidized either by O_2, Fe(III), or other redox species.[78]

In cement industries, because sulfate causes formation of expansive ettringite ($Ca_6Al_2(SO_4)_3(OH)_{12}\cdot 26H_2O$) or gypsum, its effects have been investigated extensively.[121, 122] At the early-age (< 7 days) of hydration, restrained expansion in expansive cement Types K, M, and S can be beneficial in compensating shrinkage deformation.[63] However, after exposure to SO_4^{2-} for months or years, delayed ettringite formation in mature cement can cause cracking due to its larger volume than its original reactants, thus reducing the strength of cement.[63, 121] Sulfate may also cause gypsum ($CaSO_4$) formation in cement, which also has expansive volume, and thus has a similar effect to ettringite. Gypsum formation is, however, more controversial: Some studies reported that gypsum formed a protective layer, limiting chemical attack to the surface of the material, while others suggested that gypsum precipitation promotes spalling, which is detrimental to the integrity of the cement.[92] There are also a few studies reporting the occurrence of cement deterioration in the presence of both SO_4^{2-} and CO_2 by formation of thaumasite ($Ca_3Si(OH)_6(CO_3)(SO_4)\cdot 12H_2O$), but thaumasite formation requires a low temperature (4–10 °C) and a pH above 10.5, conditions not relevant to GCS.[63] Therefore, under GCS conditions, where the results of CO_2 attack are clear within two weeks,[12] the role of SO_4^{2-} is not clear.

This study focuses on CO_2 attack on cement in GCS sites, and elucidates the effects of SO_4^{2-} during CO_2 attack. In particular, we examined the chemical and mechanical changes of

cement samples after reactions under GCS relevant conditions in the presence of 0.05 M sulfate. The results were compared to findings in Chapter 2, and the mechanisms by which sulfate affects CO_2 attack on cement were explored. Findings from this study show that the sulfate dramatically reduces the cement deterioration during intense CO_2 attack, and thus should be carefully considered in experimental studies and reactive transport modeling. This information provides new insight regarding the integrity of wellbores at GCS sites, and thus the safety of GCS. This study also further quantifies mechanical property changes by CO_2 attack, and can benefit both mechanical and chemical research fields.

3.2 Experimental Section

3.2.1 Cement Paste Preparation and High Temperature/Pressure Reactions

Ordinary Portland cement (OPC), manufactured by QUIKRETE®, was mixed with water at a water-to-cement ratio of 0.5, which is within the typical range of 0.3–0.6.[41] The cement paste was cast in custom-made rubber molds with dimensions of 3 cm (l) × 1.1 cm (w) × 0.3 cm (h). This small size allows significant changes in bulk mechanical properties after 10 days' reaction. After 3 days of hardening at 100% relative humidity, the cement paste samples were de-molded, rinsed by ultrapure deionized (DI) water, and reacted in high temperature/pressure reactors. Detailed sample preparation information can be found in Chapter 2. Such 3-day hardened cement is most closely typical of the cement capping that closes a CO_2 injection well, where potential CO_2 attack can occur during the early stage of cement hydration. However, because of the similar compositions of old cement (in old wells) and freshly cast and hardened cement (in capping of

used wells), they can be altered similarly by chemical attacks, and consequently undergo similar mechanical property changes.

Table 3.1 Reaction conditions utilized in this study and the study in Chapter 2. All conditions are at 95°C and 100 bar, which are relevant to geologic CO_2 sequestration.

Condition Name	Brine Composition	Gas above the brine	Initial pH	Scenarios
N2	0.5 M NaCl	N_2	Neutral	Free of chemical attack
SO4	0.4 M NaCl; 0.05 M Na_2SO_4	N_2	Neutral	Free of CO_2 attack but have potential reactions between cement and sulfate
CO2	0.5 M NaCl	CO_2	3.0 ± 0.1	CO_2 attack after CO_2 injection
CO2SO4	0.4 M NaCl; 0.05 M Na_2SO_4	CO_2	3.0 ± 0.1, adjusted by HCl	CO_2 attack in the presence of SO_4^{2-} after CO_2 injection

Two new conditions were employed in this study, in addition to the conditions used in Chapter 2 on systems without additional SO_4^{2-}, as listed in Table 3.1. The utilized temperature, pressure, and salinity are within the range of GCS sites.[62] Under each condition, eight of cement samples were submerged into brine with an ionic strength of 0.5 M. The upper space of the reactor was filled with either N_2 or CO_2 at 100 bar. The "SO4" condition mimicked the scenario before CO_2 injection in the presence of 0.05 M sulfate in the brine. This condition helped study the possible effects of sulfate, independent of CO_2 attack. In our concurrent study, the corresponding system without additional sulfate was named the "N2" (control) condition.[119] The "CO2SO4" condition mimicked the scenario after CO_2 injection in the presence of 0.05 M sulfate, with 100 bar of CO_2 contacting the brine. In Chapter 2, the corresponding system without additional sulfate was the "CO2" condition. To minimize the effect of pH on our systems, the initial pH of the

CO2SO4 system was adjusted by HCl and measured to be the same as that of the CO2 condition. To differentiate our condition names from chemical formulas, we do not use subscripts in the condition names.

A bench-top reactor (Parr Instrument Company, IL) was used to achieve the reaction conditions. Detailed information on *in situ* pH measurement and the high temperature/pressure reactor setup is in the Supporting Information Section 3-S1.

3.2.2 Chemical Analyses

Following the methods developed in Chapter 2, to ensure that an intact core of cement remains after the reaction, we ended the reaction after 10 days, and gradually degassed the reactor for 1 hour. The aqueous phase was collected and acidified by HNO_3 for measurement of Ca and Si concentrations, using inductively coupled plasma optical emission spectrometry (ICP-OES). The concentrations of Al, Fe, and Mg were under the detection limits. The cement samples were rinsed with DI water, oven-dried at 80°C overnight to remove pore water but not combined water,[41, 95] and tested by a three-point bending machine.

After the bending tests, three of the most representative samples from each condition were mounted in epoxy resin and polished along the $w \times h$ cross-section down to a roughness of < 0.1 μm. The polished surfaces were imaged by a backscattered electron (BSE) detector on a JEOL 7001LVF FE-SEM, coupled with energy dispersive X-ray spectrometry (EDS) to analyze the elemental composition. To eliminate the charge effect in the image, low vacuum mode was used at 10 Pa. The working distance was 10 mm, the accelerating voltage was 10.00 kV, and the probe current was 16 μA. In the BSE images, the average atomic number of a phase is higher for an brighter area.[41, 96, 97] The brightest areas for cement samples are anhydrous phases, within which

the whitest parts are the Al-containing phases (C_3A and C_3AF), and the slightly grey areas are alite and belite.[41, 98] The grey areas are CH and C-S-H, and the darkest areas are pores or cracks.[41, 98] To examine the optical features of the cement samples, optical images of the cross sections were taken by an optical microscope (Zeiss Imager Microscope). To identify the phases of the cement samples, powder samples were ground from each layer of the CO2SO4 samples to obtain qualitative X-ray diffraction (XRD) patterns by a Rigaku X-ray Diffractometer. For samples without a layer structure, powder samples were ground from the bulk samples for XRD identification.

3.2.3 Solid Sample Analyses for Mechanical Property Changes

Three-point bending tests. The oven-dried cement samples were tested by a three-point bending setup in a mechanical test frame (Instron® Model 5583 mechanical test frame). A load cell (Instron® Model 2525-816) with a loading range of 500 N was used. The sample was loaded on a custom-made sample stage. A diagram of the setup of the three-point bending tests can be found in Figure 2.1a in Chapter 2, and the test parameters were maintained the same as in Chapter 2. The loading force and the deflection of the loading point on the sample beam were recorded during the test.

For a rectangular beam, the load force is converted to flexural stress (σ_f) by

$$\sigma_f = \frac{3FL}{2wh^2}, \qquad \text{Eq. (3.1)}$$

and the elasticity of the beam is represented by elastic modulus (E_f) calculated from

$$E_f = \frac{CL^2}{6h}, \qquad \text{Eq. (3.2)}$$

where F is the load force, L is the distance between supporting points, w and h are the width and height of the sample, and C is the slope of the linear part of the stress–deflection curve. The largest flexural stress a sample could stand was recorded as the modulus of rupture (MOR, i.e., flexural strength), and was used to represent the strength of the sample. For samples with the same dimensions, the area under the stress–deflection curve is proportional to the energy absorbed by the sample.[4] The post cracking behaviors of our sample are compared by the shape of the stress–deflection curve after the main drop (crack). The stress–deflection curve drops immediately to zero for a brittle material, whereas it drops gradually for a quasi-brittle material, indicating a quasi-brittle material can absorb a fair amount of energy after being cracking and before being completely broken. Detailed information on the post-cracking behavior comparison is available in the Supporting Information Section 3-S4.1.

Fracture roughness comparison. The surface profile of each sample was obtained by a laser scanner (Keyence, LJ-V7080). The roughness of the fracture surface was quantified by the line profile roughness parameter R_L, defined as the ratio of the profile length to the projected profile length, as illustrated in Figure 2-S2 in the Supporting Information for Chapter 2. The length of the projected profile line was 2 mm parallel to the h direction, and each line was composed of 21 points, including the end points. R_L is always equal to or larger than 1, and the greater the deviation of R_L from 1, the rougher the surface.

Nanoindentation. The hardness and indentation modulus (which is related to the stiffness) of microsize points on the polished cross section surface were tested by a nanoindentation machine (HYSITRON TI 950 TriboIndenter). The indentation parameters were the same as in Chapter 2. The hardness (H) and the indentation modulus (E_r) were calculated by

$$H = \frac{F_{max}}{Area}$$, and Eq. (3.3)

$$E_r = \frac{Slope\sqrt{\pi}}{2\sqrt{Area}}$$, Eq. (3.4)

where F_{max} is the maximum load by the indenting tip, *Area* is the projected contact area, and *Slope* is the initial slope of the unloading curve. E_r reflects the stiffness of the indented point. The nanoindentation diagram is shown in Figure 2.1b in Chapter 2.

3.3 Results

3.3.1 Effects of Sulfate on Samples' Appearance

After 10 days of reaction, the cement samples reacted under the SO4 condition (SO4 samples) had a grey color indistinguishable from the appearance of N2 samples, while the cement samples reacted under the CO2SO4 condition (CO2SO4 samples) had an orange tint on the surface, obviously brighter than that also observed on CO2 samples without sulfate. The color difference between CO2SO4 samples and CO2 samples is shown in the pictures of cement samples in Figure 3.1a and Figure 3-S2. Our concurrent study showed that 50% of CO2 samples had bumps on the surface, but only two pieces of the eight CO2SO4 samples from the same reaction batch had appreciable bumps.

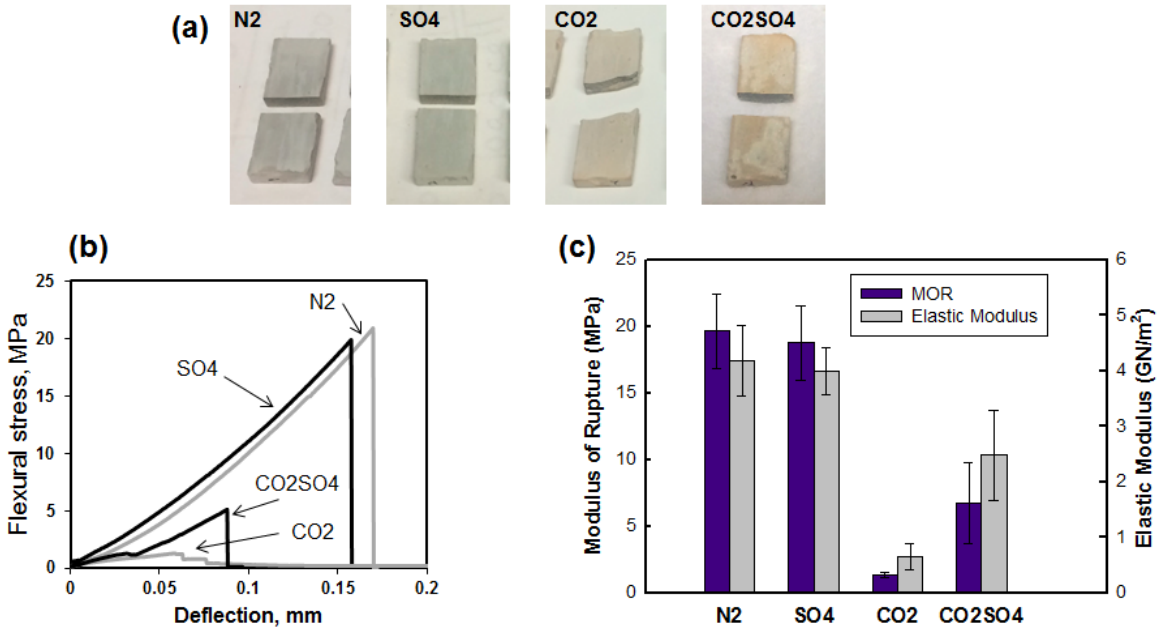

Figure 3.1 (a) Representative sample pictures after the bending test. The fracture surface of the CO2 samples is the most rough. The orange tint on the surface of the CO2SO4 is brighter than that on the surface of the CO2 sample. (b) Typical stress–deflection curves from the three-point bending tests. The curve of the SO4 sample is similar to that of the N2 sample. The curve of the CO2SO4 sample has fluctuations, corresponding to the layer structure. (c) Quantification of strength and elastic modulus of cement samples. The SO4 samples are not significantly different from the N2 samples. The CO2SO4 samples are much less deteriorated than the CO2 samples.

3.3.2 Chemical Reactions in the Presence of Sulfate

In the absence of CO_2 ($pH_{initial}$ = neutral) As with the N2 samples, the SO4 samples also had a uniform appearance on the cross section surface, without any observable layer structures. The presence of sulfate did not cause more mirocracks in the cement, contrary to the general view of sulfate attack on cement.[121, 122] Also, no ettringite or gypsum was observed from BSE-SEM (Figure 3.2) and XRD (Figure 3.3) results for both N2 and SO4 samples. The difference of the SO4 samples from the N2 samples is that there are more anhydrous Al-containing phases (C_3A and C_4AF) in the SO4 samples, as indicated by the arrows in Figure 3.2. The XRD patterns (Figure 3.3) of N2 and SO4 samples show the apparent peak for anhydrous Al-containing phases, indicating slower hydration of these phases in the cement in the presence of sulfate.

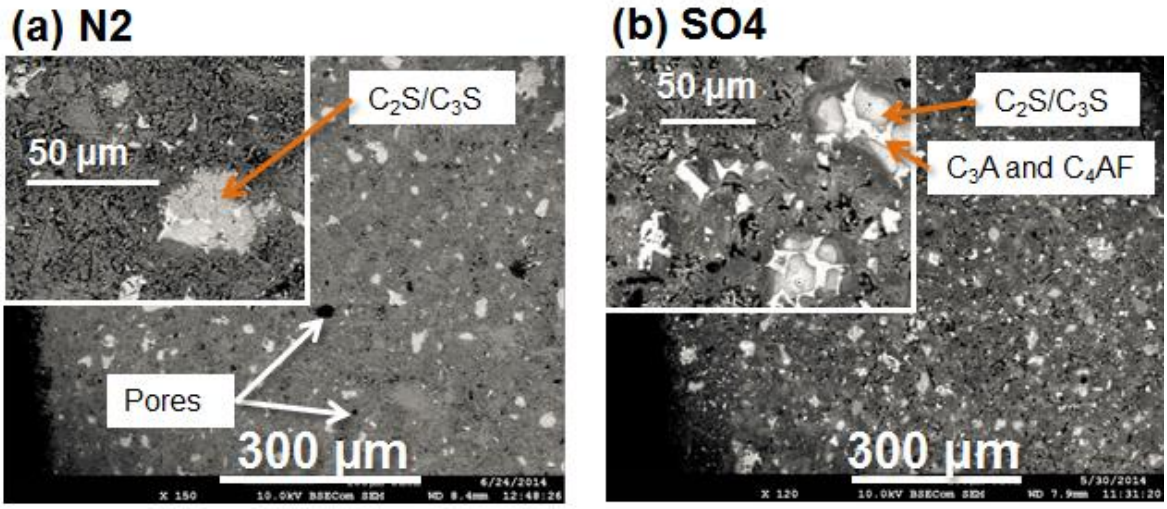

Figure 3.2 BSE images of polished cross section surfaces of cement samples reacted under conditions without CO_2 in the (a) absence and (b) presence of sulfate. The zoomed-out image of the N2 sample is adapted from Chapter 2. The left of each image is the surface of the cement, and the right of the each image is inside of the cement sample. In the presence of sulfate, the hydration of Al-containing phases is retarded. No layer structures were observed in both N2 and SO4 samples. No formation of ettringite and gypsum were observed.

In the presence of CO_2 ($pH_{initial}$ = acidic) Typical sulfate attack on cement was not observed in the CO2SO4 samples. No ettringite, gypsum, or thaumasite was identified by SEM (Figure 3.4) and XRD (Figure 3.3). A SEM image of the cross section of the CO2SO4 sample (Figure 3.4b) also shows that there is lesser amount of anhydrate Al-containing phases than in the SO4 samples (Figure 3.3b). The cement samples reacted under the CO2SO4 conditions had layer structures similar to those found in the CO2 samples (Figure 3.4); however, interestingly, the total attacked depth (i.e., sum of Regions 2–4) in CO2SO4 samples was smaller than that in CO2 samples, as shown in the BSE images in Figure 3.4 and optical images in Figure 3-S1c-d. From right (core) to left (brine–cement interface), the intact core is labeled as Region 1. In the CH-dissolved region, Region 2, all the CH and part of the C-S-H has dissolved, releasing Ca^{2+} ions. The released Ca^{2+} ions precipitated with carbonate to form the carbonated layer, Region 3. At the outside of Region 3, $CaCO_3$ was dissolved by the acidic brine, and formed Region 4. The main

chemical reactions in CO2SO4 samples were the same as those in CO2 samples, as supported by XRD results (Figure 3.3). The total CO_2-attacked depth (Regions 2–4) in CO2SO4 samples is 800 $\pm$ 10 μm, less than that of the CO2 samples (1220 $\pm$ 90 μm). The carbonated Region 3 in CO2SO4 samples is ~17% thicker than that in CO2 samples, while to the contrary, Regions 3 and 4 combined are ~ 30% thinner than in the CO2 samples (due to a thinner Region 4 in the CO2SO4 samples). In Region 2 of the CO2SO4 samples, about 50% fewer microcracks were observed than in Region 2 of the CO2 samples, based on optical microscopy images. More thicknesses of different regions in CO2SO4 and CO2 samples are listed in Table 3-S2. The aqueous concentration measurements (Table 3-S1) also confirmed that dissolution of CO2SO4 samples was less intense than dissolution of CO2 samples.

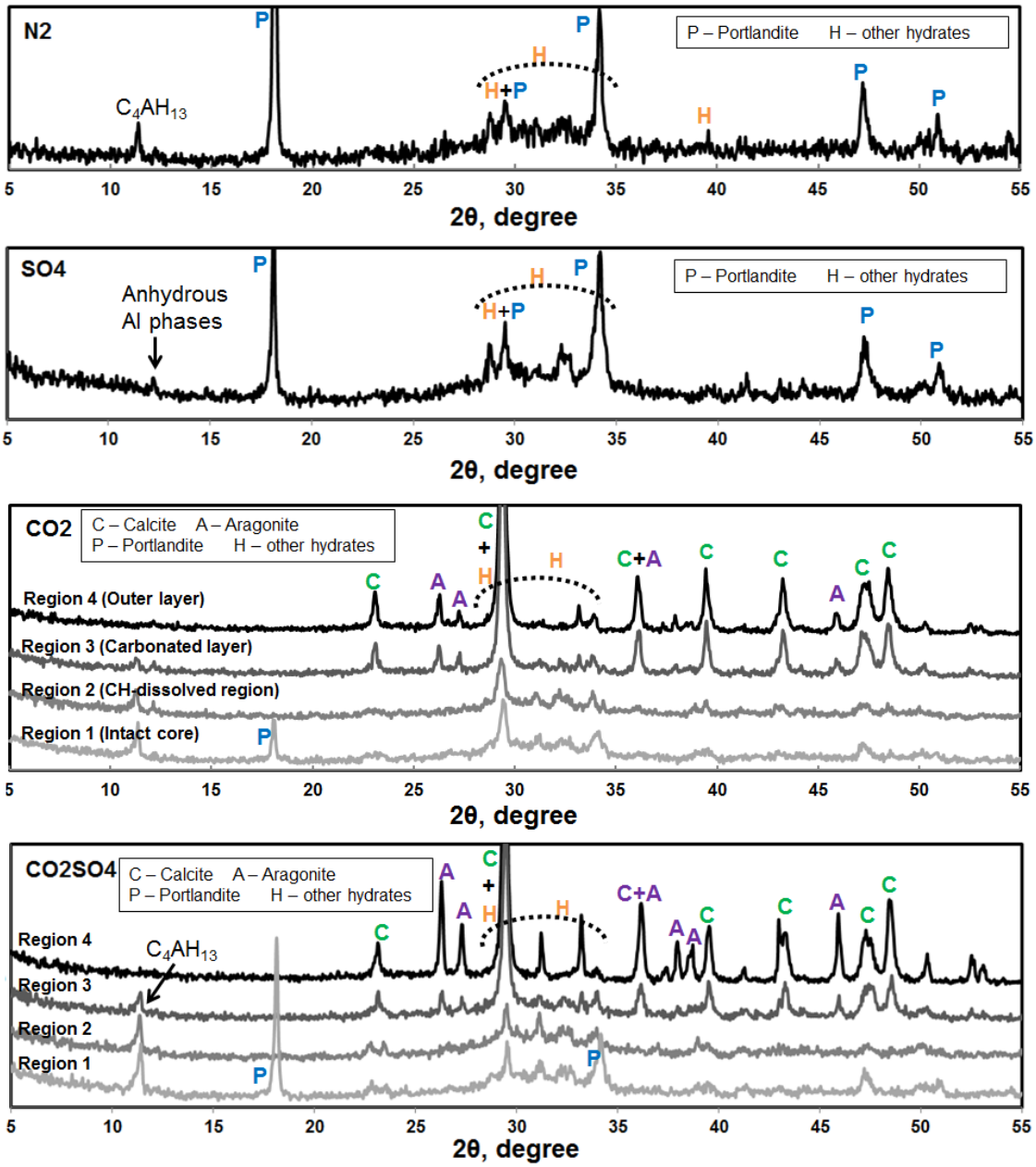

Figure 3.3 XRD patterns for samples reacted under conditions listed in Table 3.1. Under conditions without CO_2, the SO4 samples have a peak at 2θ = 12.20 corresponding to anhydrous Al-containing phases (brownmillerite, RRUFF database ID R130105), while the N2 samples have a peak at 2θ = 11.40, corresponding to the hydration product of Al-containing phases.[123, 124] This difference indicates the retarded hydration of Al-containing phases in the presence of sulfate. The XRD patterns for CO2 and CO2SO4 samples are the same for each region. The hydration of Al-containing phases in the CO2SO4 samples were not appreciably retarded.

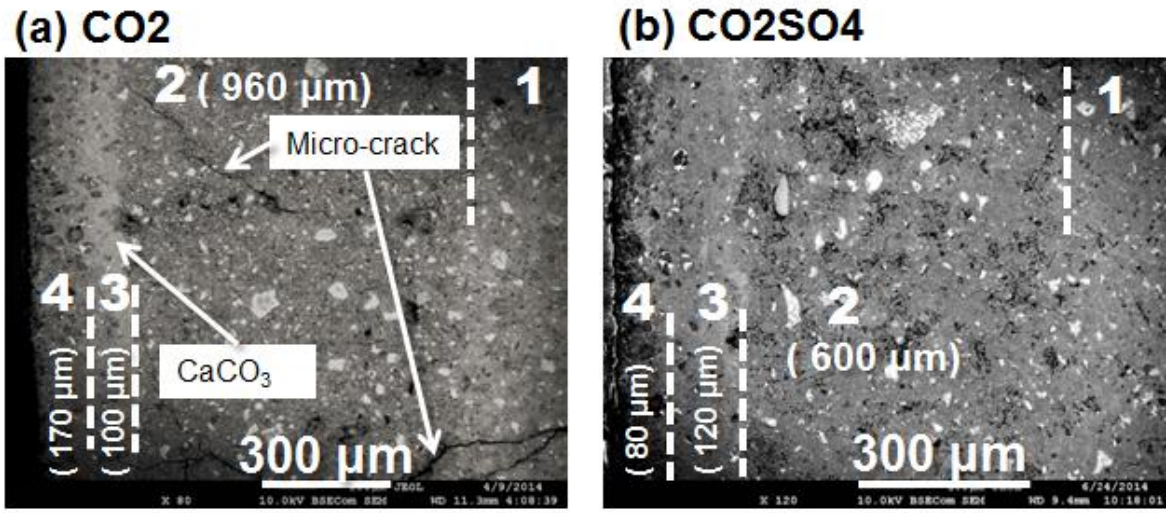

Figure 3.4 BSE images of polished cross section of cement samples attacked by CO_2 in the (a) absence and (b) presence of sulfate. The zoomed-out image of the CO2 sample is adapted from Chapter 2 on CO_2 attack and mechanical property changes.[119] The left of each image is the surface of the cement, and the right of the each image is the intact core of the cement sample. Layer structures were observed in both CO2 and CO2SO4 samples. Region 1 is the intact cement, Regions 2 is the CH-depleted region, Region 3 is the carbonated layer, and Region 4 is the surface layer. In the presence of sulfate, the carbonated layer is thicker, but the total CO_2 attacked thickness (sum of Regions 2–4) is smaller than those in the absence of sulfate. No formation of ettringite and gypsum were observed.

3.3.3 Mechanical Property Changes by Chemical Reactions

Strength and elastic modulus. In Figure 3.1b, the typical stress–deflection curves of SO4 and CO2SO4 samples from three-point bending tests are compared with those of N2 and CO2 samples. The shapes of the stress–deflection curves of SO4 samples are the same as those of N2 samples. Like the CO2 samples but to a lesser extent, the CO2SO4 samples have fluctuations in their stress–deflection curves, which are related to the change of their internal structure (i.e., change from uniformed structure to layered structure).[119] The slopes of the curves of the CO2SO4 samples fall between those of the CO2 samples and the N2/SO4 samples. Unlike the quasi-brittle CO2 samples, the CO2SO4 samples were still brittle after reaction. Further discussion of post-cracking behaviors is available in Section S4.1. Additional stress–deflection curves are shown in Figure 3-S3.

The quantification of MOR and elastic modulus is shown in Figure 3.1c. Without CO_2, the presence of sulfate did not change the mechanical properties of the cement samples significantly. However, with CO_2, in the presence of sulfate (the CO2SO4 condition), the MOR and the elastic modulus are much higher than for the CO2 samples. Contrary to the classical view of sulfate as a deteriorating factor, the presence of sulfate in our system did not cause deterioration of cement within the experimental duration, but instead significantly mitigated the CO_2 attack. Compared to the control samples, the CO2SO4 samples had only ~65% and ~40% decreases in strength and elastic modulus, while CO2 samples had ~92% and ~85 % decrease in strength and elastic modulus, respectively. The differences in CO_2-attacked depths, and in the strength and elastic modulus of the CO2 samples and CO2SO4 samples, were consistent with all our pretest batches (16–24 pretest samples for each condition).

Fracture roughness. As shown in Figure 3.1a, and Table 2-S3, except for the CO2 samples, which have rough fracture surfaces, samples reacted under all other conditions have relatively flat fracture surfaces with similar fracture roughness. Therefore, compared with the CO2 samples, a fracture in the CO2SO4 samples will expose less surface area to the reactive transport fluid in the fracture, and also will create lower tortuosity for fluid going through the bulk sample. The comparatively flat fracture surface of the CO2SO4 samples is due to the mitigated CO_2 attack. Typical fracture surfaces of the CO2 and CO2SO4 samples are shown in Figure 2-S3, and a detailed comparison of R_L is available in the Supporting Information (Table 3-S3).

Hardness and indentation modulus at microscale. The microscale hardness and indentation modulus of SO4 samples, as well as those of the intact core of both CO2 and CO2SO4 samples, were the same as those of the control samples, within the error range. Similar to CO2 samples, the carbonated layer (Region 3) in CO2SO4 samples has 2–3 times higher hardness and

indentation modulus than the intact core, while Region 2 has decreased hardness and indentation modulus, compared to the intact core. Detailed results from nanoindentation are shown in Figure 2-S4.

3.4 Discussion

In our study, sulfate effects were significantly different for conditions with and without CO_2. When the system was not exposed to CO_2, we found that the sulfate effects were related only to the retarded hydration kinetics of Al-containing phases. Because this effect did not cause observable changes in mechanical properties (Figure 3.1b, curves for N2 and SO4 samples), pertinent discussion is provided only in the Supporting Information Section 3-S4.2. Under conditions with CO_2, the presence of sulfate caused a brighter orange color on the surface of cement samples, and most importantly, minimized the CO_2 attack on cement in terms of attacked thickness, and the strength and elastic modulus of bulk samples.

3.4.1 Enhanced Orange Tint on Cement Surfaces in the Presence of Sulfate

The surface (Region 4) of CO2SO4 samples had a brighter orange tint than that of CO2 samples. In Chapter 2, by obtaining Fe content using EDS from cement samples treated with acid to enhance the orange brightness, we have experimentally demonstrated that the orange tint came from secondary precipitated phases containing Fe(III), or from adsorbed Fe(III) species. Because these phases are not quickly soluble at pH 3–5 and they appear orange, Fe (III) (hydr)oxides are likely the main constituent responsible for the orange tint.[125, 126] The brighter orange on the CO2SO4 samples than that on the CO2 samples suggests there can be greater extents of Fe(III) (hydr)oxides. Previous studies have shown that sulfate ions can form bidentate complexes on the

surface of Fe(III) (hydr)oxides, and largely inhibit the dissolution of Fe(III) (hydr)oxides.[55, 127, 128] In our CO2 cement system, the secondary precipitates in Region 4, such as $CaCO_3$ and Fe(III) (hydr)oxides, were dissolving. In the presence of sulfate, the dissolution of Fe(III) (hydr)oxides could have been inhibited. Therefore, more Fe(III) (hydr)oxides could be left in Region 4, which had a stronger orange tint than Region 4 in a CO2 system.

3.4.2 Enhanced Efficiency of the Protective Carbonate Layer

Compared with the CO2 samples, the CO2SO4 samples had less deterioration in strength and elastic modulus. This difference is consistent with the SEM-BSE images (Figure 3.4), showing that, compared to the CO2 samples, CO2SO4 samples have a thicker Region 3 and a much thinner Region 4. The carbonate layer, due to its dense texture, can act as a protective layer, hinder the diffusion of carbonic acid into the cement samples, and thus help retard cement deterioration by CO_2 attack. The protective carbonate layer tends to retreat slowly into the cement sample, because the outside of the carbonated layer is dissolving due to the continuous carbonic acid source, while the inside wall of the carbonate layer is continuously updated by newly precipitated $CaCO_3$.

Under the CO2SO4 condition, the carbonated layer is more efficient in protecting the sample from CO_2 attack. Three factors have been considered in order to understand this observation: the pH evolution of the aqueous phase, the mineralogy of the carbonate layer, and the potential inhibition effect of sulfate on $CaCO_3$ dissolution. Among the three factors, the inhibition effect of sulfate on $CaCO_3$ dissolution is the only one that explains our observation.

First, the CO2SO4 samples would dissolve slower if the pH of the system were higher. However, during the reaction, the pH of the CO2SO4 system was calculated to be equal to or lower than the pH of the CO2 system. Therefore, the pH difference cannot be the reason for the mitigated

CO_2 attack observed in the CO2SO4 system. The initial pH of CO2SO4 was adjusted by hydrochloric acid to be the same as that of the CO2 condition (pH 3.0 $\pm$ 0.1, Table 3.1). As the reaction goes on, the dissolution of cement would increase the pH. However, because sulfate can buffer the pH (i.e., resist the pH increase caused by cement's dissolution), the pH increase in the CO2SO4 system would be slower than the pH increase in the CO2 system before the equilibrium pH was reached. Using Geochemists' Workbench (GWB, Release 8.0, RockWare, Inc.), the pH evolutions as a function of the amount of portlandite dissolved were calculated for both CO2 and CO2SO4 conditions (Section 3-S4.3).

Second, the mineralogies of the carbonated layers were compared for Region 3 in both the CO2 and CO2SO4 samples (Figure 3.3). The XRD results did not show observable differences for Region 3. Under both conditions, calcite gives the most dominant signal, and similar amounts of aragonite were detected. Therefore, there are no XRD detectable mineral phases other than $CaCO_3$ acting as a protective phase in the CO2SO4 samples and hindering carbonic acid diffusion into the cement sample.

Third, the interactions of sulfate with brine–$CaCO_3$ interfaces have been considered. Possible interactions include $CaSO_4$ coating on $CaCO_3$ grains, sulfate adsorption on $CaCO_3$ grain surfaces, and incorporation of sulfate into the $CaCO_3$ lattice. In the research of acid mine drainage, sulfate is known to passivate calcite dissolution under acidic conditions, and reduces the efficiency of limestone in neutralizing acid drainage.[129-132] The proposed mechanism is the coating of gypsum on calcite. At the surface of calcite, dissolution releases Ca^{2+} ions. The Ca^{2+} ions immediately meet sulfate ions in the aqueous surroundings and precipitate as a gypsum coating on the calcite surface, thus passivating further dissolution of calcite. To test whether this was the dominant mechanism

in our CO2SO4 system, we analyzed the XRD pattern of the carbonated layer in CO2SO4 samples, but no gypsum peaks were observed, probably due to the comparatively high detection limit of XRD. To further test for a possible coating of sulfate on $CaCO_3$, we also reacted several single crystal calcite grains (Ward's Science, Iceland spar crystal) together with additional cement samples under CO2SO4 conditions. After the reaction, we thoroughly rinsed the calcite grain with DI water, then dried it with N_2, and used SEM-EDS to examine its surface. An AuPd coating was applied to increase the conductivity of the surface. Abundant distorted rhombohedral precipitates were formed epitaxially on the calcite surface, suggesting sulfate effects on the euhedral shape of calcite precipitates, but no gypsum precipitates were observed (Figure 3-S6). The caveat of this SEM imaging is that only particles larger than 1 μm were observable due to the low conductivity of calcite. It is possible that the gypsum particles coating the calcite were too small to be resolved by SEM. However, interestingly, EDS showed that the rhombohedral precipitates were $CaCO_3$, and the sulfur contents are similar for both these precipitates and the background calcite (Figure 3-S6). The S mapping for Regions 3 and 4 in the CO2SO4 samples also shows an enhanced S content on the outer side of Region 3 (Figure 3-S7). The increased extent of sulfur suggests that gypsum coatings or sulfate adsorption on calcite are possible under the CO2SO4 condition.

Sulfate can also adsorb at the Ca site on calcite surfaces.[54, 133-135] The adsorption of dissolution inhibitors (such as sulfate and phosphate) on calcite surfaces can reduce the dissolution rate of calcite by blocking the active sites. [54, 136-141] In the case of sulfate adsorption, Sjöberg suggested that the adsorption may also be the initial stage of gypsum formation.[54] In our cement experiment, dissolution of the $CaCO_3$ by acidic brine can be inhibited by sulfate adsorption on $CaCO_3$ grains.

In addition, sulfate can be incorporated into the calcite lattice during calcite precipitation in sulfate-rich environments.[141, 142] However, because the incorporation of sulfate increases the lattice dimensions and causes strains and defects,[142] the dissolution of calcite is likely to be promoted.[61] Therefore, incorporation of sulfate into $CaCO_3$ may not explain the inhibited dissolution of $CaCO_3$ in the presence of sulfate.

As a summary of the mechanisms for the enhanced protective property of the carbonated layer in the CO2SO4 systems, sulfate can inhibit dissolution of the carbonated layer by $CaSO_4$ coating on $CaCO_3$, or by sulfate adsorption on $CaCO_3$ surfaces. The protection thus afforded is more efficient than that in CO2 systems in hindering acidic brine from attacking the inner part of cement.

3.4.3 Possible Long-Term Interactions among CO_2, SO_4^{2-}, and Cement

In this study, sulfate attack via delayed ettringite formation was not observed after 10 days' reaction (which could be due to the relatively short exposure time).[63, 121] However, the aqueous sulfate ions considerably mitigated CO_2 attack by inhibiting the dissolution of the carbonated layer. Consequently, the carbonated layer more efficiently hinders diffusion of chemicals into the cement. In the short term, this effect helps mitigate CO_2 attack on cement, which is of great concern for GCS operation. In the long term, it could also help mitigate other chemical attacks. For example, in this study, we found lesser amounts of anhydrate Al-containing phases in the CO2SO4 samples than in the SO4 samples. This finding suggests that the carbonated layer hindered diffusion of external sulfate ions into the cement, and could mitigate sulfate attack at longer time scales as well.

3.5 Environmental Implications

In this study, we have provided more accurate quantitative linkages of chemical reactions with mechanical properties during CO_2 attack on cement in the presence of sulfate. In Chapter 2, we found that for a 3 mm thick rectangular cement sample, the CO_2 attack lad to a 1220 μm attacked depth from both sides, a ~93% decrease in strength, and a ~84% decrease elastic modulus. In this study, we found that in the presence of 0.05 M sulfate, the CO_2-attacked thickness was only 800 μm, and the decreases in strength and elastic modulus were 65% and 40%, respectively. Such information can help understand and predict the impact of CO_2 injection on wellbore integrity, for example, to predict how large a stress a wellbore cement can stand without fracture.

Compared with the findings on scenarios without excessive sulfate,[119] the new findings from this study highlighted the importance of considering foreign aqueous species in the CO_2 saturated brine, especially those having significant influence on $CaCO_3$ dissolution/precipitation. Some of the species are closely related to H_2S co-injection (such as SO_4^{2-}), or enhanced oil recovery (such as organic ligands). The enhanced protective efficiency of the carbonated layer in the presence of sulfate is probably opposite to our initial intuition, because in the cement industry, excessive sulfate is usually considered a deteriorating factor. In fact, the stronger carbonated layer may also help mitigate sulfate attack in the long term, because the diffusion of excessive sulfate ions into the cement is also hindered. In other words, the two deteriorating factors, CO_2 and sulfate, may mitigate the destructive effects of each other for a time period long enough for sulfate attack to manifest. Such a conclusion has significant impacts on understanding and improving the wellbore integrities at GCS sites. In the modeling work on cement deterioration at GCS sites, to repeat the experimental and site observations, we need to consider more mechanisms than CO_2

attack. In the engineered applications, the design of the wellbore should also be guided by specific site characteristics, such as the various concentrations of sulfate.

Furthermore, findings of this study can shed light on general projects which utilize cement materials in sulfated environments: seawater, groundwater, surface water, and rainwaters. In most cases, cement exposed to these environments is also exposed to ubiquitous CO_2. The simultaneous exposure of cement to CO_2 and sulfate, and the possible interactions between CO_2 attack and sulfate attack/protection are not clear for these systems. From this aspect, our study can also serve as an important reference for the general cement industry.

Acknowledgments

We would like to thank Dr. Katharine Flores for letting us to use the nanoindentator, and thank Ms. Kelly Kranjc for setting up the nanoindentation system before the tests, and providing utilities for polishing the cement surfaces. We would also thank Dr. Ruth Okamoto for providing access to the three-point bending machine, and thank Dr. Spencer Lake for providing access to the layer scanner. SEM-BSE images were collected at Washington University's Institute of Materials Science & Engineering. This study was supported by the Consortium for Clean Coal Utilization and the National Science Foundation's Career Award (EAR-1057117).

Supporting Information for Chapter 3

3-S1.Experimental setups

A bench-top reactor (Parr Instrument Company, IL) was connected to a syringe gas pump (Teledyne ISCO, Lincoln, NE). The pressure in the reactor was monitored by a barometer (Parr Instrument Company, IL) on the cap of the reactor. A controller connected to an *in situ* thermocouple automatically turning on or off the heater when the temperature in the reactor was lower or higher than the set value. Such system was used in several previous studies in our lab.[108-114, 143] A diagram of the setup is available in the Supporting Information for Chapter 2, Figure 2-S1.

The initial pH in the reaction, after injecting CO_2 and obtaining high temperature, can be measured by a pH probe designed for high pressures (1–139 bar) and temperatures (20–120 ^{o}C) (Corr Instruments, TX).[110-113, 143] Because our *in situ* pH probe is glass-based, and could be damaged if contacted with a locally basic aqueous environment, we did not monitor the pH increase as a function of time during reactions. Instead, we used Geochemists' Workbench (GWB, Release 8.0, RockWare, Inc.) to calculate the possible evolution of pH in our systems containing CO_2 (Details are available in Section 3-S4.3).

3-S2 Additional data for chemical analyses

Aqueous concentrations of Ca and Si were measured at the end of the 10 days' reaction (Table 3-S1). The aqueous concentration of Ca should not be used for comparison of cement dissolution under acidic conditions, because they could be much less than the true loss of Ca from the cement samples. During degassing and cooling of the reactor, the high concentrations of Ca

formed many secondary precipitates on the surface of the cement samples. These precipitates were removed from the reactor together with the cement sample, without being acidified for ICP measurement. Si is less preferentially leached out, and fewer secondary Si precipitates were observed on the cement samples during sampling. Therefore, Si concentrations likely deviate less than Ca from the real concentrations before degassing and cooling of the system, and they were used to compare relative cement dissolutions.

Table 3-S1 Aqueous concentrations of Ca and Si at the end of the 10 days' reaction. Data for the N2 and the CO2 conditions are the same as in Chapter 2 and are listed here for comparison. The positive and negative error bars are the standard deviation of 3 measurements of the same sample by ICP-OES.

Conditions	Ca, mM	Si, mM
N2	9.0 ± 0.3	1.62 ± 0.01
SO4	21.7 ± 0.3	1.64 ± 0.02
CO2	147.6 ± 0.5	5.33 ± 0.03
CO2SO4	234 ± 1	3.70 ± 0.03

Table 3-S2 Thicknesses of different regions of cement attacked by CO_2 in this study.

Condition	Region 2, μm	Region 3, μm	Region 4, μm	Total attacked thickness, μm
CO2	960 ± 100	100 ± 17	170 ± 35	1220 ± 90
CO2SO4	600 ± 17	117 ± 6	80 ± 10	800 ± 6

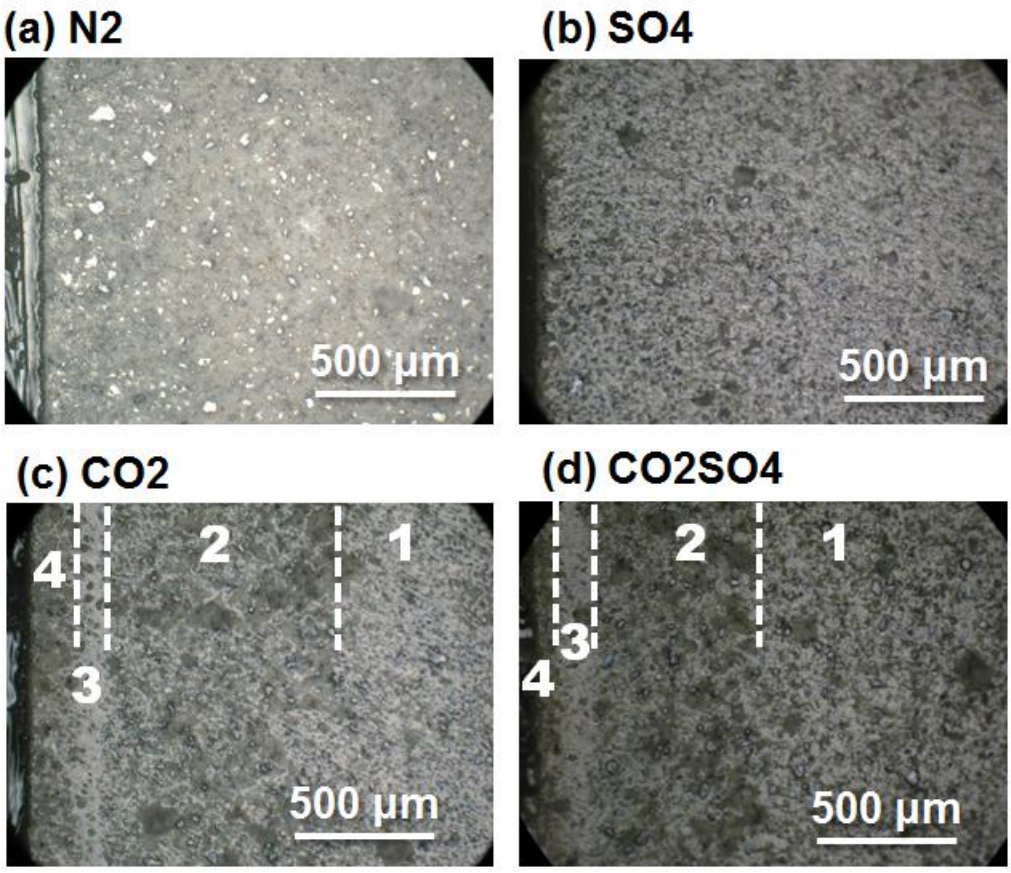

Figure 3-S1 Optical images of polished cross sections of (a) N2, (b) SO4, (c) CO2, and (d) CO2SO4 samples. Images (a) and (c) are from Chapter 2. The SO4 image does not show any evidence of sulfate attack on cement via formation of ettringite and/or gypsum. CO_2 attack on cement under the CO2SO4 condition is less severe than that under the CO2 condition.

3-S3. Additional data for mechanical property analyses

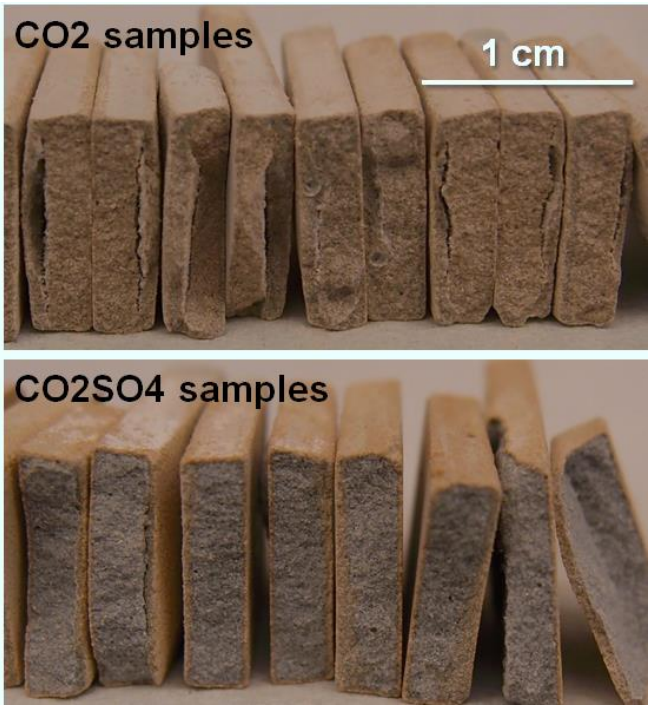

Figure 3-S2 Typical fracture surfaces of the CO2 and CO2SO4 samples. The two pictures were taken with the same background.

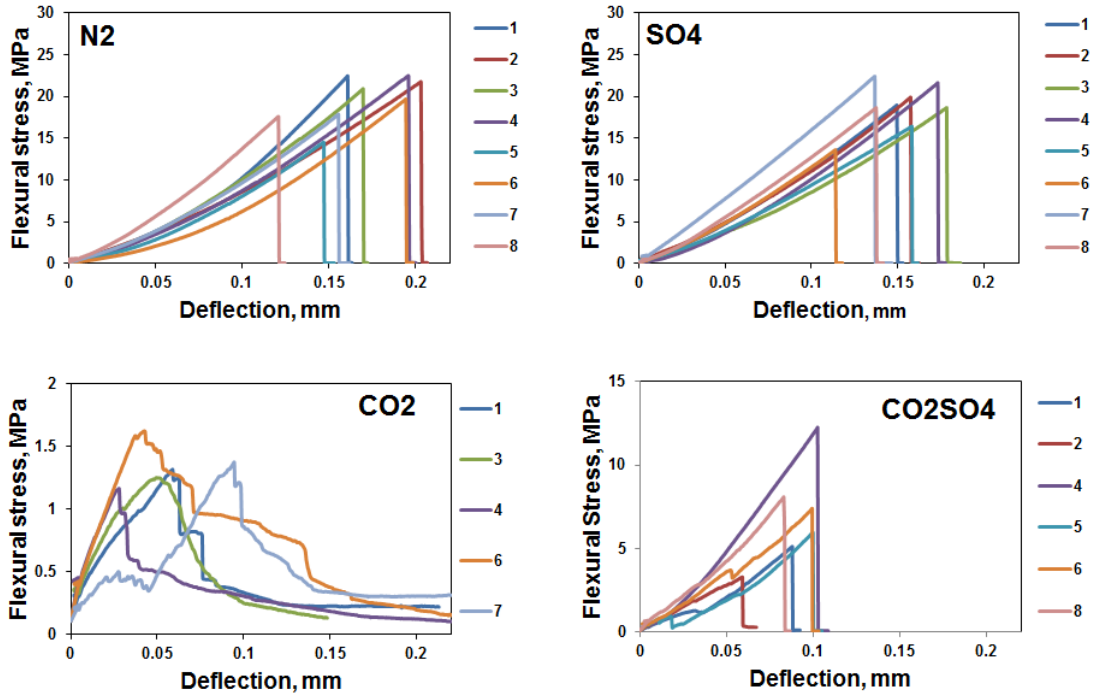

Figure 3-S3 Groups of stress–deflection curves for N2, SO4, CO2, and CO2SO4. Data for N2 and CO2 samples are from Chapter 2. The samples that were already defected before bending tests are not shown.

Table 3-S3 Fracture roughness comparison. Data for N2 and CO2 samples are from Chapter 2, and are shown here for comparison. The extent of CO_2 attack on the cement was not sufficient to increase the fracture roughness of the CO2SO4 samples.

Condition	Range of fracture roughness (R_L)	Median R_L	Average R_L
N2	1.00 – 1.05	1.00	1.02
SO4	1.00 – 1.20	1.03	1.06
CO2	1.02 – 2.39	1.14	1.35
CO2SO4	1.00 – 1.35	1.03	1.08

Hardness and Indentation Modulus

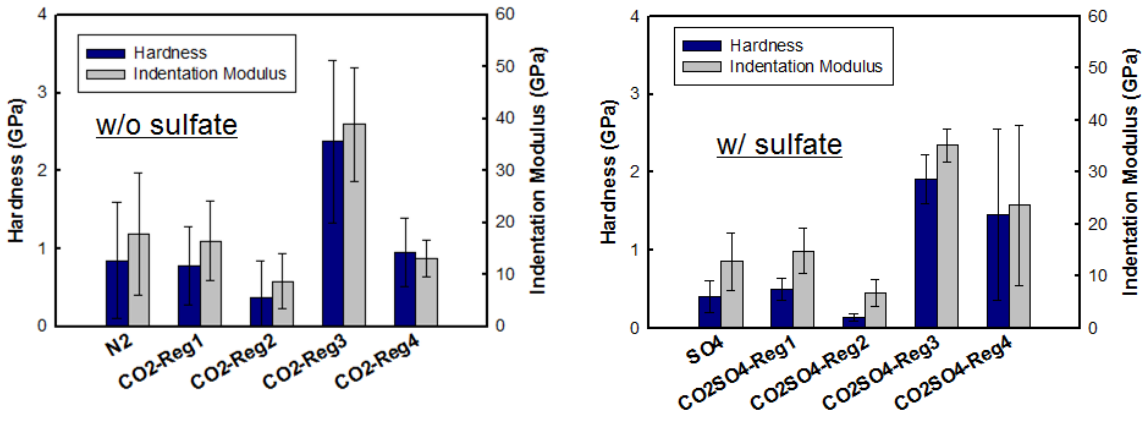

Figure 3-S4 Hardness and indentation modulus. Data for N2 and CO2 samples are from Chapter 2, and are shown here for comparison. Similar to CO2 samples, the carbonated layer (Region 3) in CO2SO4 samples has 2–3 times higher hardness and indentation modulus than the intact core, while Region 2 has decreased hardness and indentation modulus, compared to the intact core. When Region 3 partially dissolves to form Region 4, the hardness and indentation modulus are also decreased.

3-S4. Additional discussion

3-S4.1 Post-cracking behaviors of reacted samples

We found that the stress–deflection curves for the CO2 samples dropped gradually after the main crack (Figure 3-S3), while the stress–deflection curves of samples reacted under all other conditions dropped immediately. The gradual drop of the stress–deflection curves of the CO2 samples indicated that the reaction changed the samples from brittle to quasi-brittle, and after the CO_2 attack, although the samples are less strong, they can absorb more energy after the main crack happens and before being completely broken. On the other hand, the CO2SO4 samples, which also experienced CO_2 attack, had an immediate drop in the stress–deflection curves after crack, indicating the CO_2 attack in these samples was not able to change the post-crack behaviors as it did in the CO2 samples. The difference is consistent with our finding of thinner CO_2 attacked

depths from both sides of samples in the CO2SO4 samples (~800 μm) than those in the CO2 samples (~1220 μm). Due to the thinner attacked depth, the CO2SO4 samples had a thicker intact core (~1400 μm) than the CO2 samples (~560 μm). The properties of the intact core are approximated by the control samples. Therefore, the CO2SO4 samples' post-cracking behavior was not the same as that of the CO2 samples, but was closer to the N2 samples.

3-S4.2 Effects of sulfate on Al-containing phases

The reactions of Al-containing phases in cement (C_3A and C_4AF as solid solution[41]) start with hydration. The hydration of Al-containing phases are related to the time length of early hardening of cement. To slow down this process, a small amount of gypsum needs to be added to the clinker. The retardation effect of gypsum is based on the aqueous sulfate ions released by gypsum. There are two main hypotheses by which gypsum has its retardation effect.[144] One is that a hydrated layer formed together with ettringite, coating on the anhydrous grain which hinders diffusion of water into the grain. The other hypothesis is that the adsorption of sulfate ions onto the active site of Al-containing phases decreases hydration rate of the grain. Except affecting the setting time, the Al-containing phases does not contribute significantly to the mechanical properties of cement. In this study, there are more anhydrous Al-containing phases in SO4 samples than in N2 samples, because the excessive sulfate ions has retarded the hydration of these phases.

A system with Al-containing phases and gypsum may also affect the hydration kinetics of C_2S and C_3S.[144] However, we found that the strength and elastic modulus of N2 and SO4 samples were not significantly different.

Usually the Al-containing phases form ettringite with sulfate species at the early stage of hydration, and later on, as more Al-containing phases are hydrated and help take up sulfate, the

ettringite will completely or partially convert to AFm (i.e., alumina, ferric oxide, monosulfate). Later on, with excessive sulfate, AFm will further react with sulfate to form more ettringite. Ettringite is known to have larger volume, and if excessively formed, can cause cracks in cement, which is known as "sulfate attack on cement".[121, 122] In our experimental conditions, the reaction time is 10 days, likely too short for the sulfate attack to reveal, especially when the hydration of Al-containing phases are significantly retarded.

3-S4.3 Effects of sulfate on the carbonated layer

pH evolution modeled by GWB. In this study, due to the fast cement dissolution at acidic pHs in the CO2 and CO2SO4 systems, we expected the pH increase was fast. We used Geochemists' Workbench (GWB, Release 8.0, RockWare, Inc.) to calculate the possible evolution of pH in our systems containing CO_2. Using thermo.dat as the thermodynamic database, the initial brine composition was input as the basis. Values were calculated for 1 L of solution. pH was set to balance the solution charge. The fugacity of CO_2 at 95 ^oC and 100 bar was calculate by Duan's equation to be 75,[145] and was kept constant. To set up the experimentally measured initial pH in GWB, the initial pH of both the CO2 and CO2SO4 conditions were adjusted to be 3.0 by adding a certain amount of Cl^- (i.e., HCl) and letting H^+ balance the charge. Only dissolution of portlandite was considered. One or ten grams of portlandite were used as the reactant. pH evolution was plotted as a function of amount of portlandite dissolved for both CO2 and CO2SO4 conditions. Both systems had an equilibrium pH of 5.0. Before the equilibrium was reached, the pH of the CO2SO4 samples was lower by 0–0.6 for the same amount of portlandite dissolved. Because we observed slower dissolution of cement under the CO2SO4 condition, the pH difference cannot be the reason for the mitigated CO_2 attack observed in the CO2SO4 system, and there must be other mechanisms to counteract the promotion of cement dissolution by a low pH.

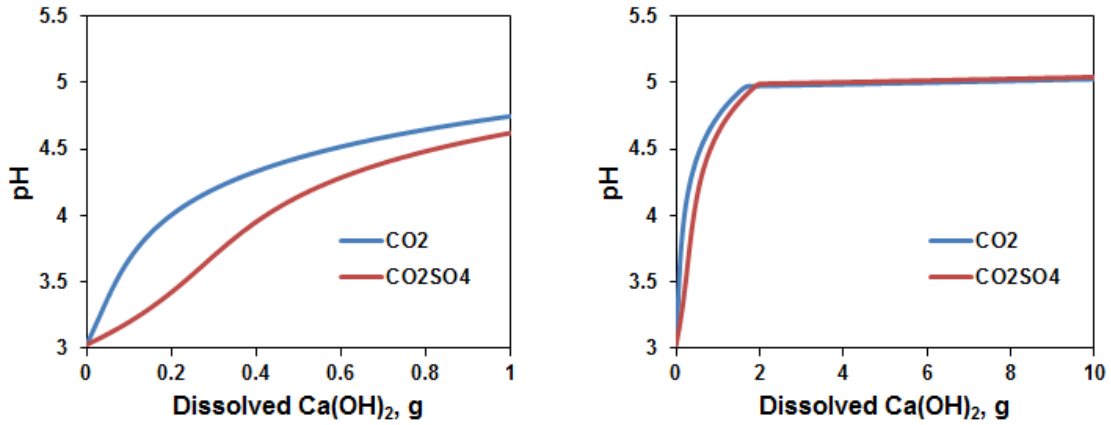

Figure 3-S5 Evolution of pH in CO2 and CO2SO4 systems calculated by GWB.

Observations of calcite reacted with cement samples under the CO2SO4 condition. The distorted rhombohedral precipitates suggest that sulfate affected the precipitation of calcite, which is rhombohedral in a pure $CaCO_3$ system. Because the conductivity of calcite is low (even after AuPd coating), the resolution may not able to resolve the small $CaSO_4$ precipitates on the calcite surface, if there is any. EDS may also collect most of the signal from the bulk calcite by penetrating the potential $CaSO_4$ coating.

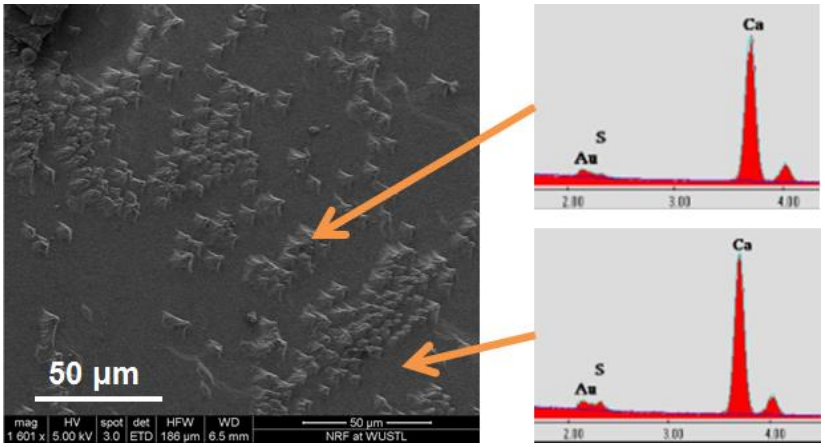

Figure 3-S6 SEM-EDS results for the surface of single crystal calcite grains reacted with cement under the CO2SO4 condition.

BSE-SEM-EDS results for sulfur mapping. BSE images were obtained for the Region 3 (carbonated layer) and Region 4 from a CO2SO4 sample. Sulfur mapping by EDS showed that the outer part of Region 3 has slightly more sulfur than the inner part. The region where sulfur is more abundant may have the coating of $CaSO_4$ on $CaCO_3$ grains and adsorption of sulfate on $CaCO_3$ surfaces. However, the sulfur distribution cannot specify which mechanism is the more dominant.

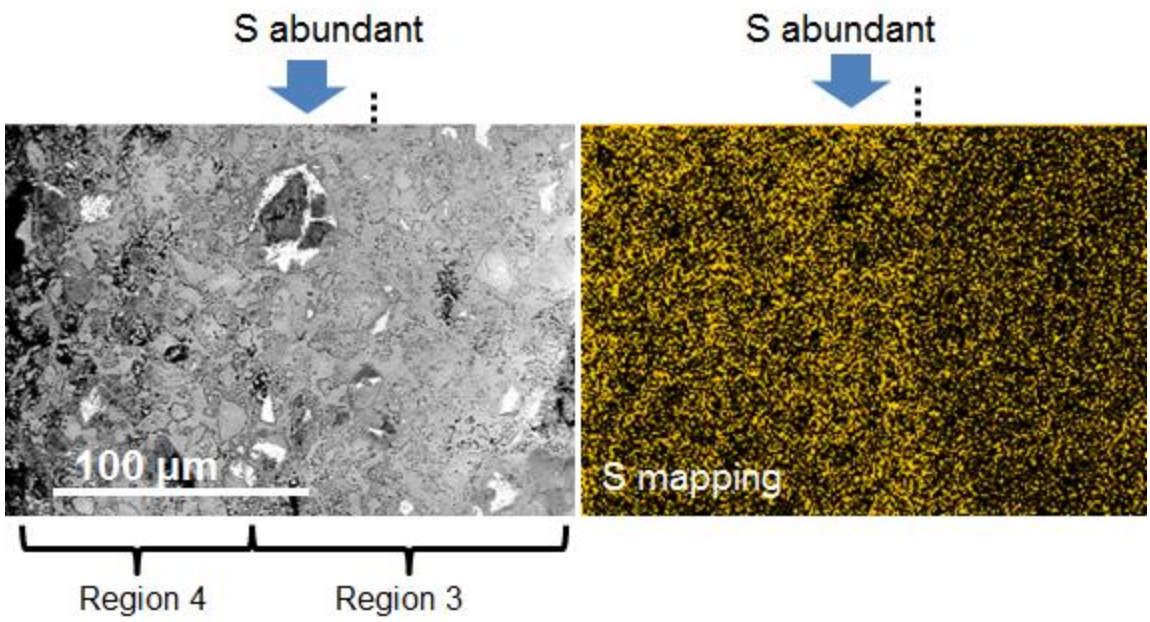

Figure 3-S7 BSE images of Region 3 and Region 4 in a CO2SO4 sample, and the sulfur mapping by EDS. The brighter area in the EDS mapping (right) has more S. The outer edge of Region 3 has more S content than inner part of Region 3.

Reproduced with permission from [Qingyun Li, Yun Mook Lim, and Young-Shin Jun. Effects of Sulfate during CO_2 Attack on Portland Cement and Their Impacts on Mechanical Properties under Geologic CO_2 Sequestration Conditions. *Environmental Science & Technology*, 2015, 49 (11), 7032-7041.] Copyright [2015] American Chemical Society.

Chapter 4: Deciphering Calcium Carbonate Precipitation during Cement Deterioration using Reactive Transport Modeling

Abstract

In the past decade, wellbore cement integrity has been investigated under geologic CO_2 sequestration conditions both experimentally and through numerical simulations. Among these studies, our work in Chapters 2 and 3 highlighted the critical roles of the portlandite(CH)-depleted zone in mechanical deterioration of the cement, as well as the significance of the cement surface's dissolution in impacting the carbonated layer's efficiency in hindering CO_2 diffusion. In this chapter, we utilized the reactive transport code CrunchTope to simulate the evolution of the CH-depleted zone as well as the dissolution of the cement surfaces observed in experiments. The modeling approach revealed two breakthrough findings. First, to reproduce the experimentally observed widening of the CH-depleted zone, the model cannot allow the $CaCO_3$ precipitation in cement to clog 100% of the porosity. The unfilled porosity can result from either fractures, grain defects, or pore-size-dependent precipitation. Second, formation of $CaCO_3$ in the reaction solution had to be enabled via incorporation of nucleation kinetics, as opposed to using a seeded system and mineral growth kinetics. Interestingly, our model predicts that the $CaCO_3$ formed in the reaction fluid is less soluble than that formed in the cement matrix, and this is further supported by experimental tests. Both the improvement of reactive transport modeling code and the mechanisms deciphered by combined experimental and modeling approaches provide an improved

understanding the interactions between fluid and geomedia in CO_2 injected subsurface environments.

4.1 Introduction

The integrity of wellbore cement is critical to ensure the safety and efficiency of geologic CO_2 sequestration (GCS), because the chemical reactions of cement with CO_2 can lead to opening of fractures and high porosity zones that can form CO_2 leakage pathways. Therefore, deterioration of wellbore cement has been investigated intensively in the past decade.[12] These studies include both experimental and modeling approaches, and have been conducted on both chemical and mechanical alteration of cement. The findings of these studies extend our understanding of the century-long topic of cement deterioration by adding the new scenario of GCS, which is characterized by a greater amount of CO_2, higher temperature, higher pressure, and higher salt concentration than in the common cement operating environments.[12] A study by Kutchko et al. clarified the chemical reactions occurring during CO_2 attack under GCS conditions.[42] As shown in Figure 4.1, upon exposure to CO_2-saturated acidic brine, Ca^{2+} ions are released from dissolution of portlandite ($Ca(OH)_2$ or CH) and partially from calcium-silicate-hydrates (C-S-H) in the cement matrix, forming a highly porous CH-depleted zone. As the Ca^{2+} ions diffuse out and encounter carbonate ions, a carbonated layer is formed via $CaCO_3$ precipitation. To some extent, the carbonated layer can protect the cement by hindering CO_2 diffusion into the cement. On the outer front of this carbonated layer, the acidic brine continues to dissolve $CaCO_3$, leading to a surface dissolution layer with enhanced porosity.[12, 42]

In addition to characterizing chemical reactions, several studies have focused on the (hydro)mechanical property changes of cement after CO_2 exposure, including changes of porosity and permeability, [49-52, 68, 69, 71, 77, 80, 85-87, 91, 94, 118, 146] and the hardness and strength of reacted cement.[52, 73, 78, 85, 91, 119, 147, 148] In our recent study presented in Chapter 2,[119] the bulk strength of CO_2-attacked cement samples was measured and related to the microscale mechanical properties. Figure 4.1a, adapted from Chapter 2, depicts the several zones in the cross section of a CO_2-attacked cement paste sample. In this diagram, two important zones deserve more attention. One is the weak CH-depleted zone, characterized by abundant microcracks and increased porosity due to dissolution of CH. The cracks and porosity that have been opened due to alteration could act as CO_2 leakage pathways,[65, 66] and the average hardness of this CH-depleted zone is only about half of that in the unattacked cement matrix.[119, 148] For the first time, the work highlighted that this weak CH-depleted zone is the key to the significant strength decrease in the bulk cement material. The wide CH-depleted zone has also been observed in previous studies, and in some cases was remarkably wide.[73, 119, 147-149] However, the factors that control the widening of this zone during the reaction are not clear, and thus it is uncertain how this zone can be limited for a stronger wellbore cement material.

The other zone requiring attention is the surface layer dissolved from the carbonated layer. Intense dissolution of the outer front of the carbonated layer makes it thinner, and reduces its efficiency in blocking CO_2 from diffusion into the cement. It was shown (in Chapter 3) that if the dissolution of the outer front of the carbonated layer is inhibited, the carbonated layer can grow thicker, and thus the cement material will undergo less deterioration by CO_2.[148] If the cement deteriorates in a flow-through system,[68, 69, 71, 73, 74, 80, 81, 86, 87, 91, 132, 146] with fresh solutions undersaturated with $CaCO_3$ introduced continuously during the reaction, it is intuitive that the

surface of the cement samples can dissolve. However, in a closed system,[42, 50-52, 72, 77-79, 82, 83, 119, 147, 148] the solution can quickly reach $CaCO_3$'s saturation due to Ca^{2+} released from portlandite, and yet the surface of the cement has also been found to continue dissolving. If strategies are to be adapted to reduce dissolution of the protective carbonated layer, we must uncover the mechanisms that cause the dissolution.

The influential parameters for the formation of the CH-depleted zone and the surface layer are numerous, such as temperature and pressure, the initial solid and aqueous conditions, the transport and composition evolution of fluid, and the thermodynamics and kinetics of reactants. To enable analysis of each condition within an applicable time and with obtainable resources, the most feasible and effective approach is reactive transport modeling. Although reactive transport modeling has been carried out in the past several years for cement deterioration under GCS conditions at both continuum[48, 49, 56, 59, 60, 89, 149-151] and pore scales[152], the focus has been on the overall attacked depth or the carbonated layer's inner front to extrapolate the results to longer terms, whereas the CH-depleted zone and the surface layer have not been fully considered. For example, the simulations done by Brunet et al. (2013) and Abdoulghafour et al. (2016) predicted the CO_2-altered cement would include a carbonated layer and a surface layer, without a specific CH-depleted zone.[49, 149] Huet et al. (2010) and Gherardi et al. (2012) quantified the CO_2 attack according to evolution of the carbonated layer.[48, 56] The predicted surface dissolution layer, on the other hand, has been produced only with open systems or constant concentrations at boundaries.[49, 56, 59, 149, 150]

In contrast to the reactive transport models mentioned above, this study sets up a reactive transport model to decipher the formation of the CH-depleted zone as well as the surface dissolution region. Also, our model featured closed boundaries that allowed accumulation of

aqueous concentrations, and accurately reflected the solid-to-liquid ratio and initial/boundary conditions used in the experiment. This work employed the CrunchTope reactive transport modeling code (a new version of CrunchFlow),[153] and updated the modeling code to incorporate user defined minimum porosity and nucleation kinetics. With the two incorporated mechanisms, CrunchTope can be applied to a wider range of systems and help to develop a better understanding of fluid–geomedia interactions.

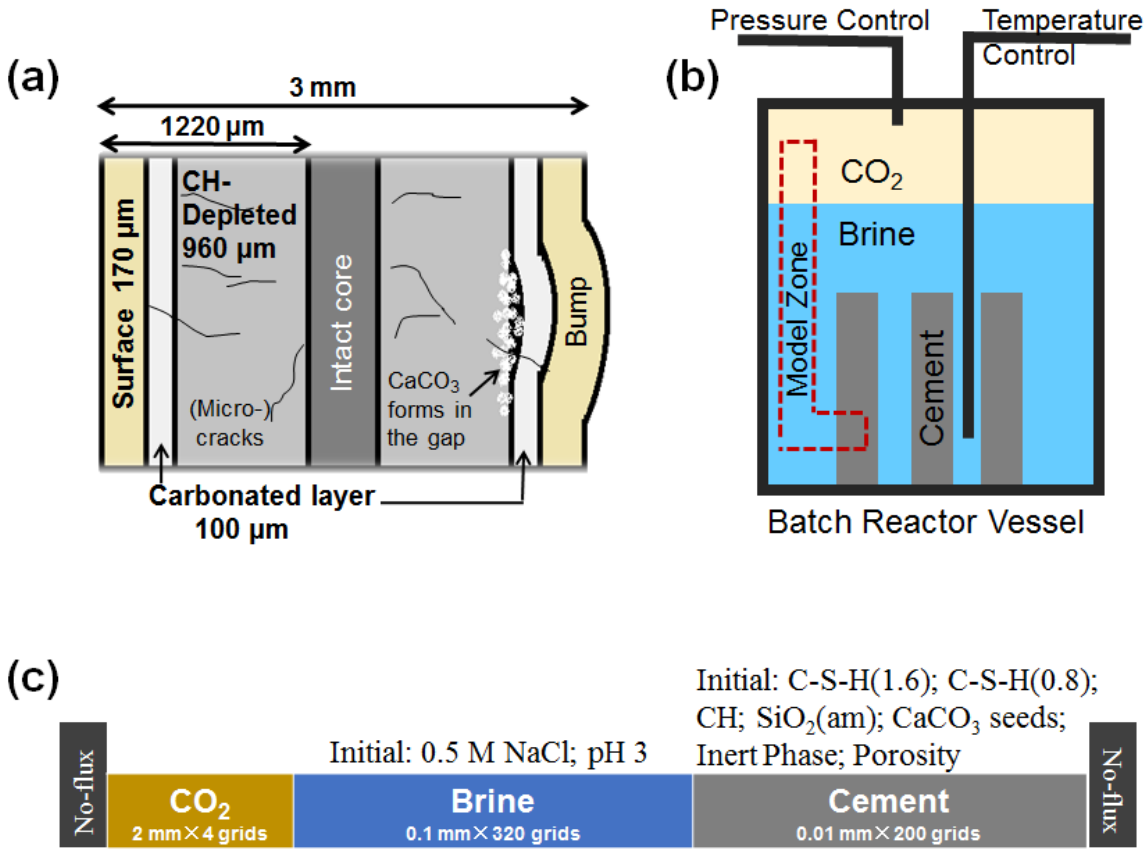

Figure 4.1 Illustration of experimental studies and modeling setup. (a) Sketch of a cross section of cement after exposure to CO_2-saturated brine for 10 days. Adapted from Chapter 2. (b) Diagram of experimental reactor. The dotted line circles the region that our 1D model captures. (c) Discretization of the reactive transport simulation.

4.2 Approaches

4.2.1 Experimental Observations

This modeling work is based on the experimental study described in Chapter 2 with extended tests for time resolved observations. The experiment was carried out using laboratory-made Ordinary Portland Cement (OPC) paste samples with dimensions of 3 cm × 1 cm × 0.3 cm, and with a water-to-cement ratio of 0.5. The cement samples were reacted in a CO_2-saturated brine (0.5 M NaCl) with a solid-to-liquid volumetric ratio of 1/16. The solution was equilibrated at 100 ± 5 bar of CO_2 in the headspace of the stagnant batch reactor. In our previous study, the reaction lasted for 10 days at 95 ^oC, and a total alteration thickness of 1220 ± 90 μm was observed, including a 960 μm CH-depleted zone, a 100 μm carbonated layer, and a 170 μm surface region. To obtain the evolution of each zone along the reaction time, more batches were reacted for 1, 3, and 6 days in this study. After the reaction, polished cross sections of the reacted samples were studied using an optical microscope (Zeiss Imager Microscope), and the depths of the individual fronts were recorded.

4.2.2 Reactive Transport Model Setup

To simulate the experimental system, a 1D model was set up using the software CrunchTope.[153] Figure 4.1b illustrates the experimental setup, in which the interfaces among supercritical CO_2, brine, and cement are enclosed by dotted lines and are extended to a 1D model, shown in Figure 4.1c.

Discretization. The 1D model has three domains, including the headspace of supercritical CO_2 on the left, the CO_2-saturated brine in the middle, and the cement paste on the right. The CO_2 section has four 2 mm grids with CO_2 at 100 bar. These four grids also include 1 vol% of brine to

facilitate CO_2 dissolution into brine. As calculated using Duan's equation of state,[145] the CO_2 fugacity decreased from 85 bar to 77 bar at the first grid of the brine domain throughout the 10 day reaction, and was considered stable because it was similar to the pressure fluctuation in the experiment. The brine section contains 320 × 100 μm grids, and the cement section contains 200 × 10 μm grids. The volumetric ratio of cement to brine was 1/16, reflecting that used in the experiment. The grids were fine enough to eliminate grid size effects.[151]

Governing equations. In CrunchTope, the governing equation that couples the chemical reaction and mass transport is

$$\frac{\partial \phi C_i}{\partial t} = \frac{\partial}{\partial x}\left(D_{ie}\frac{\partial C_i}{\partial x}\right) - \frac{\partial}{\partial x}(\phi u C_i) + \sum_{i=1}^{N} \nu_{ir} R_{ir} \,. \qquad \text{Eq. (4.1)}$$

In this equation, $\emptyset$ is porosity, C_i is the concentration for species *i*, and *t* is the time. The change of bulk concentration of species *i* with time (described by the left hand side) is expressed by three terms on the right hand side, which are the diffusion term, advection term, and reaction term, from left to right, respectively. D_{ie} is the effective diffusivity of species *i*, *x* is the dimension axis, *u* is the average linear velocity of the fluid, and *v* is the stoichiometric coefficient of the reaction that involves species *i*. In our stagnant system, the advection term is negligible, and Eq. 4.1 is simplified to include only diffusion and reaction terms on the right hand side:

$$\frac{\partial \phi C_i}{\partial t} = \frac{\partial}{\partial x}\left(D_{ie}\frac{\partial C_i}{\partial x}\right) + \sum_{i=1}^{N} \nu_{ir} R_{ir} \,. \qquad \text{Eq. (4.2)}$$

To enable the partial differential equation be solved, the diffusion term, reaction terms, and the initial and boundary conditions must be specified. **Transport.** The effective diffusion coefficient in Eqs 4.1 and 4.2, D_{ie}, was calculated from the diffusion coefficient D_i, corrected by tortuosity and porosity according to Archie's Law:

$$D_{ie} = \emptyset^m D_i \,, \qquad \text{Eq. (4.3)}$$

where $\emptyset$ is the porosity and m is the cementation coefficient.[153, 154] The coefficient D_i was assumed to be 3×10^{-9} m^2/s for all species at 95 °C. This simplification is reasonable because specifying diffusivity for individual ions did not alter the final results significantly (See the Supporting Information Figure 4-S3 for more information). The value for m was set as 2 in this study as suggested for systems without further information of m.[154] Unless the minimum porosity was reached (See Section 4.2.3), the porosity was updated every time step by subtracting from 100% the total mineral fractions:[153]

$$\emptyset = 1 - \sum_j \emptyset_{mj} \,, \qquad \text{Eq. (4.4)}$$

where $\emptyset_{mj}$ is the volumetric fraction of mineral j.

Chemical reactions. Chemical reactions include thermodynamic-controlled speciation reactions and kinetic-controlled dissolution/precipitation reactions. Parameters are listed in Table 4.1. Most thermodynamic parameters are from the EQ3/6 database.[155] The parameters for C-S-H phases are from the Thermoddem Database.[156] The kinetic rate equations for dissolution/precipitation, except for nucleation reactions, are based on transition state theory (TST),[61] and are written as

$$R = Ska_{\mathrm{H^+}}^n \left(1 - \frac{IAP}{K_{sp}}\right). \qquad \text{Eq. (4.5)}$$

In this equation, S is the surface area (calculated as the product of the mineral's mass and its specific surface area), k is the reaction coefficient, $a_{\mathrm{H^+}}$ is the activity of H^+, IAP is the ion activity coefficient, and K_{sp} is the solubility of the reacting mineral. The values for S and k are

available in the literature with large ranges. The values used in this study are calibrated within these ranges to best match our experimental results.

Table 4.1 Reactions and parameters for reactive transport modeling of cement deterioration. Thermodynamic parameters are from EQ3/6 database[155] and Thermoddem database.[156] Kinetic parameters are calibrated with our experimental observations within literature reported ranges.[48, 49, 149-151, 157-159]

Speciation Reactions (Instantaneous)	
Reaction	Log_{10} K_{eq}
$H_2O \leftrightarrow H^+ + OH^-$	-12.33
$CO_2(aq) + H_2O \leftrightarrow H^+ + HCO_3^-$	-6.358
$HCO_3^- \leftrightarrow H^+ + CO_3^{2-}$	-10.08
$CaCl_2(aq) \leftrightarrow Ca^{2+} + 2Cl^-$	-0.4445
$CaCl^+ \leftrightarrow Ca^{2+} + Cl^-$	-0.1696
$CaCO_3(aq) \leftrightarrow Ca^{2+} + H^+ + HCO_3^-$	6.165
$CaHCO_3^+ \leftrightarrow Ca^{2+} + HCO_3^-$	-1.140
$CaOH^+ + H^+ \leftrightarrow Ca^{2+} + H_2O$	10.24
$HCl(aq) \leftrightarrow H^+ + Cl^-$	-0.6262
$NaHSiO_3^- + H^+ \leftrightarrow H_2O + SiO_2(aq)$	9.134
$NaCl(aq) \leftrightarrow Na^+ + Cl^-$	0.4979
$NaHSiO_3 + H^+ \leftrightarrow H_2O + Na^+ + SiO_2(aq)$	7.849
$NaOH(aq) \leftrightarrow Na^+ + OH^-$	12.99
$NaCO_3^- + H^+ \leftrightarrow HCO_3^- + Na^+$	10.55
$NaHCO_3(aq) \leftrightarrow HCO_3^- + Na^+$	0.3712

Precipitation/Dissolution Reactions			
Mineral	Reaction	$S \times k a_{H^+}^n$	Log_{10} K_{sp}
$CaCO_3$_in_cement	$CaCO_3 + H^+ \leftrightarrow Ca^{2+} + HCO_3^-$	$10^{-3.0} a_{H^+}^{0.7}$	-0.6527
$CaCO_3$_in_brine			-0.8527
CH	$Ca(OH)_2 \leftrightarrow Ca^{2+} + 2OH^-$	$10^{-5.0}$	18.51
C-S-H(1.6)	$C\text{-}S\text{-}H(1.6) + 3.2H^+ \leftrightarrow 1.6Ca^{2+} + SiO_2(aq) + 4.18H_2O$	$10^{-7.8}$	23.70
C-S-H(1.8)	$C\text{-}S\text{-}H(0.8) + 1.6H^+ \leftrightarrow 0.8Ca^{2+} + SiO_2(aq) + 2.3H_2O$		9.538
SiO_2(am)	$SiO_2(am) \leftrightarrow SiO_2(aq)$	$10^{-6.5}$	-2.191

Initial and Boundary Conditions. To simulate CO_2 attack on Portland cement, the hydrated cement composition can be simplified to include only CH and C-S-H, and small amounts of amorphous SiO_2, and $CaCO_3$.[89, 160] This simplification is valid because other components, such as Fe- and Al-containing hydrated phases are much less abundant than the CH and C-S-H phases, and their reaction with CO_2 does not contribute to mechanical deterioration of the cement. In cement, C-S-H exists as a semi-amorphous gel with varying ratios of calcium to silicon.[41] We included two of the compositions, denoted as C-S-H(1.6) with a higher Ca-to-Si ratio and C-S-H(0.8) with a lower Ca-to-Si ratio. The number in parentheses indicates the Ca-to-Si ratio. For the $CaCO_3$ phase, to avoid unnecessary confusion with $CaCO_3$ phase transformations between polymorphs, we utilized parameters for calcite, following common procedure in cement modeling,[48, 52, 56, 59, 149] with the exception that an additional "calcite" phase with slightly higher solubility is also included as one of our approaches to better simulate experimental findings. The less soluble $CaCO_3$ is formed in the brine grid cells, and is termed "$CaCO_3$_in_brine," and the more soluble $CaCO_3$ forms in the cement grid cells, and is termed "$CaCO_3$_in_cement." $CaCO_3$ phases and solubilities will be considered and discussed in later sections.

For the initial condition in the cement domain, we assumed the majority of the cement reactive phases were C-S-H(1.6) and CH, with a minor composition of C-S-H(0.8), possibly from hydration at low-Ca zones, a minor SiO_2 component from incomplete reaction with CH to form C-S-H, and negligible $CaCO_3$, from unavoidable exposure to atmospheric CO_2 during cement hardening/hydration. The amounts of C-S-H(1.6) and CH were determined from reported X-ray fluorescence (XRF) results on OPC powder before hydration.[119] Estimation details can be found in the Supporting Information 4-S1.

The initial condition for the solution domain was set according to that used in the experiments. The solution contains 0.5 M of NaCl. Ion activity coefficients were calculated using the extended Debye–Hückel (i.e., B-dot) equation. The CO_2 solubility in this solution at 100 bar and 95 ^oC was calculated using Duan's equation.[145] The concentration of Cl^- was tuned slightly so that under the high pressure of CO_2 at elevated temperature, the initial pH of the solution in our model was 3.0. The initial compositions of the brine and the cement domains in our 1D model are summarized in Table 4.2.

Table 4.2 Initial conditions for cement and brine domains in the model.

Initial condition for cement							
Composition	C-S-H(1.6)	C-S-H(0.8)	CH	SiO(am)	$CaCO_3$_in_cement	Inert	Porosity
Volume Fraction	0.31	0.05	0.16	0.01	0.00001	0.27	0.20

Initial conditions for brine				
Condition	NaCl(M)	pH	Inert Teflon (volume fraction)	$CaCO_3$_in_brine (volume fraction)
Value	0.5	3.0	0.01for selective grid cells	None

To capture the features of the closed batch reactor used in our experiment, the two boundaries of our 1D model were both no-flux boundaries, which allowed evolution of solute concentrations throughout the reaction.

4.2.3 Incorporation of Minimum Non-Zero Porosity and Nucleation Kinetics

Minimum porosity. We utilized the updated CrunchTope code to set a minimum porosity. In continuum scale models, the porosity is calculated using Eq. 4.4. If minerals continue to precipitate, the porosity will continue to decrease until it approaches zero ($\emptyset \sim 10^{-4}$). Because this

near-zero-porosity zone limits diffusion of the reactive fluid into the cement, the precipitation reaction will slow due to lack of reactants reaching the cement.

In real systems, it is not likely that the precipitation will decrease the porosity to near zero in every case. To incorporate this phenomenon in the model, the updated CrunchTope code introduced a "transport porosity", $\emptyset_t$, which is the same as $\emptyset$ in Eq. 4.4 when $\emptyset$ is larger than the minimum porosity (i.e., $\emptyset_{min}$), but remains at $\emptyset_{min}$ if $1-\sum_j \emptyset_{mj}$ is lower than $\emptyset_{min}$:

$$\emptyset_t = \begin{cases} 1-\sum_j \emptyset_{mj}\ , & 1-\sum_j \emptyset_{mj} > \emptyset_{min} \\ \emptyset_{min}\ , & 1-\sum_j \emptyset_{mj} < \emptyset_{min} \end{cases} . \qquad \text{Eq. (4.6)}$$

When $1-\sum_j \emptyset_{mj}$ in a grid cell is below $\emptyset_{min}$, reactive fluid is still accessible by the grid cell, and thus precipitation reactions could not be inhibited by lack of reactants, unless further code modification was made. To avoid precipitation reaction continuing to predict an overall mineral fraction larger than 100%, the precipitation rates had to be slowed down by two empirical equations:

$$R' = F \times R \quad \text{and} \qquad \text{Eq. (4.7)}$$

$$F = \left(\frac{1-\sum_j \emptyset_{mj}}{\emptyset_{min}}\right)^f, \qquad \text{Eq. (4.8)}$$

where *F* is an factor to scale down the precipitation rates to 0 when $1-\sum_j \emptyset_{mj}$ approaches 0, and f is an empirical exponent.

Nucleation Kinetics. Nucleation is the process of formation of a new phase out of the original phase, and is an important process in geomedia.[37-39] For example, the nanoscale nuclei can generate a large reactive surface area for further reactions. Also, the size of the nuclei can match

that of the pore-throats in geomedia, and thus can largely influence the permeability of the medium if they form at pore-throats.[161] However, despite the importance of nucleation, it is usually skipped in reactive transport models due to lack of thermodynamic and kinetic parameters. The common approach to nucleate new phases is to include a small amount of minerals to provide sufficient surface area to start precipitation according to Eq. 4.5. This approach does not always predict the experimental observations well. For example, in our experiments, secondary $CaCO_3$ precipitation was observed in the brine at the end of the reaction. If a small amount of $CaCO_3$ were included in the brine domain in the initial condition, these $CaCO_3$ seeds would be quickly dissolved before the dissolution of cement could increase the brine pH from pH 3 to equilibrium pH 5. In this case, secondary precipitation had to be started by nucleation.

The updated CrunchTope incorporates the nucleation rate equation[30, 61, 162, 163]

$$J = J_0 \exp\left(-\frac{\Delta G^*}{kT}\right), \qquad \text{Eq. (4.9)}$$

in which ΔG^* is expressed by

$$\Delta G^* = \frac{16\pi \upsilon^2 \alpha^3}{3k^2T^2[\ln\left(\frac{IAP}{K_{sp}}\right)]^2} \ . \qquad \text{Eq. (4.10)}$$

In the equations above, J_0 is a kinetic factor, ΔG^* is the nucleation energy barrier, υ is the molecular volume of nucleating phase, α is the effective interfacial energy, and k is the Boltzmann constant. We assume $CaCO_3$ nucleation happens on an inert foreign substrate, because most of the observed secondary $CaCO_3$ in our experiment was on the Teflon liner of the reactor. Such a foreign substrate could decrease interfacial energies for nucleation reaction. We utilized υ and K_{sp} for calcite (unless further modification is specified); α = 47 mJ/m^2, measured in our studies in Chapters

5 and 6,[163, 164] and J_0 on the order of 10^{-8} mol/m^2/s, measured in our work presented in Chapter 7 . The unit for J_0 is for $CaCO_3$ nucleation on a foreign substrate. Therefore, a small amount of Teflon inert was added in the selected brine grids 250 μm away from cement surface, so that $CaCO_3$_in_brine could start nucleating on these inert surfaces. To avoid $CaCO_3$_in_brine precipitation blocking fluid transport in the brine domain (which is unlikely to happen in real reactors), the molar volume of $CaCO_3$_in_brine was manually reduced in the database.

4.3 Results and Discussion

4.3.1 Experimental Observations and Calibrated Modeling Results

The experimental results of this study correlated well with those in Chapter 2. Optical images of cement cross sections reacted with CO_2 for 1, 3, 6 days are shown in Figure 4-S1. The quantified front depths are plotted in Figure 4.2a. The CH front propagates quickly and almost linearly with reaction time, while the inner front of the carbonated layer moves much more slowly into the inner matrix of cement. The surface dissolution layer was not observable on the Day 1 and Day 3 samples, but was obvious on the Day 6 and Day 10 samples.

The modeling results, with the incorporated mechanisms of minimum porosity and nucleation kinetics, are also shown in Figure 4.2a. The reaction fronts in the cement predicted by our model match well with the experimental results. The slight deviation at early reaction times between modeling and experimental results may come from the uncertainty related to the pre-equilibrium of the reaction condition in both the experiment and model. Cement surface dissolution was not predicted by our model for Day 1 and Day 3, consistent with experimental

observations. Using Day 10 as an example, the results for mineral fractions, porosity, pH, saturation for $CaCO_3$ phases, and reaction rates are shown in Figure 4.2(b-f).

4.3.2 $CaCO_3$ Precipitation Could not Fill 100% of the Pore Spaces

In our model, a minimum porosity of 1.5% was obtained by calibrating the modeling using experimental results. This non-zero porosity is important for the formation and continuous widening of the CH-depleted zone. The modeling results without minimum porosity control, shown in Figure 4-S2, predict formation of a CH-depleted zone but not continuous widening throughout the 10-day reaction. In this case, the formation of the CH-depleted zone can happen because at the beginning of the reaction, when $CaCO_3$ precipitation is not able to fill most of the pore space, the acidic brine can dissolve the CH front down to 330 μm below the cement surface. After the $CaCO_3$ precipitation has filled the pore space and resulted in a porosity $\leq 10^{-4}$, the cement becomes passivated, and barely evolves further.

The inefficiency of the carbonated layer in passivating the cement sample can be attributed to several possible causes, including the formation of fractures, defects in the carbonated layer (due to local break points on the layer or due to gaps at grain boundaries), and pore-size-dependent precipitation. These possible causes are illustrated in Figure 4.3.

Our study in Chapter 2 showed that the carbonated layer occasionally included (micro)cracks, either due to the propagation of microcracks originating in the weak CH-depleted zone or due to the expansive $CaCO_3$ quickly formed in a local space. These fractures open pathways for CO_2 transport through the carbonate layer (Figure 4.3a), and when they are averaged with the surrounding composition, the porosity of the overall carbonated layer is then larger than zero.

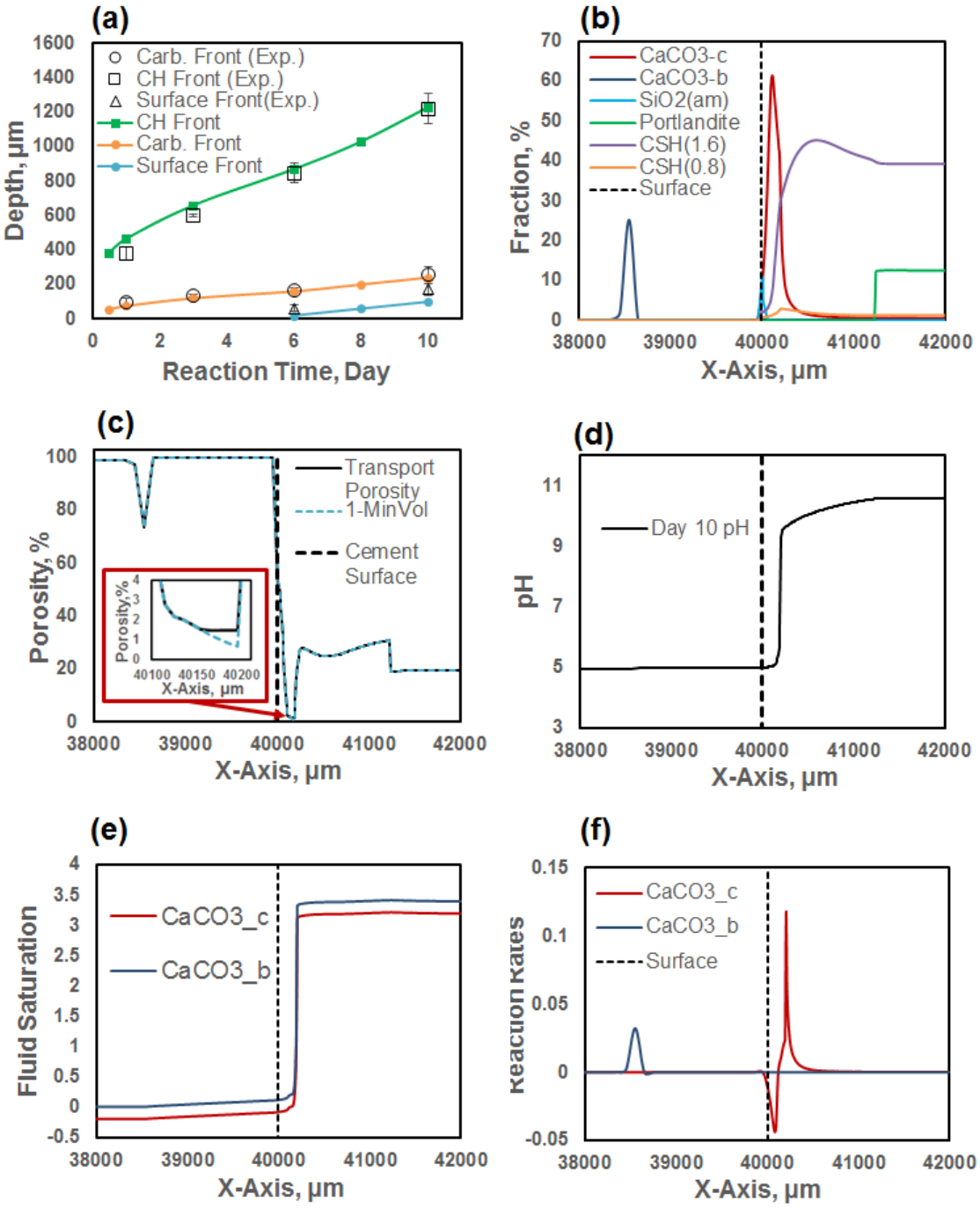

Figure 4.2 Time-resolved experimental results and modeling results. (a) Comparison of mineral fronts in the cement matrix at different reaction times. With updated CrunchTope code, the results from modeling reproduce experimental results. (b) Mineral fractions at Day 10. The dotted line indicates the interface between the brine and cement domains. The $CaCO_3$_in_brine starts from the nucleation reaction. Note that the molar volume of $CaCO_3$_in_brine is manually reduced in the database to facilitate fluid transport in the brine grid cells. (c-f) The porosity, pH, calcite saturation, and reaction rates predicted by our model for Day 10.

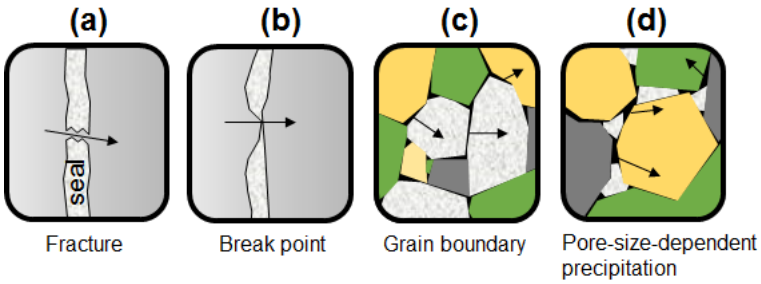

Figure 4.3 Illustration of possible causes for inefficiency of the carbonated layer in filling all the pores space. Arrows in the figures indicate the possible pathways for CO_2.

Another possible explanation for inefficient passivation is that the carbonated layer might have defects. The carbonated layer has ragged fronts, as can be observed from the optical images in Figure 4-S1. If the carbonated layer were thin, it might have local break points (Figure 4.3b). Also, the mineral composition of the carbonated layer is a combination of $CaCO_3$ and silicates. It is possible that there are gaps along grain boundaries (Figure 4.3c).

The last possible explanation is related to the fact that mineral precipitation can be pore-size-dependent.[165, 166] In the case of $CaCO_3$ precipitation, Stack et al. showed that the $CaCO_3$ preferred to form in macropores as opposed to nanopores (~ 8 nm) when the silica pore walls were not chemically modified.[166] The remaining pore spaces can then be pathways for CO_2 transport (Figure 4.3d). For cementitious materials, previous studies using small angle neutron scattering reported that the material has a small pore population with ~ 5 nm diameters, apart from large pore populations, and that the small pore population accounts for 1–2% of the overall porosity.[167, 168] This percentage of the small-pore population, which might be left open during $CaCO_3$ precipitation, is consistent with the minimum porosity of 1.5% calibrated in our model.

In this study, the minimum porosity was assumed to be constant, because further information about the evolution of the minimum porosity in real systems is not available. When

the reaction time is long, the evolution of the minimum porosity could have significant effects on cement deterioration. In this sense, the reactive transport model in this study is only for mechanistic investigation, and cannot be used for extrapolating results for longer reaction times.

4.3.3 Nucleation of $CaCO_3$ in Brine Promotes Cement Surface Dissolution

Before the nucleation rate law is incorporated, the model does not predict dissolution of the cement surface layer. Results without including nucleation are shown in Figure 4-S3. In that case, the surface of the cement does not dissolve because the Ca^{2+} dissolved from CH keeps accumulating in the brine, and the solution becomes supersaturated with respect to $CaCO_3$, with no driving force to dissolve the $CaCO_3$ on the cement surface.

The experimental observation of secondary precipitated $CaCO_3$ in brine pointed the way to include precipitation of $CaCO_3$ in the brine grid cells to serve as a Ca^{2+} sink. However, this approach works only if we have two $CaCO_3$ phases with different solubilities. If the $CaCO_3$ formed in the cement matrix and the $CaCO_3$ formed in the brine have the same solubility, the system cannot transfer Ca^{2+} from $CaCO_3$ on the cement surface to the same $CaCO_3$ phase in the brine. Therefore, we hypothesized that the $CaCO_3$ formed in brine is less soluble than the $CaCO_3$ formed in cement, so that the $CaCO_3$ precipitation in brine can lower the saturation with respect to the $CaCO_3$ in the cement matrix, driving the outer front of the carbonated layer to dissolve. The more soluble $CaCO_3$ phase in cement can be explained by (i) altered $CaCO_3$ lattice size by incorporating foreign ions and/or (ii) precipitation in confinement.

To compare the lattice dimensions of $CaCO_3$ in cement and in brine, additional experiments were conducted for 6 and 10 days (reaction times for which we had previously observed the dissolution layer on the cement surface). After the reaction, precipitates were collected from the

brine and from the carbonated layer in the cement, and were ground to pounder for mineralogy analysis using X-ray diffraction (Bruker D8 Advance). Detailed procedures can be found in the Supporting Information 4-S3. The XRD results (Figure 4.4) show that in both the 6-day and 10-day systems, the precipitates are mixtures of aragonite and calcite. All aragonite had the same lattice dimension, whereas calcite in cement has peaks on the left of the peaks for calcite in brine, indicating that calcite in cement has larger lattices. The larger lattices could be caused by incorporation of foreign ions which were more concentrated in cement pore water than in brine. One possible incorporated ion is SO_4^{2-} which is usually present in cement composition, and is known to increase lattice size and enhance solubility of $CaCO_3$ if incorporated.[169-172]

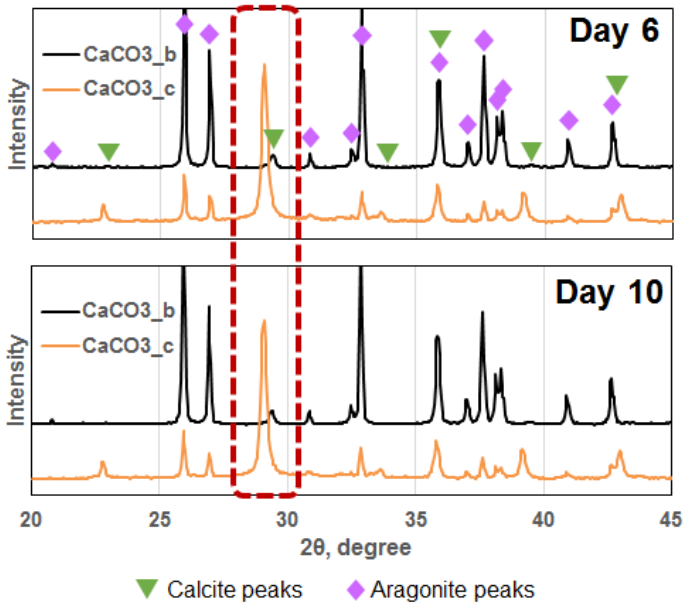

Figure 4.4 Characterization of $CaCO_3$ phases. All aragonite had the same lattice size, whereas the $CaCO_3$_in_cement (or CaCO3_c in legend) had larger lattices than $CaCO_3$_in_brine (or CaCO3_b in legend) probably due to incorporation of large ions such as SO_4^{2-}. This trend is the same for Day 6 and Day 10 systems. The RRUFF database was used for phase identification.

Another possible reason for the more soluble $CaCO_3$ in cement is related to the behavior of $CaCO_3$ in a confined space. Because precipitation in confinement requires the precipitates to be smaller and have greater surface curvature (not necessarily have different lattice dimensions), the result is higher solubility than for precipitates formed in free space.[40] Stephens et al. (2010) also reported that in their experiment $CaCO_3$ precipitated in confinement were stabilized in the more soluble form.[173] In the cement system, $CaCO_3$_in_cement was precipitated as a dense and hard zone, indicating that $CaCO_3$ was precipitated in confined spaces. Thus, $CaCO_3$_in_cement could be more soluble than $CaCO_3$_in_brine.

To avoid complication with $CaCO_3$ polymorphs, calcite K_{sp} was used for $CaCO_3$_in_brine, and the $\log_{10}K_{sp}$ for $CaCO_3$_in_cement was assumed to be 0.2 higher. This $\log_{10}K_{sp}$ difference is similar to that between calcite and aragonite, large enough to distinguish two phases and small enough to allow co-existence in one system.

The presence of two $CaCO_3$ phases in our model allow the cement surface layer to be predicted because the precipitation of less soluble $CaCO_3$_in_brine can drive the brine to be undersaturated with respect to $CaCO_3$_in_cement, as shown in Figure 4.2e. The surface layer is not predicted for Day 1 and Day 3, because at these reaction times, the brine is still accumulating Ca^{2+} from CH dissolution to reach $CaCO_3$ saturation. When the $CaCO_3$ supersaturation is high enough to surpass the nucleation barrier, nucleation of $CaCO_3$_in_brine will start the precipitation to form a sink of Ca^{2+} in the closed system.

4.4 Environmental Implications

This work provides mechanistic insights into deterioration of wellbore cement, which is of importance for safer and more efficient CO_2 storage and other energy-related subsurface operations. Both the non-zero minimum porosity and the $CaCO_3$ nucleation mechanisms have great implications for real-world applications.

As shown in the study, the porosity in the carbonated layer can have a great impact on widening of the weak CH-depleted zone. To hinder widening of the CH-depleted zone, a carbonated layer with less open pore space is desired. The protective efficiency of the carbonated layer can be improved, and thus widening of the CH-depleted zone can be prevented, by engineering applications to inhibit fracture formation in the carbonated layer, by promoting less defective grain boundaries, by forming a thicker carbonated layer, and by diminishing the pore-size dependency of $CaCO_3$ precipitation. For example, if the $CaCO_3$ precipitation rate is slightly suppressed by an inhibitor, the ions can then have more time to diffuse into pores to form a less defective carbonated layer.[148] Another example is to modify the chemistry of pore walls to trigger $CaCO_3$ precipitation in nanopores.[166]

The nucleation of $CaCO_3$ of a more stable phase in reactive fluid is also meaningful. In a GCS environment, the fluid contacting to the cement is likely to be saturated with $CaCO_3$. The results shown in this study strikingly indicate that the cement surface can still dissolve in this scenario, because a less soluble $CaCO_3$ phase can nucleate in the brine. However, a minor modification of the fluid composition by introducing a chemical, such as SO_4^{2-} and Mg^{2+},[169-172] that prefers a more soluble $CaCO_3$ phase in the brine is feasible, so that the cement surface can be less dissolved.

These mechanisms also help us understand the reaction systems better. For example, the previous study on cement deterioration presented in Chapter 3 introduced 50 mM of sulfate ions in the reaction brine, and found that the CO_2 attack on cement has been mitigated significantly.[148] In Chapter 3, we experimentally verified that this mitigation was due to less cement surface dissolution caused by sulfate ion adsorption on $CaCO_3$ grains. Here, utilizing the findings of the current study, we point out two additional possible explanations. First, sulfate ions can decrease the $CaCO_3$ precipitation rate in cement, allowing more time for ions to diffuse into pores and arrange themselves in a less defective carbonated layer structure. Second, when the sulfate ion concentration is comparatively high in the brine, $CaCO_3$_in_brine can incorporate sulfate ions and become more soluble, and thus the difference between the solubility of $CaCO_3$_in_brine and the $CaCO_3$_in_cement is smaller, causing slower dissolution of the $CaCO_3$_in_cement.

In addition to understanding and improving cement systems, the results are also transformative for understanding the interactions of rocks with CO_2-saturated fluid. When supercritical CO_2 or CO_2-saturated brine flows through formation rocks or shale fractures, the main geochemical interactions, as with cement, involve both the dissolution of the rock matrix, which releases cations, and precipitation of carbonates that fix CO_2 in mineral forms.[174] The process is similar to cement deterioration on an elongated time scale. The updated modeling code can thus be utilized to understand and simulate rock–CO_2 interactions as well.

Acknowledgments

This work was supported by the Center for Nanoscale Control of Geologic CO_2, an Energy Frontier Research Center funded by the U.S. Department of Energy, Office of Science, Office of Basic Energy Sciences, under Award Number DE-AC02-05CH11231.

Supporting Information for Chapter 4

4-S1. Calculation of Initial Cement Composition

The initial compositions of the cement grid cells were determined using XRF results reported in the Supporting Information for Chapter 2, Table 2-S1.

Assuming 100 g of anhydrate cement powder, the calculated primary elemental components are 0.96 mole of Ca, 0.32 mole of Si, 0.004 mole of Fe, and 0.05 mol of Al. Distributing these elements to anhydrous products gives 0.17 mole of C_2S, 0.15 mole of C_2S, 0.05 mole of C_3A, and 0.004 mole of C_4AF. During the hydration of cement, the main components of Portland cement powder, alite ($3CaO\text{-}SiO_2$, or C_3S) and belite ($2CaO\text{-}SiO_2$, or C_2S), react with water to form C-S-H. The hydration reactions can be written as

$$C_3S + (1.4 + x)H = C_{1.6}SH_{x+1} + 1.4CH \quad \text{and} \qquad \text{Eq. (4-S1)}$$

$$C_2S + (0.4 + x)H = C_{1.6}SH_x + 0.4CH \qquad \text{Eq. (4-S2)}$$

for C_2S. Considering only calcium silicates, the hydrated products from the hydration reaction are 0.32 mole of C-S-H and 0.30 mole of CH. Using reported densities for gel C-S-H and CH,[175] the calculated C-S-H volume and CH volume are 27 and 10 cm^3, in which the CH volume occupies about 14% of the total paste volume. Keeping the relative ratio of C-S-H to CH, the C-S-H occupies about 38% of the total volume. Because the cement pastes used in our studies were comparatively newly hardened, the initial composition of CH and porosity in the CrunchTope model was increased slightly to mimic our situation. The resulting initial composition used in our model is shown in Table 4.1 in the main text.

4-S2. Additional Results and Images

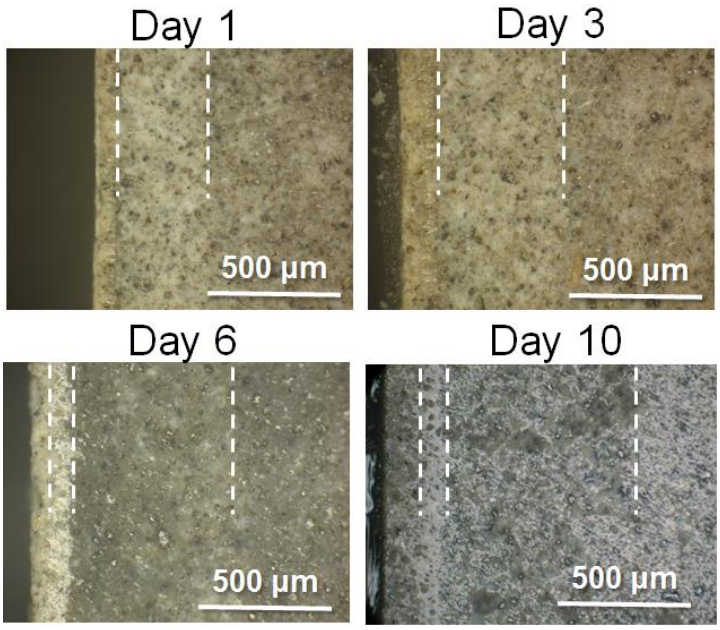

Figure 4-S1 Optical images of reacted cement at Days 1, 3, 6, and 10. The image for Day 10 is adapted from Chapter 2.

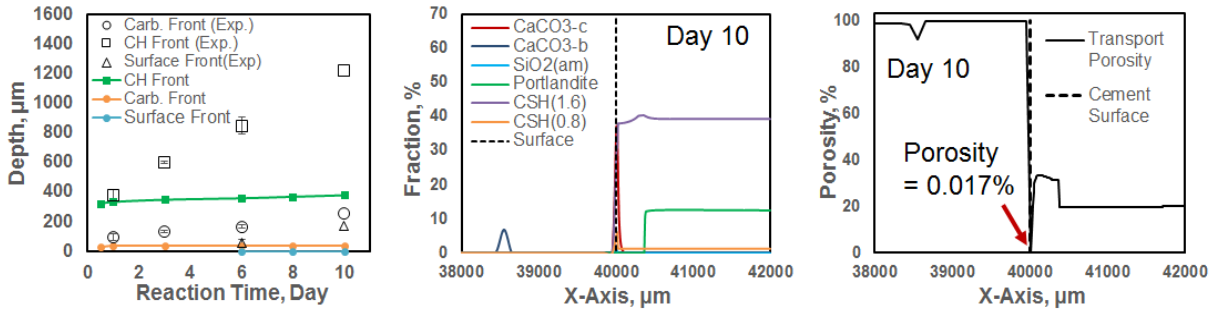

Figure 4-S2 Simulation results without minimum porosity control. The results show that without setting a minimum porosity, the evolution of the CH-depleted zone observed in experiments could not be predicted by the model. The first grid cell on the cement side has a porosity of 0.017%, which is low enough to passivate cement.

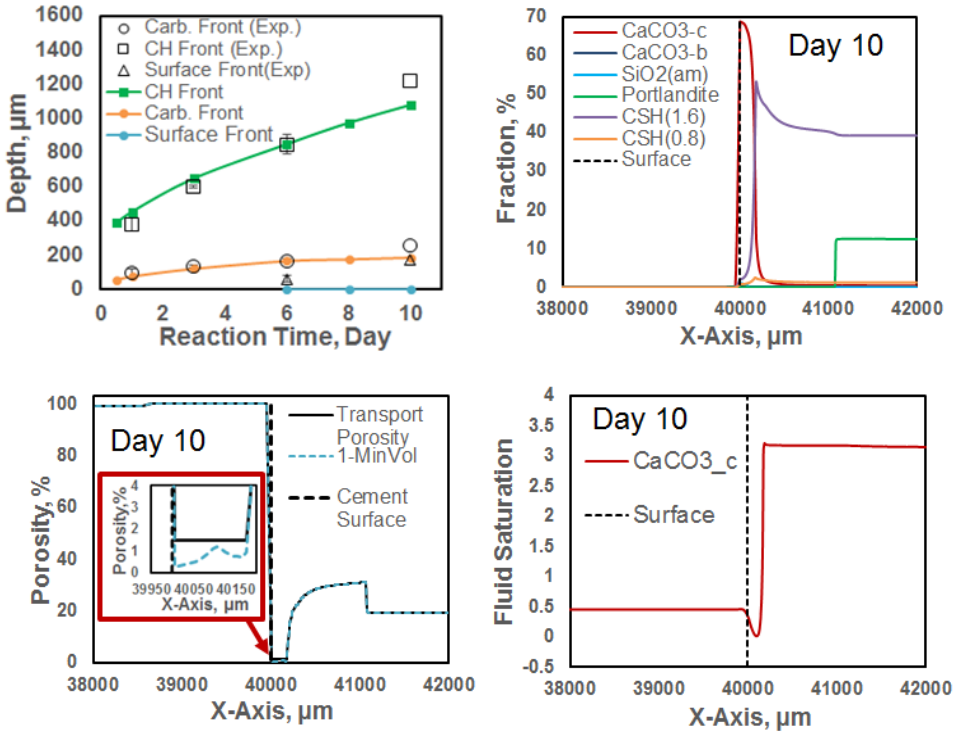

Figure 4-S3 Simulation results without nucleation kinetics. Although the widening of the CH-depleted zone is predicted, the dissolution of the cement surface is not reproduced (red inset box), because the brine is supersaturated with respect to $CaCO_3$_in_cement.

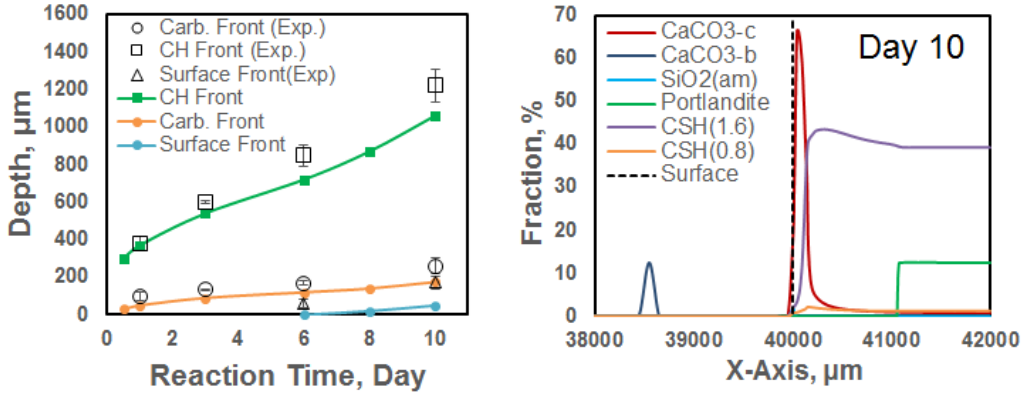

Figure 4-S4 Modeling results with the ion-specific diffusion coefficients listed in Table 4-S2. Considering the uncertainty of the diffusivity estimations, the differences between these results and those predicted with a fixed diffusion coefficient (3×10^{-9} m^2/s) are not significant.

Table 4-S2. Diffusion coefficient D_i estimated for individual ions.[49, 59, 176, 177]

Species	D_i, $10^{-9}m^{-2}/s$
H^+	8.379
Ca^{2+}	0.714
OH^-	4.743
CO_3^{2-}	0.860
HCO_3^-	1.062
$CO_2(aq)$	1.719
Cl^-	1.809
Na^+	1.197
Other	3.000

4-S3. Description of the $CaCO_3$ Phase Comparison Experiments

After the reaction, the reactor was degassed for 30 min and precipitates were collected from the brine, most of which were attached to the Teflon liner inside the stainless steel reactor wall. The precipitates were rinsed with ultrapure deionized water (DI water, resistance > 18 MΩ) and dried with nitrogen gas. The precipitates collected from the 10-day system had a mass of ~ 0.1g, much more than those collected from the 6-day system (0.02 g), as shown in Figure 4-S5. This difference indicates that most of the precipitates were formed during the reaction rather than during degassing, because both the 6-day and 10-day system had similar degassing procedures. After these precipitates were fully dried, they were ground to powder for XRD characterization.

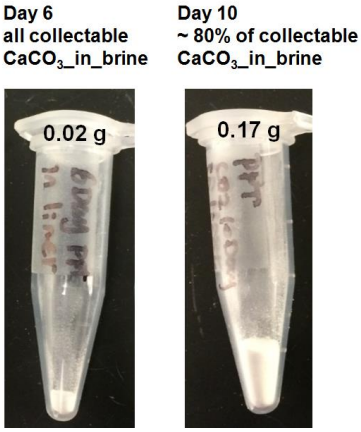

Figure 4-S5. Amounts of $CaCO_3$_in_brine collected from Day 6 and Day 10 systems for XRD analyses.

The cement samples were taken out of the reactor and rinsed with DI water, and then dried at ~50 ^{o}C in the oven for ~ 5 hours. After the samples were dried, XRD sample powder was prepared from the carbonated layer.

Chapter 5: Interfacial Energies for Heterogeneous Nucleation of Calcium Carbonate on Mica and Quartz

Results of this chapter have been published in *Environmental Science & Technology*, 2014, 48 (10), 5745-5753

Abstract

Nucleation is an importance process in several research areas, including materials synthesis, biomineralization, and geochemistry. In the previous chapters, the critical role of nucleation in wellbore cement deterioration was shown using experimental and modeling approaches. In this chapter, we present an experimental study to acquire interfacial energies controlling the thermodynamically favored $CaCO_3$ nucleation on quartz and mica. *In situ* grazing incidence small angle X-ray scattering (GISAXS) was used to measure nucleation rates at different supersaturations. The rates were incorporated into nucleation rate equation $J = J_0 \exp\left(-\frac{\Delta G^*}{kT}\right)$ to calculate the effective interfacial energies (α). *Ex situ* Raman spectroscopy identified both calcite and vaterite as the $CaCO_3$ polymorphs in our experimental system. However, vaterite is likely to be the phase of the heterogeneously formed nuclei. The α was 24 mJ/m^2 for the vaterite–mica system, and 32 mJ/m^2 for the vaterite–quartz. The smaller α of the $CaCO_3$–mica system led to smaller particle and often higher particle densities on mica. A contributing factor affecting α in our system was the smaller bond length mismatch between $CaCO_3$ and mica compared to that between $CaCO_3$ and quartz. The extent of hydrophilicity and the surface charge could not explain the observed $CaCO_3$ nucleation trend on mica and quartz. The findings of this study provide new

thermodynamic parameters for subsurface reactive transport modeling and contribute to our understanding of mechanisms where heterogeneous $CaCO_3$ formation is a concern.

5.1 Introduction

For several reasons calcium carbonate ($CaCO_3$) has long been of interest in many branches of science. It is abundant in geological environments, and it is biologically crucial and reactive, and thus of high interest in biomimetic mineralization.[13, 178, 179] Calcium carbonate formation is also one of the ultimate CO_2 trapping mechanisms in geologic CO_2 sequestration (GCS).[8, 62, 180] Furthermore, calcium carbonate is useful in paper and plastic production,[13, 181] and, conversely, its formation can cause detrimental scaling in oil pipes and water treatment facilities.[42, 182-184] Therefore, elucidating $CaCO_3$ formation is important to advance our understanding of natural and engineered environmental phenomena and to guide engineering applications in environmental science as well as materials science.

Because of its versatile applications and numerous environmental implications, $CaCO_3$ precipitation has been extensively investigated,[182, 183, 185-188] but most previous studies did not separate the nucleation process from growth, aggregation, or ripening. In reactive transport models, seeded systems are usually used at the beginning of mineral precipitation, mainly because of the lack of parameters to set up the nucleation process.[37] In many cases, however, nucleation manifests itself to be an important step. For example, nucleation can generate large reactive surface areas,[37] and nucleation rates have been considered to be the determining factor in mineral precipitation rates.[189, 190] So far, methods such as *in situ* pH[191] and Ca^{2+} activity measurements by a Ca-ion-selective-electrode[192] have been used to indirectly extract nucleation kinetics from bulk solution

chemistry where simultaneous nucleation and growth occurred.[193] Some direct measurements of nucleation rates have also been carried out. Optical microscopy, one of the most straightforward techniques, allows determining nucleation rates by directly measuring the number of particles formed per unit of time.[32, 33, 35, 188] A caveat of optical microscopy studies is that they are valid only under the assumption that nucleated particles will grow larger than the resolution limit without aggregation or Ostwald ripening. Other microscopy techniques include atomic force microscopy (AFM),[186, 187, 194] scanning electron microscopy (SEM),[194, 195] and transmission electron microscopy (TEM).[196] However, these techniques probe only a limited observation area, which limits their ability to yield reliable statistical average counts of nucleated particles. To address these difficulties, Jun et al. (2010) introduced *in situ* small angle X-ray scattering (SAXS)/grazing incidence small angle X-ray scattering (GISAXS) to study *in situ* nucleation of iron (hydr)oxides on quartz surfaces and in solution, providing direct information on critical nucleus sizes, shapes, and their formation kinetics.[197] To measure the heterogeneous $CaCO_3$ nucleation rate on quartz surface, Fernandez-Martinez et al. (2013) used *in situ* GISAXS with a specifically-designed flow-through cell.[31] The flow-through reaction cell (an open system) maintains a constant fluid supersaturation with respect to $CaCO_3$ (s), which is a crucial classical nucleation theory (CNT) parameter controlling nucleation rates.[31]

The application of CNT to $CaCO_3$ is complicated, because $CaCO_3$ exists in different polymorphs and can first precipitate, in many cases, as metastable phases instead of the most thermodynamically stable phase, calcite (Ostwald step rule).[198, 199] These metastable phases include amorphous calcium carbonate (ACC), vaterite, and aragonite. [28] To apply CNT on nucleation kinetics, $CaCO_3$ phase needs to be either assumed or identified. In addition, the phase and kinetics of heterogeneous $CaCO_3$ precipitation can be affected by substrates.[32, 33, 35] A recent

study of heterogeneous $CaCO_3$ precipitation on organothiol self-assembled monolayers (SAMs) concluded that calcite nucleated directly on the surface, and was not transformed from amorphous precursors. The calcite nucleation rates were in good accordance with CNT with a reduced thermodynamic barrier.[33]

Apart from affecting precipitate kinetics and polymorphs on surfaces, the substrate can also influence the dominant reaction processes (either nucleation, growth, or Ostwald ripening)[200] and the chemical compositions of precipitates.[201] In particular, substrates can create different interfacial energies among the substrate, the solution, and the precipitates, resulting in different heterogeneous nucleation rates. Fernandez-Martinez et al. (2013) experimentally obtained a value of 36 mJ/m^2 for the effective interfacial energy controlling $CaCO_3$ nucleation on quartz under experimental solution conditions. They assumed the precipitated phase was calcite, and approximated the system to be nucleation-dominant (meaning that particle growth was slow enough to be ignored).[31] Several questions naturally come up: what will happen if other mineral surfaces with different surface natures are used as substrates? For example, if mica, another environmentally abundant mineral often found in GCS sites,[202] is used as $CaCO_3$ precipitation substrate, it cannot be predicted whether precipitation will be nucleation-dominant as we found in the quartz case under similar experimental conditions. If the nucleation process does not dominate, is there a way to separate nucleation from growth? What phases of $CaCO_3$ are formed? What is the interfacial energy of the $CaCO_3$–mica system?

This work seeks to answer these questions and to determine the effective interfacial energies of $CaCO_3$–mica and $CaCO_3$–quartz systems in aqueous environments. We compared $CaCO_3$ nucleation rates and critical nucleus (smallest observable particle) sizes on mica and quartz substrates at different supersaturations. We also identified the $CaCO_3$ phases of micro-sized

particles and suggested a $CaCO_3$ phase for nanoparticles in the system. This study provides new information about $CaCO_3$ nucleation on quartz and mica substrates, specifically, the interfacial energies for heterogeneous nucleation. The findings provide useful information for environmental geochemistry, such as geologic CO_2 sequestration modeling, where many thermodynamic parameters are needed,[203, 204] for bio-mineralogy where $CaCO_3$ formation is expected on biofilm surfaces,[179, 205] and for industries where pipeline/membrane scaling is a concern. The data analysis methods also can be applied to other types of nanoparticle formation studied by *in situ* small angle X-ray scattering.

5.2 Experimental Section

5.2.1 Substrate Preparation

Quartz and mica are abundant minerals in GCS sites, comprising up to 16–61% and 10–33%, respectively, of shales that often are caprocks.[206] In this work, muscovite ($K_2Al_4(Al_2Si_6)O_{20}(OH)_4$) was used as a model mica. (001) surface muscovite sheets were purchased from Goodfellow Cambridge Limited (UK), and the (100) surface of quartz substrates were purchased from MTI Corporation (USA). Substrates were prepared as described in the Supporting Information Section 5-S1.

5.2.2 Solution Chemistry

$CaCl_2$ and $NaHCO_3$ reservoir solutions were prepared from ACS reagent grade $CaCl_2$ or $NaHCO_3$, and volumetrically mixed together to generate the concentrations listed in Table 5.1. The Ca^{2+} concentrations were chosen based on the composition of typical formation water, where the general Ca concentration range has been reported as 0.01–0.2 M.[207] The HCO_3^- concentrations

were chosen to obtain an optimal supersaturation for the experimental reaction time. The pHs and supersaturations ($\ln\left(\frac{\mathrm{IAP}}{K_{sp}}\right)$) of the mixed solutions were calculated using the Geochemist's Workbench (GWB, Release 8.0, RockWare, Inc.) with the thermo_minteq database. Specifically, IAP is the ionic activity product of (Ca^{2+})(CO_3^{2-}) and K_{sp} is the solubility product of $CaCO_3$. The database uses K_{sp}(calcite) = $10^{-8.48}$, and K_{sp}(vaterite) = $10^{-7.91}$.[208] Based on reported K_{sp}(ACC) = $10^{-6.40}$,[209] all the conditions are undersaturated with respect to ACC. Because GWB calculates the supersaturations in $\log_{10}\left(\frac{\mathrm{IAP}}{K_{sp}}\right)$, we have converted the results from $\log_{10}\left(\frac{\mathrm{IAP}}{K_{sp}}\right)$ to $\ln\left(\frac{\mathrm{IAP}}{K_{sp}}\right)$. Within the reaction time range, the pH of the $NaHCO_3$ did not change, indicating that the CO_2 dissolving or degassing is not a concern.

Table 5.1 Solution conditions used in this study. Supersaturation (σ) is defined as ln(IAP/K_{sp}), where IAP is the ionic activity product (Ca^{2+})(CO_3^{2-}), and K_{sp} is the solubility product of minerals written as a subscript of σ. K_{sp} in the database for calcite and vaterite are $10^{-8.48}$ and $10^{-7.91}$, respectively.[208] Utilizing K_{sp}(ACC) = $10^{-6.40}$,[209] all the conditions are undersaturated with respect to ACC. Values of σ and pH were calculated by Geochemist's Workbench (GWB, Release 8.0, RockWare, Inc.) using the thermo_minteq database. pHs were not adjusted, and were reasonably constant in all conditions (pH ~ 8).

Condition name	$CaCl_2$, M	$NaHCO_3$, M	$\ln(\frac{\mathrm{IAP}}{K_{sp-calcite}})$	$\ln(\frac{\mathrm{IAP}}{K_{sp-vaterite}})$	pH
C1	0.05	0.01	4.61	3.30	7.89
C2	0.025	0.005	3.73	2.43	7.97
C3	0.025	0.0025	3.05	1.74	7.97
C4	0.01	0.0025	2.72	1.42	8.06

5.2.3 Synchrotron-Based Grazing Incidence Small Angle X-Ray Scattering (GISAXS)

GISAXS experiments were conducted at beamline 12-ID-B at the Advanced Photon Source (Argonne National Laboratory, USA). Incidence X-ray energy was 14 keV, and the sample-to-

detector distance was 2.06 m. At this distance, the range of magnitude of the scattering vector q was 0.005 to 0.4 $Å^{-1}$. To ensure high surface sensitivity, the incident angle was set as 0.11° for both quartz ($\theta_{critical}$ = 0.14°) and mica ($\theta_{critical}$ = 0.15°), which gives a calculated reflectivity 98.8% for quartz and 98.6% for mica. Before each run, the fluid cell and tubing were rinsed by 1% HCl and then by water to remove any $CaCO_3$(s) from the previous run. Two identical peristaltic pumps (model WPX1-F1/8S4−C, Welco Co. Ltd., Tokyo, Japan) pumped reservoir solutions into a micro mixer (residence time < 1 s) and then pumped the mixed solution into the GISAXS cell at a constant flow rate of 5.6 mL/min. The amount of homogeneous nucleation in the cell was below the detectable limit of transmission SAXS. Waste solutions were pumped out of the cell from the outlet on top of the cell (Figure 5-S1). The flow-through setup generated a constant saturation condition in the cell. After the well-mixed solution was connected with the cell, images were taken within 3 minutes. Exposure time was 90 seconds for each image, followed by 150 seconds between two exposures. All four conditions in Table 5.1 were used for mica, and C1, C2, and C3 were used for quartz.

After images were obtained, horizontal cuts of each two-dimensional scattering data were extracted along the Yoneda wing, where the scattering intensities by particles on the surface were enhanced the most.[210, 211] Possible fluctuations of incoming beam intensity were corrected for in each data set, using the Kapton window scattering peak as an internal standard. For each run, the first cut after correction was used as background and subtracted from later corrected cuts. The resulting scattering intensity I(q) was plotted with respect to the magnitude of the scattering vector q. Two methods were used to generate nucleation rates from I(q) vs. q plots.

Method 1: GISAXS invariant method

This method is suited for systems where nucleation is the dominant process, i.e., where the observed increase in the scattered intensity comes mainly from the formation of new nuclei, and where particle growth is negligible.[31] The invariant (Q) is calculated by $Q = \int I(q)q^2 \mathrm{d}q$, and Q is proportional to the total particle volume, which in turn is proportional to the total particle number in a nucleation-dominant system. The increase rate of the invariant (linear part) with time is thus proportional to the nucleation rate in an arbitrary unit.

Method 2: GISAXS intensity fitting method

This method can be applied to more general systems where nucleation, growth, and aggregation are significant. On the I(q) vs. q plot, the interaction of X-rays with particles can be expressed by the following equation:[212]

$$I(q) = N \cdot \Delta\rho^2 \cdot \{\int D(R) \cdot [V(R)]^2 \cdot P(q,R) \cdot \mathrm{d}R\}\left[I_{pow}q^{-p} + S(q)\right]. \qquad \text{Eq. (5.1)}$$

In this equation, N is the total particle number; $\Delta\rho$ is the difference of scattering length density between particles and background; $D(R)$ is the size distribution of particles, which is assumed to be the Schultz distribution in this study. $\mathrm{V}(R)$ is the volume of a particle with radius R; $P(q,R)$ is the form factor, the expression of which for spherical particles is $\left\{\frac{3[\sin(qR)-qR\cos(qR)]}{qR^3}\right\}^2$. Further, $I_{pow}q^{-p}$ expresses the power law (or Porod law) at the small q ranges which provide information about the aggregates, where I_{pow} is a factor weighting the intensity contribution from the power law, and p is the power law slope. Finally, $S(q)$ is the structure factor, which is equal to one ($S(q) = 1$) for dilute systems.

Using Eq. 5.1, the total particle number N (in arbitrary units) can be fitted at each elapsed time point. The fitting allows obtaining relative changes of the total particle number over time, the linear part of which is used to determine the nucleation rate. More details of the fitting method are available in the Supporting Information Section 5-S3.

5.2.4 Classical Nucleation Theory (CNT)

The nucleation rate (J) and the critical nucleus size (r_c) in classical nucleation theory are expressed as:[162]

$$J = J_0 \exp\left(-\frac{\Delta G^*}{kT}\right) = J_0 \exp\left\{-\frac{16\pi v^2 \alpha^3}{3k^3T^3\left[\ln\left(\frac{IAP}{K_{sp}}\right)\right]^2}\right\} \text{ and} \qquad \text{Eq. (5.2)}$$

$$r_c = \frac{2v\alpha}{kT\ln\left(\frac{IAP}{K_{sp}}\right)}. \qquad \text{Eq. (5.3)}$$

where J_0 is a kinetic factor related to the frequency and efficiency of collision, ΔG^* is the height of the free energy barrier that the system has to overcome to form a critical nucleus (J/mol), α is the effective interfacial energy (mJ/m^2), v is the molecular volume of the forming phase (cm^3/molecule), k is the Boltzman constant (1.38×10^{-23} J·K^{-1}), T is the temperature (K), and $\ln\left(\frac{\mathrm{IAP}}{K_{sp}}\right)$ is the supersaturation, After taking natural logarithm of both sides of Eq. 5.2, the equation can be re-written as:

$$\ln(J) = \ln(J_0) - \frac{16\pi v^2 \alpha^3}{3k^3T^3\left[\ln\left(\frac{IAP}{K_{sp}}\right)\right]^2} = \ln(J_0) - \frac{B}{\left[\ln\left(\frac{IAP}{K_{sp}}\right)\right]^2} \qquad \text{Eq. (5.4)}$$

By regressing $\ln(J)$ over $1/\left[\ln\left(IAP/K_{sp}\right)\right]^2$, the effective interfacial energy can be obtained by $\alpha = \left(\frac{B \cdot 3k^3T^3}{16\pi v^2}\right)^{1/3}$. In this study, the molecular volumes of calcite (density = 2.710 g/cm^3) and vaterite (density = 2.645 g/cm^3) (mindat.org) were used for α calculations.

5.2.5 Atomic Force Microscopy (AFM)

To directly show the morphologies of particles nucleated on the substrates, *ex situ* AFM was used as a complementary technique to GISAXS experiments. All conditions in Table 5.1 were conducted for both mica and quartz substrates. However, the substrates in the C1 conditions became too rough due to the collection of homogeneously nucleated particles, and thus were not scanned by AFM. Substrates were prepared as described above, and were reacted for 2 hours. After 2 hours, the substrate was taken out of the GISAXS cell, gently rinsed with ethanol, and dried with pure nitrogen gas. Ethanol was used instead of DI water to prevent nanoparticle dissolution by DI water. Substrates were scanned by AFM within 5 hours of reaction. AFM tapping mode was used (AFM, Veeco Inc.) to collect height, amplitude, and phase images. Tapping mode probes were purchased from Brucker (Model: RTESP, Part: MPP-11100-10). Detailed AFM tip information is provided in the Supporting Information Section 5-S7. Nanoscope 7.20 software was used to process images.

During the AFM image analyses, particle densities (#/μm^2) were determined from height images. Because heterogeneously nucleated particles have a strong epitaxial relationship with substrates, they distribute very evenly on the substrates,[197, 213] while the homogeneously formed and settled particles are larger and randomly distributed on the substrates. Here, we focus only on the evenly distributed particles (i.e., heterogeneously nucleated particles). If nucleation rates were assumed to be constant during the 2 hour experiment, the measured densities would be proportional

to the nucleation rates. This method of roughly estimating nucleation rates is referred to as the "particle density method" in later sections.

5.2.6 Raman Spectroscopy

Within one day of performing the AFM experiments, we analyzed the particles on substrates by Raman spectroscopy (Renishaw® inVia Raman Microscope) to determine the polymorph of $CaCO_3$ particles at a detection limit of ~2 μm. A laser with a wavelength of 514 nm was used. A calibration was performed using a standard quartz wafer (Renishaw®). WIRE software was used to process the measurements and record the data. Spectra of freshly reacted quartz and mica were also obtained to make sure that other phases were not missed due to the delay from the end of reaction to the acquisition of the Raman spectra.

5.2.7 Scanning Electron Microscopy (SEM)

After conducting Raman spectroscopy, we imaged the same substrates using SEM (FEI Nova NanoSEM 2300). Substrates were coated with AuPd to increase conductivity, and 10.00 kV was the electron accelerating voltage. The working distance was 5–6 mm. The surfaces and shapes of particles larger than ~ 800 nm in diameter were imaged clearly.

5.3 Results

5.3.1 Nature of $CaCO_3$ Polymorphs Observed on Substrates

According to *ex situ* Raman spectra, vaterite and calcite were two polymorphs of $CaCO_3$ formed in both mica and quartz systems. Crystals with rhombohedral shapes were identified as calcite, while the round, elliptic, and flower-like crystals were vaterite. Figure 5.1 (Top) and Figure 5-S2 show the Raman spectra of $CaCO_3$ on mica and quartz, respectively. Amorphous calcium

carbonate formation was not observed. The freshly reacted mica and quartz substrates also showed calcite and vaterite as the two $CaCO_3$ polymorphs after 2 hours reaction, without any observable ACC phase. SEM images (Figure 5.1 (Bottom) and Figure 5-S3) demonstrate that these two polymorphs have different shapes and surface roughnesses. Different vaterite morphologies were observed due to different orientations and combinations of the round, flat particles (Figure 5-S3). Vaterite presented a rougher surface than calcite, as shown in the zoomed-in images (Figure 5.1).

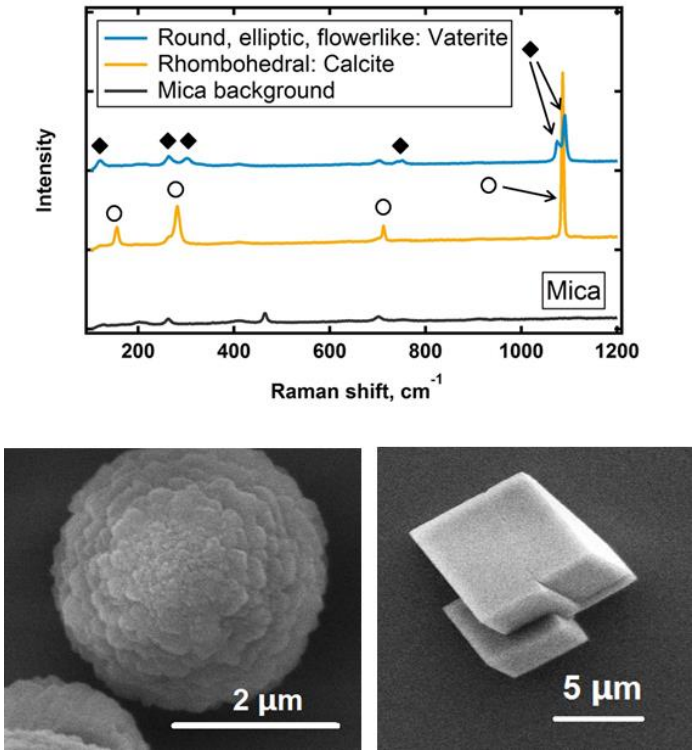

Figure 5.1 (Top) Raman spectra of $CaCO_3$ particles formed on mica substrates. The rhombohedral particles are calcite, and other shapes (round, elliptic and flower-like) are vaterite. No other $CaCO_3$ phases were detected. The peak positions match well with calcite (○) and vaterite (◆) reference spectra.[214] (Bottom) SEM images of a typical surface of vaterite and calcite, taken from C1 and C3 conditions on mica. The images show that the vaterite surface is rougher than the calcite surface. Particles under other conditions appear to have the same trend. Note that the particles in this figure are likely homogeneously formed and have settled to the substrate.

The caveat of SEM and Raman spectroscopy observations is that the observed particles were micrometer scale. In GISAXS and AFM experiments, however, we have observed the

heterogeneous nucleated particles to be several nanometers in size. Also, in our study, the particles observed by SEM and Raman spectroscopy have random orientations without any epitaxial relationship with substrates, while previous studies showed that micrometer $CaCO_3$ precipitates heterogeneously formed and grew in the preferred orientation that lowered the free energy of the system.[29, 33] Based on the large size and random orientations of $CaCO_3$ particles, the particles in SEM and Raman images must have either formed homogeneously and then settled, or evolved from heterogeneously formed particles through growth, aggregation, or ripening. We hypothesized that heterogeneous particles first forming on mica and quartz surfaces were vaterite, or ACC, rather than calcite, for three reasons: First, AFM images did not show rhombohedral shapes in evenly distributed particles (Figure 5.2); second, GISAXS did not show an observable scattering pattern of faceted particles (Figure 5-S4); and third, nanometer nuclei are less thermodynamically stable than micrometer particles.[215] If all nuclei formed as calcite, the phase of $CaCO_3$ particles should be all calcite. To be able to present micrometer particles as vaterite, the nucleated phases should be either vaterite or ACC, less thermodynamically stable phases (Figure 5-S3).

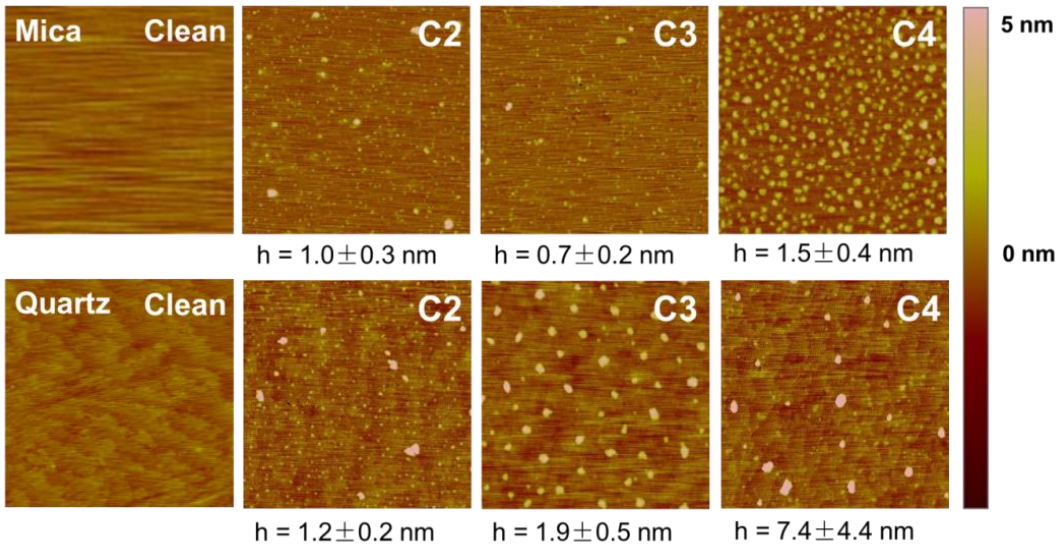

Figure 5.2 AFM images of mica and quartz substrates after 2 hours of reaction at different supersaturations (Table 5.1). Substrates reacted under C1 conditions for 2 hours are too rough to be scanned by AFM and thus are not shown here. Evenly distributed small particles are heterogeneously formed, and their sizes are listed at the bottom of each image. The size is larger for mica-C2 than mica-C3 (opposite to the trend) due to the uncertainty introduced by extremely small particle sizes. Higher supersaturation generates smaller particle sizes. At the same supersaturation, there are more particles on mica than on quartz, and this is more obvious in low supersaturations (C3 and C4). No rhombohedral or faceted particles are shown in the images. Clean substrates are also shown as a comparison. All images are 1μm × 1 μm scan size.

5.3.2 *In situ* GISAXS Observations of Nucleation on Mica and Quartz Substrates

GISAXS experiments recorded the continuous increase of intensity, I(q), over q of ~ 0.02–0.08 $Å^{-1}$, which is related to the evolution of heterogeneous $CaCO_3$ particles on the substrates.[31] While GISAXS provides quantitative information about particle size, number, shape, and inter-particle interactions, we focused on particle size and number to provide nucleation rates in this study. Representative I(q) vs. q plots for mica and quartz are shown in Figure 5.3. Additional $I(q)$ vs. q plots are shown in Figure 5-S5, and time-resolved particle numbers are shown in Figure 5-S6 in the Supporting Information. No apparent induction time was observed under our experimental conditions. The faster increase of intensity at higher supersaturations indicates faster

precipitation (i.e., greater total particle volume) rates. Fitting the data according to Eq. 5.1 and using the Schultz distribution, we calculated the in-plane radii of gyration (R_g). Sample C3 for quartz could not be fitted because of its weak scattering. Because particle scattering intensities were monitored starting before nucleation and concluding with the end of the reaction, it can be assumed that the first fitted R_g are close to the critical nucleus radii (r_c) of the particular system. Therefore, the smallest observable particle radius R_g is used as estimate of r_c. The earliest observable radii were 3.0 nm, 4.4 nm, 4.4 nm, and 4.5 nm for C1, C2, C3, and C4 on mica, and were 3.6 nm and 5.2 nm for C1 and C2 on quartz. The fitting quality of C1, C2 was better than that of C3 and C4 due to the stronger signal. The critical nucleus radius increased with decreasing supersaturations, which is consistent with CNT (Eq. 5.3).

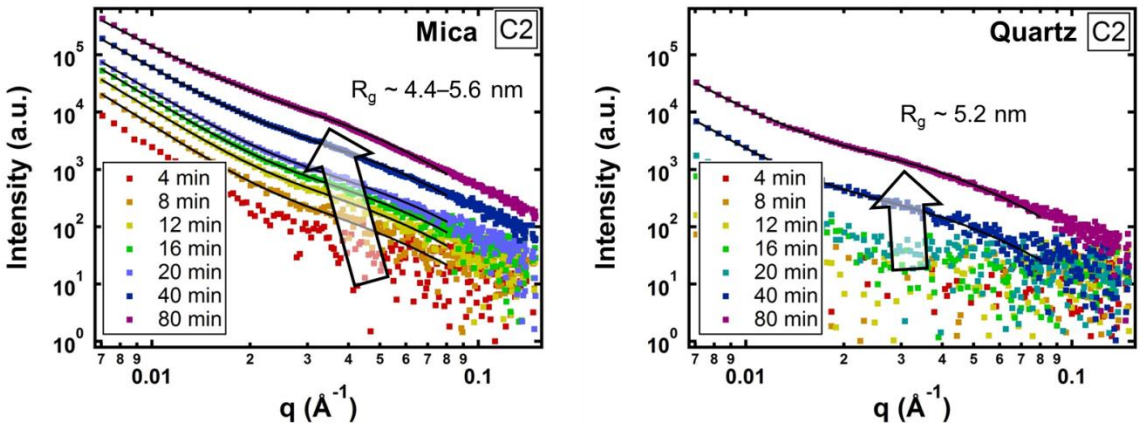

Figure 5.3 Representative GISAXS data cuts along the Yoneda wing. $CaCO_3$ formation on mica and quartz at the second highest supersaturations (C2, Table 5.1) is compared. Black lines are the fitted data. The arrow shows the peak position evolution (q inversely proportional to particle size). The mica substrate has a more significant increase in intensity (more precipitation), a larger peak position (smaller particle size), and a bigger shift in peak position (faster particle growth). The GISAXS data for all conditions are shown in the Supporting Information Section 5-S6.

Furthermore, particle growth was not obvious in most samples, except in the highest supersaturation. This can be seen in $I(q)$ vs. q plots (Figure 5.3). Each $I(q)$ curve has a peak at a

distinct *q* value, which is inversely proportional to particle size. The peak position in the data did not shift significantly in most samples, indicating that nucleation was dominant over growth for these cases. However, growth was evident for the C1 condition on mica and quartz (Figure 5-S5) after ~30 min reaction time. Under C1 conditions, R_g increased by 2.7 nm (90%) on mica and by 0.4 nm (11%) on quartz within one hour after nuclei were first observed by GISAXS. Under C2 conditions, the particle radius increased by 0.5 nm on mica (11%) and remained unchanged on quartz within one hour after nuclei were observable.

5.3.3 *Ex situ* AFM Observations of Nucleation on Mica and Quartz Substrates

Trends in particle size and density observed by AFM are consistent with those observed by GISAXS, although absolute values are different. As shown in Figure 5.2, particle sizes on both substrates are smaller under higher supersaturations. The heights of particles nucleated on mica under conditions C2 and C3 have comparatively large uncertainties, because the particles are mostly just larger than the range of the image noise level of ~ 0.5 nm, with the exception of smaller particles that have been blurred by the noise. These particle sizes are much smaller than those observed by GISAXS. There are three possible reasons: First, the particle size may have decreased upon dehydration; second, particles may have partially dissolved during rinsing after reaction, although we do not anticipate significant dissolution of precipitates by ethanol; and third, AFM measures the vertical heights of particles as an indicator of particle sizes, while GISAXS measures the in-plane (horizontal) radii of gyration of particles to represent particle sizes; the two parameters may not be the same if the particle is not perfectly spherical with a contact angle of 90°.

Particle densities (#/μm^2) are higher at higher supersaturations (Figure 5-S7), indicating faster nucleation rates. Particle densities under conditions C2 and C3 on mica are hard to compare, because the particle sizes are just above the noise level (~ 0.5 nm), and have comparatively large

uncertainties in measured height. Moreover, particle density is higher on mica than on quartz under the same supersaturation (Figure 5-S7), and this difference becomes more significant at lower supersaturations. In other words, particle density on quartz decreases faster with decreasing supersaturation than does particle density on mica. Differences in absolute values between AFM and GISAXS, although the results have similar trends, indicate possible discrepancies between *in situ* and *ex situ* results using similar conditions.

5.3.4 Effective Interfacial Energy (α) Calculations

Three different approaches were used to calculated effective interfacial energies in Eq. 5.2: (1) the invariant method using *in situ* GISAXS data, (2) the fitting method using *in situ* GISAXS data, and (3) the particle density method using *ex situ* AFM data. While the three approaches obtained nucleation rates differently, as described in the Experimental Section, all followed the same procedure to calculate α. Because the slope of $\ln(J)$ over $1/\left[\ln\left(IAP/K_{sp}\right)\right]^2$ is used in α calculation, although the absolute values of J are different from each method, the slopes are comparable among all methods.

The effective interfacial energies calculated by the three different methods are listed for comparison in Table 5-S1. The error ranges come from uncertainties related to the weighted linear regression. The invariant method gives almost the same values as the fitting method when applied to a system where nucleation is dominant over growth. This method also works for samples with low signal-noise ratios (C3 condition on quartz). If the system has significant particle growth, the invariant Q (proportional to the particle volume) will increase more with reaction time than if the system has only nucleation. In that case, the fitting method is recommended, because it allows for the separation of nucleation from growth by fitting the total particle number contributed by

nucleation, as well as the particle size change contributed by growth. The only limitations are that it requires high data quality and that the system must not have appreciable Ostwald ripening. Finally, the particle density method gives the smallest α values among the three methods. This is likely because the nucleation rates were not always linear within 2 hours, and particles are too small to be counted accurately using AFM.

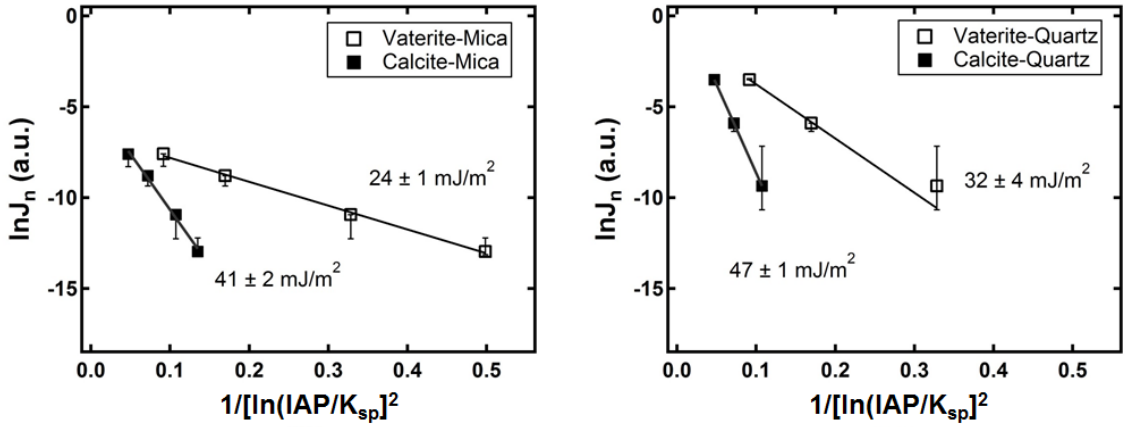

Figure 5.4 Effective interfacial energies of $CaCO_3$–mica and $CaCO_3$–quartz systems. Data presented are samples with best signal-noise ratios, and error bars are data ranges which were used in the weighted least square regressions. Calculated effective interfacial energies are shown in the figure, uncertainties of which are from the standard deviation of the regressed slope. Nucleation rate, *J*, in the mica figure (left) is generated using the fitting method, while *J* in the quartz figure (right) is generated by the invariant plot. The *J* values can be compared within each figure, but cannot be compared between figures.

Here, we report α of the $CaCO_3$–mica system calculated by the fitting method, which, unlike the invariant method, reliably separates nucleation from growth (Figure 5.4). We report α of the $CaCO_3$–quartz system calculated by the invariant method, which works for the C3 condition on quartz, where the signal was too weak to fit. Because we concluded that vaterite nucleated first, unless we had ACC in our experimental systems, we calculated α values for vaterite and substrate systems as $\alpha_{vaterite-mica}$= 24 mJ/m^2 and $\alpha_{vaterite-quartz}$ = 32 mJ/m^2. However, where calcite needs to be assumed as the phase of the nuclei, such as in transport reactive models where phase transformation is not included to avoid complicating the scenario, we also report α values for the

assumed calcite–substrate systems as $\alpha_{calcite-mica}$ = 41 mJ/m^2 and $\alpha_{calcite-quartz}$ = 47 mJ/m^2. Despite of the different methods used, the relative magnitude of α on mica is smaller than that on quartz, for both polymorphs. The α results and their trends were reproduced using data from two beamtimes. The $\alpha_{calcite-quartz}$ we report here is larger than calculated in the previous experiments conducted by Fernandez-Martinez et al., of which difference, 5 mJ/m^2 is attributed to the choice of the database for the calculation of the supersaturation. In addition, different flow rates were used, and a large error was observed for the lowest supersaturation (0.01 M $CaCl_2$ and 0.0025 M $NaHCO_3$). More details on α uncertainties are available in the Supporting Information Section 5-S9.

5.4 Discussion

5.4.1 Effects of α on $CaCO_3$ Nucleation Behaviors

From the slope of $\ln(J)$ over $1/\left[\ln\left(IAP/K_{sp}\right)\right]^2$, which is proportional to the cube of α, we have obtained smaller α for the mica system than the quartz system. In practical application, if the nucleation rates on one substrate vary less significantly with changing supersaturations (i.e., smaller slope of $\ln(J)$ over $1/\left[\ln\left(IAP/K_{sp}\right)\right]^2$),[195] the substrate is expected to have smaller α. According to Eq. 5.2 and Eq. 5.3, this substrate is also expected to have a smaller critical nucleus size (proportional to α) and faster nucleation rates. Here, we discuss how consistent our system (and potentially other systems) is with CNT, with respect to the effects of α on critical nucleus sizes and nucleation rates.

As shown by GISAXS results, we observed smaller r_c on mica than on quartz at the same supersaturations, indicating that under our experimental conditions, the critical nucleus sizes were

predominantly affected by $\ln(IAP/K_{sp})$ and α. For heterogeneous nucleation, the positive relationship between r_c and α at constant IAP/K_{sp} can be affected by other factors, such as particle geometry and contact angles between particles and substrates. Assuming proportional relationship, we can calculate the α of one system as long as we know the α of another system and the r_c's for both systems. For example, if we first measured $\alpha_{vaterite–quartz}$ to be 32 mJ/m^2, then $\alpha_{vaterite–mica}$ can be calculated by comparing the r_c (approximated by comparing earliest R_g obtained using GISAXS) on mica and quartz under the C1 and C2 conditions, which gives $\alpha_{vaterite–mica}$ ~ 27 mJ/m^2. This method provides reasonable estimates, however, it assumes that Eq. 5.3 is applicable, employs the smallest observable R_g as good approximation for r_c, and requires *a priori* knowledge of the α of another system.

Eq. 5.2 implies that a substrate with a small α will have faster nucleation rates. Using GISAXS, we measured faster nucleation rates on the C2 and C3 mica than on quartz, and using AFM, we observed faster nucleation rates on C3 and C4 mica than quartz. However, at higher supersaturations (C1), the nucleation rates on mica and quartz were similar, despite the mica having a smaller α value. The only parameter in Eq. 5.2 that can account for the similar nucleation rate would be different kinetic factors, J_0, for mica and quartz.[216] Factor J_0 in Eq. 5.2 is expanded as $J_0 = A\exp(\frac{-E_a}{kT})$, where A relates to the geometry and material properties of the reactant, and E_a is the effective activation energy arising from attaching new ions onto nucleated clusters.[33, 61] Therefore, predicting a relative nucleation rate by α according to Eq. 5.2 should be approached carefully, as J_0 could also affect the nucleation rate. To the best of our knowledge, there is little experimental research on the kinetic factor, J_0. Research on the relationship between material properties and J_0 could be an interesting future direction to help us better understand the kinetics of heterogeneous nucleation.

5.4.2 Factors Contributing to α

Three substrate related factors can contribute to the kinetics of heterogeneous precipitation: The lattice mismatch between the substrate and the precipitate, the extent of hydrophilicity, and the surface charge of the substrate surfaces.[194, 200, 213, 215, 217-220] To provide insight on mechanisms responsible for the smaller α in the $CaCO_3$–mica system compared to the $CaCO_3$–quartz system, these three factors were analyzed experimentally. First, lattice mismatch is related to interfacial energy between the nuclei and the substrates (α_{sn}).[200, 213, 217, 218, 221] The larger the mismatch, the larger the α_{sn}, and the less nucleation is favored.[200, 213, 217, 218, 221] Because the $CaCO_3$ precipitates and the substrates have different crystal structures, it is challenging to obtain the exact lattice orientation of nuclei on mica/quartz at the molecular level, Therefore, the bond length mismatch was used to approximate the lattice mismatch between the nuclei and substrates.[200, 213] The calculation suggests a smaller O–O bond length mismatch (m) between $CaCO_3$ and mica ($m_{vaterite–mica}$= 11%) than that between $CaCO_3$ and quartz ($m_{vaterite–quartz}$= 19%), which could be the explanation for the smaller energy barrier for the mica system. The extents of hydrophilicity of mica and quartz, as well as the surface charge of mica and quartz powders in experimental conditions, were also tested. However, the results do not explain the more favorable $CaCO_3$ nucleation on mica than on quartz. Further details of the analysis of factors controlling α are available in the Supporting Information Section 5-S11.

5.5 Environmental Implications

Mineral trapping of CO_2 by carbonate precipitation is considered to be the safest trapping mechanism in GCS. The precipitation process can change the fluid chemistry and porosity-

permeability, affecting the fate and transport of CO_2. These processes for GCS can be modeled by reactive transport approaches, which require interfacial and bulk thermodynamic parameters as inputs.[203, 204] However, most of those models do not include nucleation as an explicit step in precipitation, but rather use seeded systems and growth kinetics as approximations. Considering that the size of nucleated $CaCO_3$ particles is comparable to the pore sizes of some rocks in GCS formations, nucleation is crucial in changing media porosity and permeability. Thus, nucleation should be incorporated into reactive transport models. To achieve this, we need to advance our kinetic and thermodynamic knowledge of the nucleation of carbonate minerals in subsurface environments. At GCS sites, pores present different mineralogies as well as topologies, and can serve as important nucleation sites. The interfacial energy, which differs for each mineral, is an important parameter controlling nucleation. Hence, the interfacial energies provided by this study are useful for incorporating nucleation into current reactive transport models as an explicit step.

In this study, we focused on the most abundant carbonate, $CaCO_3$, and obtained effective interfacial energies (α) under ambient conditions. Provided α is not a function of temperature and pressure, these parameters can be applied to GCS modeling. At least three major impacts of $CaCO_3$ precipitation during GCS are expected: First, the permeability of a GCS reservoir can be changed. Based on the new effective interfacial energies ($\alpha_{vaterite–mica}$ = 24 mJ/m^2, $\alpha_{vaterite–quartz}$ = 32 mJ/m^2, $\alpha_{calcite–mica}$= 41 mJ/m^2, $\alpha_{calcite–quartz}$ = 47 mJ/m^2), if the pore throat mainly consists of mica, $CaCO_3$ formation will reduce the pore permeability more significantly than if the dominant mineral in the throat is quartz. Second, the precipitation process can affect the geometry of pore walls by forming different amounts or different quantities and phases of $CaCO_3$. For example, the vaterite surfaces we observed are rougher than calcite surfaces, and they have larger surface area.[222] The geometry and polymorphs of $CaCO_3$ may also be changed after nucleation, by particle evolvement and

possible phase transformations. Third, different polymorphs of $CaCO_3$ may lead to different wettability of the wall surface, which is a critical factor controlling CO_2 transport and trapping.[223-228] For example, the breakthrough capillary pressure of CO_2 is proportional to the cosine of the mineral-brine-CO_2 contact angle measured in brine.[226, 228] Therefore, if the porous media is more hydrophilic (smaller contact angle), higher pressure is needed in the supercritical CO_2 ($scCO_2$) phase to transport $scCO_2$ through the media previously saturated with brine. It is reported that calcite is more hydrophobic than vaterite,[229] and it is known that the hydrophilicity/hydrophobicity is also sensitive to temperature and pressure,[224, 225] as well as surface roughness,[219] which appears different for calcite and vaterite according to our observations. Furthermore, different forms of $CaCO_3$ have different surface energies and mechanical properties,[230] which will change the properties of pore walls if they precipitate. The information reported in this chapter is not only of interest for the geologic CO_2 sequestration community, but to other fields where heterogeneous $CaCO_3$ nucleation is an important process, such as in industrial pipeline scaling, and $CaCO_3$ formation on engineered surfaces or biofilms.

Acknowledgments

The authors acknowledge Dr. Yandi Hu for valuable discussion about the experimental setup and data analysis, Drs. Xiaobing Zuo and Sönke Seifert for helping collect GISAXS data, and Ms. Jessica Ray and Dr. Namhey Lee for helping conducting experiments. We also thank Dr. Carl I. Steefel for insightful discussion about calcium carbonates in GCS field sites. The authors also acknowledge support from the Center for Nanoscale Control of Geologic CO_2, an Energy Frontier Research Center funded by the U.S. Department of Energy, Office of Science, Office of

Basic Energy Sciences under Award Number DE-AC02-05CH11231. Use of the Advanced Photon Source, an Office of Science User Facility operated for the U.S. Department of Energy Office of Science by Argonne National Laboratory, was supported by the U.S. DOE under Contract No. DE-AC02-06CH11357. ISTerre is part of Labex OSUG@2020 (ANR10 LABX56).

Supporting Information for Chapter 5

5-S1. Substrate Preparation

The (001) surface of muscovite sheets (Goodfellow Cambridge Limited, UK) were cut to 10 mm × 10 mm × 0.025 mm pieces. The (100) surface of quartz was chosen based on the previous study.[31, 164] Quartz substrates (roughness < 5 Å) with dimensions of 10 mm × 10 mm × 1 mm were purchased from MTI Corporation (USA). The quartz substrates had a step density of ~10 steps per μm. No preferential precipitation along steps was observed under our experimental conditions. These substrates were cleaned by sonication in acetone, ethanol, and isopropanol, consecutively for 20 minutes each, and sonication in water for 30 minutes. All water used in this study was ultrapure deionized (DI) water (resistivity > 18.2 MΩ·cm). Quartz substrates were further cleaned by soaking in a mixture of sulfuric acid and Nochromix® for 2 hours to remove any possible organic residuals. The cleaned substrates were stored in DI water until used for experiments. Before the experiment, muscovite pieces were glued by epoxy adhesive (DP-100, McMaster-Carr®) to 10 mm × 10 mm × 1 mm clean glass slides, and dried by ultrapure nitrogen gas. For experiments, the prepared substrates were placed in the GISAXS cell.

5-S2. Experimental GISAXS Setup

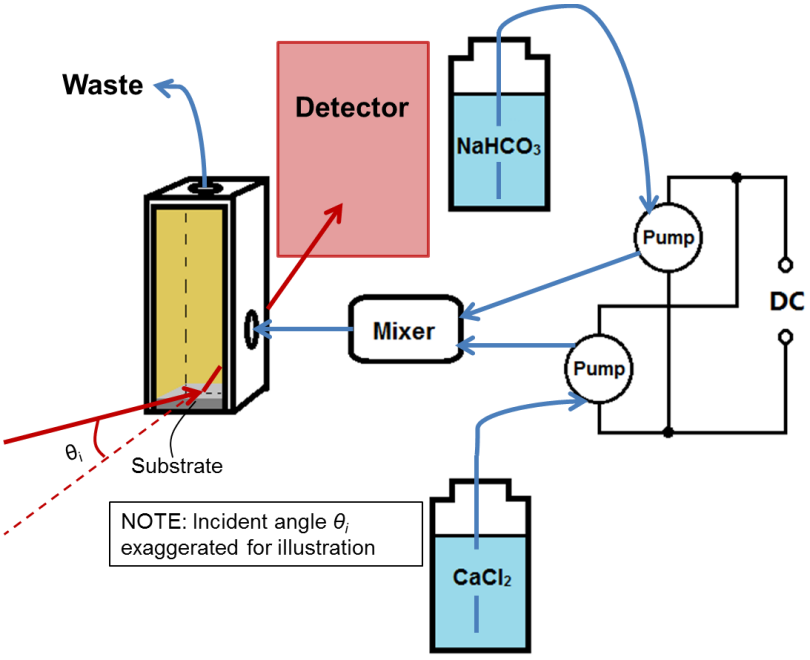

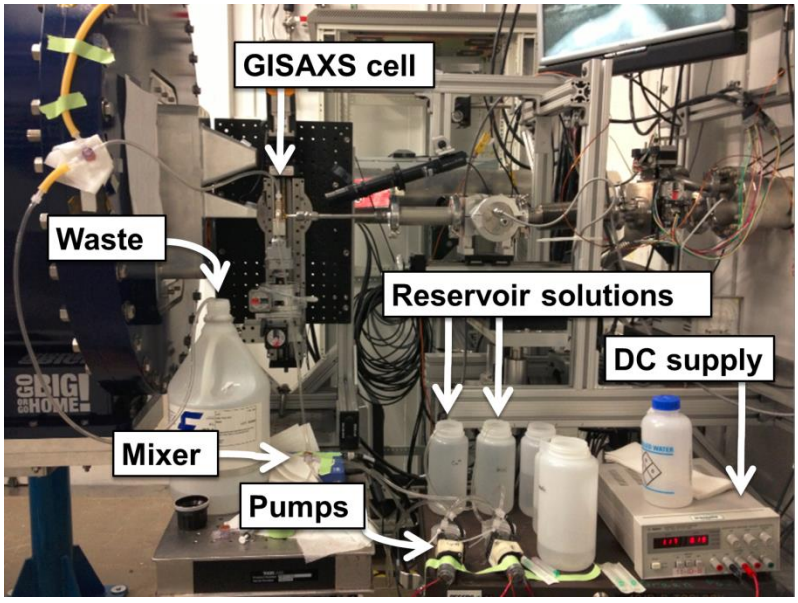

Figure 5-S1 Schematic and picture of experimental setup.

5-S3 Fitting GISAXS Data

Using Eq. 5.1, we fitted intensity data $I(q)$ over the q range from 0.007 to 0.08 $Å^{-1}$, where one distribution was probed and data had a high signal to noise ratio. $\Delta\rho$ remained constant in our system, and there was no necessity to find the absolute $\Delta\rho$ to get the needed information, so we assigned 1 for $\Delta\rho$. $S(q)$ was set as 1 because the system was dilute and no particle interaction was seen from intensity plots. Five parameters—total particle number (N), the mode (μ) and variance (σ^2) of the Schultz distribution D(R), the power law factor (I_{pow}), and the power law slope (p)—were fitted by MatLab (MATLAB R2012a Student Version (32-bit)). Chi-square (χ^2) fitting was used, and the square root of intensity was used as the weighting factor for each data point. The fitting results were accepted if χ^2 was small enough (approximately < ~ 20 for high supersaturations, and < ~5 for low supersaturations), and the resulting parameters followed the trends of adjacent time points. Then the fitted the Schultz distribution D(μ_R, σ_R) was used to calculate the average in-plane radius of gyration by $R_g = \mu_R \sqrt{\frac{3(z+8)(z+7)}{5(z+1)^2}}$, where $z = \left(\frac{\mu_R}{\sigma_R}\right)^2 - 1$. R_g was used as estimates of critical nucleus radii in GISAXS experiments. The resulting total particle number (N) was in arbitrary units (comparable within this study) because $\Delta\rho$ was an assumed number and intensity was not calibrated using standard samples. To the best of our knowledge, a calibration standard for GISAXS intensity has not yet been developed (but will be addressed later in Chapter 7 of this dissertation).

5-S4. Raman Spectra and SEM Images of Vaterite

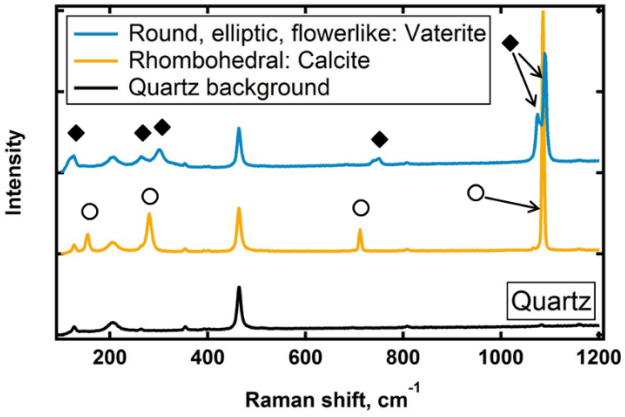

Figure 5-S2 Raman spectra of $CaCO_3$ particles formed on quartz substrates. The rhombohedral particles are calcite, and the other shapes (round, elliptic and flowerlike) are vaterite. No other $CaCO_3$ phases were detected. The peak positions match well with calcite (○) and vaterite (◆) reference spectra.[214] Note that the particles in this figure are likely homogeneously formed and have settled to the substrate.

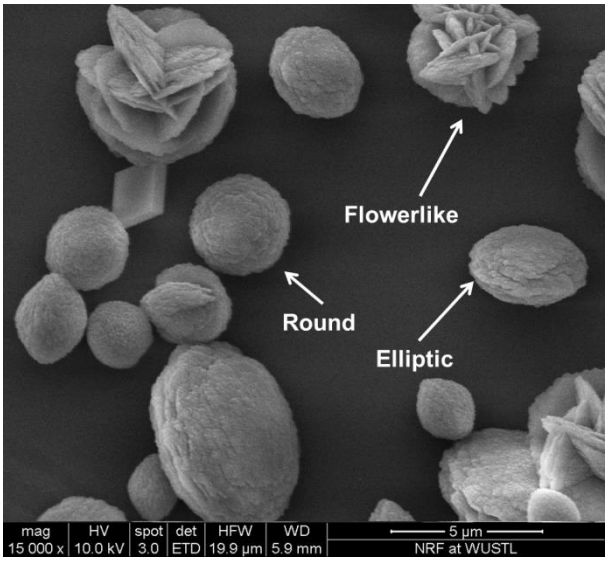

Figure 5-S3 Example SEM image showing different shapes of vaterite formed on substrates, taken from mica under the C1 condition for 2 hours. Vaterite showed several shapes (round, elliptic, and flowerlike, as indicated by arrows). The more complicated shapes appear to be assembled by small, round, flat vaterite units. All vaterite shows the same degree of roughness on the surface. Note that the particles in this figure are likely homogeneously formed and have settled to the substrate.

5-S5 GISAXS 2D Scattering Pattern

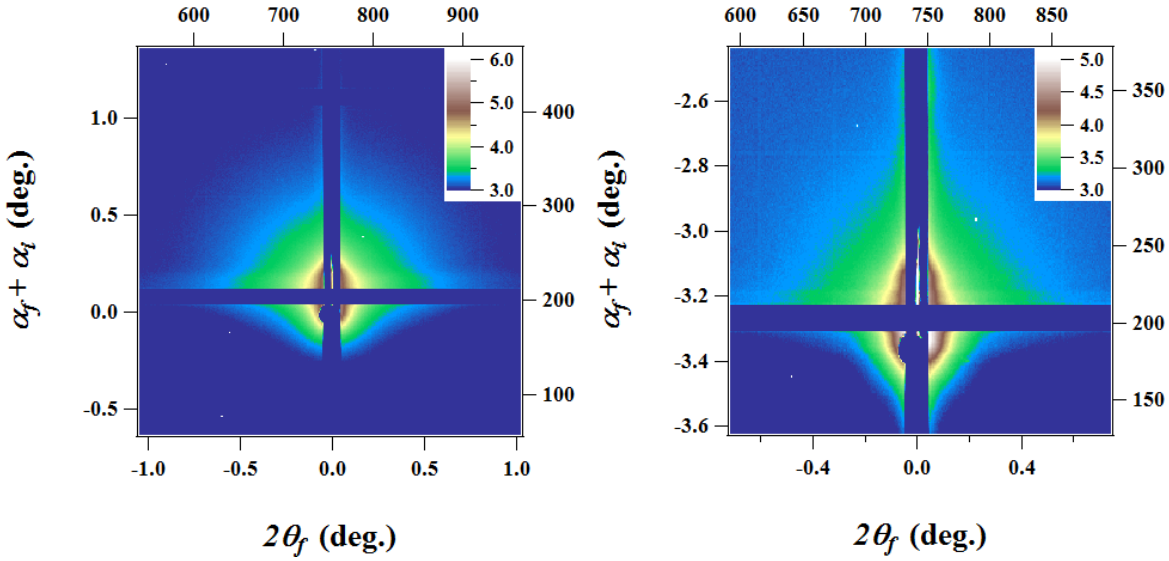

Figure 5-S4 Examples of GISAXS scattering patterns from quartz and mica substrates. Original images are shown, without background subtraction and further processing. The left image is the scattering pattern from the C2 condition on quartz at 60 min. The right image is the scattering pattern from the C3 condition on mica at 160 min. The color contrast is selected to clearly show the scattering pattern. All the patterns are symmetric, and do not show the existence of faceted particles.

5-S6 GISAXS Data for All Experimental Conditions

(a) GISAXS data of particles formed on mica

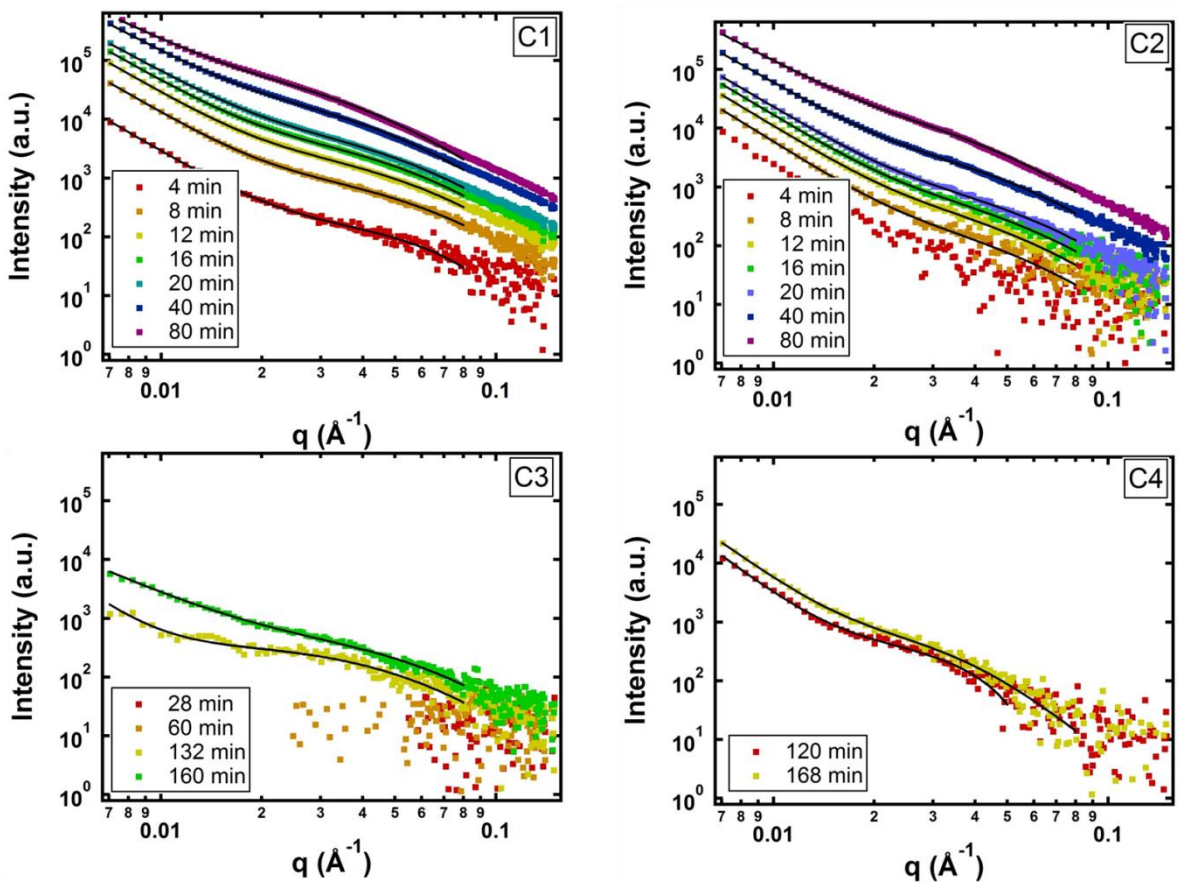

Figure 5-S5a GISAXS data of particles formed on mica. Intensities are obtained from cuts along the Yoneda wing. Solid black lines are the fitted results. Data without solid black lines were early time points that were not able to be fit due to the weak signal given by particles on the substrates. Low saturation figures show only representative time points, thus reducing the overlap of data.

(b) GISAXS data of particles formed on quartz

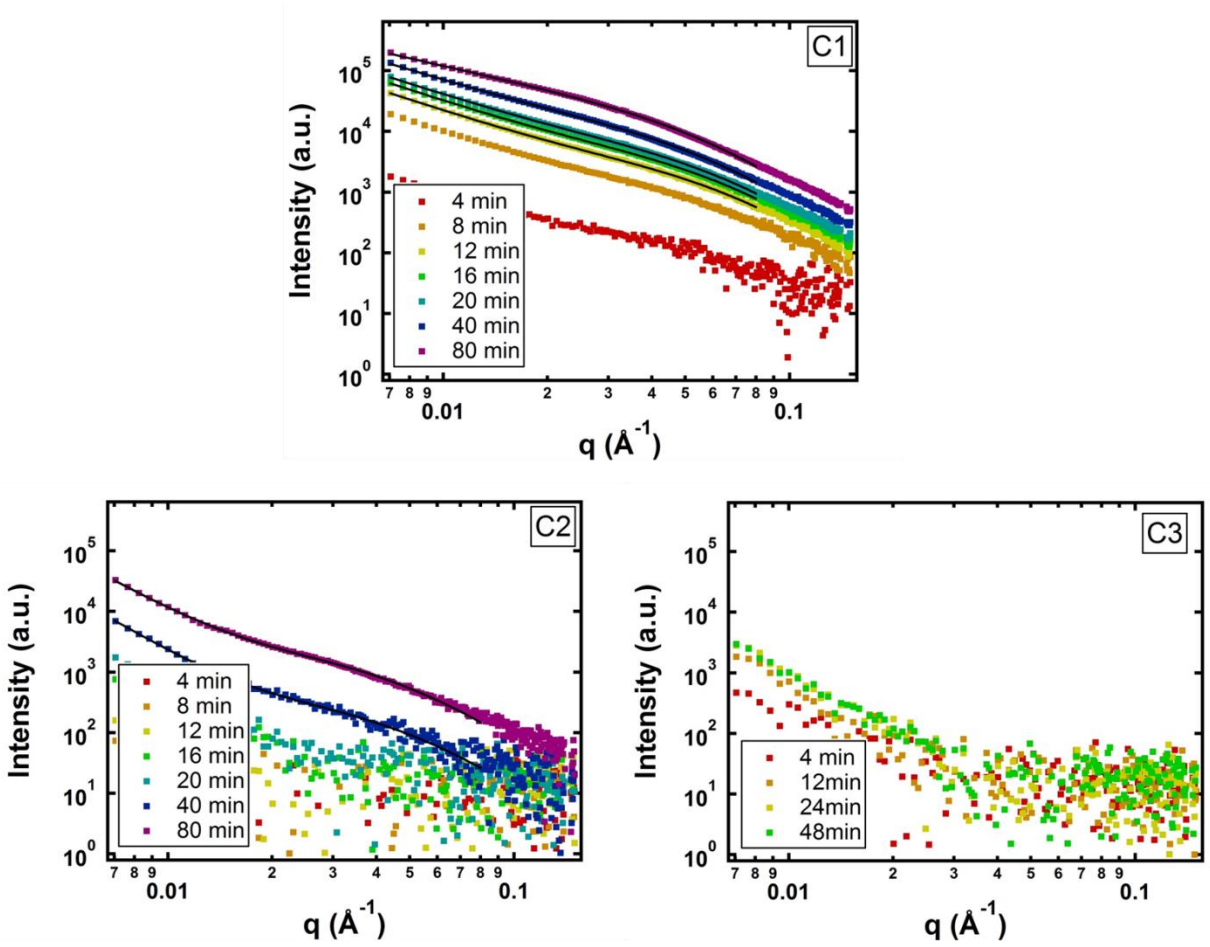

Figure 5-S5 GISAXS data of particles formed on quartz. Intensities are obtained from cuts along the Yoneda wing. Solid black lines are the fitted results. Data without solid black lines were early time points that were not able to be fit due to the weak signal given by particles on the substrates. Low saturation figures show only representative time points, thus reducing the overlap of data.

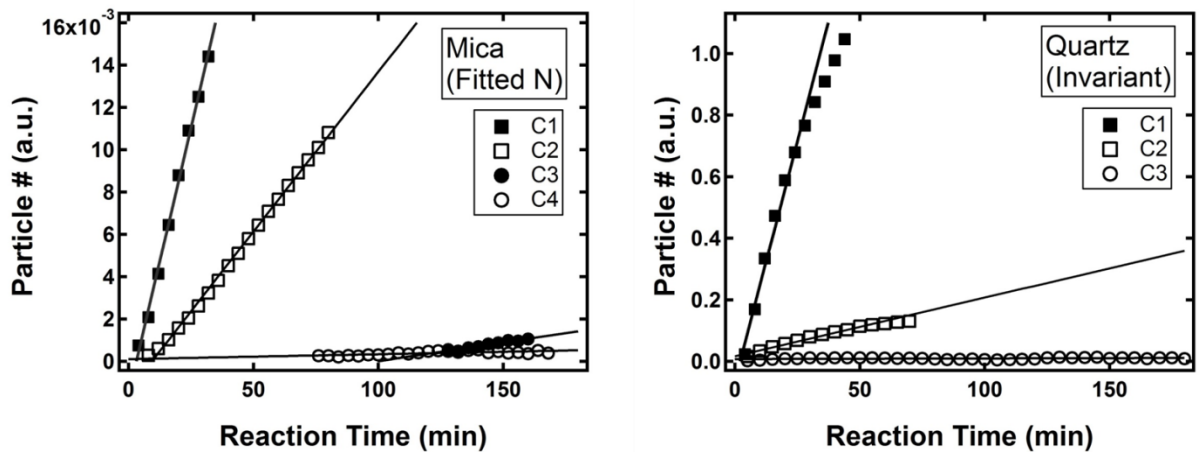

Figure 5-S6 Nucleation rate *J* on mica generated by the fitting method (left figure) and on quartz by the invariant method (right figure).

5-S7 AFM Tip Dimensions and Particle Densities in AFM Images

Probe tips were made of 0.01–0.025 Ω·cm antimony (n) doped silicon. Cantilevers were 115–135 μm long, 30–40 μm wide, and 3.5–4.5 μm thick. Cantilever spring constants were 20–80 N/m, and drive frequencies were 302-336 kHz. The nominal tip radius was 8 nm, and the tip height was 15–20 μm. The front, side, and back angles of the tip were 15 ± 2°, 25 ± 2°, and 17.5 ± 2°, respectively.

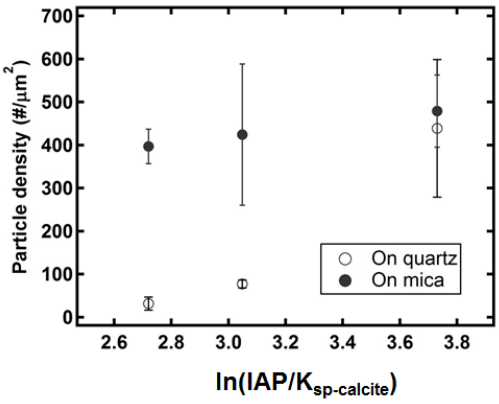

Figure 5-S7 Particle densities on AFM images shown in Figure 5.2 of the main text. Data present the average particle density of four manually counted areas, and error bars are the data range.

5-S8 Comparison among Methods in Obtaining α

Table 5-S1 Comparison of α obtained by the three methods mentioned in the Results section of the manuscript. Results from the invariant method and fitting method are very similar, while values obtained by the particle density method are smaller than values from the other two methods.

	Calcite initial polymorph		Vaterite initial polymorph	
Method \ Substrate	Mica $\alpha_{calcite\text{-}mica}$	Quartz $\alpha_{calcite\text{-}quartz}$	Mica $\alpha_{vaterite\text{-}mica}$	Quartz $\alpha_{vaterite\text{-}mica}$
Invariant	41 ± 4	47 ± 1	24 ± 3	32 ± 4
Fitting	41 ± 2	~51	24 ± 1	~34
Particle density	15 ± 4	36 ± 4	9 ± 5	20 ± 4

5-S9 Uncertainty of α values by GISAXS

Several factors contribute to error in α, and it is useful to know the error range of experimentally generated α values among different laboratories and researchers. Upon comparison with the previous study done by Fernandez-Martinez et al. (2013) with the same system setup, we found three factors that can contribute to the calculated α error. First, the database used in modeling supersaturations will affect the obtained α. This study used GWB with the thermo_minteq database to calculate $\ln(IAP/K_{sp})$. If using Phreeqc Interactive (Version 3.0.0-7430) with the minteq database, which models smaller $\ln(IAP/K_{sp})$ values than those in Table 5.1, the final α can be ~ 5 mJ/m^2 smaller. Although both databases are called minteq, some details are not the same with respect to thermodynamic constants and complexation species. These differences may have caused the difference in $\ln(IAP/K_{sp})$, and later in α.

Second, different systems may have different induction times before the nucleation rate becomes a constant, and the induction time could be affected by the flow rate of the system. The induction time is especially important for low supersaturations because it will help determine which part of the data is used for the linear regression. In Fernandez-Martinez et al.'s previous

study, which used a similar supersaturation range but with a slower stirring rate and slower flow rate (2 mL/min), the induction time for the lowest concentration was about 2–3 hours.[31] However, in the current study, with a faster stirring rate and flow rate (5.6 mL/min), there is no obvious induction within 3 hours. In other words, the induction times were very short. Therefore, faster flow rates generated more perturbation in the system, and this helped to establish a steady-state sooner.

Third, the low supersaturation conditions had weak signals, and thus had a larger error in nucleation rates. Including the low supersaturations in the ln J_n vs. $1/[\ln(IAP/K_{sp})]^2$ regression will result in an error range for α of around 7 mJ/m^2, if not more. The factors above could explain the difference in $\alpha_{\text{calcite-quartz}}$ in Fernandez-Martinez et al.'s previous study (36 mJ/m^2) and this study (47 mJ/m^2). Accounting for the difference arising from choosing GWB thermo_minteq.dat as the database and not including the lowest supersaturations in both studies, the resulting $\alpha'_{\text{calcite-quartz}}$ for both papers are within the range of 44–50 mJ/m^2. In addition, both studies obtained very good reproducibility of α values from separate beamtimes.

5-S10 Conversion from Effective Interfacial Energy α to Absolute Interfacial Energy α_{sn}

The α we measured was the effective interfacial energy in Eq. 5.2. It is a combination of three interfacial energies: the interfacial energy between liquid and substrate (α_{ls}), the interfacial energy between liquid and nuclei (α_{ln}), and the interfacial energy between substrate and nuclei (α_{sn}). For spherical particles, they combine to give α by[31]

$$\alpha = \alpha_{ln} \frac{2(1-\cos\theta)-\sin^2\theta \frac{\alpha_{ls}-\alpha_{sn}}{\alpha_{ln}}}{2^{2/3}(2-3\cos\theta+\cos^3\theta)^{2/3}} \qquad \text{Eq. (5-S1)}$$

where θ is the contact angle of precipitates on substrates. The interfacial energy of calcite ($\alpha_{ln(calcite)}$) in water has been obtained by different methods. However, this data varies much among different methods; the range of $\alpha_{ln(calcite)}$ obtained by nucleation measurement was 32–85 mJ/m^2.[215] We chose this range because we also had the nucleation reaction. For calculations, we assumed a number in the middle of this range, 59 mJ/m^2. However, there is no $\alpha_{ln(vaterite)}$ value provided by similar methods. A comparison of interfacial energy by de Leeuw (1998) via atomistic simulation reported the averaged interfacial energy of hydrated vaterite to be 77% of that of hydrated calcite.[231] So we estimated $\alpha_{ln(vaterite)}$ by multiplying $\alpha_{ln(calcite)}$ by 77% to get $\alpha_{ln(vaterite)}$ = 45 mJ/m^2. We used reported $\alpha_{ls(quartz)}$ = 168 mJ/m^2 and $\alpha_{ls(mica)}$ = 150 mJ/m^2.[232] Then the only parameter needed to calculate α_{sn} is θ, which is hard to measure due to small particle sizes. In Fernandez-Martinez et al.'s study, the contact angle was assumed to be 90°,[31] which might be too simplified to be realistic. At a certain range, varying θ changes the calculated α_{sn} greatly, and thus the value of θ is important. Therefore, we used AFM to measure the height and width of particles with horizontal dimensions of 100–300 nm, and calculated the contact angle according to Figure 5-S8 to represent contact angles of nuclei formed on substrates. The smaller particle measurements (< 30–40 nm) done by AFM do not have accurate lateral dimensions due to the AFM probe's dimensions.[213] In AFM measurements of larger particles, we made two assumptions: First, the contact angles of nuclei do not change while they grow to the particle size range of 100–300 nm. Second, the newly nucleated particles have a spherical shape.

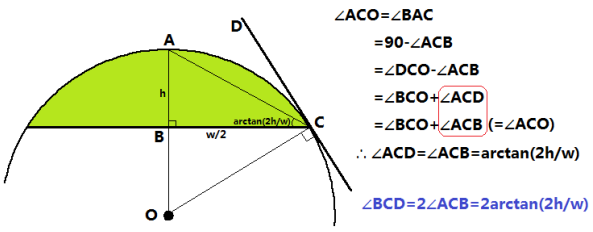

Figure 5-S8 Calculation of contact angle based on particle height (h) and width (w) measured by AFM.

Contact angles of $CaCO_3$ on substrates were 18 ± 7^o on quartz and 9 ± 8^o on mica. These contact angles will generate $\alpha_{vaterite-quartz}$ = 141 mJ/m^2, and $\alpha_{vaterite-mica}$ = 132 mJ/m^2, $\alpha_{calcite-quratz}$ = 136 mJ/m^2, and $\alpha_{calcite-mica}$ = 124 mJ/m^2. For small θ, as measured in this section, varying θ did not affect the results significantly;[31] however the large range of reported α_{ls} and α_{ln} values, especially values obtained by different methods, brings much uncertainty to the calculated α_{sn}. Although estimates of individual interfacial energies are useful to extend nucleation processes into non-aqueous systems, effective α might be a better starting point for aqueous systems, until further refinement of the parameters that α depends upon.

5-S11 Factors Controlling α

In this study, we observed that α significantly influenced heterogeneous precipitation characteristics. It is intriguing to study the factors that lead to such a different α. Such information is meaningful for understanding nucleation regarding other precipitates and other substrates. Lattice mismatch between the substrate and the precipitate, substrate hydrophobicity, and the surface charge of the substrate surfaces can be considered to control the heterogeneous precipitation.[194, 200, 213, 215, 217-220] Therefore, we analyzed these three factors regarding heterogeneous $CaCO_3$ nucleation on mica and quartz.

Lattice mismatch is related to interfacial energy between the precipitates and the substrates (α_{sn}).[200, 213, 217, 218, 221] The larger the mismatch, the larger the α_{sn}, and the less nucleation is favored.[200, 213, 217, 218, 221] A smaller α_{sn} between mica and $CaCO_3$ was calculated in Section 5-S9, so a smaller mismatch between mica and $CaCO_3$ is expected. Because the precipitates and the substrates belong to different crystal structures, and it is challenging to obtain the exact lattice

orientation of nuclei on mica/quartz at the molecular level, bond length mismatch calculations were used to approximate the lattice mismatch between the nuclei and substrates.[200, 213] Data from the MINCRYST database was used to calculate average bond lengths. Bond length mismatch (*m*) is calculated by:[213]

$$\mathrm{m} = \frac{a_A - a_B}{a_B} \times 100\% \quad , \qquad \text{Eq. (5-S2)}$$

where a_A and a_B are the bond lengths in the precipitate and in the substrate. The mismatch between metal–oxygen (M–O) bonds and oxygen–oxygen (O–O) bonds in the precipitates and substrates are shown in Table 5-S2. Because of the uncertain difference between bond length mismatch and lattice mismatch, the mismatch values in Table 5-S2 should not be taken literally. However, the results suggest a smaller mismatch between $CaCO_3$ and mica than that between $CaCO_3$ and quartz. Therefore, compared to the $CaCO_3$–quartz system, the smaller interfacial energy between $CaCO_3$ and mica could have been related to a smaller lattice mismatch between $CaCO_3$ and mica.

Table 5-S2 Calculation of bond mismatch of $CaCO_3$ on mica/quartz substrates. Data are from WWW-MINCRYST.

	O–O, Å	Bond Length mismatch (m)	M–O, Å	Bond Length mismatch (m)
Vaterite	3.1	$m_{vaterite–mica}$= 11% $m_{vaterite–quartz}$= 19% $m_{calcite–mica}$= 18% $m_{calcite–quartz}$= 27%	2.55	$m_{vaterite–mica}$= 54% $m_{vaterite–quartz}$= 58% $m_{calcite–mica}$= 43% $m_{calcite–quartz}$= 47%
Calcite	3.3		2.36	
Mica	2.8		1.65	
Quartz	2.6		1.61	

The extent of hydrophilicity of substrates can control precipitation on different substrates.[194, 233] The hydrophilicity of the quartz and mica substrates was tested by contact angle measurements, and the results were compared with the literature. Both mica and quartz are

hydrophilic. The contact angle of ultrapure water on quartz was 8.6 $\pm$ 0.6^{o}, and the contact angle of mica was 12 $\pm$ 3^{o}, so the surface of mica is slightly less hydrophilic. The contact angle measured from water drops on surfaces is affected by factors such as relative humidity and the macro-flatness of the substrate.[218, 219] In the literature, contact angles of water on mica and quartz have controversial trends due to different surface topologies, origins, and sample treatments.[200, 220, 221] Based on water adsorption experiments and the interfacial energies between mica/quartz and water, a previous study suggested that a mica surface has more affinity for water.[232] There are limited studies of the effects of hydrophobicity/hydrophilicity of the surface on heterogeneous nucleation of $CaCO_3$. Yamanaka et al. (2009) concluded that a hydrophilic surface is more favorable for $CaCO_3$ precipitation, and will result in a smaller contact angle of precipitates on substrates.[194] In our study, we have observed favorable $CaCO_3$ nucleation on mica, and the particles on mica have smaller contact angles than those on quartz. According to Yamanaka et al., mica is expected to be more hydrophilic, which is opposite from our water contact angle measurements showing mica is less hydrophilic. This inconsistency is likely due to the close similarity in hydrophilicity of mica and quartz.

Surface charges could be another factor that controls heterogeneous precipitation.[200] The surface charge of the (001) surface of mica and the (100) surface of quartz is hard to acquire. So, to find zeta potentials, we tested mica and quartz powders ground from the substrates we used in GISAXS experiments as an approximation. The mica and quartz powders were ultra-sonicated in solutions with 0.08 M ionic strength (0.01 M $NaHCO_3$ + 0.07 M NaCl) and adjusted to pH 7.7, which was close to experimental solution conditions. After centrifuging, the supernatants of both solutions were injected into zeta potential cells and measured by a Zetasizer instrument (Nano ZS, Malvern Instruments Ltd.) at room temperature. The zeta potentials were -26.9 ± 0.9 mV and -

35.5 ± 0.8 mV for mica and quartz, respectively. The slightly more negative zeta potential of the quartz surface suggests that quartz could attract more Ca^{2+} ions, which favors precipitation. However, we have observed less precipitation on quartz. Therefore, the zeta potential difference does not support a smaller interfacial energy for $CaCO_3$–mica.

Overall, the difference in bond length mismatch explains the difference of α_{sn} between mica and quartz with $CaCO_3$. The extents of surface hydrophobicity of mica and quartz surfaces are very similar, and their influence on heterogeneous precipitation is unclear. The surface charge of mica is more negative than that of quartz under our experimental conditions, and thus does not explain the smaller energy barrier on mica related to a smaller α.

Reproduced with permission from [Qingyun Li, Alejandro Fernandez-Martinez, Byeongdu Lee, Glenn A. Waychunas, and Young-Shin Jun. Interfacial Energies for Heterogeneous Nucleation of Calcium Carbonate on Mica and Quartz. *Environmental Science & Technology*, 2014, 48 (10), 5745-5753.] Copyright [2014] American Chemical Society.

Chapter 6: High Salinity Promotes $CaCO_3$ Nucleation on Quartz: Investigation of Interfacial Energies and Kinetic Factors

Results of this chapter have been submitted to a peer-reviewed journal.

Abstract

Nucleation of solid phases from supersaturated aqueous phases is affected not only by solid chemistries (Chapter 5) but also by aqueous chemistries. This chapter presents our study on effects of salinity on $CaCO_3$ nucleation on quartz. *In situ* grazing incidence small angle X-ray scattering was used to obtain the nucleation rates of $CaCO_3$ at different supersaturations ($IAP/K_{sp(calcite)}$ = $10^{1.40}$–$10^{2.00}$) and NaCl-adjusted ionic strengths (0.15–0.85 M salinity). The obtained data were used to calculate the effective interfacial energy (α) for each salinity. The α value changed from 48 mJ/m^2 at 0.15 M salinity to 35 mJ/m^2 at 0.85 M salinity. The reduction in α was due to decreased water–$CaCO_3$ interfacial energy as well as decreased $CaCO_3$–quartz interfacial energy. This study also experimentally showed that the kinetic factor in the nucleation rate equation was ~13 times smaller at high salinities than at low salinities. Combining the thermodynamic and kinetic factors, we found that nucleation rates increased with increasing salinity most obviously at low supersaturations, but barely varied at high supersaturations. In addition, high salinity also favored smaller nuclei and a shorter induction time. The findings from this study provide new kinetic and thermodynamic parameters and valuable insights applicable to complex natural and engineered systems with varying salinities.

6.1 Introduction

Nucleation of nanoscale particulates is an important process in nanomaterial synthesis, biomineralization, and geomedia alteration.[234-237] Investigation of nucleation often employs minerals commonly found in nature and engineered systems, which have comparatively available thermodynamic and kinetic parameters.[198, 235, 236, 238, 239] Calcium carbonate is one of the most frequently used model materials for nucleation studies. It is environmentally abundant in biotic and abiotic systems, and it has important applications in industry, both beneficial, such as manufactured medicines or pollutant remover, and detrimental, such as pipe scales or membrane fouling in desalination processes. In addition to nucleation, $CaCO_3$ has also been investigated to improve our knowledge of growth pathways,[24, 25] phase transformation,[27, 199] aggregation or coagulation,[28] and epitaxial attachment.[29] Information about $CaCO_3$ formation can provide new insights for general solid phases, such as inorganic nanoparticles, biomaterials, and secondary precipitates in formation rocks during energy-related subsurface operations, e.g., geologic CO_2 sequestration.

The formation of $CaCO_3$ can be expressed by a simple equation

$$Ca^{2+} + CO_3^{2-} \rightarrow CaCO_3\,(s). \qquad \text{Eq. (6.1)}$$

Although this equation is thermodynamically favorable when the solution is supersaturated with respect to the $CaCO_3$(s) phase, the surface energy of a nanometer-sized nucleus tends to destabilize the nucleus.[61, 162] Therefore, the positive surface energy of the smallest nucleus, or critical nucleus, has to be balanced by the negative bulk free energy of Eq. 6.1 in order for the nucleus to stay in the solid phase and to proceed with further precipitation processes (growth, aggregation, ripening, and phase transformation). The nucleation process can happen in solution

(homogeneous nucleation) with the water–nucleus interfacial energy as the controlling factor, or it can happen heterogeneously on a substrate surface (heterogeneous nucleation), where the effective interfacial energy, which reflects the interplay of water–nucleus, water–substrate, and nucleus–substrate interfaces, needs to be collectively considered.

The nucleation rate can be expressed by Eq. 6.2 [30, 162]

$$J = J_0 \exp\left(-\frac{\Delta G^*}{kT}\right) = J_0 \exp\left(-\frac{16\pi v^2 \alpha^3}{3k^3T^3[\ln\left(\frac{IAP}{K_{sp}}\right)]^2}\right) \quad \text{Eq. (6.2)}$$

where J_0 is a kinetic factor related to the efficiency of building blocks diffusing and attaching to an existing nucleus, and ΔG^* is the thermodynamic barrier generated by the combination of the bulk reaction free energy of Eq. 6.1 and surface energies. ΔG^* is expanded into $\frac{16\pi v^2 \alpha^3}{3k^2T^2\left[\ln\left(\frac{IAP}{K_{sp}}\right)\right]^2}$, where v is the molecular volume of the nucleating phase, α is the effective interfacial energy, k is the Boltzmann constant (1.38×10^{-23} J K^{-1}), T is temperature (K), IAP is the ion activity product, and $K_{sp}$is the solubility product of the nucleating phase. In this expansion of ΔG^*, $-kT\ln\left(\frac{IAP}{K_{sp}}\right)$ is the bulk free energy of Eq. 6.1 on a molecular basis, $\frac{IAP}{K_{sp}}$ represents the supersaturation extent of the solution, and 16π/3 is a geometric factor from the derivation of the nucleation equation for homogeneously formed spherical nuclei which have an interfacial energy with the liquid phase of α_{ln} (subscript l for liquid and n for nucleus)[61]. For heterogeneous nucleation, if 16π/3 is still used for convenience of comparison between homogeneous and heterogeneous nucleation, α in Eq. 6.2 is then a function of the nucleus geometry and the interfacial energies among the liquid, nucleus, and substrate ($\alpha = \alpha$(nucleus geometry, α_{ln}, α_{ls}, α_{ns})), in which the subscripts l, n, and s denote liquid, nucleus, and substrate, respectively. To enable mathematical feasibility, the derivation of

Eq. 6.2 was based on an imaginary pathway in which nuclei continuously evolve by adding monomers one at a time. This pathway is often referred to as the classical nucleation pathway. Despite the discovery of more realistic pathways, such as those in which pre-nucleation clusters aggregate to form initial nuclei,[198, 235, 236, 240, 241] Eq. 6.2 has been repeatedly found to successfully capture the experimentally observed nucleation rates under various conditions.[30-33, 35, 164, 236, 242] Therefore, it is used to investigate the factors affecting the nucleation of $CaCO_3$ as well as other phases, especially the effects of interfacial energies. For example, Giuffre et al. and Hamm et al. showed that the interfacial energy was a controlling factor for heterogeneous nucleation on self-assembled monolayers,[32, 35] Fernendez-Martinez et al. and Li et al. experimentally obtained the values of interfacial energies and proved their controlling role in heterogeneous $CaCO_3$ nucleation on quartz and mica.[31, 164] Yamanaka et al. found that $CaCO_3$ can be nucleated more easily on hydrophilic than hydrophobic substrates,[195] and Baumgartner et al. found that interfacial energy was critical for magnetite formation.[236] Information relating to substrates and nuclei is useful in that it provides valuable information for nuclei formation where substrate surfaces are abundant and critical. However, the effects of aqueous conditions have been less investigated, although the effective interfacial energy includes the interaction of liquid–nucleus and liquid–substrate interfaces, as well as nucleus–substrate interfaces which are also affected by aqueous conditions. In several previous studies, an increase in salinity enhanced homogeneous nucleation and growth rates of $CaCO_3$ due to the catalytic effects of salinity.[34, 243, 244] On the other hand, other studies reported unchanged or reduced nucleation rates of $CaCO_3$ due to a decrease in ion activities.[245] However, all of these previous salinity studies were based on indirect observations of nucleation from analysis of bulk solution chemistries, and were based on homogeneous nucleation, which has a much higher nucleation energy barrier than heterogeneous nucleation.

In this study, we used $CaCO_3$ as a model phase, and investigated its heterogeneous nucleation on an environmentally abundant, quartz, as the substrate. Because of the difficulty in identifying polymorphs of the nuclei with several nanometer radii, we used thermodynamic data for calcite to enable calculations. Results calculated from vaterite data are available in the Supporting Information (Figure 6-S4). The effects of salinity were investigated, and the salinity was represented as ionic strength in units of molarity (M). Four salinities were chosen, spanning the range of groundwater, seawater, and saline formation water.[207, 246] At each salinity, we were able to obtain an effective interfacial energy by regression of nucleation rates as a function of supersaturation according to the logarithmic form of Eq. 6.2:[31, 164]

$$\ln(J) = \ln(J_0) - \frac{16\pi v^2 \alpha^3}{3k^3T^3\left[\ln\left(\frac{IAP}{K_{sp}}\right)\right]^2} \qquad \text{Eq. (6.3)}$$

By fixing the nuclei and substrate materials, we were also able to compare the kinetic factors (J_0), which have been unclear for nucleation in multicomponent aqueous systems.[33, 164, 247] The obtained information is useful for various applications, including mineral trapping of CO_2 sequestration, (bio)mineralization in aquatic systems with various salinity, and formation of amorphous or crystalline materials under engineered aqueous conditions. The obtained thermodynamic and kinetic parameters not only improve the current understanding of nucleation mechanisms, but also serve as valuable references for parameter estimations in numerical predictive models. The comparison of kinetic and thermodynamic contributions, which were scarce in the past, highlights the importance of kinetic contributions at high supersaturations. Such saturation conditions are likely to happen in many subsurface geomedia (such as in concrete/cement) and engineered systems (such as materials synthesis). In this sense, the

kinetic/thermodynamic comparison is a promising starting point for investigation of the kinetic factor, which is expected to further guide the related science and technology.

6.2 Materials and Methods

6.2.1 Substrate Preparation

Quartz substrates with (100) planes were chosen for this study due to their environmental abundance. Atomicly flat (roughness < 5 Å) substrates were purchased from MTI Corporation (USA) and were cut into 1 cm by 1 cm squares to fit into our flow-through reaction cells. The substrates were cleaned by sonicating them in acetone, ethanol, isopropanol, and ultrapure deionized water (DI water, > 18.2 MΩ/m) sequentially for 20 min each. The substrates were then soaked in concentrated sulfuric acid with dissolved Nochromix® for 2 hours to remove any remaining organic contaminants. After the substrates were taken out from the sulfuric acid, they were rinsed thoroughly with DI water and stored in DI water.

6.2.2 GISAXS Experiments

In situ observations of $CaCO_3$ nucleation were carried out using grazing incidence small angle X-ray scattering at the Advanced Photon Source (Sectors 12-ID-B and 12-ID-C) at Argonne National Laboratory (USA). A flow-through system, as used in our previous study, was set up in beamline 12-ID-B and 12-ID-C.[164] The reservoir solutions of $NaHCO_3$ and $CaCl_2$ were injected into a mixer using two peristaltic pumps (WPX1-F1/8S4−C, Welco Co. Ltd., Tokyo, Japan) at the same volumetric speed to form a supersaturated solution. Upon mixing, the supersaturated solution was pumped into a reaction cell with a quartz substrate located at the bottom. The flow speed was 5.6 mL/min, and the excess solution was continuously removed from the top of the cell.

Four salinities, 0.15 M, 0.30 M, 0.50 M, and 0.85 M, were tuned with NaCl and represented by ionic strengths. At each salinity, three supersaturations (IAP/K_{sp} equal to $10^{1.40}$, $10^{1.65}$, and $10^{2.00}$) were used to obtain effective interfacial energies. The ratios of the concentrations of $CaCl_2$ to $NaHCO_3$ were fixed in the range of 4–5, and were increased proportionally to maintain the same supersaturation at a high salinity. Under these aqueous concentrations, concentrations of Ca^{2+} were expected in the saline formation water,[207] and the concentrations of HCO_3^- were set to obtained nucleation reasonable for *in situ* GISAXS observations. Detailed concentrations of the mixed supersaturated solution are shown in Table 6-S1 in the Supporting Information. All aqueous condition calculations were carried out using Geochemist's Workbench (GWB, Release 8.0, RockWare, Inc.), with the thermos_minteq database and B-dot activity coefficient equations. All supersaturations were undersaturated with respect to amorphous calcium carbonate ($K_{sp(ACC)}=10^{-6.40}$).[32, 209] GISAXS observations showed that all heterogeneous nuclei were round and without faceted surfaces. Example GISAXS 2D images are shown in the Supporting Information (Figure 6-S3). The thermodynamic data of calcite were used throughout this study to calculate the supersaturations. The formation of metastable vaterite nuclei was a possibility, but the trend obtained using thermodynamic data of other polymorphs would be the same but with different absolute values.[164]

A focused 14 keV X-ray beam was incident at an angle of 0.11° on the quartz substrate (100) surface. The beam passed through Kapton windows on the cell walls and scattered by the nuclei formed on the surface. This incidence angle is slightly lower than the critical angle of quartz. A detector 2 m away from the sample cell recorded scattering intensities within a q range of 0.005 to 0.4 $Å^{-1}$, where q is the magnitude of the scattering vector. The scattered X-rays were captured on the detector, most obviously within a horizontal zone called the Yoneda wing.[31, 164, 197, 200, 242,

[248-250] Intensities within the Yoneda wing were averaged for each q value. Intensities at q = 0.3–0.4 $Å^{-1}$ were from constant background scattering only, and were used as an internal standard to calibrate the intensities of all images. After this calibration, the data from the first image of each sample were used as the background, and subtracted from data of later time points. Plots of background–subtracted intensity (I) versus q were used to analyze horizontal nuclei sizes as well as the numbers of particles formed on quartz. The scattering vector (q) is inversely related to the lateral particle radius (r), and the scattering intensity is proportional to the number of particles. Therefore, by fitting the scattering intensity data according to nanoparticle' X-ray scattering theory,[164, 251] we were able to obtain information about the size and number of particles formed on the substrates,[31, 197, 200, 248-250] as will be further discussed in the following subsection on nucleation theory.

6.2.3 Interfacial Energy Acquisition

Eq. 6.3 can be written as

$$\ln(J) = \ln(J_0) - B \cdot \frac{\alpha^3}{[\ln\left(\frac{IAP}{K_{sp}}\right)]^2} \qquad \text{Eq. (6.4)}$$

where B is calculable from known values of υ, k, and T, and $B{\cdot}\alpha^3$ is the slope obtained from linear regression of ln J over $1/[\ln(IAP/K_{sp})]^2$. Because aqueous environments at the same salinity are similar, the J_0 value is assumed constant at a fixed salinity, and α can be calculated for that salinity. To obtain a nucleation rate, the invariants were calculated. The invariant (Q) is a value proportional to the total scattering volume on the surface, and is here calculated for q range with an acceptable signal-to-noise ratio (q = 0.01–0.1 $Å^{-1}$) according to $Q = \int I(q)q^2 \mathrm{d}q$. In terms of calculating the nucleation rate, our previous studies proved that under similar conditions, nuclei can be considered as having roughly constant volume (i.e., unchanged size distribution) under all conditions.

Therefore, the calculated scattering volume can be treated as proportional to the total particle number on the substrate.[164] The time point at which the invariant value changed from virtually zero to a linearly increasing trend was taken as the induction time, and the rate of increase of the invariant values (i.e., nucleus numbers) per unit time in the linear range was taken as the nucleation rate (Figure 6-S2). The nucleation rates are presented in arbitrary units (a.u.), and are comparable throughout this study.

6.2.4 Atomic Force Microscopy (AFM)

To directly observe nuclei on the surface at nanoscale, we supported the GISAXS results by *ex situ* AFM (Veeco Inc.) tests for Condition 1 (salinity = 0.15 M, $IAP/K_{sp} = 10^{1.40}$) and Condition 10 (salinity = 0.85 M, $IAP/K_{sp}=10^{1.40}$) listed in Table 6-S1. These two conditions had significant differences in the GISAXS results, and were also within the optimal supersaturation range for AFM tests.[164] Quartz substrates were reacted in the same way as in the GISAXS experiments. After 135 min reaction time, the substrates were taken out of the cell and rinsed with anhydrous ethanol, then immediately and thoroughly dried with high purity nitrogen. AFM images were taken within 3 hours after the substrates were taken out of the cell. Tapping mode was used to collect images, with probes purchased from Bruker (Model: RTESP, Part: MPP-11100-10).

6.2.5 Test of Interfacial Energy Changes

Since α is an effective value for the overall system, it is desired to de-convolute α with respect to the change of interfacial energies of the liquid–nucleus (α_{ln}), liquid–substrate (α_{ls}), and nucleus–substrate (α_{ns}). We experimentally tested changes of α_{ln} and α_{ls} under varied experimental conditions. Contact angle analyzer (Model: Pheonix-300, Surface Electro Optics) was used to measure the contact angle of water with different NaCl concentrations (0.15, 0.3, 0.5, and 0.85 M)

on quartz and calcite. Calcite was used to represent the $CaCO_3$ phase because it is the only polymorph of $CaCO_3$ that can generate good cleavage that is large enough for contact angle tests.

Quartz substrates were prepared in the same way as those used for GISAXS experiments. The quartz surfaces were dried with high purity nitrogen gas for contact angle measurements. Because our quartz substrates were atomically flat and produced only small deviations, only three tests were needed for reliable statistics at each salinity. Natural calcite Iceland spar crystals were purchased from Ward's Science. Because natural calcite has significant natured deviations among different specimens, we generated 20 pieces of small cleaved pieces from adjacent locations within one spar to minimize sample deviation. Before each test, the calcite substrates were cleaned by sonicating them in acetone and water for 5 min each, then dried with nitrogen thoroughly and equilibrated at room humidity for 1–2 hours. At each salinity, at least 10 contact angles were tested on different pieces of calcite. The contact angle of DI water on calcite was the same before and after all tests, indicating there were no calcite surface dissolution influences on test results.

To calculate water–quartz and water–$CaCO_3$ interfacial energy changes, the water–air interfacial energy is also needed, and this was measured using a tensiometer (K10ST, Kruss). The contact angle of water on a solid (substrate or nuclei) surface is expressed by Young's equation:

$$\cos\theta = (\alpha_{as} - \alpha_{ls})/\alpha_{al}, \text{ or} \qquad \text{Eq. (6.5a)}$$

$$\cos\theta = (\alpha_{an} - \alpha_{ln})/\alpha_{al} \qquad \text{Eq. (6.5b)}$$

where the subscript *a* is for air. The subscripts *s*, *n*, and *l* are for the substrate (quartz), nuclei ($CaCO_3$), and liquid, as defined along with explanation of Eq. 6.2.

When contact angles are measured with different salinity in water droplets, α_{as} or α_{an} does not change, and thus the change of (α_{as} – α_{ls}) or (α_{an} – α_{ln}) is due to a change of α_{ls} or α_{ln},

respectively. The increase of α_{ls} (or α_{ln}) at a salinity compared to reference salinity is calculated by $(cos\theta \times \alpha_{al})_{ref}$ - $(cos\theta \times \alpha_{al})_{measure}$. In this study, the reference salinity was set as 0.15 M.

6.2.6 Zeta Potential (ζ) Measurements

In an aqueous environment where $CaCO_3$ forms on quartz, electrostatic interactions between quartz and $CaCO_3$ or among $CaCO_3$ particles are useful for analyzing the system. Therefore, zeta potentials were obtained for $CaCO_3$ and quartz under all conditions listed in Table S6-1. Powders of $CaCO_3$ and quartz were ground and separately suspended in DI water. After centrifuging, the colloidal supernatants containing small particles of quartz or calcite were collected. Five mL of solutions with conditions listed in Table 6-S1 were freshly made for each ζ test by mixing $CaCl_2$ stock solution， $NaHCO_3$ stock solution, and DI water. In making each solution, 0.5 mL of DI water was replaced by the previously mentioned supernatant with either $CaCO_3$ or quartz particles. One mL of the freshly mixed solution was injected into a zeta cell (DTS1060C, Malvern Instruments), and the zeta potential was obtained at 25 ^{o}C.

6.3 Results and Discussion

6.3.1 Smaller Effective Interfacial Energy and Faster Nucleation at High Salinity

The system's interfacial energy, α, was reduced at high salinities, resulting in increased nucleation rates at a fixed supersaturation. Compared in Figure 6.1, the interfacial energy of the system is ~48 mJ/m^2 for 0.15 and 0.3 M salinity, but decreases to ~35 mJ/m^2 for 0.5 and 0.85 M. Correspondingly, the nucleation rates are increased at 0.5 and 0.85 M salinity, compared to those at 0.15 and 0.3 M salinity. However, this enhancement is more obvious for lower supersaturations.

For example, at the lowest supersaturation (IAP/K_{sp}=$10^{1.40}$), the nucleation rate is ~18 times faster at 0.85 M than at 0.15 M, but is almost the same at a high supersaturation of IAP/K_{sp}=$10^{2.00}$.

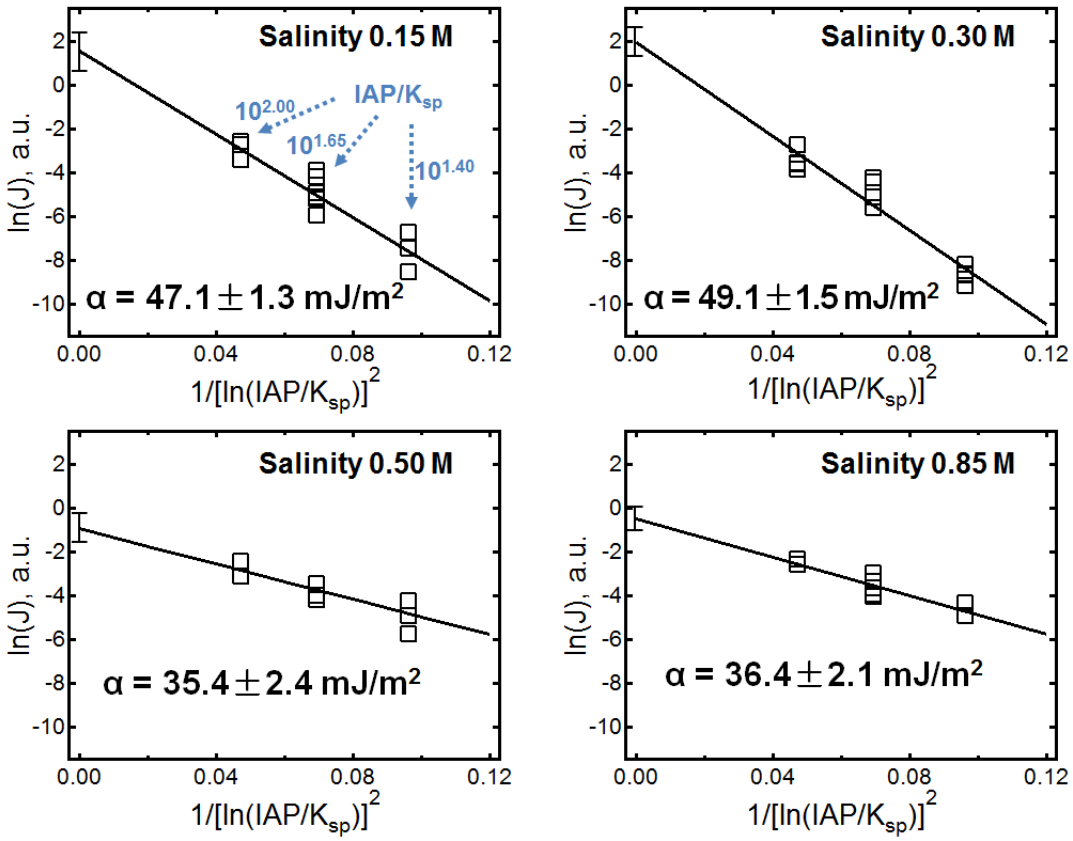

Figure 6.1 Regression of ln(J) on 1/[ln(IAP/K_{sp})]^2 and the calculated interfacial energies at different salinities according to Eq. 6.3. In each figure, from left to right on the x-axis, the data points are for IAP/K_{sp} = $10^{2.00}$, $10^{1.65}$, and $10^{1.40}$. The y-axis indicates the logarithm of the nucleation rate. The intersection with the ln(J) axis is the logarithm of kinetic factor J_0 in Eq. 6.2. At a high salinity, the interfacial energy decreases, and thus the nucleation rate increases. This is evidenced by the higher y-axis values at a fixed x-axis value in the figures in the lower row compared to those in the upper row of figures. This trend is the most obvious at low supersaturations. At high supersaturations, the nucleation rates at high salinity are almost the same as those at low salinity, because the kinetic factor is lower at high salinity. Error ranges are standard deviations from the regression uncertainties of the slope and intersection.

6.3.2 Smaller Nuclei and Shorter Induction Time at a High Salinity

The elevated salinity also caused appreciable nucleation behavior differences other than nucleation rates, including differences in nucleus size and induction time. As shown in the intensity

(I)–scattering vector (q) plots in Figure 6.2, at supersaturation of IAP/K_{sp}=$10^{1.65}$, an optimal condition to observe comparisons using GISAXS, the smallest particle lateral radius was 4.3 ± 0.2 nm for 0.15 M salinity and 3.8 ± 0.3 nm for 0.85 M salinity. The nucleus size for 0.85 M salinity increased slightly to 4.3 ± 0.7 nm at 80 min reaction time, but the nucleus size did not appreciably increase under all other conditions. For higher supersaturations ($IAP/K_{sp} = 10^{2.00}$), the slightly smaller lateral radii for high salinities was not obvious because of their small nucleus sizes, which are difficult to observe. For lower supersaturation ($IAP/K_{sp} = 10^{1.40}$), the nucleus sizes are hard to obtain through GISAXS fitting due to low signal-to-noise ratio, but they can be compared visually in *ex situ* atomic force microscopic (AFM) images in Figure 6.3 (corresponding GISAXS plots are shown in Figure 6-S1). Despite the uncertainty of the absolute values of the lateral dimensions of the nuclei caused by the AFM tip radius (10 nm), the images in Figure 6.3 still suggest smaller nuclei at high salinity. The smaller radius at a higher salinity is attributed to the smaller α at high salinity. For homogeneous nucleation, assuming a spherical nucleus, the smallest nucleus radius (critical nucleus radius) is expressed as $r_c = \frac{2v\alpha_{ln}}{kT\ln(IAP/K_{sp})}$, and is proportional to the liquid–nucleus interfacial energy. For heterogeneous nucleation, as in this study, the relationship of r_c to the α_{ln}, α_{ls}, and α_{ns} is much more complicated, and can hardly be expressed analytically. Still, r_c is positively related, though not strictly proportional, to the effective interfacial energy. In our experiments, the nuclei sizes were continuously monitored from the beginning of the experiments at 2 min intervals, much shorter than the time required for observable growth of the nuclei, so the smallest lateral radii observed approximate r_c. We obtained a smaller effective interfacial energy for high salinity, and therefore, at high salinities, the initially observed nucleus sizes were expected to be smaller.

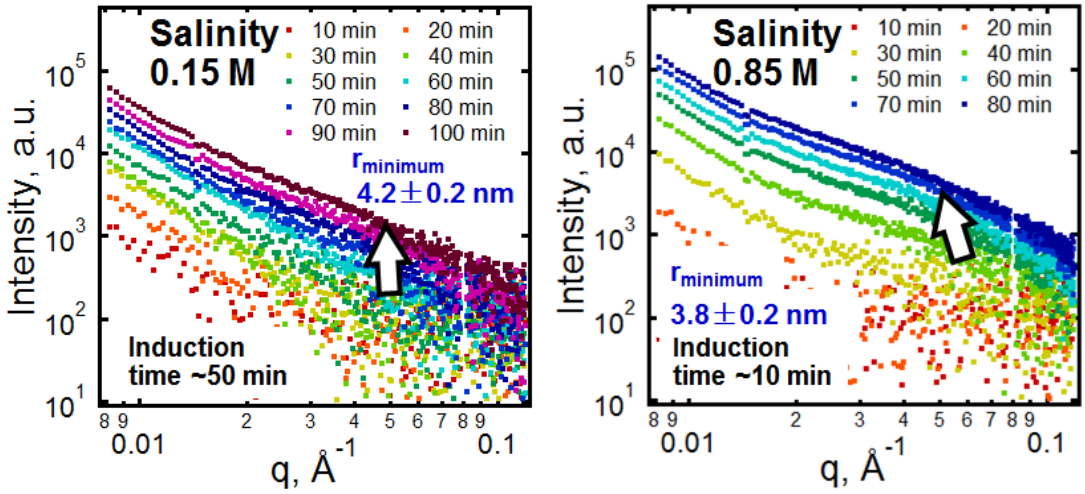

Figure 6.2 GISAXS data for salinities of 0.15 and 0.85 M at a fixed supersaturation of $IAP/K_{sp}=10^{1.65}$. In this condition, GISAXS shows the most clear comparison at different salinities. The intensity at large q results from small particles, and the intensity at low q originates from large particles. In these images, intensities in the q range of 0.02–0.1 correspond to the heterogeneous nuclei we focus on, and the slight bend in the scattering plots indicates the q value corresponding to radius of gyration of the nuclei. Arrows in the figure indicate the evolution of the main q position. At the fixed supersaturation, the high salinity system has a faster increase of intensity, corresponding to a faster nucleation rate. Also, the intensity starts to increase after a shorter induction time. The high salinity system has slightly smaller nuclei.

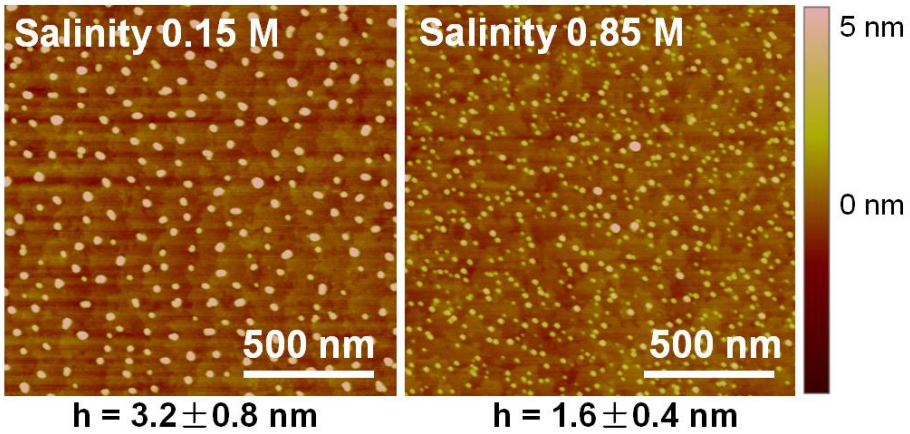

Figure 6.3 AFM height images at 0.15 and 0.85 M salinity and a fixed supersaturation of $IAP/K_{sp} = 10^{1.40}$. This condition yields optimal AFM scans of nuclei to clearly show that nuclei in high salinity are smaller than those in low salinity. The height of the particles is an average from 100 particles, and the error ranges are the standard deviations of the height.

Induction time is defined as the time period before nucleation rates are appreciable and constant, and is roughly reciprocal to the nucleation rate.[61] The alteration of induction time is most obvious at our lowest supersaturation ($IAP/K_{sp}=10^{1.40}$), where nucleation rates were comparatively slow. When the salinity was 0.15 M, the induction time was 120 min, while when the salinity increased to 0.85 M, the induction time was only 25 min. The shorter induction times at high salinity are also seen at higher supersaturations, as in Figure 6.2 for $IAP/K_{sp}=10^{1.65}$. The induction time is an important factor in particle synthesis and engineering systems. For example, the optimal retention time can be fine-tuned according to the salinity change in a chemical reactor. In another example, the mineralization of a supersaturated solution in porous media will start after a longer transport distance when the induction time is longer.

6.3.3 Changes of Water–Quartz, Water–Calcite, and Calcite–Quartz Interfacial Energies

The mechanism of the change in the α value is embedded in the alteration of individual α_{ln}, α_{ls}, and α_{cs}. From analyses of the change of each of these interfacial energies, we found that in our system, the decrease of α at high salinity was related to a decrease of water–$CaCO_3$ interfacial energy, and was possibly also related to a decrease of $CaCO_3$–quartz interfacial energy. The tested contact angles and interfacial energies among air, liquid, and solid phases are shown in Table 6.1. The interfacial energy between air and water increases when the water phase contains more salts, consistent with reported data.[252-257] The changes of α_{ln} and α_{ls} were calculated from our own contact angle tests. Data at 0.15 M salinity was used as the reference condition for calculation. The contact angles on quartz increased with increasing salinities. Similar trends were also observed in other studies.[223, 258] The resulting α_{ls} decreased slightly from 0.15 M salinity to 0.85 M salinity,

which was within the experimental error range. Therefore, we assumed that the slight decrease of α_{ls} did not change α appreciably.

Table 6.1 Summary of interfacial energies and solution contact angles on quartz and calcite. The positive and negative error ranges are sample standard deviations

Salinity	0.15 M	0.3 M	0.50 M	0.85 M
$\alpha_{\text{air-liquid}}$, mJ/m^2	70.97 ± 0.06	71.40 ± 0.00	72.03 ± 0.06	72.47 ± 0.06
Saline water contact angle on quartz, degree	7.2 ± 0.4	8.8 ± 1.1	11.0 ± 1.1	12.2 ± 1.4
α_{ls} change, mJ/m^2	0 ± 0.1	-0.2 ± 0.2	-0.3 ± 0.3	-0.4 ± 0.4
Saline water contact angle on calcite, degree	17.9 ± 2.0	16.6 ± 1.9	14.9 ± 1.7	14.3 ± 1.6
α_{lc} change, mJ/m^2	0 ± 1.1	-0.9 ± 1.1	-2.1 ± 1.0	-2.7 ± 1.0

The reported water contact angles on calcite were less consistent.[259, 260] Some of the studies reported no trend, while others reported a slight increase in the contact angle at increased salinity. The inconsistency can result from the deviation of natural calcite samples, the variable flatness of their surfaces, and the pre-test sample treatment methods. In our tests, the deviation in these factors was minimized meticulously as described in the "Materials and Methods" section, and a slight decrease of contact angle was observed at enhanced salinity, as shown in Table 6.1. Using the tested values, we calculated that the water–calcite interfacial energy decreased by 2.7 mJ/m^2 when salinity increased from 0.15 to 0.85 M. Interestingly, even if we assume a constant or a very slightly increasing (1–2 degrees) contact angle on calcite, the calculation still leads to a decrease of α_{ln} at elevated salinity, although to a lesser extent. The decrease of $CaCO_3$–water interfacial energy favors nucleation, because exchanging more area of quartz–water interface for $CaCO_3$–water interface will decrease the system's free energy.

There are two caveats in testing the interfacial energy of liquid–calcite (nucleus), α_{ln}, at varying salinities. One is that the $CaCO_3$ phase formed on quartz in this study is likely to be less stable than calcite. However, the trends in contact angle and calculated change of α_{ln} is expected to be similar for either calcite or a metastable phase, although the absolute numbers may vary. The other caveat is that this test assumed negligible change of the $CaCO_3$ structure at different salinities. Typically, fast precipitation rates favor less stable structure.[261-263] Therefore, the $CaCO_3$ formed at high salinity could be less crystallized, and thus may have a smaller interfacial energy with water.[261, 264, 265]

Although the change in $CaCO_3$–quartz interfacial energy is hard to measure experimentally, it is expected to be lower at high salinity. The interfacial energy between two epitaxial attached solids greatly depends on their lattice mismatch—the larger the mismatch, the larger the interfacial energy. When the structure types of the two solids are not identical, bond-length mismatches can be a good approximation to predicting mismatch extent.[213] The M–O bond length in $CaCO_3$ is around 2.4 Å, while the M–O bond length in quartz is around 1.6 Å (WWW-MINCRYST database, available online at http://database.iem.ac.ru/mincryst/). The averaged bond length in $CaCO_3$ could be shortened if smaller ions (i.e, Na^+ or Cl^-) were incorporated, or if nucleation rates were enhances, allowing less time for arrangement of $CaCO_3$ lattices and leaving bond lengths closer to that of quartz at the interface.[266] Both processes could reduce the $CaCO_3$–quartz interfacial energy, and both are favored in a high salinity environment. Therefore, any decrease of $CaCO_3$–quartz interfacial energy is understandable.

6.3.4 Contribution of Each Interface to the Overall Interfacial Energy

The effective interfacial energy α for heterogeneous nucleation is a complicated function of the geometry of heterogeneously formed nuclei, and of the three interfacial energies among

water, quartz, and $CaCO_3$. To analyze the sensitivity of α on each of the interfacial energies, we derived the function of α based on two assumptions: The first assumption is that heterogeneously formed nuclei resemble the top section of an ellipsoid cut by a horizontal plane, with a fixed height to lateral radius (i.e., width) ratio. Our previous study found this ratio to be around 1/6.[164] The second assumption is that the contact angle of $CaCO_3$ with quartz is determined by the equilibrium of interfacial energies among water, $CaCO_3$, and quartz. The detailed derivation and calculation is provided in the Supporting Information (6-S2). Using estimated values of α_{ls} = 168 mJ/m^2 and α_{ln} = 59 mJ/m^2 based on the literature,[164] α_{ns} was calculated to be 141 mJ/m^2. Using these interfacial energy values as the reference values for individual interfacial energies, we simulated the change of α as a function of the relative changes of the individual interfacial energies, and the results are shown in Figure 6.4. The slope of each line in Figure 6.4 is equivalent to the partial derivative of α on either α_{ls}, α_{ln}, or α_{ns}, and thus can be viewed as the sensitivity of α on that specific individual interfacial energy. The similar sensitivity of α on α_{sn} and on α_{ln} or α_{ls} highlights the importance of considering aqueous chemistry and its influence on the effective interfacial energy.

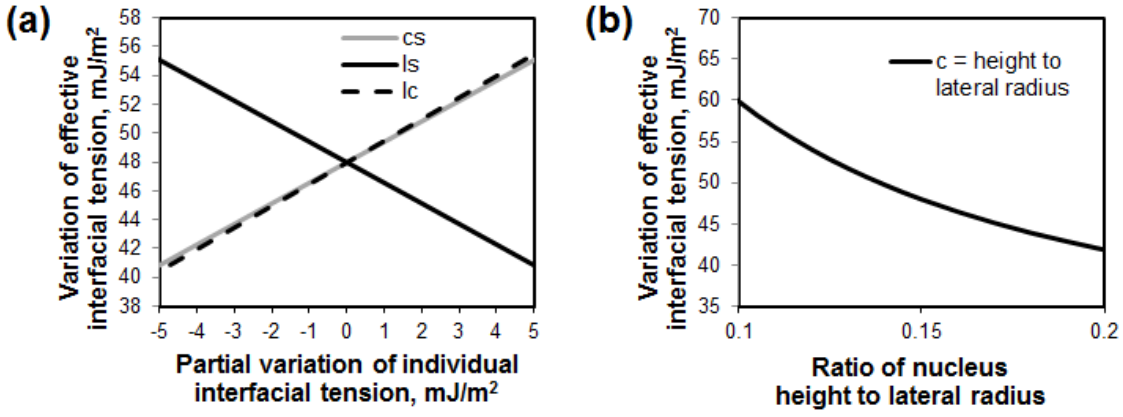

Figure 6.4 Analyses of individual interfacial energy contributions. (a) Simulated change of α as a partial function of deviations of α_{ln}, α_{ls}, or α_{ns} from their reference values. The figure shows that α is positively correlated with α_{ls}, and negatively correlated with α_{ns} and α_{ln}. The results highlight the comparable importance of α_{ln}, α_{ls}, and α_{ns} in affecting α. (b) The absolute α values are also dependent on other factors, such as slight alterations of the nuclei height to width ratio.

In Figure 6.4, the trend of α's variation as partial functions of α_{ln}, α_{ls}, and α_{ns} is more important than the absolute values of α's variation shown, because the calculated α values also depend on such geometrical features of the heterogeneously formed nuclei as the height-to-width ratio, which is hard to measure more accurately than we have here. For example, our calculation shows that the α value can be reduced by more than 10 mJ/m^2 if the height to lateral radius ratio of nuclei is increased by only 0.1 (Figure 6.4b).

6.3.5 Decreased Kinetic Factors at Higher Salinities

The interfacial energy (α) in the nucleation rate equation (Eq.6.2) is raised to the third power in the exponential term, therefore, a reduction of the interfacial energy is generally expected to enhance the nucleation rate more significantly than do other factors, such as supersaturation (IAP/K_{sp}) and temperature (T) in the denominator. At room temperature of 25 ^{o}C, if parameters other than α and IAP/K_{sp} in Eq. 6.2 are kept constant, the change of α from 48 mJ/m^2 to 35 mJ/m^2 is expected to increase the nucleation rate by ~360 times at a supersaturation of $IAP/K_{sp} = 10^{1.40}$, and by ~18 times at a supersaturation of $IAP/K_{sp} = 10^{2.00}$. In our experiments, however, we observed only ~18 times faster nucleation at $IAP/K_{sp} = 10^{1.40}$ and ~1.5 times (or almost the same) faster nucleation at $IAP/K_{sp}=10^{2.00}$. The only parameter in Eq. 6.2 that is likely to account for the discrepancy between the theoretical prediction and our experimental results is the kinetic factor, J_0. J_0 is related to the diffusion and attachment of monomers in solution or on the substrate to existing nuclei, and is also related to the possibility of nuclei in a small radius range around the critical nucleus size to form nuclei rather than falling back to aqueous species.[247] In physics, the kinetic factor for forming nuclei from air, such as ice nucleation, may be written as

$$J_0 = \mathcal{Z} \cdot v \cdot \mathrm{S}(n_c) \cdot v' \cdot \tau_0 \cdot \exp(-\frac{E_a}{kT}) \,, \qquad \text{Eq. (6.6)}$$

in which $\mathcal{Z}$ is the Zeldovich factor, describing the probability of a critical cluster to actually cross the energy barrier; v is the rate of a monomer in the mother phase to impinge directly onto an existing nuclei; S is the total surface area of critical nuclei; v' is the impingement rate of a monomer on substrate onto an existing nucleus through surface diffusion; and $\tau_0 \exp(-E_a/kT)$ is the time required for monomers to adsorb on nuclei. If similar concepts are applied to nucleation in the aqueous phase, the change of salinity is likely to affect J_0 by changing the aqueous diffusivity of monomers, the surface diffusivity of monomers, and the attachment process of monomers to nuclei. Although a detailed theoretical analysis of the kinetic factors is not the focus of this study, we extend our discussion to include one possible explanation for a lower J_0 at high salinities. From the measurement of zeta potentials of $CaCO_3$ and quartz under our experimental conditions, for all supersaturations, an increase of salinity resulted in less negative zeta potential on the quartz surface, but did not change the positive zeta potential on the $CaCO_3$ surface (Figure 6.5). This result suggests that the electrostatic attraction between $CaCO_3$ and quartz was lower at higher salinity. Therefore, the impingement rate of $CaCO_3$ monomer in solution onto the quartz surface is expected to be slower, and thus the kinetic factor can be reduced. Hence, according to Eq. 6.6, a smaller J_0 is expected.

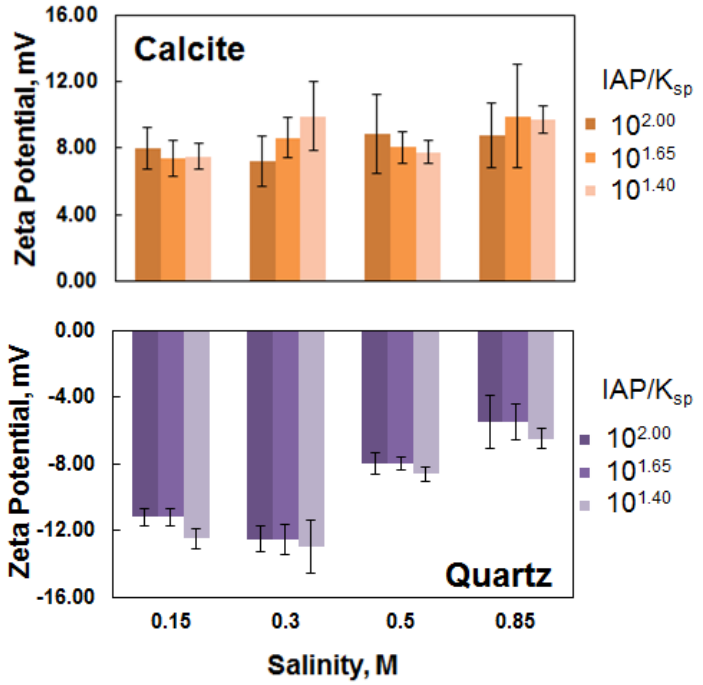

Figure 6.5 Zeta potentials of quartz and calcite particles in our experimental aqueous conditions. The quartz surface becomes less negative with increasing salinity, while the $CaCO_3$ surface maintains a similar positive zeta potential under all conditions. The zeta potentials for both quartz and $CaCO_3$ at a fixed salinity do not change as supersaturation varies.

When kinetic parameter J_0 and thermodynamic parameter α both change, it is important to know the relative contribution of each parameter to the overall nucleation rate. To quantitatively compare the kinetic factors in our experiment, the linear regression line in Figure 6.1 was extended to $1/[\ln(IAP/K_{sp})]^2=0$ (i.e., infinite supersaturation) at which the exponential term including α is zero. The intersection with the ln(J) axis is ln(J_0) for that specific salinity. The obtained ln(J_0) was the same for 0.15 and 0.30 M salinities, and was ~2.5 arbitrary units higher than ln(J_0) at 0.50 and 0.85 M salinities. This difference corresponds to an ~13 times reduction in J_0 for 0.5 and 0.85 M salinities compared to 0.15 and 0.30 M salinities. To the authors' knowledge, the kinetic factor has not previously been investigated experimentally for nucleation in aqueous solution. This study provides a quantitative discussion of the kinetic factor J_0.

It is known that J_0 can change by one to two orders of magnitude, but this change is often assumed less significant than changes of the interfacial energy.[31] In this study, we highlight that under certain conditions, especially when supersaturation is comparatively high, J_0 and α can comparably affect the nucleation rate. In particular, when salinity increases from 0.15 to 0.85 M, the increase in the nucleation rate due to a lowered α was canceled out at supersaturation of $IAP/K_{sp}=10^{2.00}$ due to a reduced J_0.

The importance of the kinetic factor, which has been overlooked in the past, not only improves our mechanistic understanding of nucleation in the environment, but can also guide practical applications, such as nanoparticle synthesis, pipeline scaling control, and CO_2 mineralization for carbon sequestration.

6.4 Conclusions

In this study, *in situ* heterogeneous nucleation of $CaCO_3$ on quartz was investigated at different salinities. The salinities (represented by ionic strengths) were tuned with NaCl and ranged from 0.15 M to 0.85 M. Through analyses of nucleation rates at different supersaturations, we obtained the effective interfacial energy (α) controlling the nucleation process for each salinity. Using the thermodynamic parameters for calcite, α was ~ 48 mJ/m^2 for 0.15 and 0.30 salinities, and was ~ 35 mJ/m^2 for 0.50 and 0.85 M salinities. This difference was due to the lower water-$CaCO_3$ and $CaCO_3$–quartz interfacial energies in high salinity systems. On the other hand, the kinetic factor in the nucleation rate equation was lower in high salinity systems, and this reduction can account for observed nucleation rates an order of magnitude slower than rates predicted solely by thermodynamic variations. New information provided by this study can help predict and

improve system operations such as membrane fouling control, pipeline scaling control, mineral trapping of pollutants, and material synthesis.

Acknowledgments

We acknowledge Drs. Byeongdu Lee, Xiaobing Zuo, and Sonke Seifert for helping us collect GISAXS data at sector 12-ID-B and 12-ID-C at the Advanced Photon Source (Argonne, IL), and acknowledge Dr. Yongman Kim for helping to collect water surface tension data. We are also grateful for Mr. Haesung Jung's help in testing zeta potentials. We appreciate Dr. Jessica Ray's valuable discussions and collaboration on contact angle tests. This work was supported by the Center for Nanoscale Control of Geologic CO_2, an Energy Frontier Research Center funded by the U.S. Department of Energy, Office of Science, Office of Basic Energy Sciences under Award Number DE-AC02-05CH11231. Use of the Advanced Photon Source, an Office of Science User Facility operated for the U.S. Department of Energy Office of Science by Argonne National Laboratory, was supported by the U.S. DOE under Contract No. DE-AC02-06CH11357.

Supporting Information for Chapter 6

6-S1 Detailed Information for This Study

Detailed information on aqueous conditions is listed in Table 6-S1. GISAXS *I–q* plots corresponding to the AFM images in Figure 6.3 is shown in Figure 6-S1. Plots of invariant values are shown in Figure 6-S2. Representative GISAXS 2D images are shown in Figure 6-S3. Interfacial energies calculated using thermodynamic parameters for vaterite are shown in Figure 6-S4.

Table 6-S1 Experimental conditions for nucleation experiments. Under all conditions, the ratios of calcium to (bi)carbonate ions are 4–5. pHs are 7.8 ± 0.1 (data range), and temperatures are 25 °C. Supersaturations are calculated using Geochemist's Workbench®, and $K_{sp} = 10^{-8.48}$ for calcite was used to quantify supersaturations. Salinity was tuned by adding NaCl to the solution.

Condition	Salinity (ionic strength)	Supersaturation, IAP/K_{sp}	$CaCl_2$, M	$NaHCO_3$, M	NaCl, M	pH
1	0.15 M	$10^{1.40}$	0.0220	0.0050	0.0880	7.92
2		$10^{1.65}$	0.0290	0.0070	0.0680	7.91
3		$10^{2.00}$	0.0500	0.0100	0.0040	7.89
4	0.30 M	$10^{1.40}$	0.0300	0.0060	0.2300	7.83
5		$10^{1.65}$	0.0370	0.0088	0.2100	7.83
6		$10^{2.00}$	0.0600	0.0130	0.1400	7.82
7	0.50 M	$10^{1.40}$	0.0340	0.0074	0.4580	7.75
8		$10^{1.65}$	0.0460	0.0100	0.4200	7.75
9		$10^{2.00}$	0.0720	0.0150	0.3400	7.75
10	0.85 M	$10^{1.40}$	0.0383	0.0090	0.9130	7.66
11		$10^{1.65}$	0.0525	0.0120	0.8740	7.66
12		$10^{2.00}$	0.0820	0.0180	0.7890	7.65

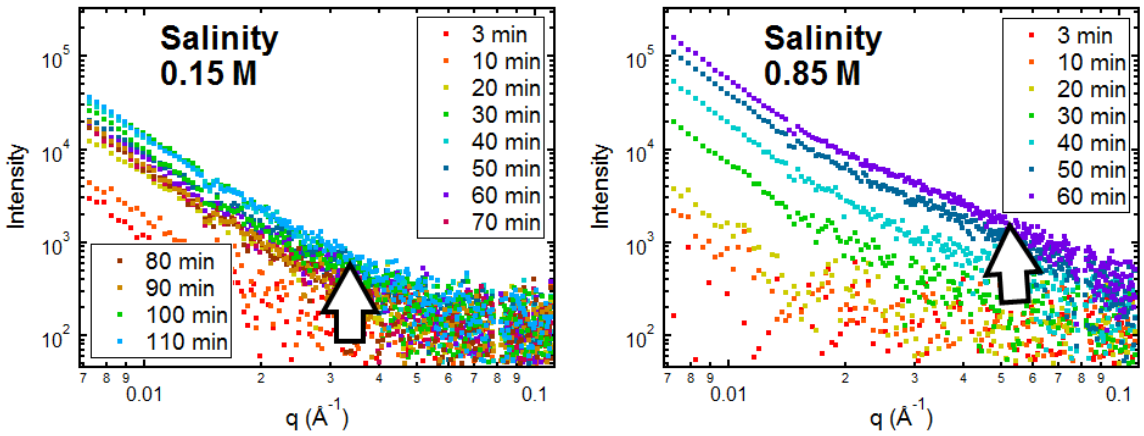

Figure 6-S1. Intensity plots for supersaturation of $IAP/K_{sp}=10^{1.40}$ at salinities of 0.15 and 0.85 M. The intensity at large q results from small particles, and intensity at low q originates from large particles. In these images, intensities in the q range of 0.02–0.1 correspond to the heterogeneous nuclei we focus on, and the slight bend in the scattering plots indicates the q value corresponding to radius of gyration of the nuclei. Arrows in the figures show the evolution of nucleus sizes and numbers. The plots correspond to the AFM images in Figure 6.3 in the main text.

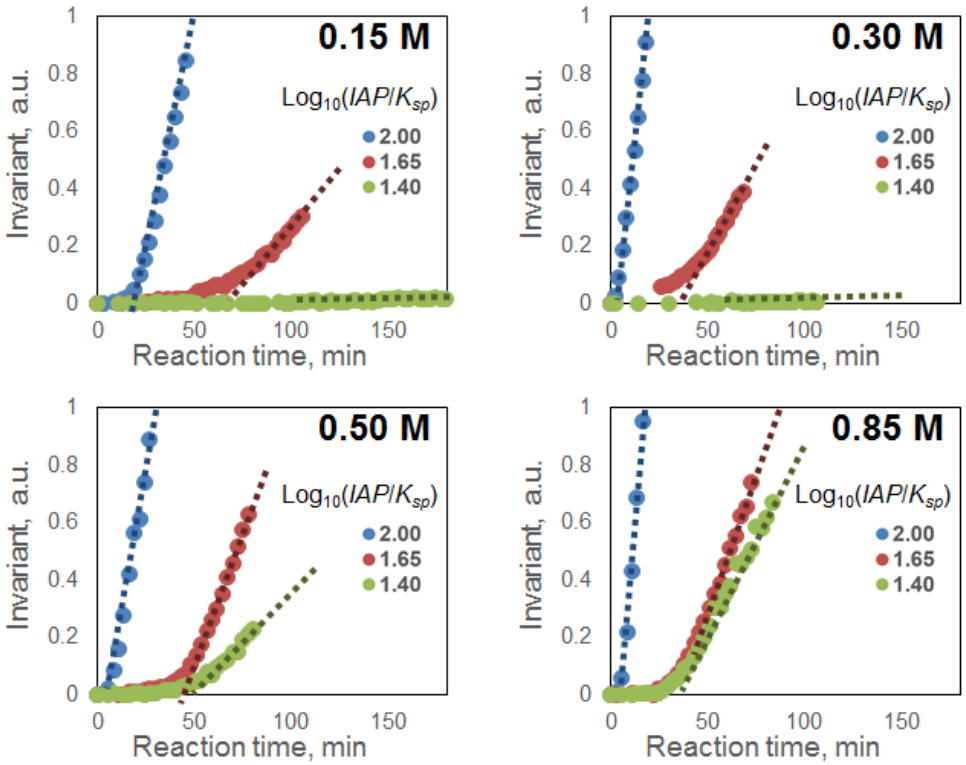

Figure 6-S2 Plots of invariant evolution with respect to reaction times. The dotted lines indicate the linear regions of the plots used for linear regression to obtain the nucleation rates.

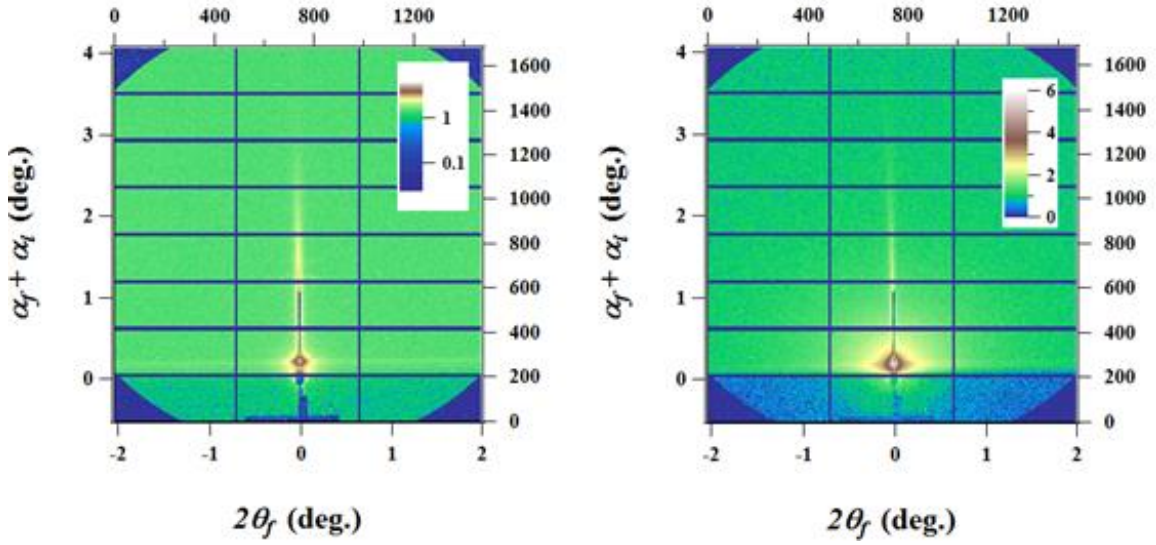

Figure 6-S3 Example GISAXS 2D images. The left image is a 130 min image for $IAP/K_{sp} = 10^{1.40}$ at salinity of 0.15 M. The right image is a 40 min image for $IAP/K_{sp} = 10^{2.00}$ at a salinity of 0.85 M. No faceted particles were observed in any of our experimental conditions.

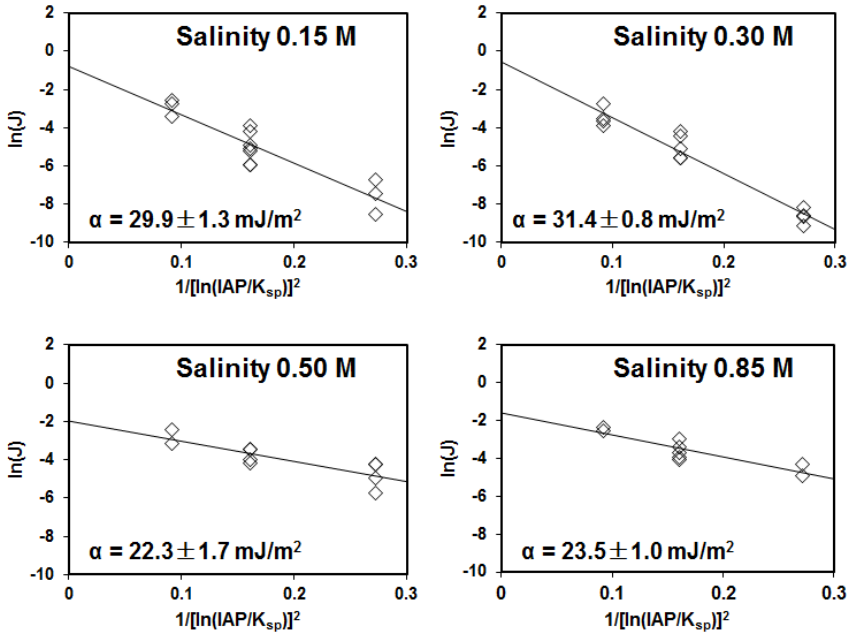

Figure 6-S4. Interfacial energies calculated using K_{sp} and the molecular volume for vaterite. The results have the same trend as those calculated using calcite parameters: The interfacial energy is lower at higher salinity, and the kinetic factor J_0 is also lower at higher salinity.

6-S2 Derivation of α and Calculation of α_{cs}.

The derivation is based on two assumptions. One assumption is that the geometry of the nuclei is part of an ellipsoid ($\frac{x^2}{a^2}+\frac{y^2}{a^2}+\frac{z^2}{b^2}=1$) and maintain constant ratio (c) of height to lateral radius (width). This assumed geometry not only allows incorporation of measured height-to-radius ratios, but also allows equilibrium of interfacial energies at the contacting line among the liquid, nuclei and the substrate. As illustrated in Figure 6-S5, R is the lateral particle radius, θ is the contact angle of the nuclei on the substrate, and c is the nuclei height to radius ratio, measured to be 0.1–0.2 (here we set c as 0.15) [164].

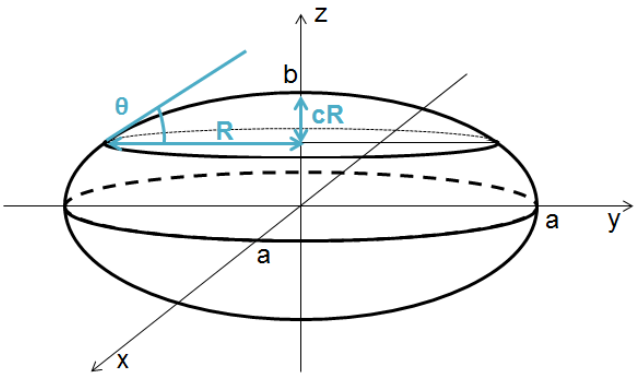

Figure 6-S5 Illustration of assumed nuclei geometry.

During heterogeneous nucleation, the liquid–substrate interface is replaced by liquid–nucleus and nucleus–substrate interfaces. The free energy for one nucleus can be written as

$$\Delta G = n\Delta G_r + S_{ln}\alpha_{ln} + S_{ns}\alpha_{ns} - S_{ls}\alpha_{ls} \ . \qquad \text{Eq. (6-S1)}$$

In this equation, ΔG_r is the free energy for the chemical reaction $Ca^{2+} + CO_3^{2-} \rightarrow CaCO_3$, and is expressed as $-kT\ln(IAP/K_{sp})$, where k is the Boltzmann constant. ΔG_r can be calculated

for systems at known temperatures and supersaturations. Also, n is the number of molecules (in this case $CaCO_3$ pairs) in the nucleus.

The second assumption is that the equilibrium of α_{ln}, α_{ls}, and α_{ns} determines the contact angle θ according to Young's equation:

$$\cos\theta = (\alpha_{ls} - \alpha_{ns})/\alpha_{ln}, \quad \text{Eq. (6-S2)}$$

and thus

$$\tan\theta = \sqrt{\alpha_{ln}^2 - (\alpha_{ls} - \alpha_{ns})^2}/(\alpha_{ls} - \alpha_{ns}). \quad \text{Eq. (6-S3)}$$

According to the ellipsoid equation, the point (-R, 0, b-cR) should be on the ellipsoid surface, and the partial derivative of z on x at that point equals tanθ. Thus,

$$\frac{R^2}{a^2} + \frac{(b-cR)^2}{b^2} = 1, \quad \text{Eq. (6-S4)}$$

and

$$z_x = \frac{\partial z}{\partial x} = \frac{bR}{a\sqrt{a^2 - R^2}} = \tan\theta. \quad \text{Eq. (6-S5)}$$

From the above two equations, *a* and *b* can be solved and written as functions of *R* and tanθ:

$$\mathrm{a} = \frac{R(\tan\theta - c)}{\sqrt{(\tan\theta)^2 - 2c\tan\theta}} \quad \text{Eq. (6-S6)}$$

and

$$\mathrm{b} = \frac{cR(\tan\theta - c)}{\tan\theta - 2c}. \quad \text{Eq. (6-S7)}$$

The interfacial areas S_{ns} and S_{ls} are both πR^2:

$$S_{ns} = S_{ls} = \pi R^2. \qquad \text{Eq. (6-S8)}$$

The liquid–nucleus interface is obtained by partially differentiating the ellipsoid equation $\frac{x^2}{a^2} + \frac{y^2}{a^2} + \frac{z^2}{b^2} = 1$ on x and y and integrating

$$S_{ln} = \iint_{D_{xy}} \sqrt{1 + z_x^2 + z_y^2}\,\mathrm{d}x\mathrm{d}y, \qquad \text{Eq. (6-S9)}$$

where

$$z_x = \frac{\partial z}{\partial x} = \frac{-\frac{b}{a^2}x}{\sqrt{1-\frac{x^2}{a^2}-\frac{y^2}{a^2}}} \qquad \text{Eq. (6-S10)}$$

and

$$z_y = \frac{\partial z}{\partial y} = \frac{-\frac{b}{a^2}y}{\sqrt{1-\frac{x^2}{a^2}-\frac{y^2}{a^2}}}. \qquad \text{Eq. (6-S11)}$$

Incorporating z_x and z_y into the equation for S_{ln}, one gets

$$S_{ln} = \iint_{D_{xy}} \frac{a\sqrt{1+\frac{b^2-a^2}{a^4}(x^2+y^2)}}{\sqrt{a^2-x^2-y^2}}\,\mathrm{d}x\mathrm{d}y \xLeftrightarrow{x^2+y^2=\rho^2,\mathrm{d}x\mathrm{d}y=\rho\mathrm{d}\rho\mathrm{d}\theta} \iint_{\sigma} \frac{\sqrt{a^2+\frac{b^2-a^2}{a^2}\rho^2}}{\sqrt{a^2-\rho^2}}\rho\mathrm{d}\rho\mathrm{d}\theta =$$

$$-\int_0^{2\pi}\mathrm{d}\theta\int_0^R \sqrt{a^2+\frac{b^2-a^2}{a^2}\rho^2}\,\mathrm{d}\left(\sqrt{a^2-\rho^2}\right) \xLeftrightarrow{\sqrt{a^2-\rho^2}=\eta} 2\pi\int_{\sqrt{a^2-R^2}}^{a}\sqrt{a^2+\frac{b^2-a^2}{a^2}(a^2-\eta^2)}\,\mathrm{d}t =$$

$$2\pi\sqrt{\frac{a^2-b^2}{a^2}}\int_{\sqrt{a^2-R^2}}^{a}\sqrt{\eta^2+\frac{a^2b^2}{a^2-b^2}}\,\mathrm{d}t. \qquad \text{Eq. (6-S12)}$$

Integration gives S_{ln} as a function of R and $\tan\theta$:

$$S_{ln} = 2\pi\frac{a^2-b^2}{a^2}\left[\frac{\eta}{2}\sqrt{\eta^2+\frac{a^2b^2}{a^2-b^2}}+\frac{a^2b^2}{2(a^2-b^2)}\ln(\eta+\sqrt{\eta^2+\frac{a^2b^2}{a^2-b^2}})\right]\Bigg|_{\eta=\sqrt{a^2-R^2}}^{\eta=a}. \quad \text{Eq.(6-S13)}$$

The number of molecules in the nucleus, n, can be calculated by dividing the volume of the nucleus by the unit molecular volume. The volume of the nucleus is obtained by integration:

$$V = \int_{b-cR}^{b}\pi\, x^2 \mathrm{d}z = \int_{b-cR}^{b}\pi\, a^2\left(1-\frac{z^2}{b^2}\right)\mathrm{d}z = \frac{\pi a^2 c^2 R^2}{3b^2}(3b-cR)\,. \quad \text{Eq.(6-S14)}$$

Because a and b are functions of R and tanθ, V is also a function of R and tanθ.

Next, we seek to express ΔG as a function of R and tanθ. Accordingly, we insert into ΔG equation the known or calculated values for v and ΔG_r, the measured ratio c (c = 0.15), the reported values for α_{lc} and α_{ls} [164, 215, 232], and the equations of a, b, S_{ls}, S_{ns}, S_{ln}, and V. We can get an expression of ΔG as a function of R and tanθ. Because tanθ is a function of unknown α_{cs}, ΔG is actually a function of only R and α_{cs}. By numerically solving $\frac{\partial \Delta G}{\partial R} = 0$ for R_c at ΔG's maximum, ΔG^* can be calculated by inserting R_c into ΔG expression, and is a function of α_{cs}.

If ΔG^* is written in the same form as in the homogeneous nucleation, as $\frac{16\pi v^2\alpha^3}{3k^2T^2[\ln\left(\frac{IAP}{K_{sp}}\right)]^2}$, the α can be solved, and is a function of α_{ns} only. Therefore, if α_{ns} is given, α can be calculated.

The reported α_{ls} and α_{ln} we have used in solving α_{ns} were for low salinity, therefore, we used an experimentally obtained value of α = 48 mJ/m^2 to solve for α_{ns}, and obtained α_{ns} = 141 mJ/m^2.

Chapter 7: Quantification of the Activation Energy and Pre-exponential Factor in the Nucleation Rate Equation for Heterogeneous $CaCO_3$ Nucleation on Quartz

Abstract

Nucleation is an important process widely occurring in natural environments and industry. However, this process is usually skipped in numerical modeling due to a lack of parameters. Here, for the first time, we experimentally quantified the apparent activation energy (E_a) and the pre-exponential factor (A) in the nucleation rate equation $J = A\exp(-\frac{E_a}{kT})\exp\left(-\frac{\Delta G^*}{kT}\right)$, using heterogeneous $CaCO_3$ nucleation on quartz as a model system. Nucleation rates were measured with *in situ* grazing incidence small angle X-ray scattering and *ex situ* atomic force microscopy, and the experiments were conducted at 12, 25, and 31 ^oC with a fixed supersaturation of $IAP/K_{sp(calcite)} = 10^{1.65}$. The value for E_a was calculated as 45 ± 7 kJ/mol, and the pre-exponential factor A was $10^{12 \pm 1.1}$ #/μm^2/min, or $10^{2.0 \pm 1.3}$ mol/m^2/min. Increasing the temperature shortened the induction time, but did not appreciably change nucleus sizes. These parameters are critical to initiate numerical simulation of nucleation as an explicit step.

7.1 Introduction

In the initial step of solid precipitation in a nuclei-free system, nucleation forms a smallest daughter phase from a supersaturated mother phase, and this process produces large areas for further evolution of the daughter phase, such as growth, ripening, aggregation and agglomeration,

phase transformation, and crystallization. This nucleation process, especially when it happens on a foreign surface (heterogeneous nucleation), is widely encountered in the fields of geochemistry,[200, 248, 267] biomineralization,[238] nanomaterial synthesis,[268, 269] pipeline scaling control,[270] and drug production.[271]

Due to the wide occurrence and importance of nucleation, it would be useful to simulate and predict it using numerical modeling approaches, as demonstrated by several studies and our own work presented in Chapter 4.[37, 272-274] However, current numerical simulations of crystalline formation usually skip the nucleation process by introducing seeds of the precipitating phase into the initial condition of the system. The seeded model might miss the importance characteristics of nucleation, such as the high specific reactive surface area of nuclei[37] and the rate-limiting role of nucleation.[190]

To enable simulation of nucleation process, kinetic and thermodynamic parameters are needed. Up till now, except for the commonly used solubility products (K_{sp}) and phase density, the known parameters are still very limited. For thermodynamic parameters, the interfacial energies for homogeneous nucleation (i.e., nucleation in solution) are reported for several common minerals,[61, 232] with large data ranges. On the other hand, the interfacial energies for heterogeneous nucleation (i.e., nucleation on a foreign surface) are less well reported. Among the limited information for heterogeneous nucleation, Fernandez-Martinez et al. and Li et al. reported that the interfacial energies for heterogeneous nucleation of $CaCO_3$ on quartz were as low as 35–50 mJ/m^2,[31, 164] and the overall system interfacial energy can be affected appreciably by individual interfacial energies among nuclei, substrates, and solutions.[32, 35, 164, 166, 200]

Kinetic factors are even less well known, beyond the fact that the J_o in the nucleation rate equation

$$J = J_0 \exp\left(-\frac{\Delta G^*}{kT}\right) = A\exp(-\frac{E_a}{kT}) \exp\left(-\frac{\Delta G^*}{kT}\right) \quad \text{Eq. (7.1)}$$

can be expanded into $A\exp(-E_a/kT)$,[33, 162, 247, 275] where A is related to, but not limited to, ion diffusion and nuclei surface properties, and E_a is the apparent activation energy. Generally, J_0 is believed to be less important than the deviation of interfacial energies,[247] and most experimental studies have assumed a constant J_0 term.[31-33] However, a recent study compared the influences of kinetic factors and interfacial energies on nucleation rates, and highlighted that the two aspects are equally important under relatively high supersaturations.[163] This result brought up the necessity of quantifying J_0 in order to estimate the nucleation process reliably. For homogeneous nucleation in aqueous solutions, the J_0 value was estimated by Neilson (1964) to be $D/5d$, where D is the diffusion coefficient of ions, and d is the molecular diameter.[276] For more widely occurring heterogeneous nucleation, to the authors' knowledge, estimations of J_0 are hardly known.

Therefore, this study seeks to experimentally measure E_a and A for more accurate estimation of J_0 in Eq. 7.1. The model system employed by this study is heterogeneous nucleation of $CaCO_3$ on quartz, because this system involves two of the most common materials, and because thermodynamic parameters are reported for exactly the same setup, so that system errors are minimized. To enable calculation of E_a, *in situ* observations of $CaCO_3$ nucleation in solution with a constant supersaturation of $IAP/K_{sp(calcite)} = 10^{1.65}$ were conducted at 12, 25, and 31 ^oC using grazing incidence small angle X-ray scattering (GISAXS). Atomic force microscopy (AFM) was employed to calibrate the arbitrary unit of nucleation rates obtained in GISAXS tests. This GISAXS-AFM calibration method is newly developed, and has potential for wider application in GISAXS data acquisition research. Further, the kinetic parameters obtained in this study set critical baselines for modeling nucleation as an explicit step.

7.2 Experimental Section

7.2.1 Substrate Preparation

Environmentally abundant quartz was used as the substrate for heterogeneous nucleation experiments. Atomically flat quartz substrates with a polished (100) plane (roughness < 5 Å) were purchased from MTI Corporation. The substrates were cut into 1 cm × 1 cm squares and cleaned by sonication in acetone, ethanol, isopropanol, and ultrapure ionized water (DI water, 18.2 MΩ/cm) successively for 20 min each. Then they were soaked in sulfuric acid and Nochromix® for 2 hours to remove any remaining organic compounds. The substrates were then rinsed thoroughly with DI water and stored in DI water for experimental use. The cleaned substrates were scanned using AFM to ensure the cleanness of the surface.

7.2.2 Aqueous Chemistry

To generate an oversaturated solution with respect to $CaCO_3$ at constant supersaturation, we used a flow-through system. A $NaHCO_3$ solution and a $CaCl_2$ solution were driven by two peristaltic pumps into a micro-mixer. Using Geochemist's Workbench (GWB, Release 8.0,RockWare, Inc.) and thermo_minteq database, we quantified the supersaturation of the mixed solution to be $IAP/K_{sp} = 10^{1.65}$ at 12, 25, and 31 ºC. These conditions are chosen because they are within the detection window of both GISAXS and AFM within a reasonable reaction time. To quantify the aqueous supersaturation, the solubility product ($K_{sp} = 10^{-8.48}$) of calcite was used for calculation. The oversaturated solution was then injected into our reaction cell (2 mL volume) at a volumetric flow rate of 5.6 mL/min. A piece of quartz substrate on the bottom of the reaction cell was in contact with the freshly injected solution. Waste solution was exhausted from the top of the cell and collected. A diagram of the experimental setup is shown in Figure 7.1.

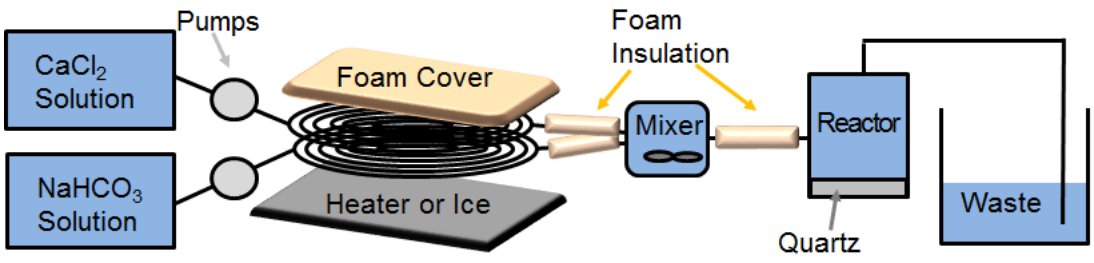

Figure 7.1. Setup of the flow-through system used to monitor $CaCO_3$ nucleation at different temperatures.

To obtain the same supersaturation of the mixed solution at different temperatures, the concentration of $CaCl_2$ was tuned slightly to maintain a supersaturation fixed at $IAP/K_{sp}=10^{1.65}$. The ratio of Ca/HCO_3^- was kept at 3.6–4.4 for all conditions, and the pH was within a 7.8–8.0 range. To control the system temperature, before mixing, the solutions of $CaCl_2$ and $NaHCO_3$ were either heated in the tubing using a heating plate, or cooled with a water/ice mixture. To minimize heat transport through tubing walls, the tubes after the temperature control component were covered with insulating foam. The temperature of the each supersaturated solution was measured before and after the reaction at the inlet of the reaction cell, and the temperature fluctuation was less than 1 ºC from the target value.

7.2.3 *In situ* Grazing Incidence Small Angle X-ray Scattering (GISAXS)

In situ GISAXS data were collected at beamline 12-ID-B at the Advanced Photon Source (Argonne National Laboratory, USA). The reaction cell was aligned in the beam line. The front and back wall of the cell were made of Kapton film, allowing transmission of X-rays. A 14 keV X-ray beam incidence onto the substrate at an incident angle of 0.11º was scattered by particles on the substrate. The scattered X-rays were collected by a detector 2 m away from the sample downstream of the beam. The scattering intensity from the particles on the quartz surface was

obtained in the same way as described in our previous studies.[164] The intensity (I) was plotted versus the scattering vector (q). The scattering vector is in the reciprocal space of the horizontal dimension of the particles, and was 0.008–0.4 $Å^{-1}$ in our setup, corresponding to particles with an in-plane radius of 0.8–40 nm. Scattering with q values larger than 0.1 $Å^{-1}$ was background scattering with low signal-to-noise ratio, and was not used for analysis. The total volume of heterogeneously formed nuclei with radii within 3–30 nm were calculated using the invariant method:[164] the invariant (Q) was calculated by $Q = \int I(q)q^2 \mathrm{d}q$ for q = 0.01–0.1 $Å^{-1}$, which can be treated as the volume of nuclei with a radius of 3–30 nm, with an arbitrary unit. In our systems, nucleus size did not vary significantly, and thus the invariant value was also proportional to the number of nuclei. For GISAXS data with a high signal-to-noise ratio, we have also fitted the data to obtain the nuclei number with arbitrary units (as described in detail in Chapter 5),[164] which showed great consistency with the invariant method (Figure 7.2). The rates of nucleus number (obtained from the fitting method) increases were recorded as nucleation rates with arbitrary units. The variation of these nucleation rates obtained at different temperatures was used for calculation of the apparent activation energy E_a.

7.2.4 *Ex situ* Atomic Force Microscopy (AFM)

To calibrate the arbitrary nucleation rates obtained with GISAXS with absolute nucleation rates, and to visually observe the nanometer nuclei, we complemented the GISAXS experiment with *ex situ* AFM experiments. The experiments were conducted as described in the GISAXS section, except that the reaction was ended at different time points. At the desired reaction time, the substrate was taken out of the cell. The residual reaction solution was immediately rinsed off with ethanol to end the reaction. Ethanol (100%) was used instead of water to minimize dissolution of $CaCO_3$ nuclei. The substrate was then dried with ultra-pure nitrogen gas, and immediately

scanned using AFM to prevent aging of the nuclei. Only the evenly distributed particles on the surface were counted to obtain the nuclei density (#/μm^2), because the even distribution corresponds to the epitaxial attachment of the nuclei on the substrate. The larger, randomly distributed particles were formed in solution and settled on the surface. The manually counted nucleus densities per unit area were used to calibrate the arbitrary nucleation rate obtained with GISAXS. Tapping mode was used to collect images. AFM probes used in this study were purchased from Bruker (Model: RTESP, Part: MPP-11100-10).

7.2.5 Calculation of E_a and the Pre-exponential Factor A

The heterogeneous nucleation rate (#/um^2/s) was given by Eq. 7.1 in the Introduction, and is here further expanded and rearranged into[61, 162, 247]

$$J = A\exp\left(-\frac{E_a}{kT}\right)\exp\left(-\frac{\Delta G^*}{kT}\right) = A\exp\left(-\frac{E_a+\Delta G^*}{kT}\right) \quad \text{and} \qquad \text{Eq. (7.2)}$$

$$\Delta G^* = -\frac{16\pi\upsilon^2\alpha^3}{3k^2T^2\left[\ln\left(\frac{IAP}{K_{sp}}\right)\right]^2} \quad . \qquad \text{Eq. (7.3)}$$

In Eq. 7.3, υ is the molecular volume of nuclei (cm^3/molecule) and can be estimated using molecular weight of the nucleating material. α is the effective interfacial energy of the system. In our previous studies, the interfacial energy at room temperature for $CaCO_3$ nucleation on quartz was experimentally found to be 47.1 ± 1.3 mJ/m^2.[163, 164] The k in the denominator is the Boltzmann constant (1.3 × 10^{-23} J/K), T is temperature in Kelvin, IAP is the ion activity product $(Ca^{2+})(CO_3^{2-})$, and K_{sp} is the solubility product of the nucleating $CaCO_3$ phase (K_{sp}=10$^{-8.48}$).[208] To simplify the process of incorporating nucleation in reactive transport modeling, phase transformation of $CaCO_3$ is not considered at this stage. Because calcite is the most used mineral in reactive transport models

for $CaCO_3$ precipitation, this study uses υ and K_{sp} for calcite. With these parameters, the ΔG^* can be calculated.

Fitting the nucleation rates obtained with GISAXS at different temperatures according to Eq. 2, the sum of (E_a+ΔG^*) was obtained, and thus E_a was calculated with the calculated ΔG^*. Once the apparent activation energy E_a was calculated, and the absolute nucleation rate (#/m^2/s) was obtained, the pre-exponential factor A was readily calculable with a unit of number of nuclei per unit area of substrate per unit time. However, to incorporate the nucleation process in multiphase reactive transport models, the unit for nucleation rate is expected to be the change of fluid concentration per unit of substrate surface area. Therefore, the factor A was further combined with the in-plane nuclei radius obtained using GISAXS, the height-to-radius ratio obtained in our previous studies, as well as the molecular volume of $CaCO_3$, so that the final A with units of mol/m^2 of substrate/s was obtained.

7.3 Results

7.3.1 Apparent Activation Energy E_a

X-ray scattering intensities from the heterogeneously formed nuclei are shown in Figure 7.2a-c. Under all the conditions, the radii of the nuclei were 4.7 ± 0.7 nm, without significant difference. Nuclei growth was not appreciable, and therefore the nucleation process was considered to be dominant over mineral growth.

The nuclei numbers versus reaction times are plotted in Figure 7.2d. Two methods (the invariant method and the fitting method) used for extracting nuclei number with arbitrary units (a.u.) are shown on the left and right y-axes, respectively, and they are consistent. The slopes from

the linear regressions were taken as nucleation rates, and the intersection of regressed lines with the x-axis were taken as the induction times. The logarithms of these nucleation rates were regressed over 1/T according to a rearrangement of Eq. 7.2, $\ln(J) = \ln A - \frac{\Delta G^* + E_a}{kT}$, and the resulting $\Delta G^* + E_a$ was 61.5 ± 5.8 kJ/mol.

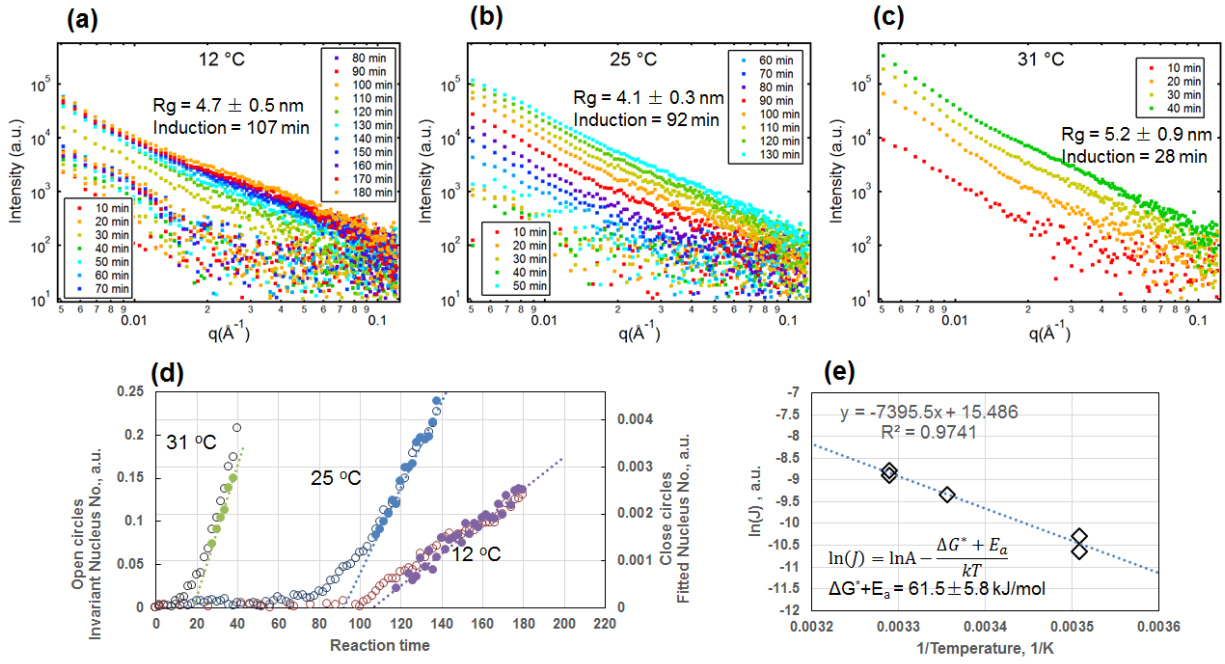

Figure 7.2 Acquisition of ($\Delta G^* + E_a$) using grazing incidence small angle X-ray scattering. (a-c) Plots of scattering intensities over scattering vector *q*. In all systems, the nuclei sizes are similar. The higher the temperature, the faster the reaction and the shorter the induction time. (d) Plots of invariant values (proportional to nuclei numbers) and fitted nuclei numbers with respect to reaction times. The dotted lines are from linear regression of the fitted nucleus numbers over reaction times. The slopes of these regressed lines are taken as nucleation rates, *J*. (e) Plot of ln(*J*) versus 1/*T*. Linear regression was conducted to calculate the sum of ($\Delta G^* + E_a$).

To calculate E_a, the value of ΔG^* was calculated according to Eq. 7.3. Utilizing the value for interfacial energy, $\alpha = 47.1 \pm 1.3$ mJ/m^2, obtained in our previous studies for the same system,[163, 164] ΔG^* was calculated as 16 ± 3 kJ/mol. Subtraction of ΔG^* from the sum of ($\Delta G^* + E_a$) gave E_a equal to 45 ± 7 kJ/mol.

7.3.2 Calibrated Nucleation Rates

Example AFM images of heterogeneously formed nuclei are shown in Figure 3a. Evenly distributed small nuclei are manually counted within a unit area of one square-micrometer. The GISAXS-obtained particle numbers under the same condition and at the same reaction time were read from Figure 7.2d on the right y-axis. Figure 7.3b shows the plot of nuclei numbers counted from AFM images versus GISAXS-obtained nuclei numbers. Each data point in Figure 7.3b was generated from at least three 1 μm^2 areas within one piece of quartz substrate. The scattering of the data points is due to a typical 20–30 min uncertainty in the induction time for 12 ºC and 25 ºC samples.

7.3.3 Pre-exponential Factor *A*

Regression of the counted particle numbers over the GISAXS-obtained arbitrary particle numbers with a fixed intersection at point (0,0) provided the correction factor from arbitrary numbers to absolute numbers, specifically, $(17.5 \pm 0.35)\times10^5$. With this correction factor, the nucleation rates from GISAXS data were corrected from arbitrary units to # of nuclei/μm^2/min (Table 7.1). The absolute value of the pre-exponential factor A was calculated in the similar way, according to the regression result ($\ln A = 15.5\pm2.4$) shown in Figure 7.2(e), with units of # of nuclei/μm^2/min, or units of #/m^2/s. The value of A is 9.4×10^{11} #/μm^2/min, or 1.6×10^{22} #/m^2/s. According to the standard deviation of regression result for $\ln A$, A has one order of magnitude uncertainty.

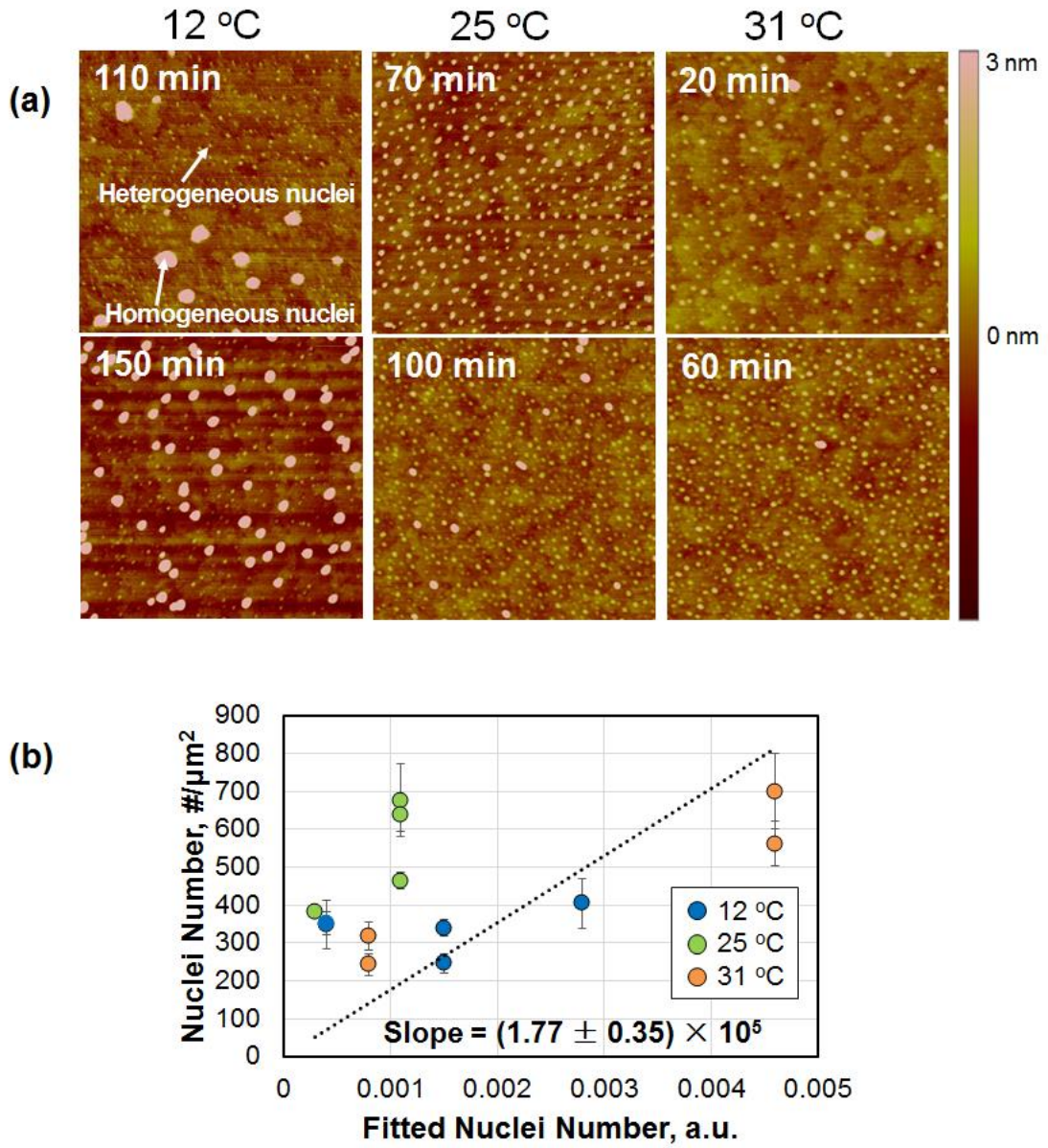

Figure 7.3 Calibration of GISAXS data using AFM. (a) Example AFM images (1×1 μm^2) of nuclei formed under different temperatures for various reaction times. The evenly distributed particles are heterogeneously formed, while the larger particles are homogeneously formed and settled to the quartz substrate surface. (b) Plot and regression of counted particle numbers with units of #/μm^2 over the arbitrary particle numbers obtained from fitting GISAXS data.

7.3.4 Unit Conversion of Nucleation Rates

According to the in-plane nuclei radius of 4.7 ± 0.7 nm, and the nuclei geometry studied in our previous studies,[163, 164] the individual nuclei volume was calculated as 4.1 ± 1.8 nm^3. The standard deviation of nuclei volume was expected to be reduced for materials that generate larger nuclei, because large nuclei are easier to measure accurately. Multiplication of individual nuclei volumes (m^3) and nucleation rates (#/m^2/s) gives nucleation rates in volume of nuclei per unit area of substrate surface per unit time (i.e., $m^3/m^2/s$). If the $CaCO_3$ phase is assumed to be calcite, as commonly used in reactive transport modeling approaches, the moles of Ca^{2+} or CO_3^{2-} ions consumed from fluid can be calculated by dividing the volume nucleation rates ($m^3/m^2/s$) by the molar volume of calcite (m^3/mol), where the molar volume is just the product of the reciprocal of calcite density and the molecular weight of calcite:

$$\upsilon = \frac{1}{\rho} \times MW \ . \qquad \text{Eq. (7.4)}$$

If the nucleating $CaCO_3$ phase is assumed to be other than calcite, the K_{sp} and molecular volume should be correspondent to that specific phase, but the methods for obtaining E_a and A are the same as presented for calcite.

The obtained nucleation rate was in moles of Ca^{2+} or CO_3^{2-} ions consumed per unit area of substrate surface per unit time (i.e., $m^3/m^2/s$). Since the pre-exponential factor A has the same units as the nucleation rate J, the unit conversion method for A is the same as that for J. The calculated values for J and A with different units are shown in Table 7.1.

Table 7.1 Nucleation rates and pre-exponential factors obtained in this study. The error ranges are standard deviations from the experimental data.

Temperature and pre-exponential factor	Fitted Nucleation Rate (a.u./min)	Absolute Nucleation Rate (#/μm^2/min)	Absolute Nucleation Rate (nm^3/μm^2/min)	Absolute Nucleation Rate (mol/m^2/min)
12 ºC	$(3.4 \pm 0.1) \times 10^{-5}$	6.1 ± 1.2	24 ± 12	$(6.6 \pm 3.2) \times 10^{-10}$
25 ºC	$(8.8 \pm 0.4) \times 10^{-5}$	15.5 ± 3.2	63 ± 31	$(17.1 \pm 8.3) \times 10^{-10}$
31 ºC	$(15 \pm 1) \times 10^{-5}$	27.0 ± 5.6	108 ± 52	$(29 \pm 14) \times 10^{-10}$
A	$\exp(15.5 \pm 2.4)$ or $10^{6.7 \pm 1.0}$	$\exp(27.6 \pm 2.5)$ or $10^{12.0 \pm 1.1}$	$\exp(29.0 \pm 2.9)$ or $10^{12.6 \pm 1.3}$	$\exp(4.6 \pm 2.9)$ or $10^{2.0 \pm 1.3}$

7.4 Discussion

7.4.1 Newly Developed GISAXS-AFM Method

The successful acquisition of kinetic factors in this study proved the validity of a new method for calibration of GISAXS data using AFM. In SAXS and GISAXS data acquisition, standard glassy carbon samples are commonly used to calibrate the scattering intensity obtained from different beamtimes. But methods for calibration of scattering intensity with absolute particle numbers for GISAXS were scarce. In this study, we developed the GISAXS-AFM method to transform GISAXS-obtained particle numbers on the substrate from arbitrary to absolute units. This method can be extended for calibration of particle numbers in other experimental systems using GISAXS as the detection technique, such as those used in (bio)material sciences, geosciences, and environmental sciences. However, several considerations are important in carrying out this method.

The first consideration is the range of experimental conditions. In our study, the $CaCO_3$ nuclei were several nanometers in radius. GISAXS is able to observe nuclei with radii between 1-80 nm. However, to have accurate AFM data, the nuclei should be several nanometers. Smaller

nuclei are hard to resolve clearly in AFM, whereas too large particles tend to hide small features. Besides particle size, particle density (#/unit area) is also important. GISAXS requires a considerable coverage of the substrate by nuclei to have a high signal-to-noise ratio, especially when the electron density of the nuclei is low, but a large number of nuclei are likely to aggregate into groups of nuclei, thus are hard to count from AFM images. The particle size and particle density on the substrate surface are functions of reaction conditions, and thus the conditions should be adjusted to enable acceptable data quality for both GISAXS and AFM. To obtain good data for GISAXS and AFM, and thus reliable statistics for parameter acquisition of E_a and factor A, our study determined the experimental condition to be at $IAP/K_{sp}=10^{1.65}$ and a temperature range of 12 –31 ^{o}C.

The second consideration is the match of *in situ* and *ex situ* tests. If both AFM and GISAXS tests are *ex situ*, the sample preparation for both techniques should be identical. However, if one of the techniques is *in situ*, the situation is more complicated, because the system setup for the *in situ* test with one technique might not be applicable for *in situ* test with the other technique. In this study, for example, the systems were designed for *in situ* GISAXS measurement, but the same setup cannot be used for *in situ* AFM tests, which require a special reaction cell and a much slower flow rate. Therefore, we did the AFM test *ex situ*. In this and similar cases, it is important to preserve the sample close to its *in situ* status. For example, instead of rinsing off the unreacted solution from the substrate with water, we used ethanol to prevent dissolution of nuclei by water. After ethanol rinsing, the samples were dried as fast as possible with ultra-pure nitrogen. The nuclei were then scanned with AFM immediately to prevent nuclei aging through aggregation, desiccation, or phase transformation. Despite the care with which *ex situ* AFM samples were

prepared, we are aware of the possible discrepancies between the *ex situ* samples and the *in situ* samples, and therefore would rely on *in situ* data (e.g., nuclei size) if available.

For different materials, these considerations might differ in details. However, with modifications, our proposed method for calibrating GISAXS intensities with absolute particle densities is transformative for calibrations of other materials tested using GISAXS.

7.4.2 Relative Importance of Thermodynamic (ΔG^*) and Kinetic (E_a) Energy Barriers.

The overall energy barrier for nucleation reactions is a combination of the kinetic energy barrier, E_a, and the thermodynamic energy barrier, ΔG^*. The thermodynamic energy barrier ΔG^* is usually referred to as "nucleation energy barrier" because it is characteristic of nucleation reactions, whereas apparent activation energy exists for virtually all chemical reactions. ΔG^* can be considerably large, thus hindering the start of precipitation in many aqueous system, such as in seed-free nanoparticle synthesis, in pipelines with scale inhibitors, or in geomedia experiencing dissolution of primary minerals and precipitation of secondary minerals. However, previous knowledge of $J_0=A\exp(-E_a/kT)$ was limited. For homogeneous nucleation, estimating the theoretical value of J_0 was possible, but for heterogeneous nucleation, even the order of magnitude of J_0 was not clear. Due to the limited information, it was hard to analyze the relative importance of ΔG^* over E_a.

This study fills this knowledge gap. The acquired J_0 allows estimation of nucleation kinetics of the correct order of magnitude, and the value of E_a enables analysis of the comparative importance of ΔG^* and E_a. As an example, Figure 7.4 shows the variation of ΔG^* as a function of either the effective interfacial energy α, or the supersaturation of the solution. The dotted lines

indicate the magnitude of E_a for comparison. The results show that at a supersaturation of $IAP/K_{sp}=10^{1.65}$, the thermodynamic energy barrier ΔG^* is larger than E_a if the effective interfacial energy α is larger than 68 mJ/m^2. Also, at a fixed α value of 47 mJ/m^2, ΔG^* exceeds E_a for supersaturations lower than $IAP/K_{sp} = 10^{0.9}$. The relative importance of kinetic and thermodynamic factors is thus revealed.

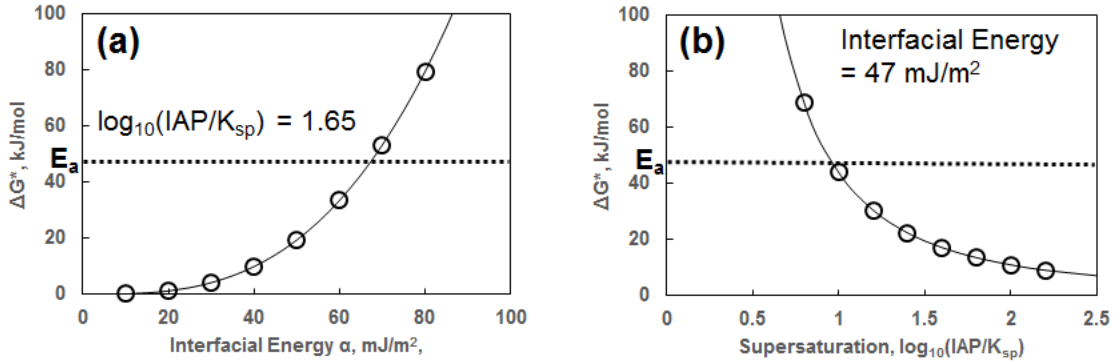

Figure 7.4. Comparison of kinetic energy barrier E_a with thermodynamic energy barrier ΔG^* for heterogeneous nucleation of $CaCO_3$ on quartz. Dotted lines are the level of E_a for comparison. Figure (a) is generated with a fixed $IAP/K_{sp}=10^{1.65}$ and varying α. Figure (b) is generated with a fixed α equal to 47 mJ/m^2 and varying $IAP/K_{sp}=10^{1.65}$. Calculations of ΔG^* are based on Eq. 7.3.

The quantification of E_a also facilitates further investigation of J_0 for nucleation in the aqueous phase. For heterogeneous nucleation in the gaseous phase, it is reported that the J_0 term is related to the impingent rate of monomers onto existing nuclei through either gaseous diffusion or surface diffusion, to the adsorption efficiency of monomers on nuclei, to the total nuclei surface area at critical size, and finally to the possibility of a critical nucleus to actually pass ΔG^*. Drawing an analogy to heterogeneous nucleation in the aqueous phase, we propose that the apparent activation energy can be understood as a combined energy barrier from monomer diffusion in

solution, monomer diffusion on the surface, adsorption of monomers on the substrate, and adsorption of monomers on nuclei.

7.5 Conclusions

This study is the first attempt to quantify kinetic terms in the nucleation rate equation, i.e., A and E_a, in the equation $J = A\exp(-\frac{E_a}{kT})\exp\left(-\frac{\Delta G^*}{kT}\right)$. The obtained apparent activation energy E_a is 45 ± 7 kJ/mol, and the pre-exponential factor A is $10^{12.0 \pm 1.1}$ # of nuclei / μm^2 of quartz substrate surface area / min, or $10^{2.0 \pm 1.3}$ mol of Ca^{2+} or CO_3^{2-} consumed from fluid / m^2 of quartz substrate surface area / min. The kinetic energy barrier E_a is associated with the series of reactions to incorporate a monomer into existing nuclei, and it is higher than the thermodynamic energy barrier ΔG^* when interfacial energy α is lower than 68 mJ/m^2, or when the supersaturation of the solution is higher than $IAP/K_{sp} = 10^{0.9}$ for the case of $CaCO_3$ precipitation. With these parameters and information, further investigation of nucleation process using reactive transport modeling can be facilitated, and an improved understanding of the comparative kinetic and thermodynamic factors' contributions to overall precipitation can be achieved.

Acknowledgments

We acknowledge Drs. Byeongdu Lee, Xiaobing Zuo, and Sönke Seifert for helping to collect GISAXS data. This work was supported by Center for Nanoscale Control of Geologic CO_2, an Energy Frontier Research Center funded by the U.S. Department of Energy, Office of Science, Office of Basic Energy Sciences, under Award Number DE-AC02-05CH11231. Use of the

Advanced Photon Source, an Office of Science User Facility operated for the U.S. Department of Energy Office of Science by Argonne National Laboratory, was supported by the U.S. DOE under Contract No. DE-AC02-06CH11357.

Chapter 8: Conclusions and Future Directions

8.1 Conclusions

To better understand interactions between geomedia and fluids in subsurface environments, in this dissertation, Portland cement was used as a model geomedium. Chemical and mechanical alterations of cement, in which $CaCO_3$ plays an important role as both a reactant and a product of related geochemical reactions, were characterized. Both experimental and modeling approaches were employed for this research, with a particular focus on $CaCO_3$ formation for detailed analyses of $CaCO_3$ nucleation. Experimental results on $CaCO_3$ nucleation facilitated our modeling investigation, which further clarified the mechanisms in our experiments.

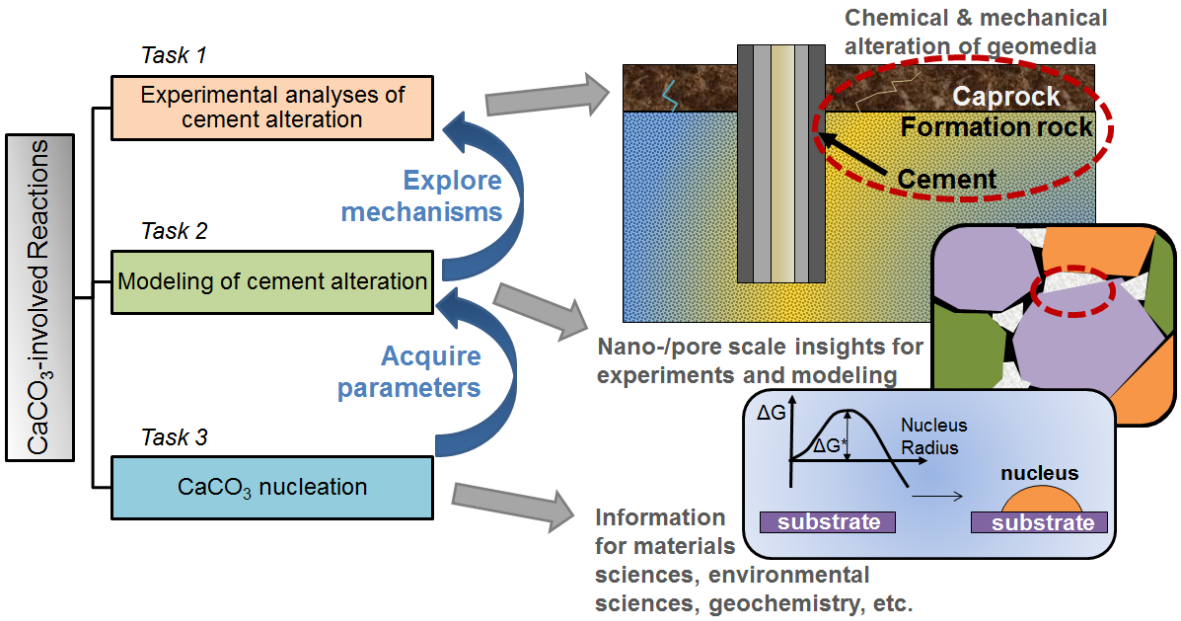

Figure 8.1 Relations among Tasks and their implications.

Task 1 focused on an experimental study of the chemical and mechanical alterations of wellbore cement under GCS conditions. Experiments were carried out in the presence and absence

of additional sulfate ions in the brine. Cement samples developed layer structures after CO_2 attack. The CO_2-attacked depth was 1220 μm for samples reacted without additional sulfate, resulting in a ~80% decrease of sample strength and elastic modulus. The weakened macroscale mechanical properties are mainly related to the microscale portlandite-depleted region in the cement samples. The CO_2-attacked samples were also more ductile and had rougher fracture surfaces. In the presence of 0.05 M sulfate, the CO_2 attacked thickness was only 800 μm, and the decrease of strength and elasticity were both ~50%. The mitigated CO_2 attack on cement was due to the coating of gypsum and/or sorption of sulfate on the $CaCO_3$ grains in the carbonated layer, reducing the dissolution rate of $CaCO_3$. Task 1 findings provide important insights into modeling and predicting wellbore integrity in energy-related subsurface operation.

In **Task 2**, we further investigated the mechanisms of portlandite-depleted zone formation using the reactive transport modeling software, CrunchTope. By calibrating the model using experimental data, two geochemical mechanisms were critical to capture the experimentally observed reaction fronts: First, precipitation of secondary phases cannot fill the pore space completely, likely because of fractures or defects in the precipitation zone, or because insufficient $CaCO_3$ precipitation in nanopores. This mechanism was incorporated into our continuum model using a "minimum porosity limit", which scales down the secondary phase precipitation rate when the porosity reaches the minimum porosity limit. A minimum porosity of 1.5% enabled our model to predict the experimentally observed brine transport in cement, and it is also a reasonable porosity approximation in the fields. Second, secondary $CaCO_3$ precipitation in brine, starting with its nucleation rate, is important. If $CaCO_3$ precipitation in the brine is not considered, the model with closed boundaries predicts that the dissolution of the cement surface should stop when the brine is saturated with $CaCO_3$. However, during experiments, continuous dissolution was observed at the

cement surface. This discrepancy suggests that the secondary phases in brine and in cement have different thermodynamics, such that the phases in cement can dissolve and re-precipitate in the brine. After the modeling code was updated with the nucleation rate law for a stable $CaCO_3$ phase in the brine, the model accurately predicted the dissolution of the cement surface as observed in experiments. This task highlights the importance of including pore scale insights and nucleation in the overall model of a geochemical/geotechnical problem.

Task 3 aimed at acquiring thermodynamic and kinetic parameters for $CaCO_3$ nucleation, and elucidating the nucleation mechanisms. It is split into three sections: The first aims to compare mica and quartz as the nucleation substrates. The second section evaluates the effects of salinity, and the third quantifies the kinetic factors in the nucleation equation. Known thermodynamic parameters for calcite were used in calculations to avoid unnecessary complications with $CaCO_3$ phase transformation. While the absolute values will be shifted, the trends will be the same if parameters for other $CaCO_3$ phases are used for calculation. Regarding substrate comparison, the interfacial energy for $CaCO_3$ nucleation on mica was 41 ± 2 mJ/m^2, lower than the energy of 47 ± 1 mJ/m^2 for nucleation on quartz. Correspondingly, the nuclei were smaller in the mica system, and the nucleation rates were faster than in the quartz system. Focusing on the quartz system, we found that the interfacial energy decreased with increasing salinity, from ~48 mJ/m^2 in 0.15 and 0.30 M salinities to ~35 mJ/m^2 in 0.50 and 0.85 M salinities. Meanwhile, the kinetic factors A and E_a also changed such that the $A\exp(-\frac{E_a}{kT})$ term in the nucleation rate equation, $J = A\exp(-\frac{E_a}{kT})\exp\left(-\frac{\Delta G^*}{kT}\right)$, was lower at high salinities. The overall effects of high salinity were increased nucleation rates for a given supersaturation, decreased nucleus size, and shortened induction times. $CaCO_3$ nucleation was further investigated at 0.15 M salinity over a temperature

range of 12–31 ºC. The change of temperature did not appreciably affect nucleus sizes. From the calibration of GISAXS intensities with AFM images, E_a and A were calculated to be 45 kJ/mol and $10^{2.0 \pm 1.3}$ mol/m^2/min, respectively. These outcomes strengthened our understanding of nucleation and enabled reactive transport modeling to include the nucleation reaction, and important factor in improving model accuracy.

8.2 Recommended Future Directions

Our new understanding and insights gained over the course of this research open the doors to broader and deeper studies on related topics.

To elucidate interactions between geomedia and fluid, this study used cement as a model geomedium and CO_2 saturated brine as the fluid. The system can be extended to include more geomedia, more complex solution compositions, or conditions other than those occurring during GCS. For example, the dissolution and precipitation reactions between naturally-present rocks and CO_2-saturated brine can follow the same trend as in cement.[174] During GCS operation, the CO_2 plume or CO_2-saturated brine is pushed through formation rocks by the injection pressure. Under ideal operation conditions, CO_2 mineralization should not happen near to the injection point, where it can block injection fluids, nor too far away, where it may not trap CO_2 efficiently.[40] In this case, holistic investigations of CO_2 reactive transport through porous formation rock, using both experimental approaches to understand geochemical reactions and modeling approaches to predict larger scales and longer reaction times, can help estimate the CO_2 mineralization locations and optimize CO_2 injection parameters (e.g., tuning the injection rates and pressures and adjusting the chemical composition of injected fluid). Another key factor which needs to be examined is the reactivity of shales that act as a caprock to trap CO_2. As a barrier for CO_2 structural trapping, it is important to determine whether the fractures or open pores in shale can lead to CO_2 leakage and whether CO_2 can trigger precipitation to seal these shale fractures and pores. Previous studies have focused mostly on the dissolution of reactive minerals, such as carbonates, in shale matrices when exposed to acidic brine.[277] However, the precipitation of carbonate and other minerals, which is expected to prevent CO_2 leakage, has not been studied sufficiently, especially in real shales.[278]

In addition, further research is needed to strengthen the linkage between chemical reactions and mechanical changes. Results from Task 1 show that when geomedia have been altered chemically, their mechanical properties can also change, altering their tendency to fracture. The fracture geometries will also change accordingly, thus changing the reactive surface areas and fluid transport pathways. Therefore, when bridging chemical reactions and mechanical changes of geomedia, both the chemical-reaction-induced mechanical property changes and the aftermath of these mechanical property changes should be considered. Further investigations should focus on more tightly linking geochemistry and geomechanical alterations.

Specific studies are recommended to more fully characterize the cement system. In Task 2, we found that cement deterioration under GCS conditions can be mitigated by the formation of a thicker and less porous carbonated layer. Thus, we recommend that further studies determine which conditions promote stronger carbonated layers. For example, the brine composition can be tuned to inhibit the precipitation of stable forms of $CaCO_3$, thus helping to prevent dissolution from the cement surface. Alternatively, the dissolution of the cement surface could be inhibited by adding a proper inhibitor in the solution. As a result, the carbonated layer in these systems is expected to be thicker and more protective. Findings in Task 2 also suggest that if $CaCO_3$ precipitation can fill more pore spaces, cement deterioration will be mitigated. Corresponding strategies include modifying the solid chemistry of cement pore walls to trigger $CaCO_3$ precipitation in nanopores, or modifying the mechanical properties of cement to hinder fracture formation.

In terms of nucleation, we recommend further studies on nucleation in confined pore spaces, because Task 2 suggested that the $CaCO_3$ phase formed in pores can have different solubility than that formed in a free space. We also recommend studies on the effects of organic

compounds on nucleation, because organic compounds are abundant in subsurface environments, especially in depleted oil/gas reservoirs. The nucleating materials should not be limited to $CaCO_3$, but rather thermodynamic and kinetic parameters for nucleation should be measured or estimated for a range of minerals. Thus, a database for nucleation reaction can be built. Incorporating phase transformation is another future direction. In this study, phase transformation has not been included, but it is expected that nanometer-sized nuclei have different properties than bulk materials, such as specific surface area, surface reactivity, molecular volume, and solubility. A demonstration of the importance of phase transformation during nucleation and growth will be instructive, and will smooth the transition from nucleation to surface growth in reactive transport models.

In summary, studies presented in this dissertation demonstrated coupled chemical and mechanical alterations in cement under GCS conditions, revealed the importance of pore scale insights in reactive transport of acidic brine in cement, and obtained vital information regarding $CaCO_3$ nucleation kinetics and thermodynamics. These research outcomes pave the way for further studies on the reaction and transport of fluid in geomedia, on more closely coupling chemical and mechanical geomedia changes, on finding engineering strategies to improve wellbore cement integrity, and on nucleation in more dynamic and complex systems.

References

1. Le Quéré, C.; Moriarty, R.; Andrew, R. M.; Canadell, J. G.; Sitch, S.; Korsbakken, J. I.; Friedlingstein, P.; Peters, G. P.; Andres, R. J.; Boden, T., Global Carbon Budget 2015. *Earth System Science Data* **2015,** *7*, (2), 349-396.

2. Brown, D.; Cabbage, M.; McCarthy, L.; Norton, K., NASA, NOAA Analyses Reveal Record-Shattering Global Warm Temperatures in 2015. In NASA press release; 2016.

3. Allison, I.; Bindoff, N.; Bindschadler, R.; Cox, P.; de Noblet, N.; England, M.; Francis, J.; Gruber, N.; Haywood, A.; Karoly, D., *The Copenhagen Diagnosis: Updating the World on the Latest Climate Science*. Elsevier: 2011.

4. Metz, B.; Davidson, O.; De Coninck, H.; Loos, M.; Meyer, L. *IPCC Special Report on Carbon Dioxide Capture and Storage*; 2005.

5. IEA, O., Energy Technology Perspectives. In Paris: 2008.

6. Oelkers, E. H.; Cole, D. R., Carbon Dioxide Sequestration a Solution to a Global Problem. *Elements* **2008,** *4*, (5), 305-310.

7. DePaolo, D. J.; Cole, D. R., Geochemistry of Geologic Carbon Sequestration: An Overview. *Rev. Mineral. Geochem.* **2013,** *77*, (1), 1-14.

8. Benson, S. M.; Cole, D. R., CO_2 Sequestration in Deep Sedimentary Formations. *Elements* **2008,** *4*, (5), 325-331.

9. Jun, Y. S.; Giammar, D. E.; Werth, C. J., Impacts of Geochemical Reactions on Geologic Carbon Sequestration. *Environ. Sci. Technol.* **2013,** *47*, (1), 3-8.

10. Audigane, P.; Gaus, I.; Pruess, K.; Xu, T. In *Reactive Transport Modeling using TOUGHREACT for the Long Term CO_2 Storage at Sleipner, North Sea*, Fourth Annual Conference on Carbon Capture and Sequestration DOE/NETL, 2005; 2005.

11. Lu, J.; Kharaka, Y. K.; Thordsen, J. J.; Horita, J.; Karamalidis, A.; Griffith, C.; Hakala, J. A.; Ambats, G.; Cole, D. R.; Phelps, T. J., CO_2-Rock–Brine Interactions in Lower Tuscaloosa Formation at Cranfield CO_2 Sequestration Site, Mississippi, USA. *Chem. Geol.* **2012,** *291*, 269-277.

12. Carey, J. W., Geochemistry of Wellbore Integrity in CO_2 Sequestration: Portland Cement-steel-brine-CO_2 Interactions. *Rev. Mineral. Geochem.* **2013,** *77*, (1), 505-539.

13. Tegethoff, F. W.; Rohleder, J. W.; Kroker, E., *Calcium Carbonate: from the Cretaceous Period into the 21st Century*. Springer: 2001.

14. Nogues, J. P.; Fitts, J. P.; Celia, M. A.; Peters, C. A., Permeability Evolution due to Dissolution and Precipitation of Carbonates using Reactive Transport Modeling in Pore Networks. *Water Resour. Res.* **2013**.

15. Nemati, M.; Voordouw, G., Modification of Porous Media Permeability, using Calcium Carbonate Produced Enzymatically *in situ*. *Enzyme Microb. Technol.* **2003,** *33*, (5), 635-642.

16. Zheng, Z.; Tokunaga, T. K.; Wan, J., Influence of calcium carbonate on U (VI) sorption to soils. *Environmental Science & Technology* **2003,** *37*, (24), 5603-5608.

17. Cai, G.-B.; Zhao, G.-X.; Wang, X.-K.; Yu, S.-H., Synthesis of polyacrylic acid stabilized amorphous calcium carbonate nanoparticles and their application for removal of toxic heavy metal ions in water. *J. Phys. Chem. C* **2010,** *114*, (30), 12948-12954.

18. Bissen, M.; Frimmel, F. H., Arsenic—A Review. Part II: Oxidation of Arsenic and Its Removal in Water Treatment. *Acta Hydrochim. Hydrobiol.* **2003,** *31*, (2), 97-107.

19. Koyikkal, S., *Chemical Process Technology and Simulation* PHI learning: 2013; p 352.

20. Whiffin, V. S.; van Paassen, L. A.; Harkes, M. P., Microbial Carbonate Precipitation as a Soil Improvement Technique. *Geomicrobiology Journal* **2007,** *24*, (5), 417-423.

21. Antony, A.; Low, J. H.; Gray, S.; Childress, A. E.; Le-Clech, P.; Leslie, G., Scale formation and control in high pressure membrane water treatment systems: A review. *Journal of Membrane Science* **2011,** *383*, (1), 1-16.

22. Waly, T.; Kennedy, M. D.; Witkamp, G.-J.; Amy, G.; Schippers, J. C., The role of inorganic ions in the calcium carbonate scaling of seawater reverse osmosis systems. *Desalination* **2012,** *284*, 279-287.

23. Yu, L. L.; Sun, X. R.; Wang, B. H.; Lei, L., The Influencing Factors of $CaCO_3$ Scaling in Oilfield. *Appl. Mech. Mater.* **2012,** *170*, 1230-1233.

24. Sand, K. K.; Rodriguez-Blanco, J. D.; Makovicky, E.; Benning, L.; Stipp, S. L. S., Crystallization of $CaCO_3$ in Water–Alcohol Mixtures: Spherulitic Growth, Polymorph Stabilization, and Morphology Change. *Cryst. Growth Des.* **2011,** *12*, (2), 842-853.

25. Teng, H. H.; Dove, P. M.; De Yoreo, J. J., Kinetics of Calcite Growth: Surface Processes and Relationships to Macroscopic Rate Laws. *Geochim. Cosmochim. Acta* **2000,** *64*, (13), 2255-2266.

26. Radha, A.; Forbes, T. Z.; Killian, C. E.; Gilbert, P.; Navrotsky, A., Transformation and Crystallization Energetics of Synthetic and Biogenic Amorphous Calcium Carbonate. *Proceedings of the National Academy of Sciences* **2010,** *107*, (38), 16438-16443.

27. Ihli, J.; Wong, W. C.; Noel, E. H.; Kim, Y.-Y.; Kulak, A. N.; Christenson, H. K.; Duer, M. J.; Meldrum, F. C., Dehydration and Crystallization of Amorphous Calcium Carbonate in Solution and in Air. *Nat. Commun.* **2014,** *5*.

28. Nielsen, M. H.; Aloni, S.; De Yoreo, J. J., In Situ TEM Imaging of $CaCO_3$ Nucleation Reveals Coexistence of Direct and Indirect Pathways. *Science* **2014,** *345*, (6201), 1158-1162.

29. Stephens, C. J.; Mouhamad, Y.; Meldrum, F. C.; Christenson, H. K., Epitaxy of Calcite on Mica. *Cryst. Growth Des.* **2009,** *10*, (2), 734-738.

30. De Yoreo, J. J.; Waychunas, G. A.; Jun, Y.-S.; Fernandez-Martinez, A., *In Situ* Investigations of Carbonate Nucleation on Mineral and Organic Surfaces. *Rev. Mineral. Geochem.* **2013,** *77*, (1), 229-257.

31. Fernandez-Martinez, A.; Hu, Y.; Lee, B.; Jun, Y.-S.; Waychunas, G. A., In Situ Determination of Interfacial Energies between Heterogeneously Nucleated $CaCO_3$ and Quartz Substrates: Thermodynamics of CO_2 Mineral Trapping. *Environ. Sci. Technol.* **2013,** *47*, (1), 102-109.

32. Hamm, L. M.; Giuffre, A. J.; Han, N.; Tao, J.; Wang, D.; De Yoreo, J. J.; Dove, P. M., Reconciling Disparate Views of Template-Directed Nucleation Through Measurement of Calcite Nucleation Kinetics and Binding Energies. *Proc. Natl. Acad. Sci. USA.* **2014,** *111*, (4), 1304-1309.

33. Hu, Q.; Nielsen, M. H.; Freeman, C.; Hamm, L.; Tao, J.; Lee, J.; Han, T. Y.-J.; Becker, U.; Harding, J.; Dove, P., The Thermodynamics of Calcite Nucleation at Organic Interfaces: Classical vs. Non-Classical Pathways. *Faraday Discuss.* **2012,** *159*, (1), 509-523.

34. Bischoff, J. L., Kinetics of Calcite Nucleation: Magnesium Ion Inhibition and Ionic Strength Catalysis. *J. Geophys. Res.* **1968,** *73*, (10), 3315-3322.

35. Giuffre, A. J.; Hamm, L. M.; Han, N.; De Yoreo, J. J.; Dove, P. M., Polysaccharide Chemistry Regulates Kinetics of Calcite Nucleation through Competition of Interfacial Energies. *Proc. Natl. Acad. Sci. USA.* **2013,** *110*, (23), 9261-9266.

36. Liu, X. Y.; Tsukamoto, K.; Sorai, M., New Kinetics of $CaCO_3$ Nucleation and Microgravity Effect. *Langmuir* **2000,** *16*, (12), 5499-5502.

37. Steefel, C. I.; Van Cappellen, P., A New Kinetic Approach to Modeling Water-rock Interaction: The Role of Nucleation, Precursors, and Ostwald Ripening. *Geochim. Cosmochim. Acta* **1990,** *54*, (10), 2657-2677.

38. Thomas, J. J., A New Approach to Modeling the Nucleation and Growth Kinetics of Tricalcium Silicate Hydration. *J. Am. Ceram. Soc.* **2007,** *90*, (10), 3282-3288.

39. Thomas, J. J.; Jennings, H. M.; Chen, J. J., Influence of Nucleation Seeding on the Hydration Mechanisms of Tricalcium Silicate and Cement. *J. Phys. Chem. C* **2009,** *113*, (11), 4327-4334.

40. Stack, A. G., Precipitation in Pores: A Geochemical Frontier. *Rev. Mineral. Geochem.* **2015,** *80*, 165-190.

41. Taylor, H. F., *Cement Chemistry*. Thomas Telford: 1997.

42. Kutchko, B. G.; Strazisar, B. R.; Dzombak, D. A.; Lowry, G. V.; Thaulow, N., Degradation of Well Cement by CO_2 under Geologic Sequestration Conditions. *Environ. Sci. Technol.* **2007,** *41*, (13), 4787-4792.

43. Alemu, B. L.; Aagaard, P.; Munz, I. A.; Skurtveit, E., Caprock Interaction with CO_2: A Laboratory Study of Reactivity of Shale with Supercritical CO_2 and Brine. *Appl. Geochem.* **2011,** *26*, (12), 1975-1989.

44. Yin, H.; Zhou, J.; Jiang, Y.; Xian, X.; Liu, Q., Physical and Structural Changes in Shale Associated with Supercritical CO_2 Exposure. *Fuel* **2016,** *184*, 289-303.

45. Zhang, L.; Kim, Y.; Jung, H.; Wan, J.; Jun, Y.-S., Effects of Salinity-Induced Chemical Reactions on Biotite Wettability Changes under Geologic CO_2 Sequestration Conditions. *Environ. Sci. Technol. Lett.* **2016,** *3*, (3), 92-97.

46. Steefel, C.; Appelo, C.; Arora, B.; Jacques, D.; Kalbacher, T.; Kolditz, O.; Lagneau, V.; Lichtner, P.; Mayer, K. U.; Meeussen, J., Reactive Transport Codes for Subsurface Environmental Simulation. *Computat. Geosci.* **2015,** *19*, (3), 445-478.

47. Steefel, C. I.; DePaolo, D. J.; Lichtner, P. C., Reactive Transport Modeling: An Essential Tool and a New Research Approach for the Earth sciences. *Earth Planet. Sci. Lett.* **2005,** *240*, (3), 539-558.

48. Gherardi, F.; Audigane, P.; Gaucher, E. C., Predicting Long-term Geochemical Alteration of Wellbore Cement in a Generic Geological CO_2 Confinement Site: Tackling a Difficult Reactive Transport Modeling Challenge. *J. Hydrol.* **2012,** *420*, 340-359.

49. Brunet, J.-P. L.; Li, L.; Karpyn, Z. T.; Kutchko, B. G.; Strazisar, B.; Bromhal, G., Dynamic Evolution of Cement Composition and Transport Properties under Conditions Relevant to Geological Carbon Sequestration. *Energy Fuels* **2013,** *27*, (8), 4208-4220.

50. Jung, H. B.; Um, W., Experimental Study of Potential Wellbore Cement Carbonation by Various Phases of Carbon Dioxide during Geologic Carbon Sequestration. *Appl. Geochem.* **2013,** *35*, 161-172.

51. Kutchko, B. G.; Strazisar, B. R.; Huerta, N.; Lowry, G. V.; Dzombak, D. A.; Thaulow, N., CO_2 Reaction with Hydrated Class H Well Cement under Geologic Sequestration Conditions: Effects of Flyash Admixtures. *Environ. Sci. Technol.* **2009,** *43*, (10), 3947-3952.

52. Barlet-Gouédard, V.; Rimmelé, G.; Porcherie, O.; Quisel, N.; Desroches, J., A Solution Against Well Cement Degradation under CO_2 Geological Storage Environment. *Int. J. Greenh. Gas Control* **2009,** *3*, (2), 206-216.

53. Keller, S. J., *Analyses of Subsurface Brines of Indiana*. State of Indiana, Department of Natural Resources, Geological Survey: 1983.

54. Sjöberg, E. L., Kinetics and Mechanism of Calcite Dissolution in Aqueous Solutions at Low Temperatures. **1978**.

55. Zhu, M.; Northrup, P.; Shi, C.; Billinge, S. J.; Sparks, D. L.; Waychunas, G. A., Structure of Sulfate Adsorption Complexes on Ferrihydrite. *Environ. Sci. Technol. Lett.* **2013,** *1*, (1), 97-101.

56. Huet, B. M.; Prevost, J. H.; Scherer, G. W., Quantitative Reactive Transport Modeling of Portland Cement in CO_2-saturated Water. *Int. J. Greenh. Gas Control* **2010,** *4*, (3), 561-574.

57. Scherer, G. W.; Huet, B., Carbonation of Wellbore Cement by CO_2 Diffusion from Caprock. *Int. J. Greenh. Gas Control* **2009,** *3*, (6), 731-735.

58. Watson, C.; Savage, D.; Wilson, J.; Benbow, S.; Walker, C.; Norris, S., The Tournemire Industrial Analogue: Reactive-Transport Modelling of a Cement–Clay Interface. *Clay Miner.* **2013,** *48*, (2), 167-184.

59. Zhang, L.; Dzombak, D. A.; Nakles, D. V.; Brunet, J.-P. L.; Li, L., Reactive Transport Modeling of Interactions between Acid Gas (CO_2 + H_2S) and Pozzolan-Amended Wellbore

Cement under Geologic Carbon Sequestration Conditions. *Energy Fuels* **2013,** *27*, (11), 6921-6937.

60. Gherardi, F.; Audigane, P., Modeling Geochemical Reactions in Wellbore Cement: Assessing Pre-injection Integrity in a Site for CO_2 Geological Storage. *Greenh. Gases* **2013,** *3*, (6), 447-474.

61. Lasaga, A. C., *Kinetic Theory in the Earth Sciences*. Princeton University Press: 1998.

62. Jun, Y.-S.; Giammar, D. E.; Werth, C. J., Impacts of Geochemical Reactions on Geologic Carbon Sequestration. *Environ. Sci. Technol.* **2013,** *47*, (1), 3-8.

63. Neville, A. M., *Properties of Concrete*. Fifth ed.; Prentice Hall: 2012.

64. Rendell, F.; Jauberthie, R.; Grantham, M., *Deteriorated Concrete: Inspection and Physicochemical Analysis*. Thomas Telford: 2002.

65. Gasda, S. E.; Bachu, S.; Celia, M. A., Spatial Characterization of the Location of Potentially Leaky Wells Penetrating a Deep Saline Aquifer in a Mature Sedimentary Basin. *Environ. Geol.* **2004,** *46*, (6-7), 707-720.

66. Nordbotten, J. M.; Celia, M. A.; Bachu, S.; Dahle, H. K., Semianalytical Solution for CO_2 Leakage through an Abandoned Well. *Environ. Sci. Technol.* **2005,** *39*, (2), 602-611.

67. Carey, J. W.; Wigand, M.; Chipera, S. J.; WoldeGabriel, G.; Pawar, R.; Lichtner, P. C.; Wehner, S. C.; Raines, M. A.; Guthrie Jr, G. D., Analysis and Performance of Oil Well Cement with 30 Years of CO_2 Exposure from the SACROC Unit, West Texas, USA. *Int. J. Greenh. Gas Control* **2007,** *1*, (1), 75-85.

68. Newell, D. L.; Carey, J. W., Experimental Evaluation of Wellbore Integrity Along the Cement-Rock Boundary. *Environ. Sci. Technol.* **2012,** *47*, (1), 276-282.

69. Duguid, A.; Radonjic, M.; Scherer, G. W., Degradation of Cement at the Reservoir/Cement Interface from Exposure to Carbonated Brine. *Int. J. Greenh. Gas Control* **2011,** *5*, (6), 1413-1428.

70. Gaboreau, S.; Lerouge, C.; Dewonck, S.; Linard, Y.; Bourbon, X.; Fialips, C.; Mazurier, A.; Prêt, D.; Borschneck, D.; Montouillout, V., In-situ Interaction of Cement Paste and Shotcrete with Claystones in a Deep Disposal Context. *Am. J. Sci.* **2012,** *312*, (3), 314-356.

71. Huerta, N. J.; Hesse, M. A.; Bryant, S. L.; Strazisar, B. R.; Lopano, C. L., Experimental Evidence for Self-limiting Reactive Flow Through a Fractured Cement Core: Implications for Time-dependent Wellbore Leakage. *Environ. Sci. Technol.* **2012,** *47*, (1), 269-275.

72. Jung, H. B.; Jansik, D.; Um, W., Imaging Wellbore Cement Degradation by Carbon Dioxide under Geologic Sequestration Conditions using X-Ray Computed Microtomography. *Environ. Sci. Technol.* **2012,** *47*, (1), 283-289.

73. Mason, H. E.; Du Frane, W. L.; Walsh, S. D.; Dai, Z.; Charnvanichborikarn, S.; Carroll, S. A., Chemical and Mechanical Properties of Wellbore Cement Altered by CO_2-rich Brine using a Multianalytical Approach. *Environ. Sci. Technol.* **2013,** *47*, (3), 1745-1752.

74. Carey, J. W.; Svec, R.; Grigg, R.; Zhang, J.; Crow, W., Experimental Investigation of Wellbore Integrity and CO_2–Brine Flow Along the Casing–Cement Microannulus. *Int. J. Greenh. Gas Control* **2010,** *4*, (2), 272-282.

75. Crow, W.; Carey, J. W.; Gasda, S.; Brian Williams, D.; Celia, M., Wellbore Integrity Analysis of a Natural CO_2 Producer. *Int. J. Greenh. Gas Control* **2010,** *4*, (2), 186-197.

76. Scherer, G. W.; Kutchko, B.; Thaulow, N.; Duguid, A.; Mook, B., Characterization of Cement from a Well at Teapot Dome Oil Field: Implications for Geological Sequestration. *Int. J. Greenh. Gas Control* **2011,** *5*, (1), 115-124.

77. Kutchko, B. G.; Strazisar, B. R.; Lowry, G. V.; Dzombak, D. A.; Thaulow, N., Rate of CO_2 Attack on Hydrated Class H Well Cement under Geologic Sequestration Conditions. *Environ. Sci. Technol.* **2008,** *42*, (16), 6237-6242.

78. Zhang, L.; Dzombak, D. A.; Nakles, D. V.; Hawthorne, S. B.; Miller, D. J.; Kutchko, B. G.; Lopano, C. L.; Strazisar, B. R., Characterization of Pozzolan-Amended Wellbore Cement Exposed to CO_2 and H_2S Gas Mixtures under Geologic Carbon Storage Conditions. *Int. J. Greenh. Gas Control* **2013,** *19*, 358-368.

79. Zhang, L.; Dzombak, D. A.; Nakles, D. V.; Hawthorne, S. B.; Miller, D. J.; Kutchko, B. G.; Lopano, C. L.; Strazisar, B. R., Rate of H_2S and CO_2 Attack on Pozzolan-Amended Class H Well Cement under Geologic Sequestration Conditions. *Int. J. Greenh. Gas Control* **2014,** *27*, 299-308.

80. Cao, P.; Karpyn, Z.; Li, L., Dynamic Changes in Wellbore Cement Integrity Due to Geochemical Reactions in CO_2-rich Environments. *Water Resour. Res.* **2013,** *49*, 1-11.

81. Duguid, A.; Scherer, G. W., Degradation of Oilwell Cement due to Exposure to Carbonated Brine. *Int. J. Greenh. Gas Control* **2010,** *4*, (3), 546-560.

82. Kutchko, B. G.; Strazisar, B. R.; Hawthorne, S. B.; Lopano, C. L.; Miller, D. J.; Hakala, J. A.; Guthrie, G. D., H_2S–CO_2 Reaction with Hydrated Class H Well Cement: Acid-gas Injection and CO_2 Co-Sequestration. *Int. J. Greenh. Gas Control* **2011,** *5*, (4), 880-888.

83. Jacquemet, N.; Pironon, J.; Saint-Marc, J., Mineralogical Changes of a Well Cement in Various H_2S-CO_2(-brine) Fluids at High Pressure and Temperature. *Environ. Sci. Technol.* **2007,** *42*, (1), 282-288.

84. Matteo, E. N.; Scherer, G. W.; Huet, B.; Pel, L., Understanding Boundary Condition Effects on the Corrosion Kinetics of Class H Well Cement. *Energy Procedia* **2011,** *4*, 5370-5376.

85. Matteo, E. N.; Scherer, G. W., Experimental Study of the Diffusion-Controlled Acid Degradation of Class H Portland Cement. *Int. J. Greenh. Gas Control* **2012,** *7*, 181-191.

86. Abdoulghafour, H.; Luquot, L.; Gouze, P., Characterization of the Mechanisms Controlling the Permeability Changes of Fractured Cements Flowed through by CO_2-rich Brine. *Environ. Sci. Technol.* **2013,** *47*, (18), 10332-10338.

87. Walsh, S. D.; Du Frane, W. L.; Mason, H. E.; Carroll, S. A., Permeability of Wellbore-Cement Fractures Following Degradation by Carbonated Brine. *Rock Mech Rock Eng.* **2013,** *46*, (3), 455-464.

88. Walsh, S. D.; Mason, H. E.; Du Frane, W. L.; Carroll, S. A., Experimental Calibration of a Numerical Model Describing the Alteration of Cement/Caprock Interfaces by Carbonated Brine. *Int. J. Greenh. Gas Control* **2014,** *22*, 176-188.

89. Fabbri, A.; Jacquemet, N.; Seyedi, D., A Chemo-Poromechanical Model of Oilwell Cement Carbonation under CO_2 Geological Storage Conditions. *Cem. Concr. Res.* **2012,** *42*, (1), 8-19.

90. Xu, T.; Kharaka, Y. K.; Doughty, C.; Freifeld, B. M.; Daley, T. M., Reactive Transport Modeling to Study Changes in Water Chemistry Induced by CO_2 Injection at the Frio-I Brine Pilot. *Chem. Geol.* **2010,** *271*, (3), 153-164.

91. Walsh, S. D.; Mason, H. E.; Du Frane, W. L.; Carroll, S. A., Mechanical and Hydraulic Coupling in Cement–Caprock Interfaces Exposed to Carbonated Brine. *Int. J. Greenh. Gas Control* **2014,** *25*, 109-120.

92. Allahverdi, A.; Škvára, F., Acidic Corrosion of Hydrated Cement Based Materials. *Ceram.-Silik.* **2000,** *44*, (4), 152-160.

93. Bruckdorfer, R. In *Carbon Dioxide Corrosion in Oilwell Cements*, SPE Rocky Mountain Regional Meeting, 1986; Society of Petroleum Engineers: 1986.

94. Fabbri, A.; Corvisier, J.; Schubnel, A.; Brunet, F.; Goffé, B.; Rimmele, G.; Barlet-Gouédard, V., Effect of Carbonation on the Hydro-Mechanical Properties of Portland Cements. *Cem. Concr. Res.* **2009,** *39*, (12), 1156-1163.

95. Maierhofer, C.; Reinhardt, H.-W.; Dobmann, G., *Non-Destructive Evaluation of Reinforced Concrete Structures: Non-destructive Testing Methods*. Elsevier: 2010; Vol. 2.

96. Lloyd, G. E., Atomic Number and Crystallographic Contrast Images with the SEM: A Review of Backscattered Electron Techniques. *Mineral. Mag.* **1987,** *51*, (359), 3-19.

97. Scrivener, K. L., Backscattered Electron Imaging of Cementitious Microstructures: Understanding and Quantification. *Cem. Concr. Compos.* **2004,** *26*, (8), 935-945.

98. Walker, H. N. *Petrographic Methods of Examining Hardened Concrete: A Petrographic Manual*; 1997.

99. Stutzman, P., Chemistry and Structure of Hydration Products. In *Cements Research Progress*, 1997; pp 29-65.

100. Schmid, S. R.; Hamrock, B. J.; Jacobson, B. O., *Fundamentals of Machine Elements*. CRC Press: 2013.

101. Hibbeler, R. C.; Fan, S., *Statics and Mechanics of Materials*. Prentice Hall Singapore: 2004.

102. Standard, A. S. T. M., C 1018, Standard Test Method for Flexural Toughness and First Crack Strength of Fibre Reinforced Concrete (Using Beam with Third-point Loading). In 1997.

103. Charkaluk, E.; Bigerelle, M.; Iost, A., Fractals and Fracture. *Eng. Fract. Mech.* **1998,** *61*, (1), 119-139.

104. Davidson, D., Fracture Surface Roughness as a Gauge of Fracture Toughness: Aluminium-particulate SiC Composites. *J. Mater. Sci.* **1989,** *24*, (2), 681-687.

105. Issa, M. A.; Issa, M. A.; Islam, M. S.; Chudnovsky, A., Fractal Dimension—A Measure of Fracture Roughness and Toughness of Concrete. *Eng. Fract. Mech.* **2003,** *70*, (1), 125-137.

106. Sabir, B.; Wild, S.; Asili, M., On the Tortuosity of the Fracture Surface in Concrete. *Cem. Concr. Res.* **1997,** *27*, (5), 785-795.

107. Zhang, M.; Bachu, S., Review of Integrity of Existing Wells in Relation to CO_2 Geological Storage: What do We Know? *Int. J. Greenh. Gas Control* **2011,** *5*, (4), 826-840.

108. Yang, Y.; Min, Y.; Jun, Y.-S., A Mechanistic Understanding of Plagioclase Dissolution Based on Al Occupancy and T–O Bond Length: from Geologic Carbon Sequestration to Ambient Conditions. *Phys. Chem. Chem. Phys.* **2013,** *15*, (42), 18491-18501.

109. Yang, Y.; Min, Y.; Jun, Y.-S., Structure-Dependent Interactions Between Alkali Feldspars and Organic Compounds: Implications for Reactions in Geologic Carbon Sequestration. *Environ. Sci. Technol.* **2012,** *47*, (1), 150-158.

110. Yang, Y.; Ronzio, C.; Jun, Y.-S., The Effects of Initial Acetate Concentration on CO_2–Brine-Anorthite Interactions under Geologic CO_2 Sequestration Conditions. *Energ. Environ. Sci.* **2011,** *4*, (11), 4596-4606.

111. Shao, H.; Ray, J. R.; Jun, Y.-S., Effects of Salinity and the Extent of Water on Supercritical CO_2-induced Phlogopite Dissolution and Secondary Mineral Formation. *Environ. Sci. Technol.* **2011,** *45*, (4), 1737-1743.

112. Shao, H.; Ray, J. R.; Jun, Y.-S., Effects of Organic Ligands on Supercritical CO_2-induced Phlogopite Dissolution and Secondary Mineral Formation. *Chem. Geol.* **2011,** *290*, (3), 121-132.

113. Hu, Y.; Ray, J. R.; Jun, Y.-S., Biotite–Brine Interactions under Acidic Hydrothermal Conditions: Fibrous Illite, Goethite, and Kaolinite Formation and Biotite Surface Cracking. *Environ. Sci. Technol.* **2011,** *45*, (14), 6175-6180.

114. Hu, Y.; Ray, J. R.; Jun, Y.-S., Na^+, Ca^{2+}, and Mg^{2+} in Brines Affect Supercritical CO_2–Brine–Biotite Interactions: Ion Exchange, Biotite Dissolution, and Illite Precipitation. *Environ. Sci. Technol.* **2012,** *47*, (1), 191-197.

115. Min, Y.; Kubicki, J. D.; Jun, Y.-S., Plagioclase Dissolution during CO_2–SO_2 Cosequestration: Effects of Sulfate. *Environ. Sci. Technol.* **2015,** *49*, (3), 1946-1954.

116. Pollard, A. M.; Heron, C., *Archaeological Chemistry*. Royal Society of Chemistry: 2008.

117. Paige, C.; Snodgrass, W.; Nicholson, R.; Scharer, J., An Arsenate Effect on Ferrihydrite Dissolution Kinetics under Acidic Oxic Conditions. *Water Res.* **1997,** *31*, (9), 2370-2382.

118. Wigand, M.; Kaszuba, J. P.; Carey, J. W.; Hollis, W. K., Geochemical Effects of CO_2 Sequestration on Fractured Wellbore Cement at the Cement/Caprock Interface. *Chem. Geol.* **2009,** *265*, (1), 122-133.

119. Li, Q.; Lim, Y. M.; Flores, K. M.; Kranjc, K.; Jun, Y.-S., Chemical Reactions of Portland Cement with Aqueous CO_2 and Their Impacts on Cement's Mechanical Properties under CO_2 Sequestration Conditions. *Environ. Sci. Technol.* **2015,** *49*, (10), 5476-5483.

120. Database, W., Wyoming Database for Formation Waters: Sulfate Concentrations. In.

121. Skalny, J.; Brown, P., *Sulfate Attack on Concrete*. Taylor & Francis: 2002.

122. Neville, A., The Confused World of Sulfate Attack on Concrete. *Cem. Concr. Res.* **2004,** *34*, (8), 1275-1296.

123. Frias, M.; Sánchez de Rojas, M. I.; Santamaría, J.; Rodríguez, C., Recycling of Silicomanganese Slag as Pozzolanic Material in Portland Cements: Basic and Engineering Properties. *Cem. Concr. Res.* **2006,** *36*, (3), 487-491.

124. Gameiro, A. L.; Silva, A. S.; Veiga, M. d. R.; Velosa, A. L., Lime-metakaolin Hydration Products: a Microscopy Analysis. *Materiali in Tehnologije* **2012,** *46*, (2), 145-148.

125. Schwertmann, U., Solubility and Dissolution of Iron Oxides. In *Iron Nutrition and Interactions in Plants*, Springer: 1991; pp 3-27.

126. Schwertmann, U.; Cornell, R. M., *Iron Oxides in the Laboratory*. John Wiley & Sons: 2008.

127. Bondietti, G.; Sinniger, J.; Stumm, W., The Reactivity of Fe(III)(hydr)oxides: Effects of Ligands in Inhibiting the Dissolution. *Colloids Surf. Physicochem. Eng. Aspects* **1993,** *79*, (2), 157-167.

128. Stumm, W., Reactivity at the Mineral-Water Interface: Dissolution and Inhibition. *Colloids Surf. Physicochem. Eng. Aspects* **1997,** *120*, (1), 143-166.

129. Rimstidt, D.; Huminicki, D. In *The Effect of Gypsum Coatings and Hydrodynamic Factors on Anoxic Limestone Drain Performance*, Proc. West Virginia Mine Drainage Task Force Symposium, Morgantown, WV, 2006; 2006; pp 109-110.

130. Soler, J. M.; Boi, M.; Mogollón, J. L.; Cama, J.; Ayora, C.; Nico, P. S.; Tamura, N.; Kunz, M., The Passivation of Calcite by Acid Mine Water: Column Experiments with Ferric Sulfate and Ferric Chloride Solutions at pH 2. *Appl. Geochem.* **2008,** *23*, (12), 3579-3588.

131. Walker, R. A.; Wilson, K.; Lee, A. F.; Woodford, J.; Grassian, V. H.; Baltrusaitis, J.; Rubasinghege, G.; Cibin, G.; Dent, A., Preservation of York Minster Historic Limestone by Hydrophobic Surface Coatings. *Sci. Rep.* **2012,** *2*.

132. Wilkins, S. J.; Compton, R. G.; Taylor, M. A.; Viles, H. A., Channel Flow Cell Studies of the Inhibiting Action of Gypsum on the Dissolution Kinetics of Calcite: A Laboratory Approach With Implications for Field Monitoring. *J. Colloid Interface Sci.* **2001,** *236*, (2), 354-361.

133. Walter, L. M., Relative Efficiency of Carbonate Dissolution and Precipitation During Diagenesis: A Progress Report on the Role of Solution Chemistry. **1986**.

134. Cowan, C. E.; Zachara, J. M.; Resch, C. T., Solution Ion Effects on the Surface Exchange of Selenite on Calcite. *Geochim. Cosmochim. Acta* **1990,** *54*, (8), 2223-2234.

135. Gomari, K.; Hamouda, A.; Denoyel, R., Influence of Sulfate Ions on the Interaction Between Fatty Aids and Calcite Surface. *Colloids Surf. Physicochem. Eng. Aspects* **2006,** *287*, (1), 29-35.

136. Compton, R. G.; Brown, C. A., The Inhibition of Calcite Dissolution/Precipitation: Mg^{2+} Cations. *J. Colloid Interface Sci.* **1994,** *165*, (2), 445-449.

137. Compton, R. G.; Brown, C. A., The Inhibition of Calcite Dissolution/Precipitation: 1, 2-Dicarboxylic Acids. *J. Colloid Interface Sci.* **1995,** *170*, (2), 586-590.

138. Compton, R. G.; Pritchard, K. L.; Unwin, P. R.; Grigg, G.; Silvester, P.; Lees, M.; House, W. A., The Effect of Carboxylic Acids on the Dissolution of Calcite in Aqueous Solution. Part 1.—Maleic and Fumaric Acids. *J. Chem. Soc., Farad. T. 1* **1989,** *85*, (12), 4335-4366.

139. Brown, C. A.; Compton, R. G.; Narramore, C. A., The Kinetics of Calcite Dissolution/Precipitation. *J. Colloid Interface Sci.* **1993,** *160*, (2), 372-379.

140. Morse, J. W.; Arvidson, R. S., The Dissolution Kinetics of Major Sedimentary Carbonate Minerals. *Earth-Sci. Rev.* **2002,** *58*, (1), 51-84.

141. Morse, J. W.; Arvidson, R. S.; Lüttge, A., Calcium Carbonate Formation and Dissolution. *Chem. Rev.* **2007,** *107*, (2), 342-381.

142. Kontrec, J.; Kralj, D.; Brečević, L.; Falini, G.; Fermani, S.; Noethig-Laslo, V.; Mirosavljević, K., Incorporation of Inorganic Anions in Calcite. *Eur. J. Inorg. Chem.* **2004,** *2004*, (23), 4579-4585.

143. Hu, Y.; Jun, Y.-S., Biotite Dissolution in Brine at Varied Temperatures and CO_2 Pressures: Its Activation Energy and Potential CO_2 Intercalation. *Langmuir* **2012,** *28*, (41), 14633-14641.

144. Quennoz, A., Hydration of C_3A with Calcium Sulfate Alone and in the Presence of Calcium Silicate. **2011**.

145. Duan, Z.; Sun, R., An Improved Model Calculating CO_2 Solubility in Pure Water and Aqueous NaCl Solutions from 273 to 533 K and from 0 to 2000 bar. *Chem. Geol.* **2003,** *193*, (3), 257-271.

146. Wolterbeek, T. K.; Peach, C. J.; Spiers, C. J., Reaction and Transport in Wellbore Interfaces under CO_2 Storage Conditions: Experiments Simulating Debonded Cement–Casing Interfaces. *Int. J. Greenh. Gas Control* **2013,** *19*, 519-529.

147. Hangx, S. J.; Linden, A. v. d.; Marcelis, F.; Liteanu, E., Defining the Brittle Failure Envelopes of Individual Reaction Zones Observed in CO_2-Exposed Wellbore Cement. *Environ. Sci. Technol.* **2016,** *50*, (2), 1031-1038.

148. Li, Q.; Lim, Y. M.; Jun, Y.-S., Effects of Sulfate during CO_2 Attack on Portland Cement and Their Impacts on Mechanical Properties under Geologic CO_2 Sequestration Conditions. *Environ. Sci. Technol.* **2015,** *49*, (11), 7032-7041.

149. Abdoulghafour, H.; Gouze, P.; Luquot, L.; Leprovost, R., Characterization and Modeling of the Alteration of Fractured Class-G Portland Cement During Flow of CO_2-Rich Brine. *Int. J. Greenh. Gas Control* **2016,** *48*, 155-170.

150. Brunet, J.-P. L.; Li, L.; Karpyn, Z. T.; Huerta, N. J., Fracture Opening or Self-Sealing: Critical Residence Time as a Unifying Parameter for Cement–CO_2–Brine Interactions. *Int. J. Greenh. Gas Control* **2016,** *47*, 25-37.

151. Marty, N. C.; Tournassat, C.; Burnol, A.; Giffaut, E.; Gaucher, E. C., Influence of Reaction Kinetics and Mesh Refinement on the Numerical Modelling of Concrete/Clay Interactions. *J. Hydrol.* **2009,** *364*, (1), 58-72.

152. Raoof, A.; Nick, H.; Wolterbeek, T.; Spiers, C., Pore-Scale Modeling of Reactive Transport in Wellbore Cement under CO_2 Storage Conditions. *Int. J. Greenh. Gas Control* **2012,** *11*, S67-S77.

153. Steefel, C. I., CrunchFlow. *Software for Modeling Multicomponent Reactive Flow and Transport. User's Manual. Lawrence Berkeley National Laboratory, Berkeley* **2009**.

154. Holzbecher, E., *Environmental Modeling: using MATLAB*. Springer Science & Business Media: 2012.

155. Wolery, T. J., *EQ3/6: A Software Package for Geochemical Modeling of Aqueous Systems: Package Overview and Installation Guide (version 7.0)*. Lawrence Livermore National Laboratory Livermore, CA: 1992.

156. Database, T. http://thermoddem.brgm.fr/

157. De Windt, L.; Marsal, F.; Tinseau, E.; Pellegrini, D., Reactive Transport Modeling of Geochemical Interactions at a Concrete/Argillite Interface, Tournemire Site (France). *Phys. Chem. Earth* **2008,** *33*, S295-S305.

158. Palandri, J. L.; Kharaka, Y. K. *A Compilation of Rate Parameters of Water-Mineral Interaction Kinetics for Application to Geochemical Modeling*; DTIC Document: 2004.

159. Wertz, F.; Gherardi, F.; Blanc, P.; Bader, A.; Fabbri, A. In *Modeling CO_2-Driven Cement Alteration at Well-Caprock Interface*, TOUGH Symposium, 2012; 2012.

160. Neuville, N.; Lécolier, E.; Aouad, G.; Rivereau, A.; Damidot, D., Effect of Curing Conditions on Oilwell Cement Paste Behaviour during Leaching: Experimental and Modelling Approaches. *CR. Chim.* **2009,** *12*, (3), 511-520.

161. Shao, C.; Yang, Z.; Zhou, G.; Lu, G., Pore Network Modeling of Water Block in Low Permeability Reservoirs. *Petroleum Science* **2010,** *7*, (3), 362-366.

162. De Yoreo, J. J.; Vekilov, P. G., Principles of Crystal Nucleation and Growth. *Rev. Mineral. Geochem.* **2003,** *54*, (1), 57-93.

163. Li, Q.; Jun, Y.-S., Heterogeneous Calcium Carbonate Nucleation in Saline Solution: Thermodynamic and Kinetic Contributions. In *251st ACS National Meeting*, San Diego, USA, 2016.

164. Li, Q.; Fernandez-Martinez, A.; Lee, B.; Waychunas, G. A.; Jun, Y.-S., Interfacial Energies for Heterogeneous Nucleation of Calcium Carbonate on Mica and Quartz. *Environ. Sci. Technol.* **2014,** *48*, (10), 5745-5753.

165. Emmanuel, S.; Ague, J. J.; Walderhaug, O., Interfacial Energy Effects and the Evolution of Pore Size Distributions during Quartz Precipitation in Sandstone. *Geochim. Cosmochim. Acta* **2010,** *74*, (12), 3539-3552.

166. Stack, A. G.; Fernandez-Martinez, A.; Allard, L. F.; Bañuelos, J. L.; Rother, G.; Anovitz, L. M.; Cole, D. R.; Waychunas, G. A., Pore-Size-Dependent Calcium Carbonate Precipitation Controlled by Surface Chemistry. *Environ. Sci. Technol.* **2014,** *48*, (11), 6177-6183.

167. Pearson, D.; Allen, A.; Windsor, C.; Alford, M. N.; Double, D., An Investigation on the Nature of Porosity in Hardened Cement Pastes using Small Angle Neutron Scattering. *J. Mater. Sci.* **1983,** *18*, (2), 430-438.

168. Allen, A.; Windsor, C.; Rainey, V.; Pearson, D.; Double, D.; Alford, N. M., A Small-Angle Neutron Scattering Study of Cement Porosities. *J. Phys. D: Appl. Phys.* **1982,** *15*, (9), 1817.

169. He, S.; Morse, J. W., The Carbonic Acid System and Calcite Solubility in Aqueous Na-K-Ca-Mg-Cl-SO_4 Solutions From 0 to 90 ^{o}C. *Geochim. Cosmochim. Acta* **1993,** *57*, (15), 3533-3554.

170. Gledhill, D. K.; Morse, J. W., Calcite Solubility in Na–Ca–Mg–Cl Brines. *Chem. Geol.* **2006,** *233*, (3), 249-256.

171. Akin, G.; Lagerwerff, J., Calcium Carbonate Equilibria in Solutions Open to the Air. II. Enhanced Solubility of $CaCO_3$ in the Presence of Mg^{2+} and SO_4^{2-}. *Geochim. Cosmochim. Acta* **1965,** *29*, (4), 353-360.

172. Chong, T.; Sheikholeslami, R., Thermodynamics and Kinetics for Mixed Calcium Carbonate and Calcium Sulfate Precipitation. *Chem. Eng. Sci.* **2001,** *56*, (18), 5391-5400.

173. Stephens, C. J.; Ladden, S. F.; Meldrum, F. C.; Christenson, H. K., Amorphous Calcium Carbonate is Stabilized in Confinement. *Adv. Funct. Mater.* **2010,** *20*, (13), 2108-2115.

174. Deng, H.; Molins, S.; Steefel, C.; DePaolo, D.; Voltolini, M.; Yang, L.; Ajo-Franklin, J., A 2.5 D Reactive Transport Model for Fracture Alteration. *Environ. Sci. Technol.* **2016**.

175. Thomas, J.; Jennings, H. Science of Concrete. http://people.ce.gatech.edu/~kk92/hyd07.pdf

176. Poisson, A.; Papaud, A., Diffusion Coefficients of Major Ions in Seawater. *Mar. Chem.* **1983,** *13*, (4), 265-280.

177. Li, Y.-H.; Gregory, S., Diffusion of Ions in Sea Water and in Deep-Sea Sediments. *Geochim. Cosmochim. Acta* **1974,** *38*, (5), 703-714.

178. Weiner, S.; Dove, P. M., An Overview of Biomineralization Processes and the Problem of the Vital Effect. *Rev. Mineral. Geochem.* **2003,** *54*, (1), 1-29.

179. Barker, W. W., Biomineralization. In *Clays and Clay Minerals*, 2004; Vol. 52, pp 657-657.

180. Lal, R., Carbon Sequestration. *Philos. T. R. Soc. B* **2008,** *363*, (1492), 815-830.

181. Mori, Y.; lIsogai, A.; Enomae, T., Application of Caterite-Type Calcium Carbonate Prepared by Ultrasound of Ink Jet Paper. *J. Imaging Sci. Technol.* **2010,** *54*, (2), 020504-020504-6.

182. Chen, T.; Neville, A.; Yuan, M., Calcium Carbonate Scale Formation—Assessing the Initial Stages of Precipitation and Deposition. *J. Petrol. Sci. Eng.* **2005,** *46*, (3), 185-194.

183. Al Nasser, W. N.; Shaikh, A.; Morriss, C.; Hounslow, M. J.; Salman, A. D., Determining Kinetics of Calcium Carbonate Precipitation by Inline Technique. *Chem. Eng. Sci.* **2008,** *63*, (5), 1381-1389.

184. Andritsos, N.; Karabelas, A. J.; Koutsoukos, P. G., Morphology and Structure of CaCO3 Scale Layers Formed under Isothermal Flow Conditions. *Langmuir* **1997,** *13*, (10), 2873-2879.

185. Inskeep, W. P.; Bloom, P. R., An Evaluation of Rate Equations for Calcite Precipitation Kinetics at PCO_2 Less than 0.01 atm and pH Greater than 8. *Geochim. Cosmochim. Acta* **1985,** *49*, (10), 2165-2180.

186. Dove, P. M.; Hochella Jr, M. F., Calcite precipitation mechanisms and inhibition by orthophosphate: In situ observations by Scanning Force Microscopy. *Geochim. Cosmochim. Acta* **1993,** *57*, (3), 705-714.

187. Vavouraki, A. I.; Putnis, C. V.; Putnis, A.; Koutsoukos, P. G., An Atomic Force Microscopy Study of the Growth of Calcite in the Presence of Sodium Sulfate. *Chem. Geol.* **2008,** *253*, (3–4), 243-251.

188. Ben Amor, Y.; Bousselmi, L.; Bernard, M. C.; Tribollet, B., Nucleation-Growth Process of Calcium Carbonate Electrodeposition in Artificial Water—Influence of the Sulfate Ions. *J. Cryst. Growth* **2011,** *320*, (1), 69-77.

189. Wilkinson, M.; Haszeldine, R. S., Fibrous Illite in Oilfield Sandstones – a Nucleation Kinetic Theory of Growth. *Terra Nova* **2002,** *14*, (1), 56-60.

190. Giammar, D. E.; Bruant, R. G.; Peters, C. A., Forsterite Dissolution and Magnesite Precipitation at Conditions Relevant for Deep Saline Aquifer Storage and Sequestration of Carbon Dioxide. *Chem. Geol.* **2005,** *217*, (3), 257-276.

191. Koutsoukos, P. G.; Kontoyannis, C. G., Prevention and Inhibition of Calcium Carbonate Scale. *J. Cryst. Growth* **1984,** *69*, (2–3), 367-376.

192. Verdoes, D.; Kashchiev, D.; van Rosmalen, G. M., Determination of Nucleation and Growth Rates from Induction Times in Seeded and Unseeded Precipitation of Calcium Carbonate. *J. Cryst. Growth* **1992,** *118*, (3–4), 401-413.

193. Neilsen, A. E., Nucleation in Aqueous Solution. In *Crystal Growth*, Peiser, H. S., Ed. Oxford: Pergamon Press: 1967; pp 419-430.

194. Yamanaka, S.; Ito, N.; Shimosaka, A.; Shirakawa, Y.; Hidaka, J., AFM Investigation for the Initial Growth Processes of Calcium Carbonate on Hydrophilic and Hydrophobic Substrate. *Cryst. Growth Des.* **2009,** *9*, (7), 3245-3250.

195. Yamanaka, S.; Ito, N.; Akiyama, K.; Shimosaka, A.; Shirakawa, Y.; Hidaka, J., Heterogeneous Nucleation and Growth Mechanism on Hydrophilic and Hydrophobic Surface. *Adv. Powder Technol.* **2012,** *23*, (2), 268-272.

196. Wang, Y. W.; Kim, Y. Y.; Stephens, C. J.; Meldrum, F. C.; Christenson, H. K., *In Situ* Study of the Precipitation and Crystallization of Amorphous Calcium Carbonate (ACC). *Cryst. Growth Des.* **2012,** *12*, (3), 1212-1217.

197. Jun, Y.-S.; Lee, B.; Waychunas, G. A., *In Situ* Observations of Nanoparticle Early Development Kinetics at Mineral−Water Interfaces. *Environ. Sci. Technol.* **2010,** *44*, (21), 8182-8189.

198. Navrotsky, A., Energetic Clues to Pathways to Biomineralization: Precursors, Clusters, and Nanoparticles. *Proc. Natl. Acad. Sci. USA.* **2004,** *101*, (33), 12096-12101.

199. Radha, A. V.; Forbes, T. Z.; Killian, C. E.; Gilbert, P. U. P. A.; Navrotsky, A., Transformation and Crystallization Energetics of Synthetic and Biogenic Amorphous Calcium Carbonate. *Proc. Natl. Acad. Sci. USA.* **2010,** *107*, (38), 16438-16443.

200. Hu, Y.; Neil, C.; Lee, B.; Jun, Y.-S., Control of Heterogeneous Fe (III)(hydr) Oxide Nucleation and Growth by Interfacial Energies and Local Saturations. *Environ. Sci. Technol.* **2013,** *47*, (16), 9198-9206.

201. Toman, K.; Taylor, P. R., Epitaxial Growth of Dolomite on Mica. *Am. Mineral.* **1974,** *59*, 871-872.

202. Chadwick, R. A.; Zweigel, P.; Gregersen, U.; Kirby, G. A.; Holloway, S.; Johannessen, P. N., Geological reservoir characterization of a CO2 storage site: The Utsira Sand, Sleipner, northern North Sea. *Energy* **2004,** *29*, (9–10), 1371-1381.

203. Krupka, K. M.; Cantrell, K. J.; McGrail, B. P. *Thermodynamic Data for Geochemical Modeling of Carbonate Reactions Associated with CO_2 sequestration - Literature Review*; Pacific Northwest National Laboratory (PNNL): 2010.

204. Johnson, J. W.; Nitao, J. J.; Knauss, K. G., Reactive Transport Modeling of CO_2 Storage in Saline Aquifers to Elucidate Fundamental Processes, Trapping Mechanisms and Sequestration Partitioning. *Geol. Soc. Spec. Publ.* **2004,** *233*, 107-128.

205. Phillips, A. J.; Lauchnor, E.; Eldring, J.; Esposito, R.; Mitchell, A. C.; Gerlach, R.; Cunningham, A. B.; Spangler, L. H., Potential CO_2 Leakage Reduction through Biofilm-Induced Calcium Carbonate Precipitation. *Environ. Sci. Technol.* **2012,** *47*, (1), 142-149.

206. Cole, D. R.; Chialvo, A. A.; Rother, G.; Vlcek, L.; Cummings, P. T., Supercritical fluid behavior at nanoscale interfaces: Implications for CO2 sequestration in geologic formations. *Philos. Mag.* **2010,** *90*, (17-18), 2339-2363.

207. Kharaka, Y.; Hanor, J., *Deep Fluids in the Continents: I. Sedimentary Basins*. 2003; Vol. 5, p 605.

208. Bethke, C.; Yeakel, S., The Geochemist's Workbench®, Version 8.0. Hydrogeology Program. University of Illinois. *Urbana* **2009**.

209. Brečević, L.; Nielsen, A. E., Solubility of Amorphous Calcium Carbonate. *J. Cryst. Growth* **1989,** *98*, (3), 504-510.

210. Renaud, G.; Lazzari, R.; Revenant, C.; Barbier, A.; Noblet, M.; Ulrich, O.; Leroy, F.; Jupille, J.; Borensztein, Y.; Henry, C. R., Real-time Monitoring of Growing Nanoparticles. *Science* **2003,** *300*, (5624), 1416-1419.

211. Lee, B.; Seifert, S.; Riley, S. J.; Tikhonov, G.; Tomczyk, N. A.; Vajda, S.; Winans, R. E., Anomalous Grazing Incidence Small-Angle X-Ray Scattering Studies of Platinum Nanoparticles Formed by Cluster Deposition. *J. Chem. Phys.* **2005,** *123*, 074701.

212. Narayanan, T., Synchrotron Small-Angle X-Ray Scattering Studies of Colloidal Suspensions. In *Applications of Synchrotron Light to Scattering and Diffraction in Materials and Life Sciences*, Gomez, M.; Nogales, A.; Garcia-Gutierrez, M. C.; Ezquerra, T. A., Eds. Springer Berlin Heidelberg: 2009; Vol. 776, pp 133-156.

213. Jun, Y.-S.; Kendall, T. A.; Martin, S. T.; Friend, C. M.; Vlassak, J. J., Heteroepitaxial Nucleation and Oriented Growth of Manganese Oxide Islands on Carbonate Minerals under Aqueous Conditions. *Environ. Sci. Technol.* **2005,** *39*, (5), 1239-1249.

214. Gabrielli, C.; Jaouhari, R.; Joiret, S.; Maurin, G., *In Situ* Raman Spectroscopy Applied to Electrochemical Scaling. Determination of the Structure of Vaterite. *J. Raman Spectrosc.* **2000,** *31*, (6), 497-501.

215. Forbes, T. Z.; Radha, A. V.; Navrotsky, A., The Energetics of Nanophase Calcite. *Geochim. Cosmochim. Acta* **2011,** *75*, (24), 7893-7905.

216. Kalikmanov, V. I., Heterogeneous Nucleation. In *Nucleation Theory*, Springer Netherlands: 2013; Vol. 860, pp 253-276.

217. Markov, I. V., *Crystal Growth for Beginners: Fundamentals of Nucleation, Crystal Growth and Epitaxy*. World Scientific Singapore: 2003.

218. Zheleva, T.; Jagannadham, K.; Narayan, J., Epitaxial Growth in Large-Lattice-Mismatch Systems. *J. Appl. Phys.* **1994,** *75*, (2), 860-871.

219. Quéré, D., Wetting and Roughness. *Annu. Rev. Mater. Res.* **2008,** *38*, 71-99.

220. Ethington, E. F., *Interfacial Contact Angle Measurements of Water, Mercury, and 20 Organic Liquids on Quartz, Calcite, Biotite, and Ca-Montmorillonite Substrates*. US Geological Survey: 1990.

221. Van der Merwe, J., Structure of Epitaxial Crystal Interfaces. *Surf. Sci.* **1972,** *31*, 198-228.

222. Nehrke, G.; Van Cappellen, P., Framboidal Vaterite Aggregates and Their Transformation into Calcite: A Morphological Study. *J. Cryst. Growth* **2006,** *287*, (2), 528-530.

223. Kim, Y.; Wan, J.; Kneafsey, T. J.; Tokunaga, T. K., Dewetting of Silica Surfaces upon Reactions with Supercritical CO_2 and Brine: Pore-Scale Studies in Micromodels. *Environ. Sci. Technol.* **2012,** *46*, (7), 4228-4235.

224. Bikkina, P. K., Contact Angle Measurements of CO_2–Water–Quartz/Calcite Systems in the Perspective of Carbon Sequestration. *Int. J. Greenh. Gas Control* **2011,** *5*, (5), 1259-1271.

225. Wang, S.; Edwards, I. M.; Clarens, A. F., Wettability Phenomena at the CO_2–Brine–Mineral Interface: Implications for Geologic Carbon Sequestration. *Environ. Sci. Technol.* **2012,** *47*, (1), 234-241.

226. Chiquet, P.; Broseta, D.; Thibeau, S., Wettability alteration of caprock minerals by carbon dioxide. *Geofluids* **2007,** *7*, (2), 112-122.

227. Alkan, H.; Cinar, Y.; Ülker, E., Impact of Capillary Pressure, Salinity and *In Situ* Conditions on CO_2 Injection into Saline Aquifers. *Transport porous Med.* **2010,** *84*, (3), 799-819.

228. Heath, J. E.; Dewers, T. A.; McPherson, B. J.; Nemer, M. B.; Kotula, P. G., Pore-lining phases and capillary breakthrough pressure of mudstone caprocks: Sealing efficiency of geologic CO_2 storage sites. *Int. J. Greenh. Gas Control* **2012,** *11*, 204-220.

229. Rodriguez-Blanco, J. D.; Shaw, S.; Benning, L. G., The Kinetics and Mechanisms of Amorphous Calcium Carbonate (ACC) Crystallization to Calcite, via Vaterite. *Nanoscale* **2011,** *3*, (1), 265-271.

230. Sekkal, W.; Zaoui, A., Nanoscale Analysis of the Morphology and Surface Stability of Calcium Carbonate Polymorphs. *Sci. Rep.* **2013,** *3*.

231. de Leeuw, N. H.; Parker, S. C., Surface Structure and Morphology of Calcium Carbonate Polymorphs Calcite, Aragonite, and Vaterite: An Atomistic Approach. *J. Phys. Chem. B* **1998,** *102*, (16), 2914-2922.

232. Tarasevich, Y. I., Surface Energy of Oxides and Silicates. *Theor. Exp. Chem.* **2006,** *42*, (3), 145-161.

233. Ray, J. R.; Lee, B.; Baltrusaitis, J.; Jun, Y.-S., Formation of Iron (III)(hydr) Oxides on Polyaspartate- and Alginate-Coated Substrates: Effects of Coating Hydrophilicity and Functional Group. *Environ. Sci. Technol.* **2012,** *46*, (24), 13167-13175.

234. Brinker, C. J.; Scherer, G. W., *Sol-Gel Science: the Physics and Chemistry of Sol-Gel Processing*. Academic press: 2013.

235. Smeets, P. J.; Cho, K. R.; Kempen, R. G.; Sommerdijk, N. A.; De Yoreo, J. J., Calcium Carbonate Nucleation Driven by Ion Binding in a Biomimetic Matrix Revealed by In Situ Electron Microscopy. *Nat. Mater.* **2015,** *14*, 394-339.

236. Baumgartner, J.; Dey, A.; Bomans, P. H.; Le Coadou, C.; Fratzl, P.; Sommerdijk, N. A.; Faivre, D., Nucleation and Growth of Magnetite from Solution. *Nat. Mater.* **2013,** *12*, (4), 310-314.

237. Xu, Z.; Yang, Y.; Zhao, W.; Wang, Z.; Landis, W. J.; Cui, Q.; Sahai, N., Molecular Mechanisms for Intrafibrillar Collagen Mineralization in Skeletal Tissues. *Biomaterials* **2015,** *39*, 59-66.

238. Chen, L.; Jacquet, R.; Lowder, E.; Landis, W. J., Refinement of Collagen–Mineral Interaction: A Possible Role for Osteocalcin in Apatite Crystal Nucleation, Growth and Development. *Bone* **2015,** *71*, 7-16.

239. Dokter, W. H.; van Garderen, H. F.; Beelen, T. P.; van Santen, R. A.; Bras, W., Homogeneous versus Heterogeneous Zeolite Nucleation. *Angew. Chem. Int. Edit.* **1995,** *34*, (1), 73-75.

240. Gebauer, D.; Völkel, A.; Cölfen, H., Stable Prenucleation Calcium Carbonate Clusters. *Science* **2008,** *322*, (5909), 1819-1822.

241. De Yoreo, J., Crystal Nucleation: More than One Pathway. *Nat. Mater.* **2013,** *12*, (4), 284-285.

242. Radha, A. V.; Fernandez-Martinez, A.; Hu, Y.; Jun, Y.-S.; Waychunas, G. A.; Navrotsky, A., Energetic and Structural Studies of Amorphous $Ca_{1-x}Mg_xCO_3 \cdot nH_2O$ ($0 =< x =< 1$). *Geochim. Cosmochim. Acta* **2012,** *90*, (0), 83-95.

243. Zuddas, P.; Mucci, A., Kinetics of Calcite Precipitation From Seawater: II. The Influence of the Ionic Strength. *Geochim. Cosmochim. Acta* **1998,** *62*, (5), 757-766.

244. Zhang, Y.; Dawe, R., The Kinetics of Calcite Precipitation from a High Salinity Water. *Appl. Geochem.* **1998,** *13*, (2), 177-184.

245. Zhong, S.; Mucci, A., Calcite and Aragonite Precipitation from Seawater Solutions of Various Salinities: Precipitation Rates and Overgrowth Compositions. *Chem. Geol.* **1989,** *78*, (3), 283-299.

246. Appelo, C. A. J.; Postma, D., *Geochemistry, Groundwater and Pollution*. CRC press: 2004.

247. Kalikmanov, V. I., Classical Nucleation Theory. In *Nucleation Theory*, Springer: 2013; pp 17-41.

248. Hu, Y.; Li, Q.; Lee, B.; Jun, Y.-S., Aluminum Affects Heterogeneous Fe (III)(Hydr)oxide Nucleation, Growth, and Ostwald Ripening. *Environ. Sci. Technol.* **2013,** *48*, (1), 299-306.

249. Neil, C. W.; Lee, B.; Jun, Y.-S., Different Arsenate and Phosphate Incorporation Effects on the Nucleation and Growth of Iron (III)(Hydr)oxides on Quartz. *Environ. Sci. Technol.* **2014,** *48*, (20), 11883-11891.

250. Jung, H.; Jun, Y.-S., Ionic Strength-Controlled Mn (Hydr)oxide Nanoparticle Nucleation on Quartz: Effect of Aqueous $Mn(OH)_2$. *Environ. Sci. Technol.* **2015,** *50*, (1), 105-113.

251. Li, T.; Senesi, A. J.; Lee, B., Small Angle X-ray Scattering for Nanoparticle Research. *Chem. Rev.* **2016**.

252. Leroy, P.; Lassin, A.; Azaroual, M.; André, L., Predicting the Surface Tension of Aqueous 1: 1 Electrolyte Solutions at High Salinity. *Geochim. Cosmochim. Acta* **2010,** *74*, (19), 5427-5442.

253. Markovich, T.; Andelman, D.; Podgornik, R., Surface Tension of Electrolyte Solutions: A Self-Consistent Theory. *EPL-Europhys. Lett.* **2014,** *106*, (1), 16002.

254. Pegram, L. M.; Record, M. T., Hofmeister Salt Effects on Surface Tension Arise from Partitioning of Anions and Cations Between Bulk Water and the Air-Water Interface. *J. Phys. Chem. B* **2007,** *111*, (19), 5411-5417.

255. Slavchov, R. I.; Novev, J. K., Surface Tension of Concentrated Electrolyte Solutions. *J. Colloid Interface Sci.* **2012,** *387*, (1), 234-243.

256. Tuckermann, R., Surface Tension of Aqueous Solutions of Water-Soluble Organic and Inorganic Compounds. *Atmos. Environ.* **2007,** *41*, (29), 6265-6275.

257. Weissenborn, P. K.; Pugh, R. J., Surface Tension of Aqueous Solutions of Electrolytes: Relationship with Ion Hydration, Oxygen Solubility, and Bubble Coalescence. *J. Colloid Interface Sci.* **1996,** *184*, (2), 550-563.

258. Barranco, F. T.; Dawson, H. E.; Christener, J. M.; Honeyman, B. D., Influence of Aqueous pH and Ionic Strength on the Wettability of Quartz in the Presence of Dense Non-Aqueous-Phase Liquids. *Environ. Sci. Technol.* **1997,** *31*, (3), 676-681.

259. Iglauer, S.; Pentland, C.; Busch, A., CO_2 Wettability of Seal and Reservoir Rocks and the Implications for Carbon Geo-Sequestration. *Water Resour. Res.* **2015,** *51*, (1), 729-774.

260. Ray, J. R.; Tadepalli, S.; Nergiz, S. Z.; Liu, K.-K.; You, L.; Tang, Y.; Singamaneni, S.; Jun, Y.-S., Hydrophilic, Bactericidal Nanoheater–Enabled Reverse Osmosis Membranes to Improve Fouling Resistance. *ACS Appl. Mater. Interfaces* **2015,** *7*, (21), 11117-11126.

261. Spanos, N.; Koutsoukos, P. G., Kinetics of Precipitation of Calcium Carbonate in Alkaline pH at Constant Supersaturation. Spontaneous and Seeded Growth. *J. Phys. Chem. B* **1998,** *102*, (34), 6679-6684.

262. Ihli, J.; Kulak, A. N.; Meldrum, F. C., Freeze-Drying Yields Stable and Pure Amorphous Calcium Carbonate (ACC). *Chem. Commun.* **2013,** *49*, (30), 3134-3136.

263. Clarkson, J. R.; Price, T. J.; Adams, C. J., Role of Metastable Phases in the Spontaneous Precipitation of Calcium Carbonate. *J. Chem. Soc., Farad. T.* **1992,** *88*, (2), 243-249.

264. Mullin, J. W., *Crystallization*. Butterworth-Heinemann: 2001.

265. Nielsen, A. E.; Söhnel, O., Interfacial Tensions Electrolyte Crystal-Aqueous Solution, from Nucleation Data. *J. Cryst. Growth* **1971,** *11*, (3), 233-242.

266. Debenedetti, P. G.; Stillinger, F. H., Supercooled Liquids and the Glass Transition. *Nature* **2001,** *410*, (6825), 259-267.

267. Hu, Y.; Lee, B.; Bell, C.; Jun, Y.-S., Environmentally Abundant Anions Influence the Nucleation, Growth, Ostwald Ripening, and Aggregation of Hydrous Fe(III) Oxides. *Langmuir* **2012,** *28*, (20), 7737-7746.

268. Xia, Y.; Xia, X.; Peng, H.-C., Shape-Controlled Synthesis of Colloidal Metal Nanocrystals: Thermodynamic Versus Kinetic Products. *J. Am. Chem. Soc.* **2015,** *137*, (25), 7947-7966.

269. Lindberg, C.; Whiticar, A.; Dick, K. A.; Sköld, N.; Nygård, J.; Bolinsson, J., Silver as Seed-Particle Material for GaAs Nanowires–Dictating Crystal Phase and Growth Direction by Substrate Orientation. *Nano Lett.* **2016**.

270. Tomson, M.; Fu, G.; Watson, M.; Kan, A. In *Mechanisms of Mineral Scale Inhibition*, International Symposium on Oilfield Scale, 2002; Society of Petroleum Engineers: 2002.

271. Parambil, J. V.; Poornachary, S. K.; Tan, R. B.; Heng, J. Y., Template-Induced Polymorphic Selectivity: the Effects of Surface Chemistry and Solute Concentration on Carbamazepine Crystallisation. *CrystEngComm* **2014,** *16*, (23), 4927-4930.

272. Ievlev, A. V.; Jesse, S.; Cochell, T. J.; Unocic, R. R.; Protopopescu, V. A.; Kalinin, S. V., Quantitative Description of Crystal Nucleation and Growth from in Situ Liquid Scanning Transmission Electron Microscopy. *ACS Nano* **2015**.

273. Zimmermann, N. E.; Vorselaars, B.; Quigley, D.; Peters, B., Nucleation of NaCl from Aqueous Solution: Critical Sizes, Ion-Attachment Kinetics, and Rates. *J. Am. Chem. Soc.* **2015,** *137*, (41), 13352-13361.

274. Poonoosamy, J.; Curti, E.; Kosakowski, G.; Grolimund, D.; Van Loon, L.; Mäder, U., Barite Precipitation Following Celestite Dissolution in a Porous Medium: A SEM/BSE and μ-XRD/XRF Study. *Geochim. Cosmochim. Acta* **2016,** *182*, 131-144.

275. Vehkamäki, H., *Classical Nucleation Theory in Multicomponent Systems*. Springer Science & Business Media: 2006.

276. Nielsen, A. E., *Kinetics of Precipitation*. Pergamon Press Oxford: 1964.

277. Fitts, J. P.; Peters, C. A., Caprock Fracture Dissolution and CO_2 Leakage. *Rev. Mineral. Geochem.* **2013,** *77*, (1), 459-479.

278. Power, I. M.; Harrison, A. L.; Dipple, G. M.; Wilson, S. A.; Kelemen, P. B.; Hitch, M.; Southam, G., Carbon Mineralization: from Aatural analogues to Engineered Systems. *Rev. Mineral. Geochem.* **2013,** *77*, (1), 305-360.

Curriculum Vitae

Qingyun Li

Department of Energy, Environmental and Chemical Engineering
Washington University, St. Louis, MO 63130
Tel(Cell): 314-560-9329
Email: qingyun.li@wustl.edu

EDUCATION

08/2011 – 08/2016
Ph.D. in Energy, Environmental and Chemical Engineering Washington University, St. Louis, MO, USA
Dissertation: "Calcium Carbonate Formation in Energy-Related Subsurface Environments and Engineered Systems"

09/2007 – 07/2011
B.S. in Environmental Sciences, Peking University, Beijing, China
Thesis: "Influence of Surfactant on the Deposition Kinetics of Bacteriophage MS2 on Mineral Surface"
B.A. in Economics (coursework-based), Peking University, Beijing, China

PROFESSIONAL EXPERIENCE

2011-present **Graduate Research Assistant,** Department of Energy, Environmental and Chemical Engineering, Washington University.

- Heterogeneous $CaCO_3$ nucleation and precipitation on silicate mineral surfaces from aqueous solution
- Homogeneous and heterogeneous ferric (hydr)oxides nucleation and precipitation in solution and on mineral surfaces
- Chemical and mechanical alteration of cement under conditions relevant to geologic CO_2 sequestration
- Dissolution and morphology changes of mica's basal and edge surfaces under geologic CO_2 sequestration conditions
- Colloidal stability of CeO_2 nanoparticles in aqueous solution in the presence of Fe^{2+} ions

2016 **Member of Graduate Student Committee** for department's faculty search.

2012-present **Outreach Program Lecturer and Lab Instructor** for middle school students in St. Louis area (approx. twice a year).

2012-2013 **Teaching Assistant** for ChE476 "Properties of Materials" and ChE351 "Engineering Analysis of Chemical Systems"

2010-2011 **Undergraduate Research Assistant**, College of Environmental Sciences and Engineering, Peking University.

- Deposition behaviors of bacteriophage MS2 on clay mineral surfaces using quartz crystal microbalance with dissipation monitoring.
- Transport of *Escherichia coli* through silica sand porous media suing column setup.

HONORS AND AWARDS

- Graduate Student Award for Research, Department of Energy, Environmental and Chemical Engineering, Washington University, March, **2016**
- Travel Grant from the North Central Section of the Geological Society of America to attend GSA North-Central Section Meeting, March, **2016**
- Graduate Student Awards in Environmental Chemistry in the Division of Environmental Chemistry of the American Chemical Society, February **2016**
- Geochemical Society Student Travel Award to attend the short course on "Pore Scale Geochemical Processes" and the 2015 Goldschmidt Meeting, August **2015**
- Travel Award to attend Synchrotron Environmental Science VI, Advanced Photon Source, Argonne National Laboratory, September **2014**

JOURNAL PAPERS

1. **Qingyun Li**, Yun Mook Lim, and Young-Shin Jun, "Effects of Sulfate during CO_2 Attack on Portland Cement and Their Impacts on the Mechanical Properties under Geologic CO_2 Sequestration Conditions." *Environmental Science & Technology*, **2015**, *49* (11), 7032–7041

2. **Qingyun Li**, Yun Mook Lim, Katharine M. Flores, Kelly Kranjc, and Young-Shin Jun, "Chemical Reactions of Portland Cement with Aqueous CO_2 and Their Impacts on Cement's Mechanical Properties under Geologic CO_2 Sequestration Conditions." *Environmental Science & Technology*, **2015**, *49* (10), 6335–6343

3. Xuyang Liu, Jessica R. Ray, Chelsea W. Neil, **Qingyun Li**, and Young-Shin Jun. "Enhanced Colloidal Stability of CeO_2 Nanoparticles by Ferrous Ions: Adsorption, Redox

Reaction, and Surface Precipitation." *Environmental Science & Technology*, **2015**, *49* (9), 5476-5483.

4. **Qingyun Li**, Alejandro Fernandez-Martinez, Byeongdu Lee, Glenn A. Waychunas, and Young-Shin Jun. "Interfacial Energies for Heterogeneous Nucleation of Calcium Carbonate on Mica and Quartz." *Environmental Science & Technology*, **2014**, *48* (10), 5745-5753.

5. Yandi Hu, **Qingyun Li**, Byeongdu Lee, and Young-Shin Jun. "Aluminum Affects Heterogeneous Fe (III) (Hydr)Oxide Nucleation, Growth, and Ostwald Ripening." *Environmental Science & Technology*, **2014,** *48* (1), 299-306.

6. Yun Shen, Hyunjung Kim, Meiping Tong, and **Qingyun Li**. "Influence of Solution Chemistry on the Deposition and Detachment Kinetics of RNA on Silica Surfaces." *Colloids and Surfaces B: Biointerfaces*, 2011, *82* (2), 443-449.

MANUSCRIPTS SUBMITTED/IN PREPARATION

1. **Qingyun Li** and Young-Shin Jun, "High Salinity Promotes $CaCO_3$ Nucleation on Quartz: Investigation of Interfacial Energies and Kinetic Factors, *Submitted*"

2. Yujia Min, **Qingyun Li**, Marco Voltolini, Timothy Kneafsey, and Young-Shin Jun, "Wollastonite Carbonation in Water-bearing CO_2: Effects of Particle Sizes."

3. **Qingyun Li**, Carl I. Steefel, and Young-Shin Jun, "Deciphering Calcium Carbonate Precipitation during Cement Deterioration using Reactive Transport Modeling."

4. **Qingyun Li** and Young-Shin Jun, "Quantification of the Activation Energy and Pre-exponential Factor in the Nucleation Rate Equation for Heterogeneous $CaCO_3$ Nucleation on Quartz."

CONFERENCE PRESENTATIONS

1. Zhenyu Xu, **Qingyun Li**, Timothy J. Kneafsey, Julie Sheets, David Cole, Young-Shin Jun, Laura J. Pyrak-Nolte. Modification of Fracture Geometry by Calcite Precipitation. The 50th US Rock Mechanics/Geomechanics Symposium, Houston, TX, June 26-29, 2016.

2. **Qingyun Li**, Carl I. Steefel, and Young-Shin Jun. Wellbore Cement Alteration by CO_2 and its Implications for Geologic Sequestration of CO_2 Produced from Energy

Production.(Poster) The 5th annual C3E Women in Clean Energy Symposium, Palo Alto, CA, May 31, 2016.

3. **Qingyun Li**, Yun Mook Lim, and Young-Shin Jun. Coupling the Chemical and Mechanical Alterations of Portland Cement Reacted in the Presence of Sulfate Ions under Geologic CO_2 Sequestration Conditions.(Oral) The 50th Annual Meeting of Geological Society of America North-Central Section, Champaign, IL, April 18-19, 2016.

4. **Qingyun Li**, Carl I. Steefel, Yun Mook Lim, and Young-Shin Jun. Experimental and Modeling Investigations of Portland Cement Deterioration under Geologic CO_2 Sequestration Conditions.(Oral) The 251st American Chemical Society National Meeting & Exposition, San Diego, CA, March 13-17, 2016.

5. **Qingyun Li** and Young-Shin Jun. Heterogeneous Calcium Carbonate Nucleation in Saline Solution: Thermodynamic and Kinetic Contributions.(Oral) The 251st American Chemical Society National Meeting & Exposition, San Diego, CA, March 13-17, 2016.

6. **Qingyun Li**, Carl I. Steefel, and Young-Shin Jun. Impacts of CO_2 Attack on Integrity of Cementitious Seals under Geologic CO_2 Sequestration Conditions. (Poster) EFRC Mid-term Review, Gaithersburg, MD, March 1, 2016.

7. Zhenyu Xu, Julie Sheets, **Qingyun Li**, Timothy Kneafsey, David Cole, Young-Shin Jun, and Laura Pyrak-Nolte. Modification of Fracture Apertures by Reactive Multiphase Flow. The 2015 AGU Fall meeting, San Francisco, CA, December 14-18, 2015.

8. **Qingyun Li**, Young-Shin Jun, and Carl I. Steefel. Can a Carbonated Layer Protect Wellbore Cement during Geologic CO_2 sequestration? (Oral) The 2015 AGU Fall meeting, San Francisco, CA, December 14-18, 2015.

9. **Qingyun Li**, Young-Shin Jun, and Carl I. Steefel. Incorporating Pore-scale Insights into Continuum Models for Cement Degradation under Geologic CO_2 Sequestration Conditions.(Poster) a symposium on "15f: Pore Scale and Nano-Confined Geochemical Processes," 2015 Goldschmidt conference, Prague, Czech Republic, August 17-22, 2015.

10. **Qingyun Li**, Young-Shin Jun, and Carl I. Steefel. Incorporating Pore-scale Insights into Continuum Models for Cement Degradation under Geologic CO_2 Sequestration Conditions. (Poster) "Pore Scale Geochemical Processes" GSA and MSA short course, Prague, Czech Republic, August 15-16, 2015.

11. **Qingyun Li**, Yun Mook Lim, and Young-Shin Jun. Chemical and Mechanical Alterations of Portland Cements by Aqueous CO_2 and SO_4^{2-} under Geologic CO_2 Sequestration Relevant Conditions.(Oral) Special session on "Geochemistry and

Reactive Transport in Nano-Pore Geomaterials", Division of Geochemistry, The 249th ACS National Meeting, Denver, CO, March 22-26, 2015.

12. **Qingyun Li**, Young-Shin Jun, Yun Mook Lim, Byeongdu Lee, Carl I. Steefel, Timothy J. Kneafsey, and Laura Pyrak-Nolte. Calcium Carbonate Nucleation in Brines and its Precipitation in Altered Cement under Geologic CO_2 Sequestration (GCS): Coupling Understanding between Chemical and Mechanical Properties.(Poster) 2014 Fall EFRC NCGC All hands meeting, Berkeley, CA, November 3-4, 2014.

13. Alejandro Fernandez-Martinez, Andrew Stack, **Qingyun Li**, Yandi Hu, Young-Shin Jun, Glenn A. Waychunas. Carbonate Mineral Nucleation in Nanopores and on Flat Surfaces: Understanding Interfacial Energy Controls. 24th Earth Sciences Meeting, Pau, France, October 27-31, 2014.

14. **Qingyun Li,** Byeongdu Lee, and Young-Shin Jun. Effects of Salinity on Heterogeneous Nucleation of Calcium Carbonate on Quartz: Interfacial Energies in Highly Saline Environments.(Poster) Synchrotron Environmental Science-VI conference, the Advanced Photon Source, Argonne National Laboratory, IL, September 11-12, 2014.

15. Young-Shin Jun, **Qingyun Li**, Byeongdu Lee, Alejandro Fernandez-Martinez, and Glenn A. Waychunas. Interfacial Energy guides Preferential $CaCO_3$ Nucleation on Specific Substrates. Gordon Research Conference on Biomineralization, Colby-Sawyer College, New London, NH, August 17-22, 2014.

16. **Qingyun Li**, Byeongdu Lee, Alejandro Fernandez-Martinez, Glenn A. Waychunas, and Young-Shin Jun. Calcium Carbonate Polymorphs on Mica Substrates and Their Interfacial Free Energies: Implications for Mineral Trapping Mechanisms in Geologic CO_2 Sequestration.(Oral) The 50th Anniversary Meeting of the Clay Minerals Society, University of Illinois at Urbana-Champaign, IL, October 6-10, 2013.

17. **Qingyun Li**, Alejandro Fernandez-Martinez, Byeongdu Lee, Glenn A. Waychunas, and Young-Shin Jun. Understanding Calcium Carbonate Nucleation in Heterogeneous Subsurfaces via Interfacial Energy Determination.(Poster) The 2013 Annual Mid-American Environmental Engineering Conference (MAEEC), Washington University in St. Louis, MO, September 21, 2013.

18. Young-Shin Jun, **Qingyun Li**, Alejandro Fernandez-Martinez, Yandi Hu, and Glenn A. Waychunas. Calcium Carbonate Polymorphs on Mica and Quartz Substrates and Their Interfacial Energies: Crucial Information for Predicting Permeability Changes during Geologic CO_2 Sequestration. DOE's Energy Frontier Research Center PIs meeting, Washington, D.C. July 18-19, 2013.

SYNCHROTRON X-RAY NATIONAL FACILITY BEAMTIME

1. **Qingyun Li** and Young-Shin Jun. Effects of substrate, temperature, salinity, and organic compounds on calcium carbonate nucleation on mineral surfaces. APS 12ID-B (Advanced Photon Source, Argonne National Lab) beamtime proposal (2015-3 and 2014-3): grazing incidence small angle X-ray Scattering (GISAXS) and small angle X-ray Scattering (SAXS) measurements.

2. **Qingyun Li** and Young-Shin Jun. In situ experimental observation of heterogeneous nucleation of $CaCO_3$ for modeling of CO_2 mineralization in geologic CO_2 sequestration sites. APS 12ID-B (Advanced Photon Source, Argonne National Lab) beamtime proposal (2016-1): small angle X-ray Scattering (SAXS), grazing incidence small angle X-ray Scattering (GISAXS), and grazing incidence wide angle X-ray Scattering (GIWAXS) measurements.

CERTIFICATION

Engineer-in-Training certification in Chemical Engineering, State of Missouri, 2016.

STUDENTS ADVISED

Ms. Emily Wen (January 2015-May 2015, Environmental Earth Science undergraduate, EECE WUStL undergraduate): Geologic CO_2 sequestration: cement integrity improvement for energy-related subsurface operations

Mr. Yinxuan Qiu (September 2014-December 2014, EECE WUStL master student): Cement self-healing under geologic CO_2 sequestration

Mr. Wesley Beck (June 2014-August 2014, EECE WUStL undergraduate): Geologic CO_2 sequestration

Mr. Matthew Decuir (June 2013-July 2013, Chemical Engineering, Auburn University): Mechanical properties of biotite before and after reaction under geologic CO_2 sequestration conditions

PROFESSIONAL SOCIETY MEMBERSHIPS

Member of Geological Society of America, 2016-present

Member of American Geophysical Union, 2015-present

Member of American Chemical Society, 2014-present

Member of Clay Minerals Society, 2013-2014